THE OUTER HALOES OF MASSIVE ELLIPTICAL GALAXIES

PAYEL DAS

THE OUTER HALOES OF MASSIVE ELLIPTICAL GALAXIES

PAYEL DAS

Dissertation
an der Fakultät für Physik
der Ludwig-Maximilians-Universität
München

vorgelegt von
Payel Das
aus Raj-Nilgiri, Indien

München, den 20 Januar 2011

ERSTGUTACHTER: PD Dr. Ortwin Gerhard
ZWEITGUTACHTER: Prof. Dr. Hans Böhringer

TAG DER MÜNDLICHEN PRÜFUNG: 01 April 2011

The mind is not a vessel to be filled but a fire to be kindled.

— Plutarch

Dedicated to the loving memory of my grandfathers.

ABSTRACT

This thesis has focused on the outer haloes of a sample of six massive elliptical galaxies in the nearby universe. NGC 1399 is located at the centre of the Fornax cluster, NGC 1407 and NGC 5846 at the centre of groups, and NGC 4472 (M49), NGC 4486 (M87), and NGC 4649 (M60) at the centre of sub-clumps in the irregular Virgo cluster.

A new method based on Bayesian statistics has been developed to constrain the mass distribution from density and temperature profiles of the surrounding hot gas. Dynamical models were created for NGC 4486 and NGC 5486 using Jeans equations and assuming a potential determined from X-ray observations. For NGC 1399 and NGC 4649, dynamical models were created in a range of potentials using the flexible N-body made-to-measure code, NMAGIC. Photometric constraints from surface-brightness images and kinematic constraints from long-slit, planetary nebula (PN) and globular cluster (GC) data were used.

The X-ray circular velocity curves are often lower in the central ~ 10 kpc compared to previous dynamical models and dynamical models of NGC 1399 and NGC 4649 in this work. Further out they all rise, while the dynamical circular velocity curves of NGC 1399 and NGC 4649 are approximately isothermal in the halo. The central discrepancies could be due to non-thermal contributions of $\lesssim 35\%$ in the pressure (with stronger effects in NGC 4486), multiple-temperature components in the hot gas, or mass profiles that are insufficiently general in the dynamical modelling. Discrepancies in the halo may arise from uncertainties associated with the deprojection of the temperature and density profiles, metallicity gradients, and disturbances from gas outflows.

The X-ray analyses point towards massive dark matter haloes with dark matter mass fractions of $\sim$ 35–80% at $2\,R_e$, rising to a maximum of 80–90% at the outermost radii. The dynamical models of NGC 1399 find a significantly more diffuse halo with hardly any dark matter within $1\,R_e$ and only 55% at $5\,R_e$. Despite the uncertainties in the X-ray mass distributions, the sample follows a Tully-Fisher relation with slope ~ 4, and the circular velocities and stellar luminosities at $1\,R_e$ correlate strongly with the velocity dispersion of the local environment. These relations suggest a close link between the properties of central X-ray bright elliptical galaxies and their local environments.

Kinematic data in the halo have been found to be fundamental for differentiating between mass profiles. The particular circular velocity curves and stellar density profiles of massive elliptical galaxies result in an approximate independence of the measured velocity dispersions from the anisotropy. Therefore discrete tracers, which at present generally only resolve the line-of-sight velocity distribution up to the first two moments, are able to

provide strong constraints. The PNe in NGC 4486 were also invaluable in finding the truncation of the stellar halo at $\sim$ 150 kpc. The models of NGC 4649 however found that GCs should be treated with caution as they may form a dynamically distinct system that does not trace the kinematics of the main stellar population.

A range of anisotropies were found in NGC 1399, NGC 4486, NGC 4649, and NGC 5846, pointing towards complex and varying formation histories.

ZUSAMMENFASSUNG

Diese Arbeit hat die äußeren Halos von sechs massereichen elliptischen Galaxien im nahen Universum zum Thema. NGC 1399 befindet sich im Zentrum des Fornax Galaxienhaufens, NGC 1407 und NGC 5846 in den Zentren von Galaxiengruppen und NGC 4472 (M49), NGC 4486 (M87) und NGC 4649 (M60) in den Zentren von Unterstrukturen des unregelmässigen Virgo-Haufens.

Eine neue, auf Bayesischer Statistik aufbauende Methode wurde entwickelt, um die Massenverteilung aus Dichte- und Temperaturprofilen des umgebenden heißen Gases einzugrenzen. Für NGC 4486 und NGC 5486 wurden dynamische Modelle als Lösungen der Jeans Gleichungen berechnet, mit dem aus den Röntgenbeobachtungen bestimmten Potential. Für NGC 1399 und NGC 4649 wurden mit dem flexiblen N-Körper made-to-measure Programm NMAGIC dynamische Modelle für eine ganze Reihe von Potentialen konstruiert. Die Modelle müssen den photometrischen Beobachtungsdaten aus Flächenhelligkeitsbildern genügen, sowie verschiedenen Kinematikdatensätzen von Langspalten, Planetarischen Nebeln (PN) und Kugelsternhaufen.

Verglichen mit vielen älteren dynamischen Modellen, sowie den Modellen für NGC 1399 und NGC 4649 aus dieser Arbeit, sind die Kreisgeschwindigkeiten aus Röntgenbeobachtungen in den innersten ~ 10 kpc niedrig. Zu grösseren Radien hin steigen sie jeweils an, allerdings sind die Kreisgeschwindigkeitskurven in den Halos von NGC 1399 und NGC 4649 aus dynamischen Modellen annähernd isotherm. Die Abweichungen in den inneren Bereichen könnten von nicht thermischen Beiträgen zum Druck in der Grössenordnung von $\lesssim 35\%$ herrühren (mit stärkeren Effekten in NGC 4486), von Gaskomponenten unterschiedlicher Temperaturen, oder davon, dass die Massenprofile in der dynamischen Modellierung nicht allgemein genug angesetzt waren. Abweichungen im Halo könnten Ungenauigkeiten in der Deprojektion der Temperatur- und Dichteprofile widerspiegeln, Metallizitätsgradienten, oder Störungen durch abströmendes Gas.

Die Röntgenanalyse weist auf massereiche Halos aus dunkler Materie hin, deren Anteil innerhalb $2\,R_e$ etwa $\sim$ 35–80% beträgt und zum äußersten Radius hin auf einen Maximalwert von 80–90% ansteigt. Die dynamischen Modelle für NGC 1399 lassen auf einen signifikant weniger konzentrierten Halo schließen, mit fast gar keiner dunklen Materie innerhalb von $1\,R_e$ und einem Anteil von nur 55% innerhalb $5\,R_e$. Ungeachtet der Unsicherheiten in den Röntgenmassenprofilen folgen die Galaxien der Tully-Fisher Relation mit einer Steigung von ~ 4 und die Kreisgeschwindigkeiten und stellaren Leuchtkräfte bei $1\,R_e$ korrelieren stark mit der Geschwindigkeitsdispersion der unmittelbaren Umgebung. Diese Beziehungen legen eine enge Verbindung zwischen den Eigenschaften der zentralen, röntgen-

leuchtkräftigen elliptischen Galaxien und ihrer unmittelbaren Umgebung nahe.

Kinematische Daten im Halo haben sich als fundamental erwiesen, um zwischen verschiedenen Masseprofilen zu unterscheiden. Die spezifischen Kreisgeschwindigkeitskurven und Sterndichteprofile in massereichen Galaxien sind gerade so, dass die beobachteten Geschwindigkeitsdispersionen annähernd unabhängig von der Anisotropie werden. Deshalb können auch diskrete Masseindikatoren wie die PN Geschwindigkeitsverteilung, als der man derzeit nur die ersten beiden Momente verlässlich bestimmen kann, die Massenverteilung wesentlich einschranken. Die PNe in NGC 4486 waren ferner außerordentlich wichtig, um herauszufinden, dass der stellare Halo bei etwa $\sim$ 150 kpc abbricht. Die Modelle von NGC 4649 lassen indes erkennen, dass GCs mit Vorsicht behandelt werden sollten, da sie möglicherweise ein separates dynamisches System bilden und ihre Kinematik nicht mit der stellaren Hauptpopulation übereinstimmt.

Die Variationsbreite der Anisotropien, die wir in NGC 1399, NGC 4486, NGC 4649 und NGC 5846 gefundenen haben zeigt, dass die Details der Verschmelzprozesse bei ihrer Entwicklung wichtig gewesen sein müssen.

PUBLICATIONS

Work in this thesis appears in the following publications:

Das, P., Gerhard, O., Churazov, E., Zhuravleva, I., 2010: *Steepening mass profiles, dark matter and environment of X-ray bright elliptical galaxies*, MNRAS, 409, 1362

Das, P., Gerhard, O., Coccato, L., Churazov, E., Forman, W., Finoguenov, A., Böhringer, H., Arnaboldi, M., Capaccioli, M., Cortesi, A., and 8 coauthors, 2008: *The orbital structure of the massive elliptical galaxy NGC 5846*, AN, 329, 940

Doherty, M., Arnaboldi, M., Das, P., Gerhard, O., Aguerri, J. A. L., Ciardullo, R., Feldmeier, J. J., Freeman, K. C., Jacoby, G. H., Murante, G., 2009: *The edge of the M 87 halo and the kinematics of the diffuse light in the Virgo cluster core*, A&A, 502, 771

Submitted

Das, P., Gerhard, O., Mendez, R. H., Teodorescu, A. M., de Lorenzi, F., 2011: *Using NMAGIC to probe the dark matter halo and orbital structure of the X-ray bright, massive elliptical galaxy, NGC 4649*, submitted to MNRAS

In preparation

Das, P., McNeil, E. K., Gerhard, O., Freeman, K. C., Coccato, L., Arnaboldi, M., de Lorenzi, F., 2011: *The outer halo of the central Fornax galaxy, NGC 1399*

CONTENTS

1 INTRODUCTION

The night sky is our window for viewing the billions of other galaxies in our Universe. A galaxy is a gravitationally-bound system consisting of stars, gas, and dark matter. The name originates from the Greek *galaxias* ($\gamma\alpha\lambda\alpha\epsilon\iota\alpha\sigma$), meaning 'milky', a reference to the Milky Way galaxy in which we live. Typical galaxies range from dwarfs with as few as 10^7 stars up to giant entities with 10^{12} stars. Most galaxies are 1 to 100 kiloparsecs[1] (kpc) in diameter and are usually separated by distances on the order of megaparsecs (Mpc). Some galaxies are found in the 'field', isolated from other galaxies, but the majority of galaxies are found in groups or clusters. These in turn can form larger conglomerates called superclusters. These larger structures are generally arranged into sheets and filaments, which surround immense voids in the Universe.

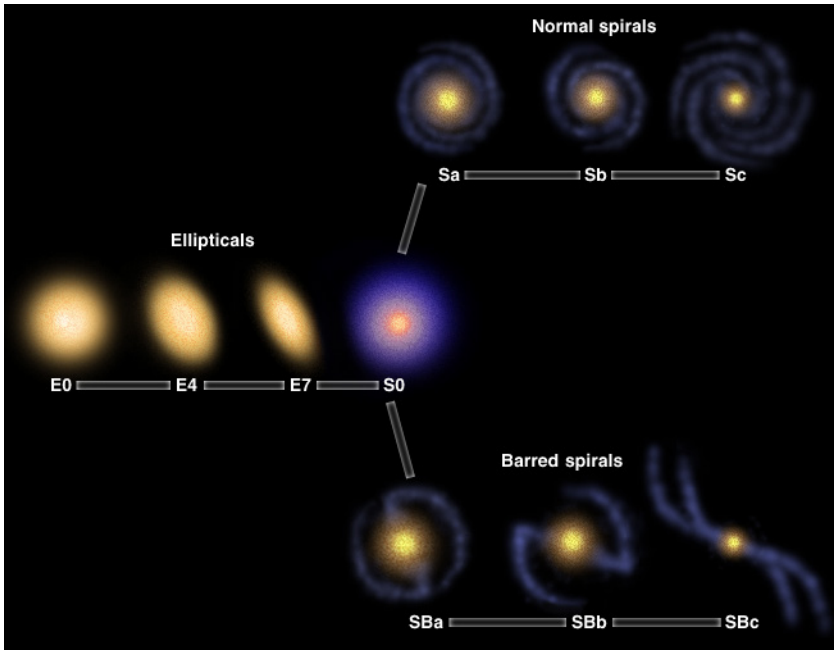

Figure 1: The Hubble Sequence, with thanks to the University of Texas, McDonald Observatory.

Historically, galaxies have been categorized according to their morphology, most notably in the Hubble Sequence (Hubble, 1936), shown in Figure 1. On the left of the point of bifurcation lie the elliptical galaxies. These have smooth, featureless light distributions and appear as ellipses in the sky. On the right are the spiral galaxies. A spiral galaxy consists of a flattened disk, with stars forming a spiral structure, and a central concentration of stars known as the bulge. Roughly half of all spirals also have

1 1 pc= 3.086×10^{16} m

a bar-like structure that extends from the central bulge and has spiral arms starting at either end. The regular spirals (S) belong in the upper branch in the Hubble diagram, while the lower branch contains the barred spirals (B). Spirals are further subdivided from 'a' ('early' spiral, large bulge compared to the disk, tightly wound and fairly smooth arms) to 'c' ('late' spiral, small bulge compared to the disk, loosely wound arms, lumpy arms with star-forming regions). Our own Milky Way is generally classed as SBb, making it a barred spiral with a relatively large bulge and quite smooth, well-defined arms.

Lenticular galaxies form a transitional class between ellipticals and spirals and occur at the bifurcation point in the Hubble diagram. These galaxies consist of a bright central bulge surrounded by an extended, disk-like structure but an absence of spiral arms and star formation. Lenticular and spiral galaxies are often referred to as 'disk' galaxies. Galaxies that do not fit into the Hubble sequence are called irregular galaxies.

Elliptical and lenticular galaxies are commonly referred to together as 'early-type' galaxies, while spirals and irregular galaxies are referred to as 'late types'. This nomenclature is the source of the common but erroneous belief that the Hubble sequence was intended to reflect an evolutionary sequence, from elliptical galaxies through lenticulars to either barred or regular spirals. It can instead be viewed as a stellar age sequence with early-type galaxies containing the oldest populations of stars, though spectroscopic observations from Trager et al. (2000) have also found the presence of young stellar populations. Revisions of the classification of early-type galaxies will be discussed below.

The present work focuses on unveiling the three-dimensional structure of some of the most massive elliptical galaxies observable in the local Universe (within a distance of 10^8 light years from our Milky Way). These galaxies are extremely bright and are believed to have a complex formation history, combining many processes that drive the evolution of galaxies. Therefore understanding how they formed will also give us an insight into the formation of other galaxies in the Universe. Firstly I will determine how mass is distributed in these galaxies between stars and 'dark matter', an unexplained component that only interacts through gravitational forces, yet dominates the mass of our Universe. Then I will uncover the distribution of the orbits of the stars, which have a memory of the processes that occurred to create the galaxy. By analysing the structure in detail, I hope to obtain a deeper insight into the role played by dark matter and the various formation mechanisms in the assembly of these systems.

Observations of nearby, elliptical galaxies are summarised in Section 1.1. Section 1.2 discusses the motions of stars in elliptical galaxies and Section 1.3 explains how one arrives at the dynamical properties of elliptical galaxies from observations. Section 1.4 discusses how knowledge of dynamical properties can be used

to place constraints on the formation mechanisms of elliptical galaxies. Finally, Section 1.5 introduces the sample of elliptical galaxies investigated in this work.

1.1 OBSERVED PROPERTIES OF NEARBY ELLIPTICAL GALAXIES

Elliptical galaxies were originally viewed as smooth and structureless, populated with old stars, and devoid of gas, dust and disks. With the improvement in the quality of observations over the last 40 years, this picture has taken quite a turn with discoveries such as central counter-rotating disks, cold and hot gas, and black holes. This Section summarises what has been learned about nearby, elliptical galaxies directly from their images and spectra in the optical and X-ray parts of the spectrum.

1.1.1 *Optical photometric properties*

Optical images of galaxies have been available since the invention of photography. They are two-dimensional projections of the three-dimensional distribution of stars in the galaxy, onto the plane of the sky. The amount of light per unit area is called the surface-brightness and is usually measured in apparent magnitudes[2] per arcsec^2.

'Isophotes' are contours of constant surface-brightness on the image, and in elliptical galaxies they have been found to be described by concentric ellipses to better than 1% (Kent, 1984; Lauer, 1985; Davis et al., 1985; Jedrzejewski, 1987; Peletier et al., 1990). The isophotes exhibit a varying degree of ellipticity, quantified by $n = 10(1 - b/a)$. b/a is the apparent axial ratio of the ellipse with projected short axis b and projected long axis a. A galaxy that appears round in the sky is E0, and E7 denotes the most elliptical galaxies observed. The sequence E0-E7 is only one of projected flattening, which is a function of the intrinsic flattening of the galaxy, and the inclination at which the galaxy is viewed.

In the late 1970s the introduction of charge-coupled device (CCD) cameras, dramatically reduced the noise in these images allowing the shapes of isophotes of galaxies to be studied in more detail (Jedrzejewski, 1987). It led to considerable improvements in extracting information efficiently from the images with a method called 'surface photometry'. This is used to describe the surface brightness distribution of a galaxy through finding the best-fitting ellipses that correspond to the observed isophotes with a Fourier analysis method. Isophotes are generally not perfectly elliptical, as illustrated in Figure 2. They can be more 'rectangular' than an ellipse ('boxy'), and sometimes they are more pointy or elongated along the major axes ('disky').

2 The apparent magnitude of a body is a measure of its brightness as seen by an observer on Earth, normalized to the value it would have in the absence of the atmosphere. The brighter the object appears, the lower the magnitude.

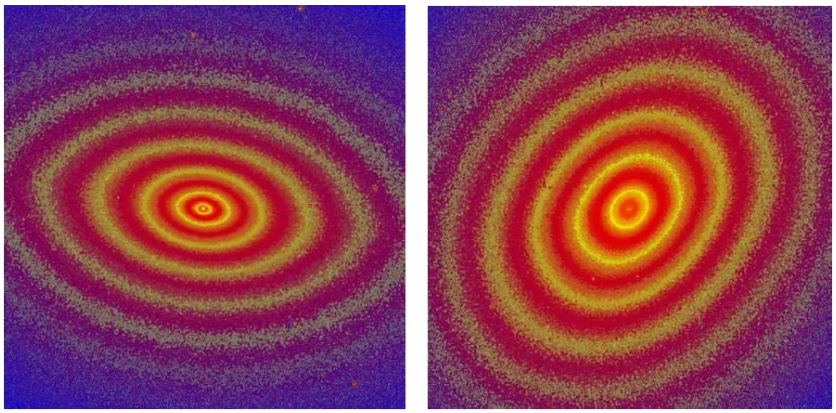

Figure 2: The left image shows NGC 821 with $a_4/a \sim +0.02$ (disky isophotes) and the right image shows NGC 2300 with $a_4/a \sim -0.02$ (boxy isophotes). With thanks to the IMPRS introductory course lectures of Ralf Bender.

The surface brightness of the isophotes is found to decrease with radius. There exists a plethora of functions for characterising surface-brightness profiles: power-law profiles, de Vaucouleur's law (de Vaucouleurs, 1948), the models of King (1966), the model of Jaffe (1983) and γ-models Dehnen (1993) to name a few. There has been a recent consensus however on the applicability to virtually all elliptical galaxies (Caon et al., 1993; Bertin et al., 2002) of the generalisation of de Vaucouleurs' law proposed by Sèrsic (Sérsic, 1963), which can be written as:

$$I(R) = I_e \exp\left[-b_m \left(\frac{R}{R_e}\right)^{1/m}\right] \tag{1.1}$$

where $I(R)$ is the surface brightness at projected radius R, R_e is the effective radius that contains half the projected light of the galaxy, I_e is the surface brightness at R_e and m is the Sèrsic shape parameter. $m = 4$ and $b_4 = 3.33$ recovers de Vaucouleurs' law. Effective radii of elliptical galaxies range between $R_e = 300$ pc – 50 kpc, and their surface brightnesses between $I_e = 10$ – 1000 $L_{\odot,B}\mathrm{pc}^{-2}$.

1.1.2 *Kinematic properties*

Information about the motions or kinematics of the stars can be obtained from observing the galaxy with a spectrograph in the optical part of the spectrum. The spectrograph disperses the light collected by the telescope mirror and produces a spectrum for each position on the sky. The observed spectrum is a sum of the spectra of all the stars along the line-of-sight (LOS), as individual stars cannot generally be resolved in galaxies outside the Milky Way and its surrounding satellite galaxies. Absorption lines in the spectrum arise mainly from the atmospheres of giant stars. The lines will be broadened and shifted due to the motion of the stars along the LOS. The shape of the line therefore has information on the LOS velocity distribution (LOSVD) of the

stars. The shape is well described by a Gaussian, with a mean equal to the bulk motion of the stars along the LOS and a width equal to the LOS dispersion in the velocities of the stars, therefore allowing us to measure moments of the LOSVD of the stars. The

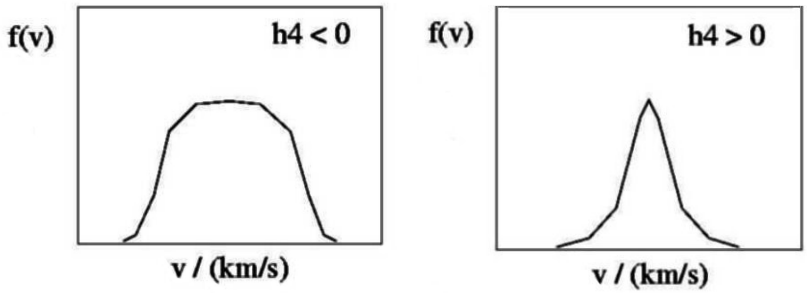

(a) (b)

Figure 3: Symmetric deviations from a Gaussian as measured by the h_4 coefficient.

advent of high-quality spectra with higher resolution and higher signal-to-noise ratio (S/N) has enabled higher-order moments of the LOSVD to be measured. These measure deviations of the line profile from a Gaussian and are most commonly parametrised by Gauss-Hermite coefficients (van der Marel & Franx, 1993; Gerhard, 1993). Odd Gauss-Hermite moments (h_3, h_5, etc.) measure asymmetric deviations from a Gaussian and even moments (h_4, h_6, etc.) measure symmetric deviations.

Most spectrographs used for obtaining kinematic observations admit light through a long, narrow slit. The light is then dispersed in the direction perpendicular to the long dimension of the slit. This method has enabled 1-D kinematics of elliptical galaxies to be traced out to 1–2 R_e (e.g. Davies, 1981; Bertola et al., 1988; Franx et al., 1989; Fried & Illingworth, 1994; Simien & Prugniel, 1997; Koprolin & Zeilinger, 2000; Pinkney et al., 2003; Matković & Guzmán, 2005) and more exceptionally out to 3–4 R_e (e.g. Mehlert et al., 2000; Corsini et al., 2008; Spolaor et al., 2010; Coccato et al., 2010).

Though many slits can be placed at different angles to obtain a more complete mapping of the kinematics in the galaxy, the process is laborious and slow. The advent of integral-field spectrographs on large-aperture, high-resolution telescopes has enabled spectra to be obtained in a 2-D field (e.g. Emsellem et al., 2004; McDermid et al., 2006). The kinematics generally only extend to about 0.5 R_e but Weijmans et al. (2009) and Proctor et al. (2009) use these techniques to map kinematics out to about 3 R_e.

The kinematic information point typically towards mean velocity profiles that rise within the central few arcsec and then flatten out. The velocity dispersion profiles either remain flat or fall in the outer parts. When rotation is present, the line profiles were always found to be asymmetric with the prograde wing steeper than the retrograde wing (Bender et al., 1994) and are more pointy than a Gaussian (i.e. $h_4 > 0$, Figure 3). At small

radii, peculiarities have been found in the mean-velocity profiles of some galaxies called kinematically-decoupled cores (KDC), which rotate in the opposite sense or perpendicular to the bulk of the galaxy. There are no corresponding peculiarities in the velocity dispersion. Studies reveal that KDCs are fairly common, occurring in maybe a quarter of all elliptical galaxies (Franx et al., 1989). With the SAURON integral-field spectrograph, Emsellem et al. (2004) found that elliptical galaxies in fact display a myriad of peculiarities including kinematic twists in the axis of rotation, central stellar discs and dust rings. These results have helped shape the new picture of elliptical galaxies as something far from 'featureless'.

There are two additional tracers of kinematics that can be resolved in nearby, elliptical galaxies and used to probe the LOSVD to larger radii where the stellar density is low and optical spectroscopy suffers from a low signal-to-noise ratio: planetary nebulae (PNe) (e.g. Ciardullo et al., 1993; Hui et al., 1995; Arnaboldi et al., 1996; Méndez et al., 2001; Teodorescu et al., 2005; Coccato et al., 2009) and globular clusters (GCs) (e.g. Forbes et al., 1996; Cohen, 2000; Peng et al., 2004; Bridges et al., 2006; Woodley et al., 2007; Lee et al., 2010)

Stars spend most of their lifetime shining as a result of nuclear fusion reactions that convert hydrogen to helium in the star's core. In stars with masses between $\sim 0.8 - 8 M_{\odot}$, the hydrogen in their cores is expended after 10^7–10^{10} years but still burns in a shell around the core. The core contracts and the outer layers of the star expand enormously and become much cooler, forming a red giant. The contraction of the core leads to an increase in its temperature and once it reaches 10^9 K, helium nuclei begin to fuse into carbon and oxygen. Helium fusion reactions are extremely temperature sensitive, with reaction rates being proportional to T^{40}, leading to instabilities that eventually expel the outer layers of the star via pulsations and strong stellar winds. The ejected outer layers are ionised by ultraviolet radiation emitted from the core and start radiating as a planetary nebula. 15% of the energy radiated from the central star is converted into photons in the characteristic green ($\lambda = 5007$) OIII emission line (Dopita et al., 1992).

PNe can be identified from this OIII emission line out to distances of 100 Mpc (Gerhard et al., 2005). LOS velocities can be measured from Doppler shifts of the lines, enabling the kinematics to be probed out to more than 7 R_e in elliptical galaxies. The work of Coccato et al. (2009) examined the PN kinematics in a sample of nearby, elliptical galaxies and showed that the number density and velocity dispersion profiles of PNe follow surface-brightness and velocity dispersion profiles measured for the total stellar population using optical images and spectra. Therefore the kinematic properties of PNe can be regarded as representative of the total stellar population.

GCs are spherical clusters of stars of size <10 pc representing another discrete population of objects that can be used as kinematic tracers of the outer halo in elliptical galaxies. For most galaxies within $\approx$ 20 Mpc, GCs can be identified through photometry with the Hubble Space Telescope (HST) and their LOS velocities can be obtained from the Doppler shifts of the absorption lines in the spectra. GCs in elliptical galaxies have a bimodal distribution: red, metal-rich GC systems and blue, metal-poor systems (Forbes et al., 1997; Harris et al., 2006), with the blue component dominating in numbers. The kinematics and surface-density profiles of GCs currently form a rather heterogeneous picture. In several galaxies, the red GCs have been found to be more concentrated towards the centre (e.g. Côté et al., 2001; Dirsch et al., 2003; Schuberth et al., 2006), and the blue GCs have been found to have higher velocity dispersions (e.g. Côté et al., 2003; Dirsch et al., 2003; Schuberth et al., 2006). In other galaxies, no difference between the two populations or reversed trends have been found (e.g. Côté et al., 2001; Hwang et al., 2008). When the density and kinematic properties follow that of the stars, it is clear that the systems are in equilibrium and reflect the 3-D dynamics of the whole galaxy. When they are different this implies that the GCs may either not be in equilibrium, or be in an equilibrium that is not representative of the main stellar population.

Despite the ability of PNe and GCs to trace kinematics deep into the halo of elliptical galaxies, the samples generally only consist of a hundred to a few hundred objects for each galaxy. Therefore one is usually only able to resolve the mean velocity and velocity dispersion moments of the LOSVD. Radial profiles of the deviations of the LOSVD from a Gaussian generally cannot be obtained. Some information may however be obtained on the deviations from a Gaussian of the LOSVD for the whole sample of objects (e.g. Napolitano et al., 2009).

1.1.3 *Fundamental plane*

Except dwarf ellipticals, (e.g. de Rijcke et al., 2005), early-type galaxies populate a 2-D surface called the fundamental plane (Dressler et al., 1987; Faber et al., 1987; Djorgovski & Davis, 1987) in the 3-D space defined by their size, (effective radius, R_e), density (average surface brightness within R_e, I_e), and energy in random motions (central velocity dispersions, σ_0). Figure 4 shows the fundamental plane (La Barbera et al., 2010) in the nearby universe (with redshift[3], $z < 0.1$) for a sample of 39,993 early-type galaxies located in a range of environments. La Barbera et al. (2010) fit the relation $\log R_e = a \log \sigma_0 - b\langle\mu\rangle_e + c$, and found

3 Redshift here refers to 'cosmological redshift', which is the stretching of light due to the Universe expanding (discussed in Section 1.4). It is a measure of distance for galaxies that are far away enough that peculiar motions due to neighbouring galaxies are negligible.

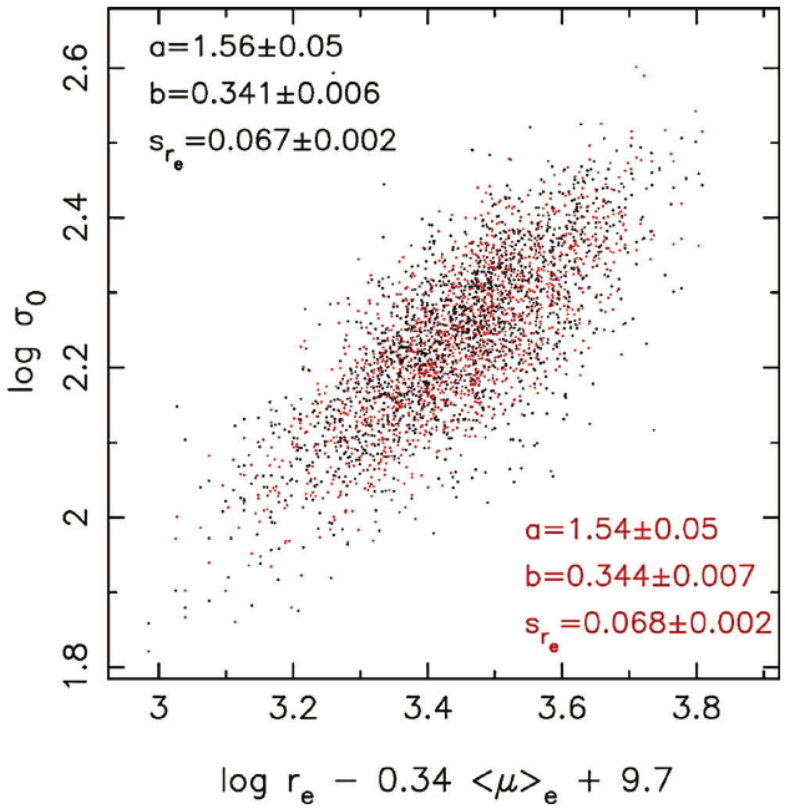

Figure 4: $\log \sigma_0$ plotted against the variable $\log R_e - b\langle\mu\rangle_e$ from La Barbera et al. (2010), for galaxies in the Sloan Digital Sky Survey (black dots) and for a toy sample of galaxies (red dots). The slopes (a and b) and scatter (s_{R_e}) are given in the corners of the plot.

that a varies from 1.38 ± 0.02 in g (green), to 1.55 ± 0.02 in K (infrared), implying a $\sim 12\%$ variation. In b the corresponding variation is negligible ($b \sim 0.316$), while c varies by $\sim 10\%$.

Important projections of the fundamental plane are 1) the Faber-Jackson law (Faber & Jackson, 1976), which finds that the luminosity of a galaxy L (obtained from integrating the surface-brightness over the galaxy volume and therefore a function of I_e and R_e) is related to σ_0 by $L \propto \sigma_0^4$ showing that more luminous galaxies are kinetically 'hotter', and 2) the Kormendy relation (Kormendy, 1977), which finds that L is correlated with R_e according to $L \propto R_e^{1.2}$, indicating that more luminous galaxies are spatially more extended than less luminous galaxies.

The fundamental plane relation is very useful in determining distances to early-type galaxies (e.g. Dressler et al., 1987; D'Onofrio et al., 1997; Blakeslee et al., 2002). I_e and σ_0 are observable quantities and are both independent of the distance of the galaxy from the observer. R_e can be estimated from the surface-brightness image in arcsec (i.e. angular width in the sky) and in physical units (kpc) from the fundamental plane relation. Then from the small-angle approximation the distance D of the galaxy is given by the ratio of R_e in kpc and R_e in arcsec.

If one assumes that an early-type galaxy can be treated as a stationary self-gravitating system, then the scalar virial theorem connects the potential energy V and the kinetic energy T by the relation $2T + V = 0$. Writing the virial theorem in terms of R_e, σ_0 and I_e (Busarello et al., 1997) gives $R_e = C\sigma_0^2 I_e^{-1}(M/L)^{-1}$, where M/L is the mass-to-light ratio and C is a combination of terms linking the 2-D observables to the corresponding 3-D physical quantities. From the fundamental plane however we have $R_e = c\sigma_0^a I_e^b$, where a and b were defined above. For the virial theorem to hold either there is a systematic variation in C and therefore the intrinsic dynamical properties of early-type galaxies (e.g. Hjorth & Madsen, 1995; Busarello et al., 1997; Nipoti et al., 2002; La Barbera et al., 2008), or there is a systematic variation in M/L, either due to differing stellar populations (e.g. Gerhard et al., 2001; Bender et al., 1993) or differing fractions of dark matter to stars (e.g. Ciotti et al., 1996; Tortora et al., 2009), or a combination of both (e.g. Prugniel & Simien, 1996; Trujillo et al., 2004; Bolton et al., 2007).

1.1.4 *X-ray properties of elliptical galaxies*

Elliptical galaxies were always believed to be gas-poor systems until the launch of the Einstein Space Observatory in 1978. The Einstein Observatory survey (Forman et al., 1979) showed that at least five non-cluster central elliptical galaxies were X-ray sources, suggesting that the emission was intrinsic to the galaxies themselves and not completely due to intracluster gas.

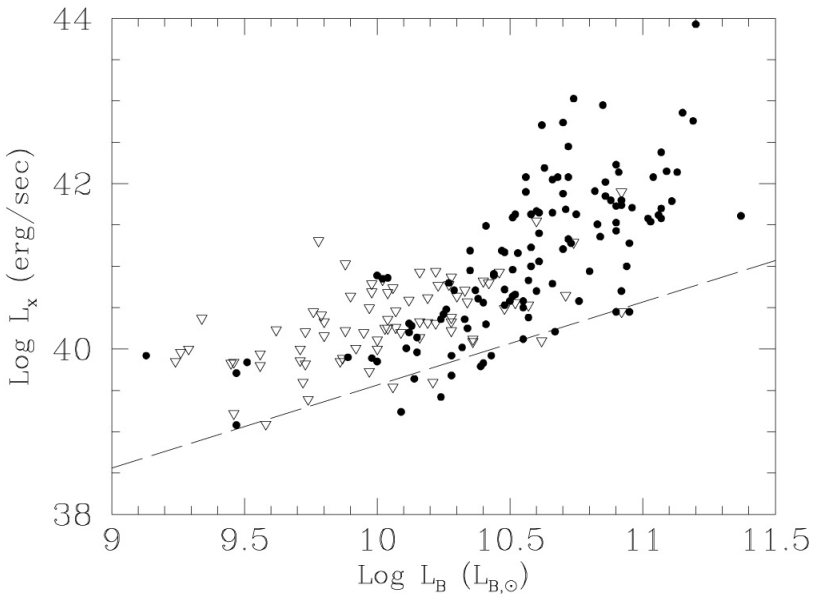

Figure 5: Bolometric X-ray luminosity L_X against B-band optical luminosity L_B for elliptical galaxies from O'Sullivan et al. (2001): X-ray detections are shown with filled circles and upper limits with open triangles. The dashed line shows $L_X \propto L_B$.

X-ray luminosities of elliptical galaxies are found to range from 10^{39} to 10^{43}erg s^{-1} and a strong correlation between the observed

X-ray luminosities (L_X) and blue optical luminosities (L_B) has been established (Forman et al., 1985; Trinchieri & Fabbiano, 1985; Canizares et al., 1987; White & Sarazin, 1991; Brown & Bregman, 1998; Beuing et al., 1999). For elliptical galaxies of low luminosity (i.e. $L_B \lesssim L_{B,\mathrm{crit}} = 3 \times 10^9 L_{B,\odot}$), O'Sullivan et al. (2001) found that $L_X \propto L_B$, similar to the correlation between optical and X-ray luminosities found in spiral galaxies (e.g. Irwin & Sarazin, 1998; Trinchieri et al., 2000). However, the X-ray emission from more luminous ellipticals ($L_B \gtrsim L_{B,crit}$) varies approximately as $L_X \propto L_B^2$ (O'Sullivan et al., 2001). Figure 5 shows that the scatter about this correlation is enormous; L_X varies by almost two orders of magnitude for galaxies with similar L_B.

The launch of the Röntgensatellite (ROSAT) in 1990 represented a significant improvement in imaging, spectral resolution and sensitivity. The X-ray spectra could be modelled in a more sophisticated way than with Einstein, allowing the discovery of two primary mechanisms for X-ray emission in early-type galaxies: a harder component attributed to integrated emission from discrete stellar-like sources and a softer component attributed to diffuse thermal emission from a hot ($\sim 10^7$ K ~ 1 keV) and low density ($< 10^{-1}\mathrm{cm}^{-3}$) gas trapped in the galaxy's potential well. The X-ray emission of the fainter elliptical galaxies has been shown to be dominated by discrete sources (Brown & Bregman, 2001). The more luminous elliptical galaxies require an additional component contributing to the total X-ray emission, i.e. the hot gas.

From the observed X-ray properties, characteristics of the hot gas can be derived. The X-ray surface-brightness can be deprojected to obtain the gas emissivity. The gas abundance and temperature can be estimated through spectral fits. The gas density can then be determined, assuming that the gas is characterised by a single density and temperature at each radius. The total gas mass can be inferred by integrating the gas density distribution.

Einstein results indicated typical gas temperatures of $T = 0.5 - 0.2$ keV and central gas densities of $n_p \sim 0.01$ cm^{-3} (Forman et al., 1985; Trinchieri et al., 1986; Sarazin, 1990). Total gas masses have a range of $10^8 - 10^{11}\, M_\odot$, supporting that X-ray bright elliptical galaxies have large gaseous haloes. The arrival of the Chandra and XMM-Newton instruments in 1999 have enabled temperature and density profiles of the gas to be probed to unprecedented detail. Both observatories have unique, complementary capabilities. While XMM-Newton has exquisite spectral resolution and a large collecting area, Chandra is the first X-ray imaging satellite with sub-arcsecond spatial resolution. The present work will be based on observations benefiting from the capabilities of both these instruments. The temperature profiles of the gas often extend to $\gtrsim 10\, R_e$ and exhibit a variety of shapes. They range from outwardly rising temperature profiles mainly in massive ellipticals and decreasing temperature profiles mainly in

low-luminosity systems (Fukazawa et al., 2006; Humphrey et al., 2006; Diehl & Statler, 2008).

1.1.5 *Dichotomy in observed properties*

Studies looking at the relation between the luminosity and the colour of early-type galaxies in the local universe have found that redder galaxies are also more luminous (Baum, 1959; Visvanathan & Sandage, 1977; Bower et al., 1992). This colour-magnitude relation is only a small part of a general dichotomy in a whole host of properties. Davies et al. (1983) compared kinematic and luminous properties in a large sample of elliptical galaxies and found that fainter elliptical galaxies rotate more rapidly than brighter galaxies and tend to be flatter. They also found that fainter elliptical galaxies could be described as oblate, isotropic[4] rotators (Binney, 1978). More optically luminous galaxies were found to have boxier isophotes (Bender et al., 1988) and to be more luminous in the radio and X-ray parts of the spectrum (Bender et al., 1989). Section 1.1.4 described how the relation between the X-ray and optical luminosities also changes with optical luminosity due to an additional contribution to the X-ray emission originating from hot gas trapped in the galaxy's potential. Optically fainter elliptical galaxies tend to have diskier isophotes and are fainter in the radio and X-ray. More luminous elliptical galaxies have systematically higher mass-to-light ratios than fainter ellipticals (Bender et al., 1989) and are dominated by random motions rather than order motions (Illingworth, 1977; Davies & Illingworth, 1983; Busarello et al., 1992). There are lower asymmetries in the LOS velocity distribution (LOSVD) compared to flat, disky ellipticals (Bender et al., 1994) and Lauer et al. (1995) used V-band images from the HST to show that the surface-brightness profiles of more luminous ellipticals have central cores that are more shallow than the outer parts, a feature not found in fainter ellipticals.

This dichotomy in the observed properties of elliptical galaxies led to a revised classification scheme proposed by Kormendy & Bender (1996), where the E0-E7 sequence of apparent flattening, is replaced by a gradation from boxiness to diskiness.

SAURON is an integral-field spectrograph mounted on the William Herschel Telescope optimised for the kinematic studies of the central regions of nearby galaxies (Bacon et al., 2001). Work on a large sample of nearby elliptical and lenticular galaxies has resulted in a new parametrisation of the dichotomy found in elliptical galaxies, in terms of the parameter $\lambda_R \equiv \langle R|V|\rangle / \langle R\sqrt{V^2+\sigma^2}\rangle$, an observable proxy for the stellar angular momentum per unit mass (Emsellem et al., 2007; Cappellari et al., 2007). The averages are luminosity-weighted and calculated over the whole SAURON field. This parameterisation separates ellip-

4 Here 'isotropic' refers to the state of the velocity dispersion tensor, and implies that the velocity dispersion is equal in x, y, and z directions.

tical galaxies into slow ($\lambda_R < 0.1$ within 1 R_e) and fast rotators ($\lambda_R > 0.1$ within 1 R_e). The fast rotators tend to be relatively low-luminosity galaxies with $M_B < -20.5$. Slow rotators tend to be brighter but are still spread over a wide range of absolute magnitudes, which differs slightly from the older definition. Almost all of the slow rotators contain a kinematically-decoupled core within the central kpc. The slow rotators tend to be fairly round ($\epsilon \lesssim 0.3$), with significant kinematical misalignments, indicating triaxiality. The fast rotators can appear quite flattened ($\epsilon \lesssim 0.7$) and generally do not show significant kinematical misalignments, indicating they are nearly axisymmetric. Several of the fast rotators contain a flattened, counter-rotating component in the centre, which is generally more metal rich than the rest of the galaxy.

1.2 DYNAMICS OF ELLIPTICAL GALAXIES

So far observations of elliptical galaxies have been discussed, giving information on the photometric and kinematic properties of elliptical galaxies. This Section gives a brief overview on how the intrinsic dynamical properties of elliptical galaxies can be described in terms of a collisionless system.

1.2.1 *Collisionless dynamics*

Celestial mechanics is the description of the motions of objects in the sky using the formalism set out by Newton's laws of motion and Newton's law of gravity. Elliptical galaxies however can contain billions of stars and therefore stellar dynamics needs to employ a statistical approach, similar to that used in classical statistical mechanics. In systems typically dealt with in statistical mechanics, such as a diffuse gas trapped in a box, the rate of collisions between the particles is significant in terms of the time for which the gas is considered. In elliptical galaxies however, the interval between collisions of stars can be shown to be much greater than the age of the Universe (Binney & Tremaine, 1987). Therefore galaxies can be treated as collisionless systems in which the stars move under the influence of the gravitational field generated by a smooth mass distribution comprised of other stars, interstellar gas and dark matter without the graininess from considering individual potentials.

1.2.1.1 *The distribution function*

Let us define our collisionless system as consisting of N identical point masses and assume an arbitrarily large relaxation time. Such a system has an infinite number of equilibria, each uniquely specified by the distribution function (DF) f such that $f(\mathbf{x}, \mathbf{v}, t)\mathrm{d}^3\mathbf{x}\mathrm{d}^3\mathbf{v}$ is the probability that at time t a randomly cho-

sen star has phase-space coordinates in the given range (Binney & Tremaine, 1987). f is normalised such that:

$$\int \mathrm{d}^3\mathbf{x}\mathrm{d}^3\mathbf{v} f(\mathbf{x},\mathbf{v},t) = 1 \tag{1.2}$$

with the integral over all of phase space.

To a good approximation, it can be assumed that stars are neither created or destroyed as the characteristic lifetime of the stars in elliptical galaxies is much longer than dynamical evolution timescales of the stars. Imposing mass conservation leads to the collisionless Boltzmann equation (CBE), which has both time-dependent solutions, and also time-independent solutions which will be equilibria of collisionless systems (Binney & Tremaine, 1987).

Phase-space equilibrium solutions can be obtained from knowledge of the integrals of motion in a potential. An integral of motion, $I(\mathbf{x},\mathbf{v})$, is a function of only the phase-space coordinates that remains constant along an orbit of a star. 3-D systems with at least three integrals of motion are 'integrable'. The Jeans theorem states that in integrable systems, any function of the integrals of motion $f(I_1, I_2, I_3, ...)$ is an equilibrium solution of the CBE. In a general 3-D potential there is only one integral of motion, energy. In a static spherical potential the three components of angular momentum are also constant along stellar orbits offering three additional integrals of motion. There are two special cases, namely the point mass (Kepler potential) and homogeneous sphere (harmonic potential), for which all orbits are closed ellipses. Therefore the orientation of the line joining the apocentre and pericentre of the orbit is conserved along the orbit, giving a fifth integral of motion. In a static axisymmetric potential, in addition to energy, one component of angular momentum is an integral of motion and there is a third integral of motion that only exists in an approximate sense.

1.2.2 *Velocity moments of the distribution function*

Velocity moments of the DF give quantities that can be more easily linked with observable quantities (see Section 1.3). For example the total density of stars ν is given by:

$$\nu = \int \mathrm{d}^3\mathbf{v} f(\mathbf{x},\mathbf{v}) \tag{1.3}$$

The moment $v_i^{n_i} v_j^{n_j} v_k^{n_k}$ of the velocity distribution of stars is given by multiplying the DF by $v_i^{n_i} v_j^{n_j} v_k^{n_k}$, integrating over all velocities and then normalising by ν. The first moment of the velocity distribution, the mean streaming velocity along i, $\bar{v}_i$ is given by:

$$\bar{v}_i = \frac{1}{\nu}\int \mathrm{d}^3\mathbf{v} v_i f(\mathbf{x},\mathbf{v}) \tag{1.4}$$

The second non-mixed moment of the velocity distribution, the root-mean-squared velocity along i, $\bar{v_i^2}$ is given by:

$$\bar{v_i^2} = \frac{1}{\nu} \int \mathrm{d}^3\mathbf{v} v_i^2 f(\mathbf{x}, \mathbf{v}) \tag{1.5}$$

The velocity dispersion tensor σ_{ij}^2 consisting of mixed and non-mixed moments is defined as:

$$\sigma_{ij}^2 = \frac{1}{\nu} \int \mathrm{d}^3\mathbf{v} (v_i - u_i)(v_j - u_j) f(\mathbf{x}, \mathbf{v}) \tag{1.6}$$

The three principal axes of this tensor define the velocity ellipsoid. The ratios of the axes measure the anisotropy of the velocity dispersion tensor, which is related to the orbital structure of the stars. In spherical systems the β parameter is a common way of quantifying the anisotropy of the velocity dispersion tensor (Binney & Mamon, 1982):

$$\beta = 1 - \frac{\sigma_\theta^2}{\sigma_r^2} \tag{1.7}$$

For $\beta \to 1$, radial velocity dispersions dominate. For $\beta = 0$, the velocity dispersion tensor is isotropic and for $\beta \to -\infty$, tangential velocity dispersions dominate. β can also be used approximately in other geometries, but then it no longer measures the ratio of the principal axes of the velocity dispersion tensor. The orbital structure in terms of higher-order moments of the DF can be similarly defined but are less often referred to in the literature.

1.2.3 *Jeans equations*

The Jeans equations describe the motion of a collection of stars through velocity moments, in a gravitational field. As comparisons between theoretical models and observational data often centre on velocity moments of the DF, rather than the DF itself, Jeans equations are a useful tool. Different orders are constructed by multiplying the CBE by powers of velocity, $v_i^{n_i} v_j^{n_j} v_k^{n_k}$ and then integrating over all velocities. They form an infinite system of equations and cannot in general be closed at any order. There is one zeroth-order moment, obtained by just integrating the CBE over all velocities. There are three first-order moments, obtained by multiplying the CBE by v_i, v_j, and v_k and then integrating over all velocities. In steady-state systems that are spherically symmetric, the three first-order moments reduce to a single equation:

$$\frac{\mathrm{d}(\nu\sigma_r^2)}{dr} + 2\frac{\beta}{r}\nu\sigma_r^2 = -\nu\frac{\mathrm{d}\Phi}{\mathrm{d}r} \tag{1.8}$$

where ν is the density distribution of the stars and Φ is the smoothed gravitational potential in which the stars move. As the Jeans equations are not closed, assumptions have to be made to obtain solutions, for example on the shape of the velocity dispersion tensor. $\beta = 0$ corresponds to an isotropic velocity dispersion tensor and a distribution function $f = f(E)$, where E is energy.

1.3 FROM OBSERVATIONS TO DYNAMICS

This Section explains methods used to specifically infer 3-D dynamical properties of elliptical galaxies from the available 2-D optical and X-ray information. Obtaining constraints from X-ray observations on the mass distribution in elliptical galaxies and obtaining constraints on both the mass distribution and orbital structure from optical observations and dynamical models in elliptical galaxies will be discussed.

1.3.1 *Mass distribution of elliptical galaxies from X-rays*

The X-ray emission from elliptical galaxies with B-band luminosities above $L_{B,\mathrm{crit}} = 3 \times 10^9 L_{B,\odot}$ is dominated by the hot gas rather than stellar sources (see Section 1.1.4). If the gas is not disturbed by mergers, or activity of an active galactic nucleus (AGN), the gas can be assumed to be in hydrostatic equilibrium (Bahcall & Sarazin, 1977; Mathews, 1978), i.e. the gravitational force acting on the gas particles is balanced by pressure forces. In spherically-symmetric systems this can be expressed as:

$$M(<r) = -\frac{r k_b T}{G \mu m_p} \left(\frac{\mathrm{d} \ln \rho}{\mathrm{d} \ln r} + \frac{\mathrm{d} \ln T}{\mathrm{d} \ln r} + \frac{P_{nt}}{P} \frac{\mathrm{d} \ln P_{nt}}{\mathrm{d} \ln r} \right) \quad (1.9)$$

where $M(<r)$ is the enclosed mass within a sphere of radius r, T is the temperature of the hot gas and ρ is the density of the hot gas. m_p is the proton mass and $\mu = 0.61$ is the molecular weight for full ionisation. In addition to the gas pressure, an additional non-thermal turbulent, magnetic or cosmic ray pressure P_{nt} may be present, though is usually considered to be negligible. Non-spherical analyses have also been attempted (e.g. Buote et al., 2002; Lee & Suto, 2003) but are generally not carried out due to uncertainties in the data.

Cowie et al. (1987); Humphrey et al. (2006); Fukazawa et al. (2006); Nagino & Matsushita (2009) applied hydrostatic equilibrium using methods where the measured temperature and density profiles are first parametrised to circumvent differentiating the observed profiles, which are often noisy. Churazov et al. (2008) avoided differentiation by interpolating to obtain only the potential profile. Nulsen & Böhringer (1995) found the most likely mass profile of NGC 4486 (M87) from temperature and density profiles using a non-parametric method, and Humphrey et al. (2009) used a parametric Bayesian analysis. These methods of obtaining the mass distribution from X-ray information have enabled the potential to be traced out to at least 20 kpc ($\sim$ 2–4 R_e) and often to 100 kpc ($\sim$ 10–20 R_e). The parametric methods used in the literature generally underestimate the range of mass profiles consistent with the data. They also introduce systematic biases in the masses derived because of the assumptions on the profile shapes. In the present work a new non-parametric Bayesian analysis is developed for applying hydrostatic equilib-

rium to data taken from both the Chandra and XMM-Newton telescopes (see Chapter 2).

1.3.2 *Mass distribution and orbital structure from dynamical models*

Section 1.2 showed how to build models of stellar systems by explicit construction of a DF that depends on the integrals of motion. Here the use of Jeans equations to constrain dynamical properties of elliptical galaxies will be described, without the explicit construction of a DF. Numerical techniques will also be discussed, which build up galaxy models from superposing DFs, stellar orbits, or particles.

1.3.2.1 *Jeans equations*

The spherical Jeans equation (1.8) relates the diagonal elements of the velocity dispersion tensor to the gravitational potential in which the stars move. The luminosity density $j(r) = \nu(r)L$, where L is the total luminosity, and radial velocity dispersion $\bar{\sigma_r^2}$ are related to the observed surface-brightness $I(R)$ and velocity dispersion $\sigma_{\rm P}(R)$ profiles in a spherical system by:

$$I(R) = 2\int_R^\infty \frac{j(r)r\mathrm{d}r}{\sqrt{r^2-R^2}} \tag{1.10}$$

$$\sigma_{\rm P}(R) = \frac{2}{I(R)}\nu r\sigma_r^2\left(1-\beta(r)\frac{R^2}{r^2}\right)\frac{r}{\sqrt{r^2-R^2}}\mathrm{d}r \tag{1.11}$$

$j(r)$ is known directly from $I(R)$ by inverting Equation (1.10). Then there are three remaining unknowns, Φ, β and σ_r but only two equations, (1.8) and (1.11).

In the absence of dark matter, $\Phi(r)$ is generated only by the particles that produce the luminosity density profile $j(r)$, and therefore $\Phi(r)$ is related to $j(r)$ via Poisson's equation. Otherwise, the potential can be derived from X-rays if available, or some functional form can be assumed for $\Phi(r)$ and a series of potentials probed to find the best one. In a fixed potential the problem is reduced to two equations with two unknowns and therefore solutions can be obtained, as first demonstrated by Binney & Mamon (1982). Tonry (1983) simplified the solutions and Dejonghe & Merritt (1992) generalised the solutions to all orders of the Jeans equations. The main problem with obtaining solutions in this way is that the functions fitted to the imperfect data do not correspond to a perfect virial equilibrium. The solutions are unstable to these deviations, resulting in central divergences. The solutions are applied to the central group galaxy NGC 5846 in Chapter 3, finding a similar result. Dejonghe & Merritt (1992) introduce a term measuring the 'inequilibrium' of a system, but this still relies on knowledge of how different the assumed profiles are from the true ones.

A more common approach for solving the Jeans equations is a forward-fitting method where a physical functional form

is assumed for $\beta(r)$, and then Equation (1.8) can be solved as a first-order differential equation with the integrating factor $e^{\int \frac{2\beta(r)}{r} \mathrm{d}r}$. Common functional forms adopted for the shape of the anisotropy profile are constant β, Osipkov-Merritt $\beta = 1/(r_a^2 + r^2)$ (Osipkov, 1979; Merritt, 1985), and $\beta = \beta_0(r_a^2 + r^2)/(r_b^2 + r^2)$ (Chapter 4). Assuming a potential given by X-rays and $\beta = \beta_0(r_a^2 + r^2)/(r_b^2 + r^2)$, the velocity anisotropy profile for NGC 4486 (M87) is derived out to 150 kpc using photometric and kinematic constraints in Chapter 4.

When only projected velocity dispersions are available, there is a degeneracy between the mass and anisotropy (Binney & Mamon, 1982). This can be circumvented if either the potential is already known (e.g. Mathews & Brighenti, 2003, and Chapter 4), or the anisotropy is known (e.g. Hui et al., 1995; Noyola et al., 2008), or if higher-order constraints such as the kurtosis are available (e.g. Łokas & Mamon, 2003; Napolitano et al., 2010).

Jeans equations have also been extended to axisymmetric (Antonuccio-Delogu, 1991; Carollo & Danziger, 1994; Arnold, 1995; Cappellari, 2008) and even triaxial systems (Statler et al., 1999; van de Ven et al., 2003) though many more unknowns are introduced into the picture, requiring some additional assumptions to be made.

1.3.2.2 *Numerical techniques*

The Jeans equations are not closed, and therefore generally there are too many unknowns. They also become increasingly complicated when fitting to higher-order moments of the LOSVD and as they relate moments of the DF, there is no way of knowing whether the DF is negative and therefore unphysical in some parts of phase space. Numerical techniques have been developed that can fit a range of data and represent a real galaxy, implicitly enforcing the DF to be positive everywhere. The main idea behind these methods is to construct a distribution function for a galaxy from a set of 'basis' functions. The best combination (usually linear) of the basis functions is found such that the projection of the system along the LOS minimises some test statistic F. A common form for the test statistic is $F = \chi^2 + S$, where χ^2 is the goodness-of-fit between the projected model and observed photometry and kinematics, and S is a smoothing function, to ensure a physical and unique solution by decreasing the number of degrees of freedom.

The Jeans theorem introduced in Section 1.2.1.1 states that for integrable systems (i.e. those that have more than three integrals of motion for the 3-D case), any function of the integrals of motion $f(I_1, I_2, I_3, ...)$ is an equilibrium solution of the CBE. Therefore the first obvious choice for the 'basis' functions are the integrals of motion. Gerhard et al. (1998) construct a library of many DFs, each a function of the integrals of motions in a spherical potential and covering a range of anisotropies to sufficiently sample phase space. For each galaxy, the DFs consistent with the luminosity

density profile $\text{æ}(r)$ of the galaxy are selected, and the total DF of the galaxy is written as a linear combination of these, each with a weight w_i. In some fixed potential Φ, the set of w_i are found such that the projected model DF best matches kinematic constraints of the galaxy, using the test statistic F defined above. This can repeated for a range of potentials to constrain the best potential. This method has been used on NGC 4697 (Dejonghe et al., 1996) and a sample of nearby elliptical galaxies with a range of luminosities (Kronawitter et al., 2000).

The integrals of motion define a torus in phase space, which is traced out by orbits of the stars. Therefore DFs can also be constructed from functions of the orbits, $f(O_1, O_2, O_3, ...)$. As orbits of stars can be followed (a method called 'orbit integration') by applying simple Newtonian dynamics, then a library of orbits can be simply constructed without explicit knowledge of the integrals of motion. This is a powerful tool in potentials where the integrals of motion are not known. Schwarzschild (1979) originally conceived the idea of constructing DFs from orbits. For some specified gravitational potential, Φ, a large number of orbits are integrated for a time much greater than the orbital time, creating a library of orbits that covers a wide range of anisotropies. The total DF of the galaxy is a linear combination of the orbits, each attributed with a weight, w_i, representing the number of stars in that orbit. The best set of w_i for all the orbits is found such that F is minimised. This can be repeated for a series of potentials to find the best potential. The analysis of the orbits in the best-fit model reveals the orbital structure of the system.

This method has been used to fit photometric and kinematic constraints to search for supermassive black holes and constrain the mass distribution and orbital structure in bulges and elliptical galaxies under spherical (Richstone & Tremaine, 1984; Rix et al., 1997), axisymmetric (Richstone, 1980; Cretton et al., 2000; Verolme & de Zeeuw, 2002; Cappellari et al., 2006; Thomas et al., 2007; Gebhardt & Thomas, 2009) and triaxial ellipsoidal (van den Bosch & de Zeeuw, 2010) assumptions.

Finally, a galaxy can be represented by a system of particles with variable weights (Syer & Tremaine, 1996; de Lorenzi et al., 2007; Dehnen, 2009; Long & Mao, 2010). If the particles trace a uniform density along a torus then the particle model is a realisation of a steady-state DF. The whole DF can be mapped out in a statistical sense by tracing the particle orbits and ensuring there are a sufficient number of particles in all regions of phase space. Particle-based models have the advantage that the integrals of motions or stellar orbits do not need to be known a priori.

The implementation of de Lorenzi et al. (2007) will be described here, as it is used to model galaxies in the present work. NMAGIC is the N-particle Made-to-measure AlGorithm mInimizing Chi-squared (NMAGIC) code, a parallel implementation of the made-to-measure method originally developed by Syer & Tremaine (1996). The orbits of the particles are integrated from

some initial particle model in a potential that may vary with time. The projected properties of the system are calculated many times in an orbit and w_i of the particles are changed adaptively to minimise the test statistic F defined as:

$$F = \mu S - \frac{1}{2}\chi^2 + \mathcal{L} \tag{1.12}$$

where S is an entropy term with weight μ, χ^2 measures deviations between the model and observed photometric and kinematic data and $\mathcal{L}$ is the log-likelihood function measuring the likelihood of a sample of discrete velocities (e.g. LOS PN and GC velocities). Here F is defined so that a maximum is sought for the best-fit model. If the potential is not known, models can be carried out in a series of potentials to constrain the best one. The great advantage of this method is in its ability to be easily generalised to systems with lower orders of symmetry.

NMAGIC has so far been applied to the intermediate-luminosity elliptical galaxies NGC 3379 and NGC 4697. In the present work it is applied to NGC 4649, a massive elliptical galaxy in the Virgo cluster (see Chapter 5) and NGC 1399, a massive elliptical galaxy at the centre of the Fornax cluster of galaxies (see Chapter 6).

1.4 FROM DYNAMICS TO THE BIGGER PICTURE

So far the observed properties of elliptical galaxies have been discussed, along with how they can be used to constrain the gravitational field in a galaxy, and the density and velocity distributions of the stars. In this Section, elliptical galaxies will be discussed in the context of the current cosmological paradigm, and how we can garner constraints on their formation from knowledge of the dark matter content and orbital structure.

1.4.1 *The current cosmological paradigm*

Stars, gas and dust fill our visible Universe, but they only make up a small part of the whole Universe. The dominant mass component is 'dark matter', which interacts only through gravitational forces. Although the constituent particles are not yet known, most work favours the theory in which they are regarded to be 'cold', i.e. they move non-relativistically, as originally proposed by Blumenthal et al. (1984).

If the energy content of the Universe is only due to the visible matter and the dark matter then it should either stop expanding and then recollapse, or the expansion rate should at least slow with time. A remarkable discovery in the late 1990s (Riess et al., 1998; Perlmutter et al., 1999), using HST observations of very distant supernovae showed that the Universe is actually expanding more quickly today compared to the past. This requires an additional contribution to the total energy of the Universe, usually referred to as 'dark energy' (Huterer & Turner, 1999) and given the symbol Λ.

The current cosmological paradigm, ΛCDM, divides the energy budget of the Universe between dark energy ($\Omega_\Lambda = 0.728$), dark matter ($\Omega_c = 0.227$) and baryonic matter ($\Omega_\Lambda = 0.045$), with a Hubble parameter of 70.4 km/s/Mpc (Komatsu et al., 2010). A Universe defined by these cosmological parameters would be almost 14 Gyr old.

1.4.2 *Hierarchical structure formation*

The structures that we observe in the Universe today are believed to have originated from quantum fluctuations in the aftermath of the Big Bang. The dark matter particles underwent gravitational collapse allowing the perturbations to grow and eventually form a dark matter halo. Larger dark matter haloes are formed by the merging of earlier generations of haloes.

Baryons are accreted onto the dark matter haloes and once sufficiently cooled collapse to form stars (Rees & Ostriker, 1977; Silk, 1977). In lower-mass haloes and in all haloes at early times, cold gas is accreted onto the centre of the halo via filaments. In higher-mass haloes gas is heated further out to the virial temperature of the halo through shocks, a possible origin for the hot gas in massive systems. Hot accretion is the accretion of this gas onto the central halo at later times as the gas cools (Dekel et al., 2009; Kereš et al., 2009).

1.4.3 *A complex picture*

The presence of a dichotomy in the observed properties of nearby elliptical galaxies (see Section 1.1.5) and the existence of dwarf and spiral galaxies suggests a complex picture of galaxy formation where different formation paths exist.

Cowie et al. (1996) looked at the star formation rates of a large sample of galaxies between redshifts of 0.2 and 1.7 and found that the characteristic luminosity of galaxies dominated by star formation has been decreasing since $z > 1$. Therefore the most massive galaxies in fact assemble their stellar mass earlier than smaller galaxies. Space-based near-ultraviolet measurements have shown specifically that the typical star formation rate in galaxies was over an order of magnitude higher at $z = 3$ than at $z = 0$ (Arnouts et al., 2005). Ground-based optical and near-infrared searches indicate that the largest galaxies were already in place by $z \sim 2$, while smaller ones continued to form stars at much lower redshifts (Fontana et al., 2004; Glazebrook et al., 2004; van Dokkum et al., 2004; Treu et al., 2005).

There has also been an observed size evolution in the most massive elliptical galaxies from $z \sim 2$ to the present day: they have become larger and less dense (Trujillo et al., 2006; van Dokkum et al., 2008; Saracco et al., 2009). Similar compact galaxies to those observed at high redshift do not exist in the local universe (Trujillo et al., 2009). Bezanson et al. (2009) showed that the

stellar density within the central 1 kpc of ellipticals at $z \sim 2.3$ is similar to that for nearby ellipticals (they differ by only a factor of ~ 2 compared to a factor of 100 when compared within 1 R_e). Bernardi (2009) showed that the sizes and velocity dispersions of massive elliptical galaxies are still evolving in the local ($z \sim 0.3$) universe.

1.4.4 *Formation of elliptical galaxies*

Toomre (1977) first hypothesised that major mergers (the progenitor galaxies are of comparable mass) could be responsible for the formation of elliptical galaxies through the process of violent relaxation (Lynden-Bell, 1967). This conjecture is supported by numerical models that show that mergers of pairs of galaxies yield triaxial remnants that can be fitted by de Vaucouleurs $R^{1/4}$ light profiles over a large range in radius and are supported by anisotropic velocity dispersions (e.g. Gerhard, 1981; Barnes, 1988, 1992; Hernquist, 1993). There are however many failures: luminous ellipticals have a mean Hubble type E2 (e.g. Franx et al., 1991), while the remnants of mergers of pairs of stellar disks are more elongated with spectral types E3-E7 (e.g. Hernquist, 1992). The remnants also exhibit large constant density cores that are too diffuse to be identified with real ellipticals (Hernquist, 1992, 1993). The remnants often exhibit kinematic properties unlike real ellipticals, such as large misalignments between their angular momenta and minor axes (Barnes, 1992; Heyl et al., 1995) showing a high degree of triaxiality. Observationally, Franx et al. (1991) determined that that only 35% of ellipticals have intrinsic misalignments of less than 15%.

The dissipational effects of gas (e.g. Rees & Ostriker, 1977; Silk, 1977; Kormendy, 1990) were proposed as a mechanism for reproducing the higher central densities observed in ellipticals and then later verified in the simulations of Mihos & Hernquist (1994). Angular momentum is removed from the gas allowing it to collapse and trigger star formation in the centre allowing higher phase-space densities to develop. Bekki & Shioya (1997) used simulations to show how the rate of gas consumption by star formation greatly affects the isophotal shapes of merger remnants. Mergers with gradual star formation are more likely to form elliptical galaxies with disky isophotes, and those with rapid star formation are more likely to form ellipticals that appear to be both boxy and disky depending on the viewing angle of the observer. The radial density profile and the compactness of the core of the merger remnant were also found to depend on the rate of gas consumption by star formation. Simulations of binary mergers including dissipational effects have also shown that increasing the gas content also allows the merger remnant to be less triaxial Cox et al. (2006); Naab et al. (2006); Jesseit et al. (2007); Hoffman et al. (2010).

Including gas in simulations can even lead to an over-density in the central region. Weil & Hernquist (1996) and Meza et al. (2003) found that this could be impeded by the merger of multiple progenitors, which prevents the accumulation of material in the centre as efficiently as is done in pair mergers.

Reproducing the dichotomy in elliptical galaxies requires a more detailed investigation of the effect of gas ratios and properties of the progenitor galaxies. Bournaud et al. (2005) and Naab et al. (2006) found that more equal-mass mergers are able to destroy any disks in the ingoing galaxies and produce more slowly rotating remnants while mergers with a lower mass ratio tend to leave disks in place and produce more quickly rotating remnants. Higher gas content also tends to produce more disky, faster rotating elliptical galaxies. Naab et al. (2006) showed that binary mergers of early-type galaxies provide an additional channel for the formation of slowly rotating elliptical galaxies. The size evolution described above in massive elliptical galaxies has been shown by recent work (Bernardi, 2009; Naab et al., 2009; Tiret et al., 2010) to be possibly due to an inside-out hierarchical growth scenario. The central region may have formed primarily by major mergers until $z \sim 1$–2 and then the outer region built up by minor mergers until the present day allowing for a size evolution but insignificant mass evolution.

1.4.5 *Constraints on galaxy formation from dark matter content*

Probing the dark matter content is a fundamental tool for constraining channels for the formation of elliptical galaxies. In simulations of the growth of dark matter haloes in the absence of baryons, Navarro et al. (1996) found that they are well characterised by a 'universal' mass density profile over a wide range of masses. The profile is constrained by a characteristic scale radius r_s reflecting the radial extent of the halo, and the concentration parameter c, which is the ratio of the virial radius r_{vir} to r_s. r_{vir} is the radius at which the mean interior density ρ_{mean} is some multiple Δ_{vir} of the critical density[5] of the Universe ρ_{crit}. The hierarchical formation history of dark matter haloes produces a correlation between the concentration parameter c and the mass contained within the virial radius M_{vir}: less massive haloes are more concentrated and therefore were formed earlier. More recent N-body studies (Navarro et al., 2004; Merritt et al., 2005; Prada et al., 2006; Navarro et al., 2010) have found that the dark matter density profiles are only approximately universal and are better described by the Einasto density profile (conference in Alma-Ata, Kazakhstan, 1963), which has the same functional form as the Sèrsic profile described in 1.1.1.

Considerations of the interplay between baryons and dark matter haloes can alter the central dark matter density profile. Gas

5 The 'critical density' is the density required of the Universe for it to eventually stop expanding and collapse on itself.

in haloes cools via emission of radiation and therefore contracts and clusters on smaller scales than the dark matter. This deepens the potential well and causes the dark matter to contract via 'adiabatic contraction' (Eggen et al., 1962; Blumenthal et al., 1986; Gnedin et al., 2004). Another effect is the transfer of angular momentum from stellar material in neighbouring systems that are being accreted (Barnes, 1988; Debattista et al., 2008), thus affecting the shape of the dark matter density profiles. The details are however not yet well understood (Duffy et al., 2010). The work of Del Popolo (2010) uses semi-analytical prescriptions for the various baryonic processes to investigate their effect on the shapes of dark matter density profiles and found that the inner logarithmic density slope may have a significant dependence on halo mass and redshift, with slopes ranging from 0.0 for dwarf galaxies to 0.4 for objects of $M \simeq 10^{13} M_{\odot}$ and 0.94 for $M \simeq 10^{15} M_{\odot}$ clusters of galaxies. The slopes increase with increasing redshift and this trend reduces going from galaxies to clusters. Thus their work argues against an even approximate universality of dark matter density profiles.

There are several simulations looking at the formation of elliptical galaxies, set in the current cosmological paradigm. Robertson et al. (2006) looked at simulations of specifically binary mergers between disks, and between spheroids, each with dark matter haloes given by the current cosmological paradigm. The fraction of gas to the total baryonic mass was varied between 0 and 40% and effects of gas cooling, physics of the interstellar medium, star formation, feedback from supernovae (explosions of the biggest stars), and the growth of supermassive black holes in the centre were included. They found that the dark matter mass fraction at 1 R_e could vary between 0.1–0.5, with higher values in the remnants of more massive, gas-poor progenitors. Naab et al. (2007) used high-resolution simulations to follow the evolution of three galaxies in the field from redshift 5 until the present day, therefore allowing for several mergers. They considered photoionisation, cooling of gas between galaxies, and star formation, and allow for a series of mergers. They found dark matter mass fractions of 0.2–0.4 at 1 R_e. Oñorbe et al. (2007) found dark matter mass fractions of 0.3–0.6 at $\sim 1\, R_e$ in elliptical objects formed at zero redshift in cosmological simulations starting with primordial abundances of gas and considering the effects of gas cooling, star formation, and supernova feedback.

In spiral galaxies the evidence for dark matter is strong with the existence of cold gas in the disk as an ideal diagnostic. The gas particles move approximately in circular orbits constrained to the plane of the disk simplifying the dynamics to a 1-D problem. Rubin et al. (1978) used Hα emission from ionised hydrogen to show that the outer parts of practically all spiral galaxies have flat rotational curves, consolidating earlier speculations by Einasto (1969), Sizikov (1969), and Freeman (1970). The application of Newtonian dynamics shows that the movement of particles in

circular orbits following a flat rotation curve is analogous to an increasing mass profile even though the light is diminishing in the outer region of the galaxy. This points towards a non-stellar halo. These results were substantiated by work analysing 21-cm emission from neutral hydrogen (e.g. Bosma & van der Kruit, 1979; van Albada et al., 1985; Sancisi et al., 1979).

As shown in Section 1.3, discerning the mass profiles of elliptical galaxies from dynamics can be complicated due to the 3-D velocity distribution and three-fold degeneracy between the mass, orbital structure and shape. Additionally the cold gas found to large radii in spiral galaxies has been depleted through star formation or ejection into the surrounding medium (Sarazin, 1986) and though other kinematics tracers do exist further out, they are sparse. Dynamical models have generally found dark matter mass fractions of $\sim$ 10%–50% of the mass within 1 R_e in nearby groups of galaxies, and the Virgo, Fornax, and Coma cluster of galaxies (Gerhard et al., 2001; Cappellari et al., 2006; Thomas et al., 2007). Further out, Gerhard et al. (2001) predict equality between the mass contributions of the dark matter and luminous components at 2–4 R_e. For the Coma galaxies with sufficiently spatially extended data (generally the less luminous ellipticals), Thomas et al. (2007) found dark matter mass fractions between 65–75% at 4 R_e while Weijmans et al. (2009) used the SAURON spectrograph in the intermediate-luminosity elliptical galaxies, NGC 3379 and NGC 821, and found fractions of 30–50% at the same radius.

Discrete tracers such as planetary nebulae (PNe) and globular clusters (GCs) have enabled the halo to be probed out to 6–7 R_e (e.g. Hui et al., 1995; Méndez et al., 2001; Romanowsky et al., 2003; Côté et al., 2003; Peng et al., 2004; Romanowsky et al., 2009; de Lorenzi et al., 2009; Shen & Gebhardt, 2010; Napolitano et al., 2010). The dark matter mass fraction at 5 R_e ranges between 0.15–0.8 (Romanowsky et al., 2003; Peng et al., 2004; Napolitano et al., 2009; de Lorenzi et al., 2009; Napolitano et al., 2010).

The mass distributions of giant elliptical galaxies can be probed using two additional methods that are also independent of the anisotropy of the orbital structure of the stars. The dark matter mass in strong gravitational lenses can be constrained within the Einsten radius, typically 0.5 R_e (e.g. the Legacy Survey, Ruff et al., 2010), and also combined with stellar dynamical modelling techniques (e.g. the Sloan Lens ACS survey, Bolton et al., 2006; Koopmans et al., 2006; Bolton et al., 2008; Auger et al., 2009). Ruff et al. (2010) found a dark matter mass fraction of 0.42 ± 0.08 within 0.5 R_e for strong lenses at $z \sim 0.5$ from the Legacy Survey (SL2S). The Sloan Lens ACS (SLACS) survey found a minimum dark matter mass fraction of 0.38 ± 0.07 at 1 R_e in massive elliptical galaxies within $z \sim 0.36$ (Bolton et al., 2008).

As described in Sections 1.1.4 and 1.3.1, the most massive elliptical galaxies also harbour copious amounts of hot, low-density gas. If the gas is relatively undisturbed then hydrostatic equi-

librium can be assumed and the total mass distribution derived from the gas density and temperature profiles (e.g. Nulsen & Böhringer, 1995; Fukazawa et al., 2006; Humphrey et al., 2006; Churazov et al., 2008; Nagino & Matsushita, 2009). The advent of the Chandra and XMM-Newton telescopes has enabled detailed mass distributions to be obtained out to 10 R_e. Analysis of Chandra observations found a reasonably flat total mass-to-light ratio in the central R_e that increases by one order of magnitude at $\sim 10\,R_e$, implying that dark matter accounts for about 90% of the total mass at this radius (Humphrey et al., 2006). Joint analyses of Chandra and XMM-Newton observations have found dark matter mass fractions of 0.14–0.50 at 1 R_e (Fukazawa et al., 2006), and ~ 0.5 at $\sim 3\,R_e$ and ~ 0.67 at $\sim 6\,R_e$ (Nagino & Matsushita, 2009).

The total mass distribution in elliptical galaxies has often been found both from dynamical and lensing analyses to be well described by an isothermal total mass distribution, i.e. the logarithmic mass density is proportional to -2 (e.g. Gerhard et al., 2001; Koopmans et al., 2006; Thomas et al., 2007; Auger et al., 2010). This corresponds to a flat circular velocity curve suggesting a strange conspiracy between luminous and dark matter. The exact division between luminous and dark matter is more difficult to constrain and work exploring different dark matter mass distributions has generally not been able to differentiate between them (Thomas et al., 2007; Napolitano et al., 2009, 2010).

Gerhard et al. (2001) found that the halo core densities and phase-space densities are at least $\sim$ 25 times larger and the halo core radii $\sim$ 4 times smaller than in spiral galaxies of the same circular velocity. Similarly, Thomas et al. (2009) found that the average dark matter density inside 2 R_e is 6.8 times larger in elliptical galaxies compared to in disk galaxies of the same B-band luminosity. At the same stellar mass, dark matter densities in ellipticals are 13.5 times higher than in spirals. They concluded an assembly redshift $(1 + z)$ of the early-type haloes that is two times larger than that of similarly bright spirals. There is also some evidence for a dichotomy in the dark matter content between slow and fast rotators as with many other properties (Bertin et al., 1994; Cappellari et al., 2006; Napolitano et al., 2009; Del Popolo, 2010, and see Section 1.1.5), possibly as a result of varying baryonic effects during their assembly histories.

1.4.6 *Constraints on galaxy formation from orbital structure*

The comparison of the orbital structure of merger remnants of simulations with that of real elliptical galaxies is a fundamental approach for obtaining constraints on the formation mechanisms involved in the creation of elliptical galaxies. The remnants of mergers have long been thought to have radially anisotropic velocity structures (Gerhard, 1981; Barnes, 1992) and this has been verified by more recent simulations (Sáiz et al., 2004; Jesseit

et al., 2005; Oñorbe et al., 2007). The inclusion of dissipational effects of gas can make the orbital structure less radial (Cox et al., 2006; Naab et al., 2006; Thomas et al., 2009; Hoffman et al., 2010).

Oblate, axisymmetric dynamical models of elliptical galaxies in nearby groups and clusters of galaxies within ~ 25 Mpc and the Coma cluster of galaxies (at ~ 100 Mpc) has found a large variety of orbital compositions (Cappellari et al., 2007; Thomas et al., 2009). Even most of the rotating ellipticals are flattened by an anisotropy in the stellar velocity dispersions. Thomas et al. (2009) attributed the apparent lack of strong radial anisotropy in early-type galaxies to the influence of dissipational processes in simulations.

1.5 OPEN QUESTIONS IN THIS THESIS

The present work focuses on massive elliptical galaxies, which are the largest stellar conglomerates in the night sky and are on the very left of the Hubble Sequence. They are preferentially found in dense and cluster environments.

The sample consists of six massive elliptical galaxies, all within 30 Mpc. NGC 1399 is located at the centre of the Fornax cluster, NGC 1407 and NGC 5846 at the centre of groups, and NGC 4472 (M49), NGC 4486 (M87) and NGC 4649 (M60) at the centre of sub-clumps in the irregular Virgo cluster. NGC 4486 is at the centre of the most massive sub-component. More details on their properties can be found in Chapter 2. Figure 6 shows optical images of the sample.

The questions addressed in this thesis are:

1. How well are mass distributions from X-rays determined and how do they compare to those from dynamical models?
2. What is the dark matter content in massive elliptical galaxies?
3. What is the distribution of stellar orbits in massive elliptical galaxies?
4. What can we learn from our analyses on the mechanisms involved in the formation of elliptical galaxies?

Though the radial range probed by X-ray observations is fantastic, there is still much dispute on the accuracy of mass profiles obtained in this way due to problems with obtaining accurate temperature and density profiles and the validity of hydrostatic equilibrium. A novel non-parametric method based on Bayesian statistics is developed and applied to deep XMM-Newton and Chandra observations to obtain total mass distributions. This is compared with previous determinations from X-ray observations and dynamical models. From the total mass distribution, the stellar and dark matter contents are inferred and their correlation with the local environment explored. This work is discussed in Chapter 2.

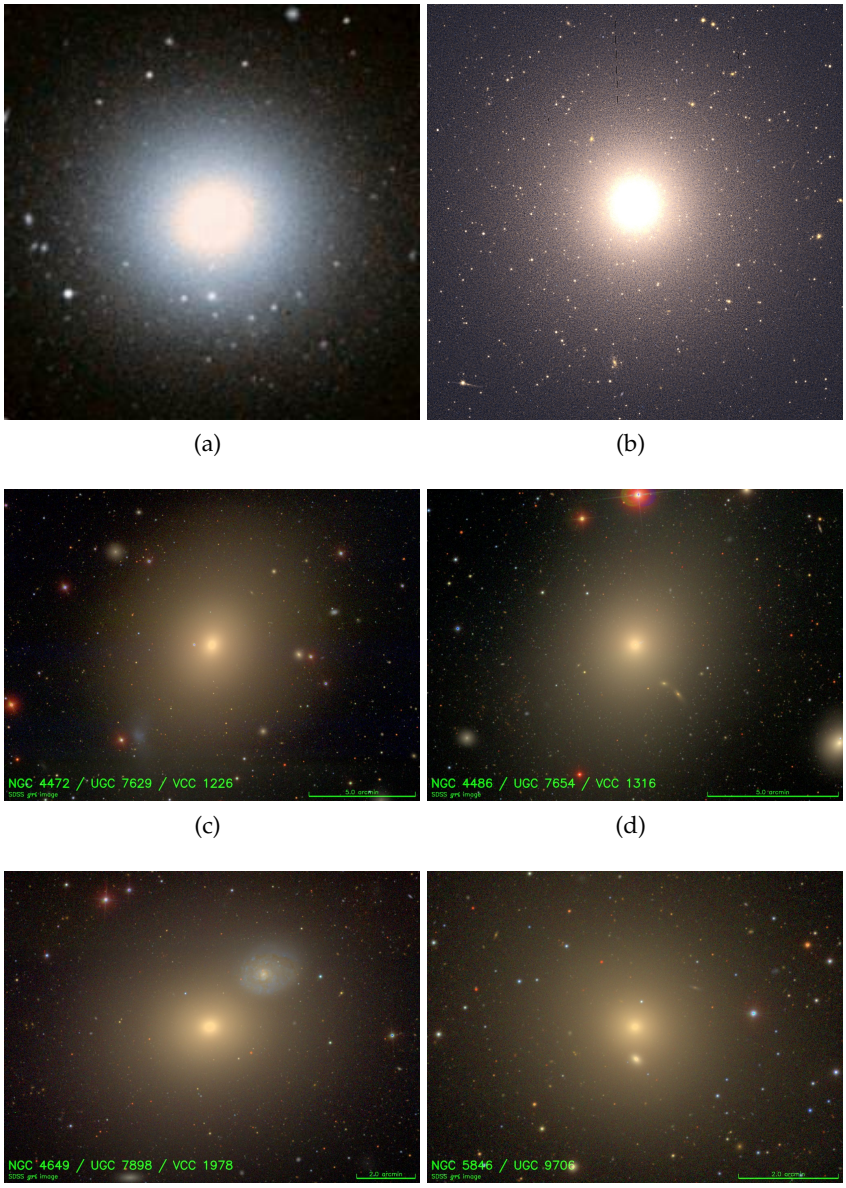

(a) (b) (c) (d) (e) (f)

Figure 6: Optical images of the sample of massive elliptical galaxies: (a) NGC 1399, (b) NGC 1407, (c) NGC 4472, (d) NGC 4486, (e) NGC 4649, and (f) NGC 5846.

Currently radially extended dynamical models are still sparse, especially in massive elliptical galaxies. Jeans equations and the made-to-measure code NMAGIC are used to fit a combination of kinematic and photometric data extending far into the halo to constrain the orbital structure there. Dynamical models of NGC 5846, NGC 4486, NGC 4649, and NGC 1399 are described in Chapters 3, 4, 5, and 6 respectively.

The results of this work, how they compare to past results, and possible future avenues of research are summarised in Chapter 7.

Part I

X-RAY PROPERTIES OF THE HOT GAS

2

STEEPENING MASS PROFILES, DARK MATTER AND ENVIRONMENT OF X-RAY BRIGHT ELLIPTICAL GALAXIES

This work was published as Das et al. (2010) in MNRAS.

We use a new non-parametric Bayesian approach to obtain the most probable mass distributions and circular velocity curves along with their confidence ranges, given deprojected density and temperature profiles of the hot gas surrounding X-ray bright elliptical galaxies. For a sample of six X-ray bright ellipticals, we find that all circular velocity curves are rising in the outer parts due to a combination of a rising temperature profile and a logarithmic pressure gradient that increases in magnitude. Therefore at large radii, mass density profiles rise more steeply than isothermal profiles, implying that we are probing the more massive group-sized haloes in which these galaxies are embedded. Comparing the circular velocity curves we obtain from X-rays to those obtained from dynamical models, we find that the former are often lower in the central $\sim$ 10 kpc. This is probably due to a combination of: i) Non-thermal contributions of up to $\sim$ 35% in the pressure (with stronger effects in NGC 4486), ii) multiple-temperature components in the hot gas, iii) incomplete kinematic spatial coverage in the dynamical models, and iv) mass profiles that are insufficiently general in the dynamical modelling. Complementing the total mass information from the X-rays with photometry and stellar population models to infer the dark matter content, we find evidence for massive dark matter haloes with dark matter mass fractions of $\sim$ 35–80% at $2R_e$, rising to a maximum of 80–90% at the outermost radii. We also find that the six galaxies follow a Tully-Fisher relation with slope $\sim$ 4 and that their circular velocities at $1R_e$ correlate strongly with the velocity dispersion of the local environment. As a result, the galaxy luminosity at $1R_e$ also correlates with the velocity dispersion of the environment. These relations suggest a close link between the properties of central X-ray bright elliptical galaxies and their environments.

2.1 INTRODUCTION

X-ray bright elliptical galaxies are massive galaxies, thought to be among the most evolved systems in our Universe with a complex formation history. They are believed to grow from mergers between smaller galaxies, and after star formation ceases at $z \sim 1$–2, they become larger and less compact through the significant ac-

Table 1: Sample of X-ray bright elliptical galaxies: (1) Galaxy name, (2) galaxy classification from NED, (3) distance taken from Tonry et al. (2001), (4) X-ray luminosity taken from O'Sullivan et al. (2001), (5) velocity dispersion of the surrounding environment and (6) source of the velocity dispersion values. References are D01 (Drinkwater et al., 2001), T06 (Trentham et al., 2006), G99 (Gavazzi et al., 1999), M05 (Mahdavi et al., 2005).

Galaxy	Classification	Distance (Mpc)	$\log L_X$ (log erg/s)	σ_{env} (km/s)	Source
(1)	(2)	(3)	(4)	(5)	(6)
NGC 1399	cD; E1 pec	19.95	41.63	370	D01
NGC 1407	E0	28.84	41.00	387	T06
NGC 4472	E2	16.29	41.43	607	G99
NGC 4486	E0-E1 pec	16.07	42.95	762	G99
NGC 4649	E2	16.83	41.28	702	G99
NGC 5846	E0-E1	24.20	41.65	322	M05

cretion of stellar material from neighbouring smaller systems (e.g. van Dokkum et al., 2008; Naab et al., 2009).

Knowledge of the total mass distributions of galaxies gives us insight into their formation history at several different levels. At the most basic level, it tells us the combined mass of these collapsed systems. If we incorporate information from photometry and stellar population models, we can disentangle the respective luminous and dark matter components. Comparing their properties with what is expected from simulations will help place constraints on current theories of galaxy evolution. The mass profile could also be used as input in dynamical models of galaxies, therefore mitigating the usual mass-anisotropy degeneracy. This would provide more stringent constraints on the orbital structure, which serves as an imprint of the processes that occurred in the past to create the galaxy. Finally, it will give us an insight into the relations between the masses of collapsed systems and the environments they reside in.

There are several methods in the literature for obtaining the mass distributions of elliptical galaxies. Dynamical models can be constructed by superposing a library of orbits (e.g. Rix et al., 1997; Gebhardt et al., 2003; Thomas et al., 2004; Cappellari et al., 2006) or distribution functions (e.g. Dejonghe et al., 1996; Gerhard et al., 1998; Kronawitter et al., 2000), or by constructing a system of particles (de Lorenzi et al., 2008, 2009) such that the projection of the system best reproduces observed surface-brightness and kinematic profiles. These models give the mass distribution and orbital structure of the galaxies simultaneously. Strong lensing gives the projected mass within the Einstein ring and weak lensing studies provide mass density profiles for a sample of galaxies (e.g. Treu & Koopmans, 2004; Mandelbaum et al., 2006; Gavazzi et al., 2007; Koopmans et al., 2009). The properties of X-ray bright elliptical galaxies allow an additional possibility for obtaining

mass distributions (e.g. Nulsen & Böhringer, 1995; Fukazawa et al., 2006; Churazov et al., 2008; Nagino & Matsushita, 2009). The X-ray spectra are dominated by lines and by continuous emission from thermal bremsstrahlung radiation produced in the surrounding halo of hot gas. The spectra can be deprojected and fitted to derive 3-D temperature and density profiles of the gas, and if we assume it is in hydrostatic equilibrium, we can derive the enclosed mass profile.

Generally the literature points towards isothermal mass distributions in elliptical galaxies, with a conspiracy between the luminous and dark matter components resulting in flat circular velocity curves similar to that found in spiral galaxies (e.g. Kronawitter et al., 2000; Koopmans et al., 2009; Churazov et al., 2010). Fukazawa et al. (2006) however, determined mass distributions of a sample of 53 elliptical galaxies from Chandra and XMM-Newton observations, and found that they are better described by power laws with an index $\gtrsim 1$, i.e. their circular velocity curves range between flat and rising. The particle-based dynamical models of de Lorenzi et al. (2008, 2009) found falling circular velocity curves for the intermediate-luminosity galaxies, NGC 3379 and NGC 4697. Thomas et al. (2007) found a range of slopes in the elliptical galaxies belonging to the Coma cluster, from their orbit-based dynamical models.

In this Chapter, we examine the isothermality of mass distributions from X-ray observations and whether they are accurate enough to derive dark matter mass profiles, to use in dynamical modelling, and to determine global properties of elliptical galaxies. To address these issues we need to apply hydrostatic equilibrium using a procedure that is as free from systematic biases as possible.

Cowie et al. (1987); Humphrey et al. (2006); Fukazawa et al. (2006); Nagino & Matsushita (2009) used methods where the measured temperature and density profiles are parameterised before applying hydrostatic equilibrium, to circumvent differentiating the observed profiles, which are often noisy. Churazov et al. (2008) avoided differentiation by calculating only the potential profile. Nulsen & Böhringer (1995) found the most likely mass profile of NGC 4486 (M87) from temperature and density profiles using a non-parametric method, and Humphrey et al. (2009) used a parametric Bayesian analysis. The parametric methods used in the literature will generally underestimate the range of mass profiles consistent with the data. They also introduce systematic biases in the masses derived because of the assumptions on the profile shapes.

We use the sample of galaxies from Churazov et al. (2010) and we discuss them and the properties of the hot X-ray gas they harbour briefly in Section 2.2. In Section 2.3 we describe the implementation of a new non-parametric Bayesian approach to obtain the total mass and circular velocity profiles from hydrostatic equilibrium. In Section 2.4 we show the results of tests of

the new method and how to optimise it. In Section 2.5 we show the total mass profiles and circular velocity curves we obtain by applying the method to the sample of galaxies, and the stellar and dark matter contributions we infer from published photometry and stellar population model mass-to-light ratios. In Section 2.6 we compare the individual circular velocity curves we obtain to previous determinations from X-rays and published dynamical models. We also examine the isothermality of the mass profiles of these galaxies, and look for any correlations that may exist between the stellar component, the total circular velocities and properties of the surrounding environment. We end with our conclusions in Section 2.7.

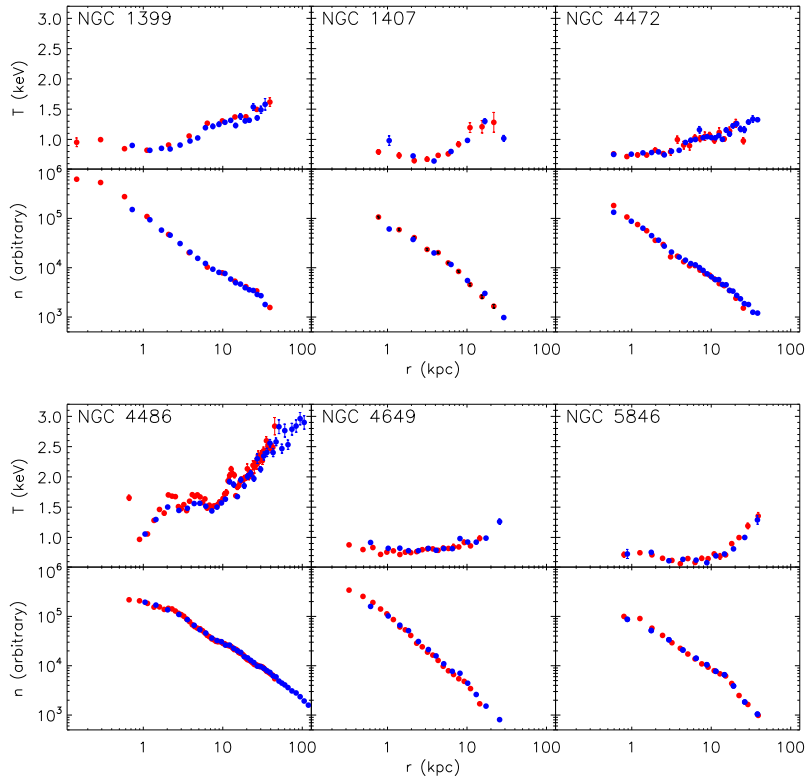

Figure 7: Properties of the hot gas surrounding the sample of six X-ray bright elliptical galaxies: Deprojected temperature (upper plot) and density profiles (lower plot) were obtained by Churazov et al. (2010) from the analysis of Chandra observations (red dots) and XMM-Newton observations (blue dots). The temperature is shown on a linear scale. The density and radii are shown on logarithmic scales.

2.2 THE SAMPLE

We work on the sample of galaxies analysed in Churazov et al. (2010). Table 1 lists the galaxies in the sample, the galaxy classification, the distances we assume, the X-ray luminosity and the velocity dispersion of the surrounding environment. NGC 1399 is located at the centre of the Fornax cluster, NGC 1407 and NGC

5846 at the centre of groups, and NGC 4472, NGC 4486 and NGC 4649 at the centre of sub-clumps in the irregular Virgo cluster. NGC 4486 is at the centre of the most massive sub-component. Drinkwater et al. (2001) determined the velocity dispersion of the environment surrounding NGC 1399 from 92 galaxies within a radius of about 2.7° (930 Mpc), Trentham et al. (2006) from 35 galaxies within about 900 kpc of NGC 1407 and Mahdavi et al. (2005) from 87 galaxies within a radius of 1.8° (777 kpc) of NGC 5846. Gavazzi et al. (1999) calculated the velocity dispersion in sub-clumps containing NGC 4472, NGC 4486 and NGC 4649 using 166, 62 and 58 galaxies respectively.

The sample galaxies harbour significant amounts of hot gas that except in the case of NGC 4486, appears relatively undisturbed, suggesting hydrostatic equilibrium.

2.2.1 *Density and temperature profiles of the hot gas*

The X-ray spectrum of the hot gas surrounding X-ray bright ellipticals consists of many emission lines and continuous emission primarily from the mechanism of thermal bremsstrahlung. To obtain information on the temperature and density profiles of the gas, the spectra are fitted with models that make assumptions about the absorption along the line-of-sight and the metal abundance in the gas.

We use the deprojected temperature and density profiles obtained by Churazov et al. (2010) from Chandra and XMM-Newton observations, shown in Figure 7. The composite profiles benefit in the central region from the high spatial resolution of Chandra and in the outer parts from the large field-of-view and collecting power of XMM-Newton. The XMM-Newton profiles are not more spatially extended than the Chandra profiles as one would normally expect, because several pointings were used with the Chandra instrument.

Churazov et al. (2010) first spherically deprojected the X-ray spectra using a non-parametric least-squares algorithm described in Churazov et al. (2003). This algorithm finds the set of 3-D spectra in spherical shells that project to best-fit the observed spectra, assuming a power-law decline in the emission outside the maximum observed radius. The deprojected spectra were then fit with the single-temperature APEC code in XSPEC, which resulted in a determination of the 3-D temperature and density for each shell. The abundance of heavy elements in the model was fixed at 0.5 solar in all shells. This was assumed because for cool gas with approximately solar abundance of heavy elements, the contributions of continuum and lines are difficult to disentangle unambiguously, resulting in an anti-correlation between the emission measure and abundance.

Figure 7 shows generally a good agreement between the Chandra and XMM-Newton profiles in the region of overlap. NGC 1399, NGC 1407, NGC 4649 and NGC 5846 have deprojected tem-

perature profiles that start around 1.0 keV in the central region, dip slightly towards 0.5 keV and then slowly increase outwards to about 1.5 keV. The temperature profile of NGC 4472 increases steadily from about 0.7 keV to 1.4 keV while the temperature profile of NGC 4486 increases much more steeply from about 1 keV to 3 keV with a small dip in between. The density profiles are much smoother than the temperature profiles. They appear to be very similar to each other with a linear decrease in a log-log scale and are therefore close to power laws.

2.3 NON-PARAMETRIC RECONSTRUCTION OF THE MASS DISTRIBUTION

If the gas is in hydrostatic equilibrium, we can obtain the mass distribution from the deprojected gas temperature and density profiles. Here we describe a new non-parametric Bayesian approach to obtain the most probable mass profiles within some confidence range.

2.3.1 *Hydrostatic equilibrium*

Hydrostatic equilibrium relates the 3-D temperature and density profiles of the gas to the 3-D mass distribution of the galaxy. If the gas is relatively undisturbed, we can assume it is in hydrostatic equilibrium. Balancing the pressure of the gas with the gravitational forces acting on it in a spherical system gives:

$$-\frac{d\Phi(r)}{dr} = \frac{1}{\rho(r)}\frac{dP(r)}{dr} \tag{2.1}$$

where ρ is the gas mass density, P the gas pressure and r is the 3-D radius from the centre of the galaxy. We assume that the gas is ideal and therefore $P = nk_BT$ and $\rho = \mu m_p n$, where n is the particle number density of the gas, and $\mu = 0.61$ is the average gas particle mass in terms of the proton mass, m_p. This value of μ corresponds to a helium number density of 7.92×10^{-2} and 0.5 solar abundance of heavier elements. Now we have related the temperature and density of the gas to the gravitational potential it resides in. We can express Equation (2.1) in terms of the circular velocity curve, a distant-independent measure of the mass, $V_c^2 = rd\Phi/dr$. The circular velocity at some radius in a galaxy is the orbital velocity of a star at that radius on a circular orbit in the same gravitational field. Equation (2.1) becomes:

$$V_c^2 = -\frac{k_bT}{\mu m_p}\frac{d\ln P}{d\ln r} \tag{2.2}$$

It can be seen that to obtain the circular velocity curve, the temperature and gradient of the logarithmic pressure is required. This is more convenient than the usual form of this equation, where both the temperature and density derivatives are required.

2.3.2 *Bayesian approach*

We would like to find the most probable logarithmic pressure gradients (and then circular velocity curve from hydrostatic equilibrium) within some confidence range given the deprojected temperature and density profiles measured from the data. Merritt & Tremblay (1994) showed that it is best to treat these problems non-parametrically because parametric methods are susceptible to systematic biases and underestimate the confidence ranges. The procedure we develop can eventually incorporate the spectral fitting and deprojection directly, but in a first step we concentrate here on generalising parametric methods on deprojected profiles to non-parametric ones. We adopt a Bayesian approach rather than the more conventional method of χ^2 minimisation for two reasons: Firstly, prior information such as the intrinsic smoothness of the profiles is easily incorporated. Secondly, the probabilistic nature of Bayesian methods means confidence ranges are more easily extracted.

Let us describe the galaxy by some model M. Bayes' theorem tells us the probability of M given the deprojected temperature and density profiles X from the X-ray observations:

$$p(M \mid X) = \frac{p(X \mid M)\, p(M)}{p(X)} \tag{2.3}$$

Taking the logarithm of both sides gives:

$$\ln(p(M \mid X)) = \ln(p(X \mid M)) + \ln(p(M)) - \ln(p(X)) \tag{2.4}$$

$p(M \mid X)$ is the posterior probability of the model given the deprojected temperature and density profiles. $p(X \mid M)$ is the likelihood probability $\mathcal{L}(M)$ of the deprojected temperature and density profiles given the model. $p(M)$ is the prior probability of the model, indicating what we thought about the probability of that model before we knew anything about the deprojected temperature and density profiles. Finally $p(X)$ is the probability of those particular deprojected density and temperature profiles, but here only acts as a normalising factor because the profiles are fixed by the X-ray observations. To obtain the most probable model profile, we need to maximise the posterior probability $p(M \mid X)$. In order to find all model profiles within some confidence range we have to find the shape of the posterior probability distribution.

We define our model $M = M(T, lpg, P, V_c, m)$, where T is the temperature, lpg is the logarithmic pressure gradient, P is the pressure, V_c is the circular velocity and m is the enclosed mass. The pressure P is obtained by integrating the logarithmic pressure gradient lpg. The circular velocity V_c is obtained by applying hydrostatic equilibrium, and the mass m follows from $V_c^2 = Gm/r$. The model T and P are compared with the deprojected T_{depro} and P_{depro} obtained from the X-ray observations and deprojection. The model functions are defined on a grid of n_{mod} logarithmically-spaced radii r, finer than the grid of n_{depro} deprojected radii r_{depro}.

We interpolate the functions to the grid of deprojected radii for the calculation of the χ^2 function below. We shall use j to denote an element on the model grid and k to denote an element on the deprojected grid. For example, $T[j]$ denotes the model temperature at the radius $r[j]$ on the model grid and $T[k]$ denotes the model temperature at the radius $r_{\rm depro}[k]$ on the deprojected grid.

We assume that the likelihood function $\mathcal{L}(M)$ takes the form of a multi-variate Gaussian:

$$\mathcal{L}(M) \propto \exp(-\chi^2/2) \tag{2.5}$$

χ^2 is the goodness-of-fit of the model temperature to the deprojected temperature and the model pressure to the deprojected pressure:

$$\chi^2 = \sum_{k=1}^{n_{\rm depro}} \left(\frac{P_{\rm depro}[k] - P[k]}{\epsilon_P[k]} \right)^2 + \sum_{k=1}^{n_{\rm depro}} \left(\frac{T_{\rm depro}[k] - T[k]}{\epsilon_T[k]} \right)^2 \tag{2.6}$$

where ϵ_P and ϵ_T are 1-σ statistical errors on the deprojected pressure and temperature profiles respectively. This choice for the likelihood function assumes a Gaussian error distribution and can be generalised if needed. To enforce physically acceptable solutions, we impose the following boundary conditions as priors on the model temperature and logarithmic pressure gradient profiles:

1. $T \geq 0$
2. $V_c \in \Re \Rightarrow lpg \leq 0$

We also need to define a smoothing prior because unlike in a parameterised model, the best-fit non-parametric model would go exactly through all the deprojected temperature and density points resulting in noisy profiles. Also, as the model grid is finer than the deprojected grid, without smoothing there would be many solutions where the model is very similar to the deprojected temperature and density at the deprojected radii but with varying values in between. Therefore, applying smoothing constraints reduces the model degeneracies by getting rid of unphysical solutions. We specifically penalise non-smooth solutions of the model temperature, logarithmic pressure gradient and resulting circular velocity curve because this is consistent within the hydrostatic framework. We define the smoothing prior as follows:

$$p(M) \propto \exp(-S) \tag{2.7}$$

S is a weighted sum of the mean-square second derivatives of the temperature, logarithmic pressure gradient and circular velocity curve:

$$S = c(S_1 + S_2 + S_3) \tag{2.8}$$

$$S_1 = \sum_{j=2}^{n_{\rm mod}-1} \left(\frac{\ln T[j+1] - 2\ln T[j] + \ln T[j-1]}{h^2} \right)^2 \tag{2.9}$$

$$S_2 = \sum_{j=2}^{n_{\rm mod}-1} \left(\frac{lpg[j+1] - 2lpg[j] + lpg[j-1]}{h^2} \right)^2 \tag{2.10}$$

$$S_3 = \sum_{j=2}^{n_{\rm mod}-1} \left(\frac{\ln V_c[j+1] - 2\ln V_c[j] + \ln V_c[j-1]}{h^2} \right)^2 \tag{2.11}$$

h is the logarithmic interval between the model radii in an equally-spaced logarithmic radial grid and $c = n_{\rm depro}\lambda/(n_{\rm mod} - 2)$ determines the weight of the smoothing term relative to the χ^2 term. It is defined so that for fixed λ, the smoothing term is independent of $n_{\rm depro}$ and $n_{\rm mod}$. λ is specified by the user and Section 2.4.2 describes how we choose its optimal value. As the second derivatives are difficult to estimate at the boundaries, we omit their contribution to the smoothing prior.

Combining the likelihood function and the priors we get the following expression for the logarithm of the posterior probability, which we call F:

$$F = \ln(p(M \mid X)) = -\frac{\chi^2}{2} - S + N \tag{2.12}$$

N is a normalisation constant, which we set to zero for convenience.

2.3.3 *The distribution of posterior probabilities*

Now that we have defined our model and the posterior probability of a particular model given the X-ray information, we need an initial model and a procedure to generate new models in order to find the distribution of posterior probabilities. Here we will discuss our initial model and the 'proposal function', a function used to generate a new model. We then describe an algorithm we implement, optimised to find the most probable model. This is similar to the method of Magorrian (1999), who found the most probable 3-D distribution of stars given a projected surface-brightness distribution. We also describe a second algorithm based on the Metropolis-Hastings sampling scheme in a Markov Chain Monte Carlo (MCMC) approach, optimised to extract confidence ranges associated with a model. We define an 'iteration' as a change proposed by the proposal function that lies within the boundary conditions.

2.3.3.1 *The initial model*

The initial model is given by $M_{\rm init}(T_{\rm init}, lpg_{\rm init}, P_{\rm init}, V_{\rm c,init}, m_{\rm init})$, calculated on the model grid. $T_{\rm init}$ is determined by fitting a

highly smoothed spline to the deprojected temperature $T_{\rm depro}$. $lpg_{\rm init}$ is set to the slope of a straight-line fit between the logarithm of the deprojected pressure, $P_{\rm depro}$ and the logarithm of the deprojected radii, $r_{\rm depro}$. $V_{\rm c,init}$ and $m_{\rm init}$ follow from applying hydrostatic equilibrium (Equation (2.2)), and the posterior probability of this initial model $F_{\rm init}$ can be calculated using Equation (2.12).

2.3.3.2 *The proposal function*

The proposal function $q(M_{i+1} \mid M_i)$ is a probability distribution that generates a model M_{i+1} from model M_i. We only make changes to the model T and lpg and then calculate the resulting model P from integrating lpg and the model V_c and m by applying hydrostatic equilibrium. The proposal function is defined as:

$$q(M_{i+1} \mid M_i) = p[j]\, G_T[j]\, G_{lpg}[j] \tag{2.13}$$

$p[j] = 1/n_{\rm mod}$, is the probability of picking point j on the model grid. $G_T[j] = p(T_{i+1}[j] \mid T_i[j])$ is the probability of going from $T_i[j]$ to $T_{i+1}[j]$ and $G_{lpg}[j] = p(lpg_{i+1}[j] \mid lpg_i[j])$ is the probability of going from $lpg_i[j]$ to $lpg_{i+1}[j]$, at the chosen grid point j. $G_T[j]$ and $G_{lpg}[j]$ are described by Gaussians centred on $T_i[j]$ and $lpg_i[j]$ respectively and with dispersions $\sigma_T[j]$ and $\sigma_{lpg}[j]$. σ_T is initially set to the root-mean squared deviation between $T_{\rm init}$ and $T_{\rm depro}$, and σ_{lpg} is initially set to the root-mean squared deviation between $lpg_{\rm init}$ and a two-point estimate of the logarithmic pressure gradient.

2.3.3.3 *Obtaining the most probable solution (non-Markov mode)*

To obtain the most probable model we want to get to the maximum of the posterior probability distribution as quickly as possible. We first relax the initial model to mitigate any bias introduced in choosing it. In this phase the proposal function is used to make a change to the model at a random point on the model grid. If the boundary conditions are met, then the proposed change is accepted and the new posterior probability F and change in posterior probability ΔF are calculated. After $n_{\rm relax}$ iterations, the relaxation phase ends and the average change in the posterior probability $\langle \Delta F \rangle$ is calculated. In the relaxation phase, it is possible for $\langle \Delta F \rangle$ to be either negative or positive as we accept all changes subject to the boundary conditions.

In the improvement phase, a change to the model is proposed via the proposal function and if the boundary conditions are met then an acceptance probability α is specified for going from model M_i to model M_{i+1}:

$$\alpha(i, i+1) = \min(1, r) \text{ where } r = \exp \frac{\Delta F}{\langle \Delta F \rangle} \tag{2.14}$$

A random number z is generated between 0 and 1. If $z \leq \alpha(i, i+1)$, the proposed change is accepted and the dispersion of the

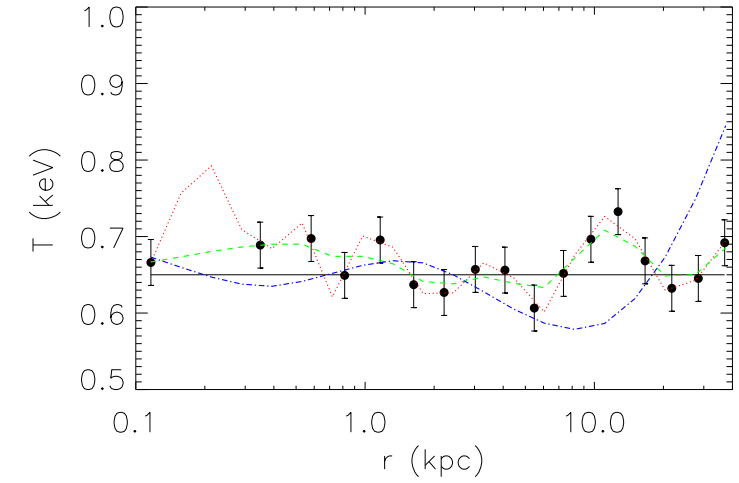

(a)

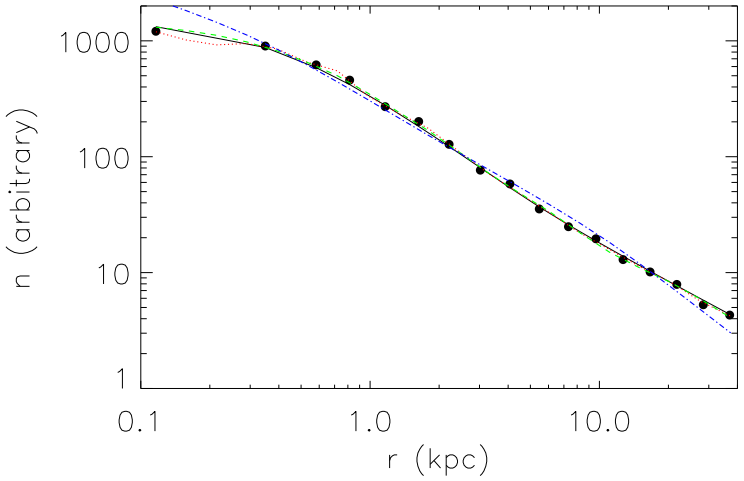

(b)

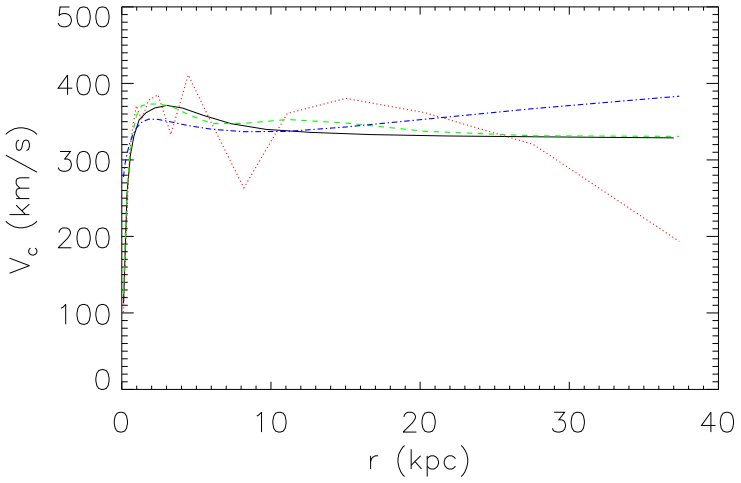

(c)

Figure 8: Application of the non-parametric analysis to a test model: The black lines show the (a) temperature, (b) density, and (c) circular velocity curves for our test model. The filled black circles show the pseudo temperature and density profiles. The remaining lines show recovered profiles from pseudo deprojected temperature and density profiles generated from the test model, assuming $\lambda = 0.001$ (red, dotted), $\lambda = 0.5$ (green, dashed) and $\lambda = 100$ (blue, dash-dotted).

proposal function is decreased, $\sigma_T[j] = \sigma_T[j]/u$ and $\sigma_{lpg}[j] = \sigma_{lpg}[j]/u$, where $u = 1.01$ to allow for fine changes. Otherwise the proposed change is rejected and $\sigma_T[j] = \sigma_T[j] \times u$ and $\sigma_{lpg}[j] = \sigma_{lpg}[j] \times u$. This update to the proposal function is made after each change to the model so that in general we follow a path that maximises the posterior probability, but still allow for the possibility of jumping away from a local maximum. The value for $\langle \Delta F \rangle$ is updated every $n_{\log}$ steps.

This procedure is continued until the model no longer significantly changes.

2.3.3.4 *Obtaining the confidence range (Markov mode)*

To obtain the confidence range we need to probe the shape of the posterior probability distribution. The most efficient way to do this is using the Metropolis-Hastings algorithm, which generates models with a probability equal to the posterior probability. In our implementation of this algorithm we have three phases. The first is a relaxation phase of the initial model as in Section 2.3.3.3 with n_{relax} iterations. The second is a tuning of the proposal function, where the proposal function is updated as in the second phase in Section 2.3.3.3. This phase ends after n_{tune} steps, defined such that the acceptance rate in the third phase is 23%. This is recommended as the most efficient rate for probing the shape of the posterior probability distributions in high-dimensional implementations of the Metropolis-Hastings algorithm (Liddle, 2009).

In the third phase we want to map out the shape of the posterior probability distribution around the maximum. The proposed changes must therefore satisfy 'detailed balance':

$$p(M_i \mid X)\, p(M_{i+1} \mid M_i) = p(M_{i+1} \mid X)\, p(M_i \mid M_{i+1}) \quad (2.15)$$

$p(M_{i+1} \mid M_i) = q(M_{i+1} \mid M_i)\, \alpha(i, i+1)$ and $p(M_i \mid M_{i+1}) = q(M_i \mid M_{i+1})\, \alpha(i+1, i)$, where the proposal function q and acceptance probability α were defined in Equations (2.13) and (2.14) respectively. This is ensured by no longer changing the proposal function and replacing the definition of r from Equation (2.14) with:

$$r = \exp \Delta F \quad (2.16)$$

r is called the Metropolis ratio. This will produce a sequence of models called a Markov chain. This is continued until the Markov chain converges to the posterior probability distribution. The initial $\sim$ 25–50% of the accepted changes is called the 'burn-in phase' and is discarded because they do not reflect the posterior probability distribution. The convergence of the Markov chain can be checked by looking at the distribution of model values at each grid point and ensuring that subsequent iterations produce insignificant changes.

Marginalisation with a Markov chain is trivial because the density of any grid point in the Markov chain will be proportional

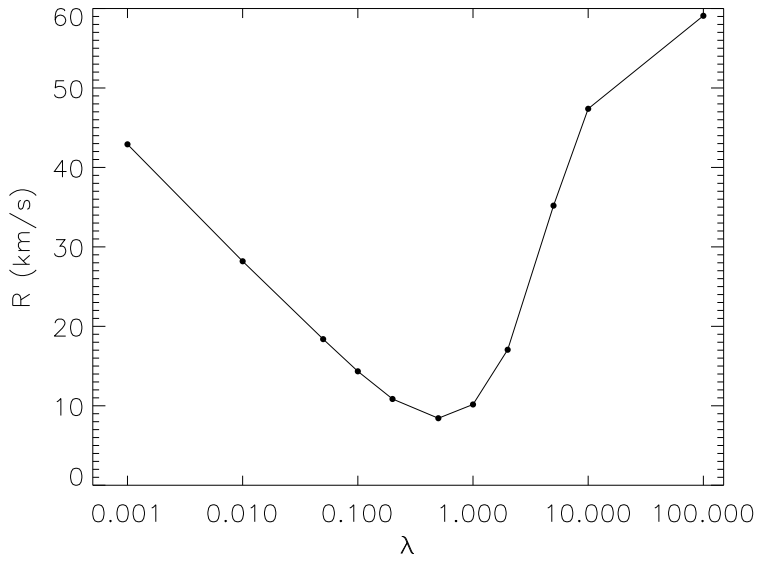

Figure 9: Residuals between the circular velocity curve of the test model and the circular velocity curves recovered by the non-parametric analysis for different values of the smoothing parameter, λ.

to the posterior distribution marginalised over the other variables. The shape of the marginal posterior density at each grid point will tell us the median and confidence ranges, and the expectation value is simply a mean of all the values generated in the Markov chain.

2.4 TESTS

We need to test the ability of the two methods to recover the circular velocity curve of a galaxy and to choose values for the parameters $n_{\rm relax}$, $n_{\rm log}$, $n_{\rm burnin}$, $n_{\rm iter}$ and λ that we have introduced in Section 2.3.2, 2.3.3.3 and 2.3.3.4.

For the relaxation phase we set $n_{\rm relax} = 3(2n_{\rm mod})$, similar to that used by Magorrian (1999). In the non-Markov mode we set $n_{\rm log} = 8(2n_{\rm mod})$, again similar to that used by Magorrian (1999). In the Markov mode we set $n_{\rm burnin}$ to 25% of the total number of accepted changes to ensure we are only sampling the posterior probability distribution. We choose the total number of accepted changes $n_{\rm iter}$ as the number of iterations after which the model no longer appears to change significantly.

To test the two modes of operation and calibrate the number of accepted changes $n_{\rm iter}$ and the smoothing parameter λ, we define a model of a typical X-ray bright elliptical galaxy, from which we draw pseudo 3-D temperature and density profiles.

2.4.1 *The test model and pseudo temperature and density profiles*

The test model is defined by a 3-D temperature profile, 3-D density profile and a circular velocity curve $[T_{\rm test}, n_{\rm test}, V_{\rm c,test}]$ typical

for a X-ray bright elliptical galaxy. These profiles are shown by the black lines in Figure 8. For the circular velocity curve we use the dynamical model of NGC 5846 by Kronawitter et al. (2000). We assume the temperature $T_{\rm test}$ is constant at 0.65 keV and then calculate the corresponding $lpg_{\rm test}$ and density ($n_{\rm test}$) profiles. $n^2_{\rm test}$ is projected and pure Poissonian statistics typical for XMM-Newton is added. The projected density profiles are then deprojected as in Churazov et al. (2008) and a deprojected density profile is obtained. We added Gaussian random deviates to the temperature assuming a constant error of 0.03 keV to complete the set of pseudo deprojected profiles shown with filled black circles in Figure 8.

2.4.2 *Choice of optimal smoothing parameter*

We use our method in the non-Markov mode to obtain the best-fit circular velocity curve for different values of λ from the pseudo deprojected temperature and density profiles. We find that $n_{\rm iter} = 10^6$ iterations is sufficient to reach a best-fit model.

A plot of the root-mean squared deviation R between the recovered circular velocity curve of the test model and the input circular velocity curve, against the smoothing parameter λ, is shown in Figure 9 where:

$$R = \left[\frac{\sum(V_{\rm c,test} - V_{\rm c,mod})^2}{n_{\rm mod}}\right]^{1/2} \tag{2.17}$$

Figure 9 shows that R has a minimum at around $\lambda_{opt} = 0.5$. A lower smoothing leads to unphysical fluctuations in the recovered model and a higher smoothing results in a recovered model that does not fit the temperature and density profiles of the test model well.

Figure 8 shows the resulting best-fit temperature, density and circular velocity curves for the minimum (0.001), maximum (100) and optimal (0.5) values for λ.

2.4.3 *Confidence range on recovered circular velocity curve*

To obtain the range of circular velocity curves within some confidence level, we have to ensure that our method is correctly probing the shape of the posterior probability. Assuming the optimal smoothing parameter found above, we now use the Markov mode on the pseudo profiles. $n_{\rm tune} = 2000$ results in an acceptance rate of about 23% in the subsequent proposed changes. We use a higher $n_{\rm iter} = 2 \times 10^6$, above which the profiles change insignificantly and choose $n_{\rm burnin} = 5 \times 10^5$, above which the expectation values calculated change insignificantly. In Figure 10 we have plotted how the circular velocity points at each radius are distributed in the Markov chain (i.e. after the burn-in phase), to illustrate the difference between using a $n_{\rm iter}$ that is too low and one that is about right. In the left plot where $n_{\rm iter} = 10^4$

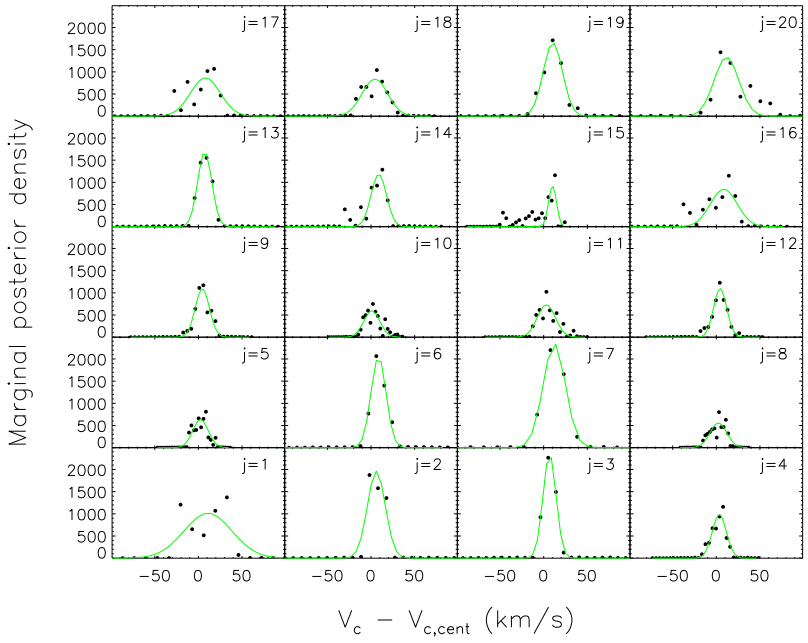

(a)

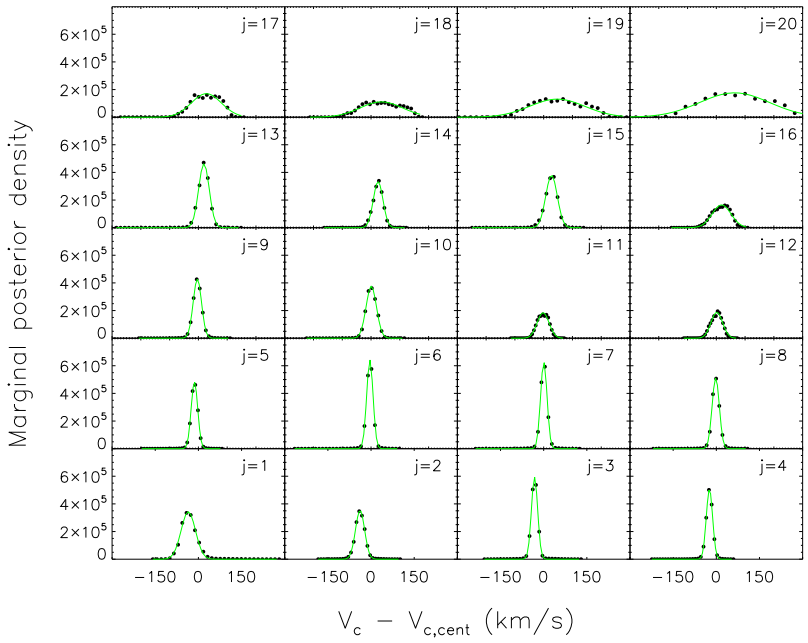

(b)

Figure 10: The circular velocity values V_c generated at each grid point j from our non-parametric analysis of the pseudo deprojected temperature and density profiles: The filled black circles show the binned number density (proportional to the marginal posterior density) of V_c values at each grid point j for (a) $n_{\rm iter} = 10^4$ and (b) $n_{\rm iter} = 2 \times 10^6$ and the green lines show the best-fit Gaussians.

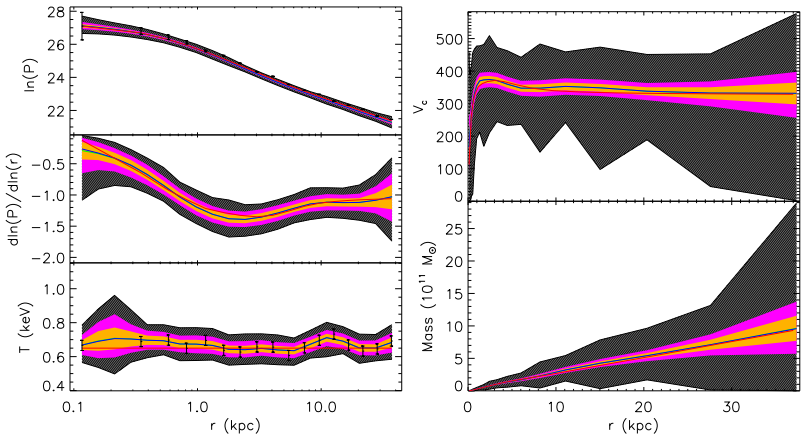

Figure 11: Application of the non-parametric analysis to the pseudo deprojected temperature and density profiles: Going counter-clockwise from the top left are the (i) logarithmic pressure, (ii) logarithmic pressure gradient, (iii) temperature, (iv) mass and (v) circular velocity profiles. The left three profiles are on a logarithmic radial scale, while the two profiles on the right are on a linear radial scale. The red lines correspond to the input test model, the green lines correspond to the recovered expected profiles and the blue lines correspond to the recovered median profiles. The grey region shows all generated points, the pink region shows the 95% confidence range and the orange region shows the 68% confidence range.

and $n_{\text{burnin}} = 5000$, the distribution of circular velocity points at each radius (i.e. the marginal posterior probability of the circular velocity curve at each grid point) have not settled to a smooth distribution, and therefore one would suspect that the chain is not yet properly sampling the posterior probability distribution. The plot on the right however shows that running the Markov chain for longer results in smooth marginal posterior probability distributions that are well described by Gaussians (illustrated by the green lines).

From Figure 10(b) the median value for the circular velocity at each radius is the circular velocity for which the marginal posterior probability is highest. The expectation value is the mean of all the circular velocity values chosen at that radius and the associated c% confidence range is given by the extrema of c% of the circular velocity values with the highest marginal posterior probabilities. Figure 11 shows the results of calculating these for all the model profiles. One can see that the median and expected profiles lie on top of each other, showing that the marginal posterior probability distributions at each radius are symmetrical. It can also be seen that the test model profiles lie within or on the boundary of the 68% confidence range. We repeat this for different sets of pseudo deprojected density and temperature profiles and we are convinced that the procedure is able to recover the circular velocity curve without a systematic bias.

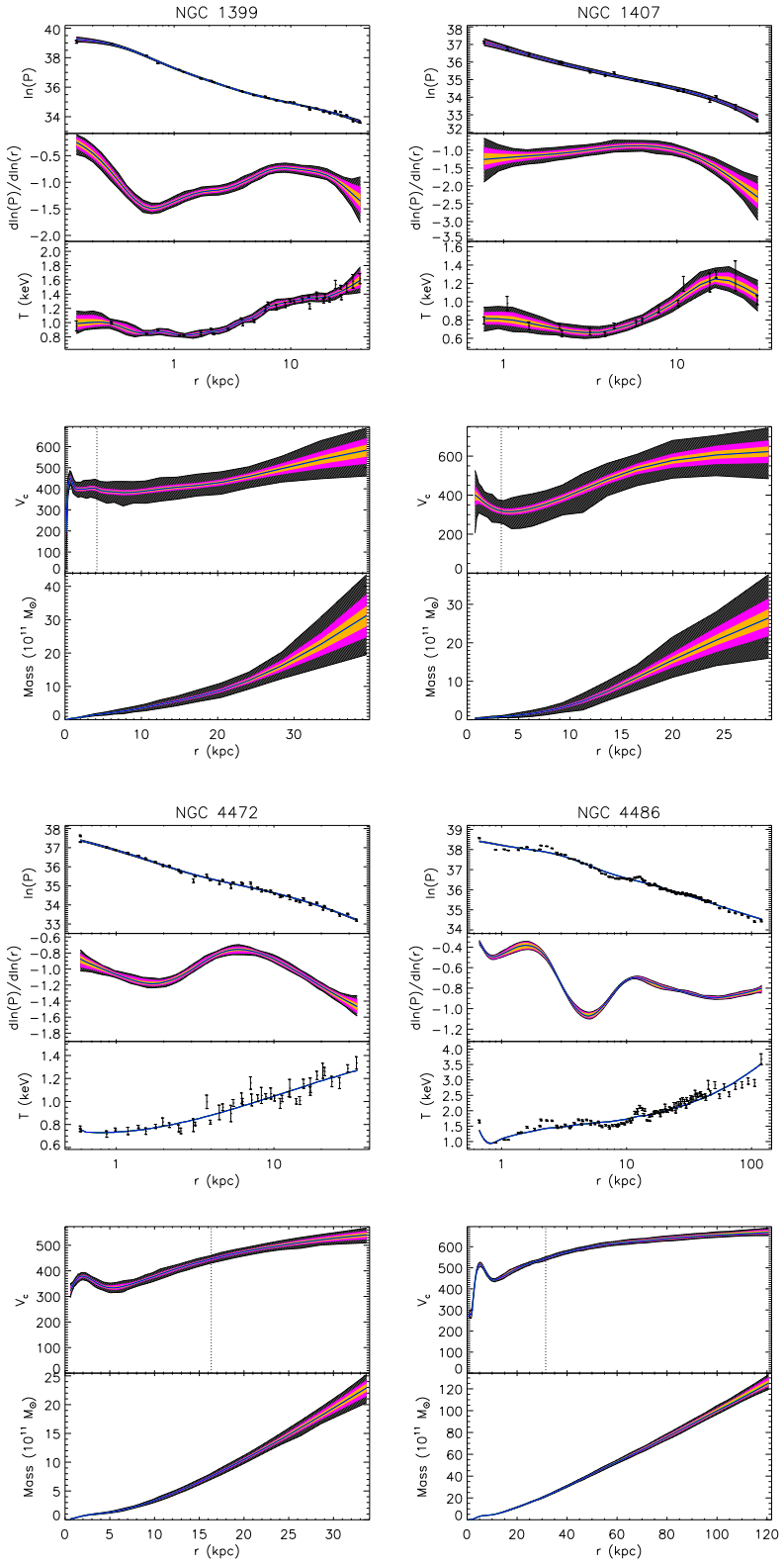

Figure 12: Application of the non-parametric analysis to the sample of six X-ray bright elliptical galaxies: Going from top down for each galaxy are shown the (i) logarithmic pressure, (ii) logarithmic pressure gradient, (iii) temperature, (iv) circular velocity and (v) mass profiles. The top three profiles are on a logarithmic radial scale, while the bottom two are on a linear radial scale. Black points on the logarithmic pressure and temperature plots show the deprojected profiles and associated statistical errors. The green and blue profiles (often indistinguishable) correspond to the expected and median profiles respectively. The grey region shows all generated points, the pink region shows the 95% confidence range and the orange region shows the 68% confidence range. The vertical black dotted lines on the circular velocity plots are at $1R_e$, given in Table 3. Continued onto next page.

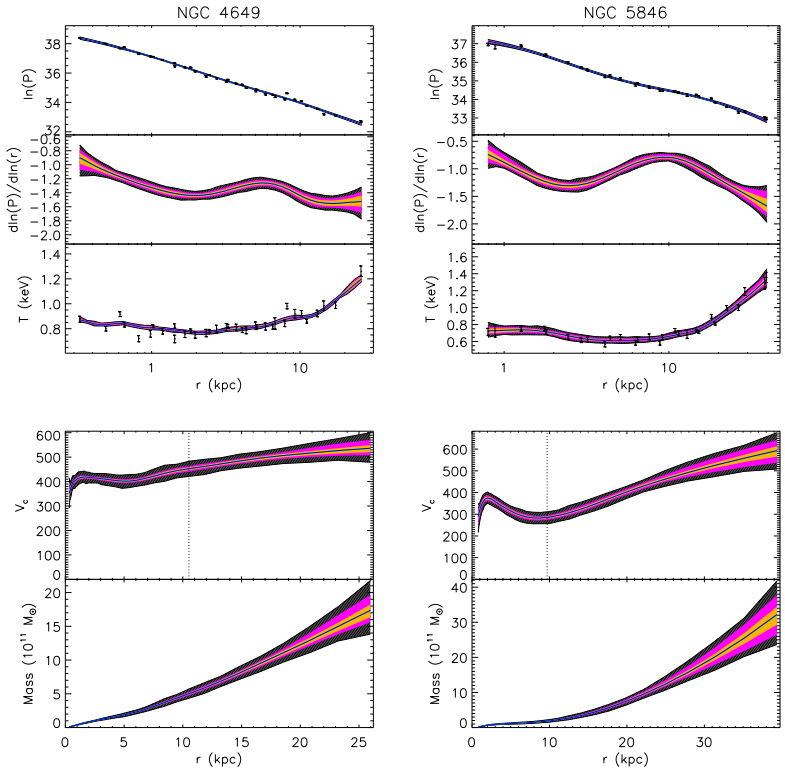

Figure 12: Continued from previous page.

2.5 TOTAL, STELLAR AND DARK MATTER MASS PROFILES

Now that we have tested the method, we can apply it to the sample of six X-ray bright elliptical galaxies to derive total mass and circular velocity profiles (Figure 12 and Table 2). We then estimate the stellar contribution to the total mass profiles using optical photometric data and stellar population models. Assuming negligible gas mass, we subtract the stellar mass from the total mass profiles to infer the dark matter mass fractions.

2.5.1 *Total mass profiles and circular velocity curves*

The fits to the deprojected logarithmic pressure and temperature profiles and the derived logarithmic pressure gradient, circular velocity and mass profiles are shown in Figure 12, for the sample of six galaxies. Columns (2)–(7) in Table 2 list the χ^2 per data point of the expected models, the enclosed mass and associated 95% confidence range at 25 kpc and the circular velocity and associated 95% confidence range at 25 kpc. We choose 25 kpc because the deprojected profiles for all the galaxies extend at least as far as this radius. We quote the χ^2 per data point rather than the χ^2 per degrees of freedom because the latter is unknown. The degrees of freedom is equal to the number of constraints subtracted by the number of parameters. In our case the number of constraints is the number of data points plus the number of

Table 2: Derived properties of the sample of six X-ray bright elliptical galaxies: (1) Galaxy name, (2) χ^2 per data point between deprojected temperature and model temperature, (3) χ^2 per data point between deprojected logarithmic pressure and model logarithmic pressure, (4) enclosed mass at 25 kpc and associated 95% confidence range, (5) circular velocity at 25 kpc and associated 95% confidence range, (6) power-law index of mass profiles on a log-log scale and associated 1-σ error, (7) power-law index of mass profiles on a log-log scale fitting only until 10 kpc and associated 1-σ error and (8) power-law index of mass profiles on a log-log scale fitting only above 10 kpc and associated 1-σ error.

Galaxy	χ^2_T	χ^2_{lnP}	M_{25} ($10^{11} M_\odot$)	$V_{c,25}$ (km/s)	ζ	$\zeta_{<10}$	$\zeta_{>10}$
(1)	(2)	(3)	(4)	(5)	(6)	(7)	(8)
NGC 1399	2.7	10.1	13.2 ± 1.1	475.0 ± 20.9	1.15 ± 0.03	1.16 ± 0.06	1.60 ± 0.06
NGC 1407	1.4	3.8	21.6 ± 7.0	608.9 ± 97.9	1.26 ± 0.07	0.88 ± 0.05	1.26 ± 0.09
NGC 4472	2.7	4.9	14.1 ± 1.0	491.8 ± 17.0	1.19 ± 0.02	1.02 ± 0.02	1.59 ± 0.01
NGC 4486	16.2	28.9	15.7 ± 0.6	520.3 ± 9.3	1.36 ± 0.01	1.60 ± 0.04	1.37 ± 0.01
NGC 4649	3.0	9.4	16.4 ± 4.3	530.4 ± 69.7	1.13 ± 0.01	1.08 ± 0.01	1.38 ± 0.01
NGC 5846	2.3	3.7	12.5 ± 1.9	463.2 ± 35.0	1.17 ± 0.05	0.88 ± 0.05	2.16 ± 0.02

constraints introduced by the smoothing, which is difficult to define.

Generally, the fits in the mean are very good. The χ^2 per data point between the deprojected temperature and model temperature ranges from 1.4 to 16.2. The χ^2 per data point between the deprojected logarithmic pressure and model logarithmic pressure ranges from 3.7 and 28.9. The χ^2 values are not comparable to the usual reduced χ^2 which is ~ 1 at the 1-σ level, because the reduced χ^2 is normalised by the number of degrees of freedom. Our χ^2 values may also be higher than expected because we have only considered statistical errors on the deprojected temperature and pressure profiles. There is also correlated/anti-correlated scatter in the deprojected temperature profiles between adjacent points as a result of the deprojection procedure (Churazov et al., 2008). AGN activity driving shock waves into the intracluster medium (e.g. Forman et al., 2007) can also result in systematic undulations in the measured temperature and density profiles. The models do not fit the deviations caused by the correlated/anti-correlated errors and by systematic errors because we have calibrated the smoothing to a test model of an ideal massive elliptical galaxy. If the statistics of the data are low as in the case of NGC 1407, then the error bars cover the correlated/anti-correlated scatter and the χ^2 values are low. The outstanding statistics (~ 0.5 Ms of Chandra observation) and very high surface brightness of NGC 4486 enables deprojected temperature and density profiles to be obtained in much narrower bins than for the other galaxies. This allows systematic deviations to be resolved, but as the errors bars are small, they do not cover the correlated/anti-correlated scatter or the systematic deviations. As a result the χ^2 values for NGC 4486 are on average about 5 times higher than for the other galaxies.

Table 3: Photometric data for the sample of six X-ray bright elliptical galaxies: (1) Galaxy name, (2) source of surface-brightness profiles, (3) band of photometry, (4) seeing values , (5) effective radii, (6) source of effective radii, (7) radius at which the optical surface-brightness profile has a gradient of 2, (8) stellar population mass-to-light ratios converted to the photometric band in column (3) and distances from Table 1, and (9) source of stellar population mass-to-light ratios. References are S00 (Saglia et al., 2000), Sp08 (Spolaor et al., 2008), K09 (Kormendy et al., 2009), Kr00 (Kronawitter et al., 2000), K10 (J. Kormendy, private communication), H09 (Hopkins et al., 2009), Z07 (Zhang et al., 2007), T00 (Trager et al., 2000), C06 (Cappellari et al., 2006).

Galaxy	Source	Band	Seeing (")	R_e (kpc)	Source	R_2 (", kpc)	$M/L\,(M_\odot/L_\odot)$	Source
(1)	(2)	(3)	(4)	(5)	(6)	(7)	(8)	(9)
NGC 1399	S00	*B*	0.05	4.17	K10	2.9, 0.28	9.7	Kr00
NGC 1407	Sp08	*B*	1	3.32	H09	2.7, 0.38	4.2	Z07
NGC 4472	K09	*V*	0.05	16.34	H09	3.5, 0.28	6.0	T00
NGC 4486	K09	*V*	0.05	31.44	H09	7.6, 0.59	7.0	C06
NGC 4649	K09	*V*	0.05	10.52	H09	4.2, 0.34	7.8	T00
NGC 5846	Kr00	*V*	0.2	9.70	Kr00	3.3, 0.39	7.2	T00

The general shape of the derived circular velocity curves can be summarised by a steep rise in the centre (except in NGC 1407) followed by a slight dip at a few to 10 kpc and then a more gentle rise outwards, reaching circular velocities of 463–609 km/s at 25 kpc. The outward rise in the circular velocity curves is a combined result of temperature profiles that rise outwards *and* logarithmic pressure gradients that increase in magnitude outwards. The dips in the circular velocity curves are a result of dips in the logarithmic pressure gradient around the same radius. These dips may reflect true changes in the mass distribution or they may be a result of shocks in the gas propagating outwards. Shock waves can be produced by an unsteady outflow of relativistic plasma from a central black hole, as in NGC 4486 (Churazov et al., 2008). The shockfront is characterised by a sharp increase in the pressure inwards and then a decrease in the rarefaction region behind the shock. This manifests itself as a dip in the circular velocity curve at the position of the shockfront in NGC 4486.

The enclosed mass profiles of all galaxies increase outwards with an increasing gradient as expected from the increasing circular velocity curves, pointing towards non-isothermal mass profiles. The 95% confidence ranges in the circular velocities and enclosed masses at 25 kpc are reasonably small and are smallest for the galaxies with the best statistics (NGC 4472 and NGC 4486) because the χ^2 values are higher as discussed above.

2.5.2 *The stellar mass contribution*

To estimate the stellar contribution to the total circular velocity curve, we use surface-brightness profiles from various sources in the literature, given in column (2) in Table 3 and shown in Figure 13(a). We deproject the surface-brightness profiles assuming a spherical stellar distribution and a power law outside the range of

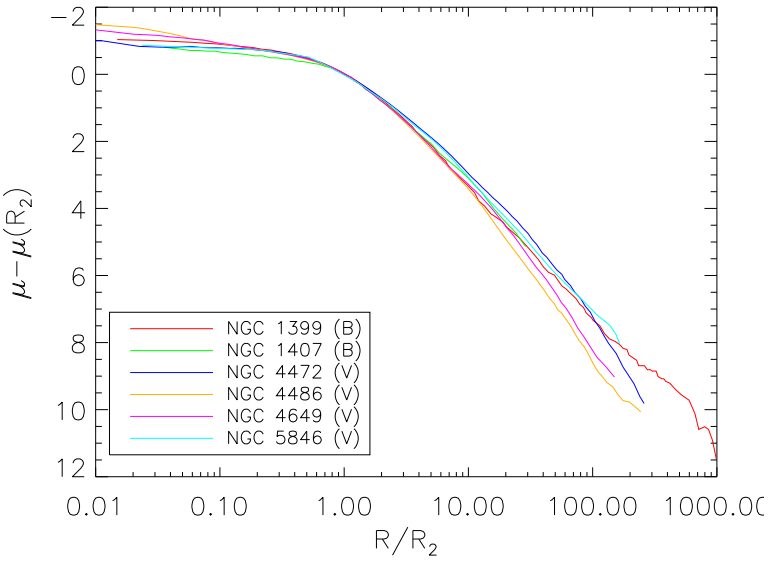

(a)

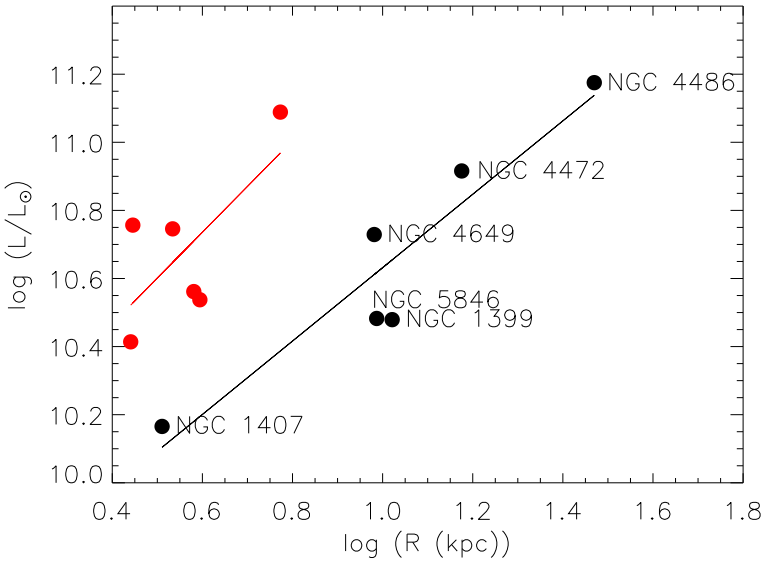

(b)

Figure 13: Luminous properties of the six X-ray bright elliptical galaxies: (a) Surface-brightness profiles scaled by R_2 (the radius where $d\mu/d\log R = 2$) and by the surface brightness $\mu(R_2)$. (b) Kormendy relation between the B-band luminosity $L_B(30R_2)$ and R_2 (red filled circles) and between the B-band luminosity $L_B(R_e)$ and R_e (black filled circles). $\log(R_2)$ has been shifted by 1 to the right. The straight red and black lines show the respective best-fit straight lines.

the data. We then integrate the resulting 3-D luminosity density profile to obtain the luminosity profile of the stars. Assuming constant stellar mass-to-light ratios with radius (columns (8) and (9) in Table 3), we obtain stellar mass profiles and stellar circular velocity curves from the luminosity profiles.

In order to find a scaling radius that best represents the luminosity of the stellar component, we examine two alternatives. The first is the mean effective radius, given in Table 3 for the sample of six galaxies. For NGC 1399 we use the determination of J. Kormendy (private communication) based on photometry in Caon et al. (1994) and Lauer et al. (2007). We calculate the mean effective radii from the major-axis effective radii and ellipticities for NGC 1407, NGC 4472, NGC 4486 and NGC 4649 determined by Hopkins et al. (2009) from photometry in Lauer et al. (2007) (NGC 1399), Bender et al. (1988) (NGC 1407) and Kormendy et al. (2009) (NGC 4472, NGC 4486 and NGC 4649). Hopkins et al. (2009) determined double-Sèrsic fits to the profiles but calculated the effective radii for the total profiles. We do not use their determination for NGC 1399 because it is based on photometry from Lauer et al. (2007), which only probes the central region. For NGC 5846, we use the mean de Vaucouleur's effective radius from Faber et al. (1989). The effective radii of massive elliptical galaxies are large and therefore require extended surface-brightness profiles with excellent sky subtraction, which we believe is true in the case of the photometry of Kormendy et al. (2009), but not in the older photometry where the sky subtraction may not be so accurate. Therefore as an alternative, we also calculate R_2 (column (6) in Table 3), the radius at which $d\mu/d\log R = 2$, where μ is in magnitudes/arcsec^2. Figure 13(a) illustrates the similarity between the general shapes of the surface-brightness profiles when the radius is scaled by R_2, and the surface brightness by its value at R_2. We obtain values of R_2 ranging between 2.7–7.6″, corresponding to 0.3–0.6 kpc, just outside typical seeing values of 1–2″. Figure 13(a) shows that R_2 is located around the radius that separates the core where the surface brightness decays gently, from the region where it starts decaying more steeply, and therefore may be mostly reflecting the core properties.

To determine which scaling radius should be used as representative of the galaxy's luminosity, we plot an analogy to the Kormendy relation (Kormendy, 1977) in Figure 13(b). We plot the B-band luminosity of the sample galaxies at $30R_2$ against R_2 and the B-band luminosity at $1R_e$ against R_e and fit straight lines through both. The best-fit straight lines have slopes of 0.74 and 0.93 and Pearson product moment correlation coefficient (PMCC) values of 0.70 and 0.94 respectively, supporting correlations at about 88% and 99% levels of significance for a sample size of six. The correlation between the effective radius and the luminosity of the stellar component is much stronger, and therefore we will use this to represent the size of the stellar component.

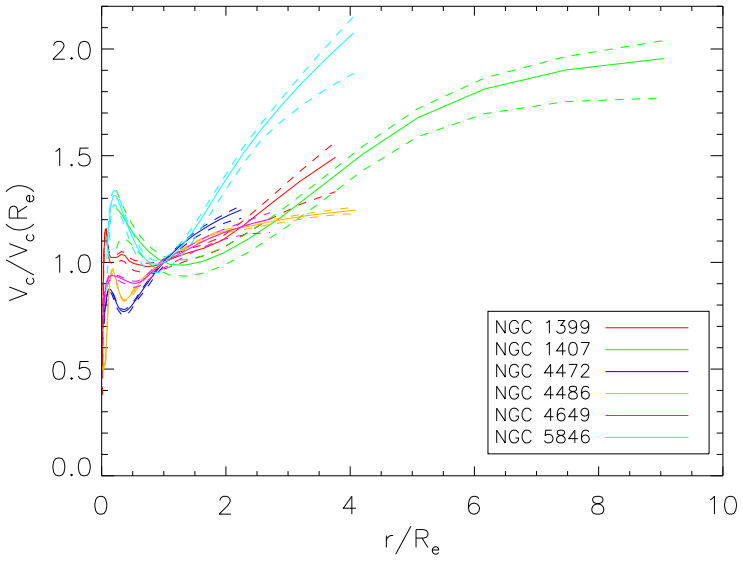

(a)

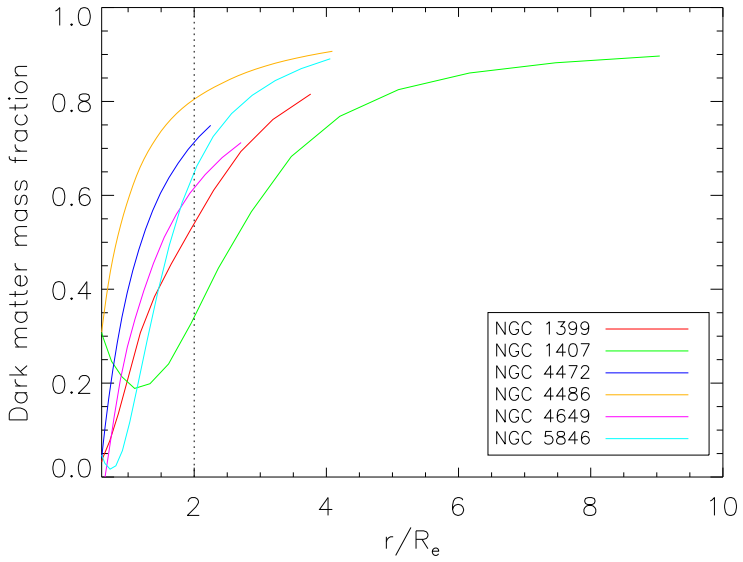

(b)

Figure 14: Total and dark matter mass properties of the six X-ray bright elliptical galaxies: (a) Total circular velocity profiles scaled by R_e in radius and the total circular velocity $V_c(R_e)$. (b) Dark matter mass fractions scaled by R_e in radius. The black dotted line highlights the dark matter mass fractions at $2R_e$.

2.5.3 *Scaled total circular velocity curves and dark matter mass fractions*

Figure 14(a) shows the scaled total circular velocity profiles of the sample of X-ray bright galaxies from the X-rays along with the 95% confidence ranges with dashed lines. The radii are scaled by R_e and the total circular velocities are scaled by their value at R_e. In the central R_e, all the profiles rise steeply then fall again before rising more gently from 0.5–1R_e. The outer rise in the circular velocity curves noted in Section 2.5.1, is more easily compared between the galaxies in this scaled plot. The curve of NGC 5846 rises most steeply. The curves of NGC 1399, NGC 1407, NGC 4472, NGC 4486 and NGC 4649 have a similar rise between 1–2R_e but the curves of NGC 1399 and NGC 1407 keep rising outwards, while the curve of NGC 4486 levels off outside 2R_e.

The mass in gas calculated from integrating the gas density profiles is $< 0.04\%$ of the mass in stars in all galaxies except in NGC 4486 where it is $\sim 0.4\%$. Therefore we treat the gas mass as negligible and assume that the baryonic mass component in the galaxy is solely due to stars. Subtracting the stellar mass determined in Section 2.5.2 from the total mass obtained from the X-rays gives the dark matter mass, shown as a fraction of the total mass in Figure 14(b), outside 0.6R_e. Below this radius the dark matter fractions we obtain for some of the galaxies are below zero, which could be a result of either an overestimate in the stellar mass-to-ratios or an underestimate in the total circular velocity curves derived from the X-rays, the latter of which we discuss in more detail in Section 2.6.2. The dark matter fractions range between 50–80% at 2$R_e \sim$ 6.5–59 kpc in all galaxies except NGC 1407 where it is $\sim 35\%$. Even further out, the profiles appear to converge to a value between 80–90%, pointing uniformly to a massive dark matter halo. The larger range in the dark matter mass fractions further in is indicative of dark matter mass profiles that have different shapes. For example the dark matter mass profile is steepest for NGC 4486, implying a more compact dark matter component.

2.6 DISCUSSION

In this section we compare the circular velocity curves we obtain from our analysis to those obtained from previous X-ray determinations and published dynamical models. We then address the issue of the isothermality of the circular velocity curves and how this compares with the literature. Finally we look at how the total circular velocity curves may be correlated with properties of the stellar components and the velocity dispersions of the environments to which the galaxies belong.

2.6.1 *Comparison with previous X-ray determinations*

Figure 15 shows the total circular velocity curves for our sample of galaxies along with their 95% confidence ranges in black solid and dashed lines. For comparison we have overplotted various X-ray determinations in the literature. The green lines are from Fukazawa et al. (2006), who used Chandra observations of NGC 1399 and NGC 4472. The blue lines are from Nagino & Matsushita (2009) who combined Chandra and XMM-Newton observations of NGC 1399, NGC 4472 and NGC 5846, and the pink line is from Zhang et al. (2007) who combined Chandra and ROSAT data in NGC 1407. Humphrey et al. (2006) (solid orange lines), Humphrey et al. (2008) (dashed orange line) and Humphrey et al. (2009) (dotted orange line) used Chandra observations of NGC 1407, NGC 4472 and NGC 4649 and finally, the cyan line is from Matsushita et al. (2002), who used XMM-Newton observations of NGC 4486. Density and temperature profiles of the hot gas were obtained from the observations and parametrised. The total circular velocity curves were then obtained by differentiating the profiles and applying hydrostatic equilibrium.

Discrepancies in the outer slopes are most likely a result of differences in the spatial extent of the data used, as the last few points anchor the outer slope. Smaller-scale differences are most likely to arise from differences in the methods used to obtain the mass profiles. The methods employed in the literature are all parametric and therefore the shapes of the mass profile will have a systematic bias. In NGC 1407 however, the discrepancy between the outer slope of the circular velocity curve of Humphrey et al. (2006) and that of our determination and the determination of Zhang et al. (2007) is more significant than between the other profiles. The source of this is unclear.

2.6.2 *Comparison with dynamical models*

Figure 15 also shows dynamical models and their confidence ranges from the literature, in red solid and dashed lines. The vertical red dotted line demarcates the radial extent of the data used in the dynamical modelling and we plot the dynamical models to twice this radius, except in the case of NGC 1407 where we plot the models until the radius deemed as reliable by the author. For NGC 1399 and NGC 5846, we use the spherical dynamical models of Kronawitter et al. (2000). They built models by superposing spherical distribution functions and adjusting the weights of their contribution to the model by comparing the projection of the model to measured surface-brightness profiles and long-slit kinematics extending to 97″ and 99″ respectively. Although this corresponds to only 5–10 kpc, the models provide a useful comparison in the central regions. 95% confidence ranges are provided on the models. For NGC 1407, we compare with the dynamical model of Romanowsky et al. (2009), who solved

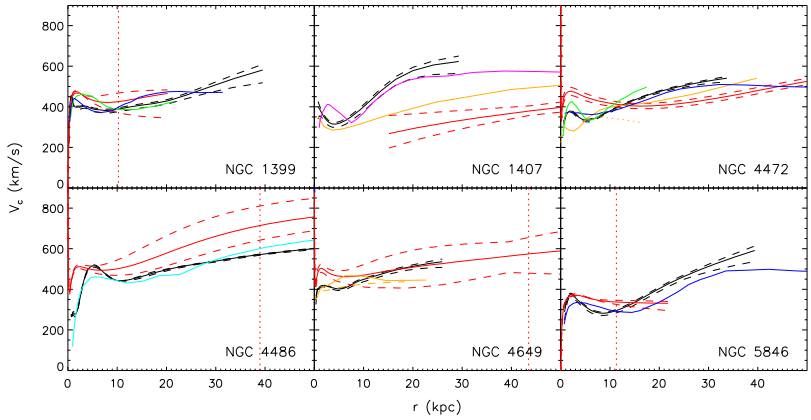

Figure 15: Total circular velocity curves determined from X-rays, compared with those from previous X-ray determinations and published dynamical models: The X-ray velocity curves and associated 95% confidence ranges determined in this Chapter are shown by the solid and dashed black lines respectively. Green lines (Fukazawa et al., 2006), blue lines (Nagino & Matsushita, 2009), the pink line (Zhang et al., 2007), orange solid, dashed and dotted lines (Humphrey et al., 2006, 2008, 2009), and the cyan line (Matsushita et al., 2002) show circular velocity curves determined from X-rays in the literature. The best-fit dynamical models along with their confidence range (for more details see text) are shown with solid and dashed red lines. The vertical red dotted line shows the radial extent of the data used in the dynamical modelling.

spherical Jeans equations for a varying anisotropy profile and fit to a surface-brightness profile and globular cluster kinematics extending out to $\sim 590''$. They provide a 68% confidence range on their model. For NGC 4472, NGC 4486 and NGC 4649 we compare with the models of Shen & Gebhardt et al. (2010, in preparation), Gebhardt et al. (2010, in preparation) and Shen & Gebhardt (2010), who used axisymmetric Schwarzschild models to fit surface-brightness profiles, integrated kinematics and globular cluster data extending to 1200″, 500″ and 533″ respectively. 68% confidence ranges are provided on the models.

Comparing the X-ray circular velocity curves of this Chapter to those from dynamical models, we find that outside the central kpc in NGC 1399, the X-ray circular velocity curve is up to 16% lower than the dynamical modelling circular velocity curve. Outside a radius of about 7 kpc though, the X-ray determination lies within the 95% confidence range on the dynamical modelling determination. In the region of overlap between the X-ray and dynamical circular velocity curves of NGC 1407, the X-ray circular velocity curve rises from about 500 to 600 km/s, while the dynamical circular velocity curve rises from about 270 to 320 km/s, showing that the X-ray velocity curve is almost twice as high throughout and therefore rises twice as steeply. The X-ray circular velocity curve of NGC 4472 is up to 27% lower than the dynamical modelling circular velocity curve within about 12 kpc, but then rises to up to 20% higher outside this radius. Within 5 kpc, the X-ray circular velocity curve of NGC 4486 is up to 45% lower than the dynamical circular velocity curve, and outside this

region, the X-ray circular velocity curve is up to 21%. For NGC 4649, the confidence ranges overlap from 7 kpc outwards and the circular velocity curves agree very well outside 10 kpc. Within this radius the X-ray circular velocity curve is at worst about 21% lower than that of the dynamical model. In NGC 5846, the X-ray circular velocity curve is up to 18% lower in the central 12 kpc than the dynamical circular velocity curve but then rises much more steeply compared to the dynamical circular velocity curve.

2.6.2.1 *Uncertainties in the X-ray analysis*

Here we discuss uncertainties in the X-ray analysis, which could explain the discrepancies we observe between the dynamical and X-ray circular velocity curves.

One subject discussed in Churazov et al. (2010) is the contribution of non-thermal components in the gas to the total pressure. The existence of these components would lead to a systematic bias in our determination of the mass profile derived from hydrostatic equilibrium as we have only considered the thermal gas pressure. Churazov et al. (2008) listed several non-thermal components that are consistent with AGN-heated cores of X-ray bright elliptical galaxies exhibiting properties of a cooling flow region: (i) Cosmic rays and magnetic fields uniformly mixed with the thermal gas, (ii) cosmic rays and magnetic fields forming bubbles that are free of thermal gas and (iii) microturbulence in the thermal gas. If the fraction of the total pressure that is due to thermal gas f_t is constant with radius, then $\phi_t = f_t \phi_{\rm true}$, where ϕ_t is the potential calculated from the thermal pressure and $\phi_{\rm true}$ is the true potential. This translates to $f_t = V_{c,t}^2 / V_{\rm c,true}^2$. As $0 \leq f_t \leq 1$, non-thermal contributions to the pressure are a possible mechanism for lowering the circular velocity curve calculated from the X-rays and therefore could explain the discrepancies we see in NGC 1399, NGC 4472, NGC 4649 and NGC 5846 in the central ~ 10 kpc and throughout NGC 4486. Calculating f_t (for $r > 1$ kpc) where the X-ray circular velocity curve is lowest compared to the dynamical circular velocity curve gives upper limits on the local contribution of non-thermal components to the total pressure of 30%, 45%, 69%, 32% and 33% in NGC 1399, NGC 4472, NGC 4649 and NGC 5846. These local, inner values are higher than those quoted in Churazov et al. (2010), where the f_t is a global estimate from fits to the total potential.

Another possible source of discrepancy could be in the assumptions made about the abundance profile in the determination of deprojected temperature and density profiles. Churazov et al. (2010) assumed a flat abundance profile for their analysis but calculated the average effect on the circular velocity curves if this assumption was relaxed. They found that the circular velocity values generally increase for their sample by a value of $\sim 2\%$. This small effect is in agreement with Werner et al. (2009), who combined very high-resolution XMM Newton data with Chandra data in NGC 4636 and concluded that allowing for a varying

abundance profile does not change the derived deprojected temperature and density profiles significantly. Churazov et al. (2010) also considered the effect of the unresolved population of low-mass X-ray binaries and estimated that this generally lowers the circular velocity curve by $\sim 2\%$, which to some extent counteracts the effect of allowing an abundance gradient.

We also consider the effect of the extrapolation in the deprojection of the spectra on the derived circular velocity profiles. The deprojected density profiles presented in Churazov et al. (2010) and in Figure 7 of this Chapter assume a power-law extrapolation based on a power-law fit to the data. We consider two alternative extrapolations of the Chandra density profile of NGC 4472, to investigate whether we can explain the discrepancy between the X-ray and dynamical circular velocity curves outside ~ 11 kpc. If the index of the power law used in the extrapolation of the density profiles becomes less negative by 0.1 (i.e. the density profile becomes more shallow), the outermost Chandra circular velocity point decreases by about 10 km/s, and effects further in are not discernible. Therefore this is not a realistic explanation for the discrepancy we observe. If instead the power-law index becomes more negative by 0.1 (i.e. density profile drops off more steeply), then the effect is to increase the circular velocity of the last two Chandra circular velocity points by $\lesssim 10$ km/s. The effects further in are negligible. This would not be sufficient to explain why the X-ray circular velocity curve is so much higher in NGC 1407 compared to the dynamical circular velocity curve.

Shocks in the gas result in a local violation of hydrostatic equilibrium and in spatial correlations in the pressure and circular velocity curves (Section 2.5.1). In NGC 4486, Churazov et al. (2008) showed a simulated shock at 2.7 arcmin (~ 13 kpc), which could correspond to the acute bump seen in the pressure and temperature profiles around this radius in Figure 12. They found that such a shock leads to a dip in the potential of NGC 4486. We observe a similar dip in the total circular velocity of NGC 4486 close to this radius. In the other galaxies, shockfronts are not obvious in the deprojected profiles, possibly due to the lower statistics compared to NGC 4486. In general, small-scale deviations from hydrostatic equilibrium are simply not fit due to the smoothing prior in our method, while a larger-scale violation results in a systematic effect.

Churazov et al. (2010) also discussed the effects of assuming spherical symmetry in their determination of the gravitational potential from X-rays and found that on average the effect is unlikely to exceed 7%. As the effect is systematic and will either increase/decrease the average slope of the potential, the resulting change in the circular velocity is of the order of 4%.

In earlier work, Churazov et al. (2008) estimated biases introduced when fitting multi-temperature plasma with a single-temperature model by comparing profiles obtained in different energy bands. In the case of NGC 4486, they compared tempera-

ture and density profiles calculated from broad-band spectra to that from hard-band spectra and found that differences are small outside 0.4 arcmin, which is a couple of kpc. Within this region however, AGN activity can result in hot and cool gas structures superposed along the line of sight. NGC 4486 is the most disturbed galaxy in our sample but this source of uncertainty could also explain some of the discrepancies we find in the central few kpc in other galaxies in the sample.

2.6.2.2 *Uncertainties in the dynamical modelling*

Here we examine uncertainties associated with the dynamical modelling methods, which could be the source for some of the discrepancies we observe between the dynamical and X-ray circular velocity curves.

In the dynamical models of Kronawitter et al. (2000), the data used extends only to 5–10 kpc. However in the X-ray bright elliptical galaxies in our sample, the density profiles of the stars are shallow in the outer parts, which implies that there is a lot of stellar mass at large radii where the orbital structure remains poorly constrained. If additionally the orbital structure of these outer stars were very radial, as in the numerical simulations of Abadi et al. (2006) and the dynamical models of de Lorenzi et al. (2008, 2009) ($\beta = 1 - \sigma_t^2/\sigma_r^2 \sim 0.5$), there would be many stars on highly elliptical orbits traversing large distances in the galaxy. In the central regions they turn around and contribute to the LOS velocity dispersion more than compared to if they were on a circular orbit there. Therefore a higher mass profile could be inferred in the central region, compared to what would be inferred if the outer kinematics are also available. To estimate how much extra mass may be inferred in the central region we look at the axisymmetric Schwarzschild models of Coma elliptical galaxies in Thomas et al. (2007). They used kinematic data extending to between 13–30 kpc, further out than for the dynamical models in Kronawitter et al. (2000), and provide 68% confidence ranges on their circular velocity profiles. Without the outer kinematics, they would have inferred a less massive dark matter halo, and therefore a higher central stellar mass-to-light ratio. Let us assume that this is approximately given by the upper boundary of the confidence range on the mass profiles in the central region. Therefore the inner mass profile would be overestimated by about 50 km/s without the outer kinematic data, which is about 10% of the circular velocities we obtain from the X-rays. Therefore it could partly but not wholly explain the discrepancies in regions where the dynamical circular velocity curves are higher than the X-ray circular velocity curves.

A similar argument is relevant in cases where the dynamical models do not have central kinematic constraints on the orbital structure, such as in NGC 1407, where only globular cluster kinematics were used from 15 kpc outwards. Central kinematic constraints are invaluable as they are usually of much higher

quality than kinematic data further out. In radially anisotropic systems in particular, they not only place stringent constraints on the central dynamical structure, but also constrain the orbital structure at least out to a few times their maximum projected radius.

An assumption on the symmetry of the stellar distribution in the dynamical models can also lead to a systematic bias. Let us consider the case where the stellar distribution is assumed to be spherical but in reality is prolate axisymmetric along the line-of-sight (LOS). Let us position the LOS along the z-axis, which will then be aligned with the long axis of the prolate ellipsoid. Therefore the velocity dispersion along the LOS is higher than in the plane of the sky. As we are measuring only the LOS velocity dispersions, a spherical dynamical model would overestimate the average 3-D velocity dispersion (σ_{3D}) and therefore also the mass and circular velocity. For an isotropic velocity dispersion tensor, $\sigma_{3D,sp} \approx \sqrt{3}\sigma_{zz}$. If the stellar mass distribution is in fact prolate along the LOS, then $\sigma_{3D,pr} = (2\sigma_{xx}^2 + \sigma_{zz}^2)^{\frac{1}{2}}$, where x and y are along the short axes and $\sigma_{xx} = \sigma_{yy}$ because of axisymmetry. The *Tensor Virial Theorem* relates the intrinsic axial ratios of the stellar mass distribution to its rotation and the anisotropy of the velocity dispersion tensor. Assuming no rotation in this galaxy gives $\sigma_{3D,pr} \approx \sigma_{zz}(1 + 2q^{0.9})^{\frac{1}{2}}$ (e.g. Gerhard, 1994), where q is the intrinsic flattening. Therefore $V_{c,true}^2/V_c^2 \approx \sigma_{3D,pr}^2/\sigma_{3D,sh}^2 \approx (1 + 2q^{0.9})/3$. This estimate does not take into account that dynamical models created assuming different shapes for the galaxies may prefer different orbit distributions, which influence the χ^2 minimisation usually employed. Nevertheless, it is a useful way for us to determine approximately how prolate a galaxy has to be along the LOS to explain the discrepancies we observe. Looking at the radii where the dynamical and X-ray circular velocity curves of NGC 1399, NGC 4472, NGC 4486, NGC 4649 and NGC 5846 are most discrepant, we find that for $r > 1$ kpc, maximum flattenings of $q = 0.52, 0.29, 0.14, 0.48, 0.47$ respectively would be required. Tremblay & Merritt (1996) found that the distribution of intrinsic, short-to-long axis ratios peaks at around 0.75 for bright elliptical galaxies. Therefore it is unlikely that prolate axisymmetry along the LOS is the cause for the observed discrepancies.

Finally, the mass profiles explored in the dynamical models are parametrised so that that stellar mass contribution follows the shape of the stellar luminosity profile (i.e. the mass-to-light ratio is constant with radius). The dark matter mass contribution is usually given by non-singular isothermal spheres or Navarro-Frenk-White profiles. This results in a bias in the shape of the mass profiles and circular velocity curves, especially noticeable in the central regions where the shape of the circular velocity profile changes most.

Based on our discussion on the uncertainties inherent in the derivation of circular velocity curves from X-rays and from dy-

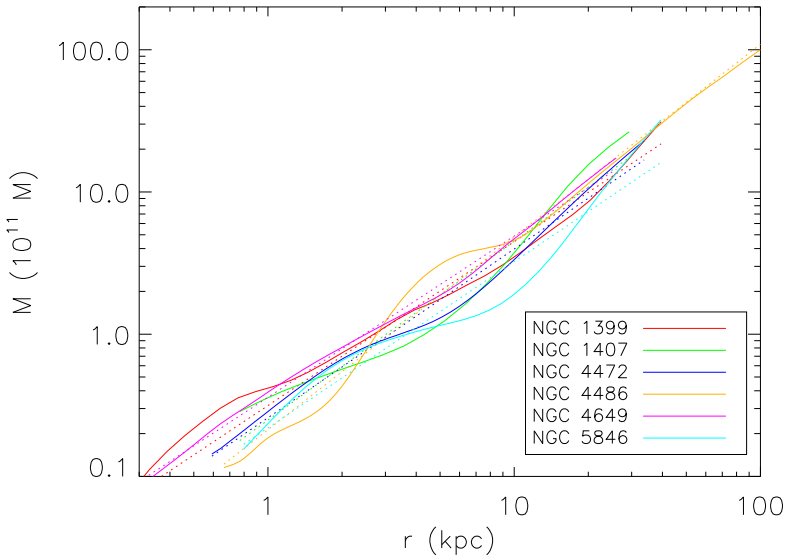

Figure 16: The non-isothermality of the mass profiles of the sample of six X-ray bright elliptical galaxies: Solid lines show the mass distributions in a double-logarithmic scale. Dotted lines show straight lines fitted to the mass distributions in this scale.

namical models, we conclude that the regions where the X-ray circular velocity curves are lower compared to dynamical circular velocity curves in NGC 1399, NGC 4472 and NGC 5846 can probably be attributed to a combination of: i) A contribution of non-thermal components to the pressure in the X-rays, ii) multiple-temperature components in the gas, iii) an incomplete spatial coverage in the kinematic data used in the dynamical models, and iv) insufficiently general mass profiles in the dynamical modelling. As the dynamical models for NGC 4486 and NGC 4649 incorporate extended kinematic data, the probable explanation is: i) the existence of non-thermal pressure components, ii) multiple-temperature components, and iii) insufficiently general mass profiles in the dynamical models only. The discrepancy between the X-ray and dynamical circular velocity curves in NGC 1407 remains unclear.

2.6.3 *How non-isothermal are the mass profiles?*

In the previous section we carried out an individual comparison between the circular velocity curves we obtained to those obtained in the literature. Here we examine the general property of rising circular velocity curves noted in Section 2.5.1. To quantify the isothermality of the circular velocity curves, we fit a power-law model $M \propto r^{\zeta}$ to the mass profiles as done by Fukazawa et al. (2006) and Humphrey et al. (2009) from their analysis of XMM-Newton and Chandra observations, and Churazov et al. (2010) on the sample we work with. Our determinations of ζ are listed in columns (6)–(8), calculated by fitting to the total mass profile,

the mass profile within 10 kpc and the mass profile outside 10 kpc. Figure 16 shows the mass profiles in a log-log scale with the best-fit models fit over the whole radial range. In this plot, the slope of the best-fit lines is equal to the power-law index ζ. For a galaxy with an isothermal mass profile, we would expect $\zeta = 1$. Fitting to the the total mass profile we find $1.13 < \zeta < 1.36$ and a mean $\langle\zeta\rangle = 1.21$. As the 1-$\sigma$ errors range between 0.01 and 0.07, the sample of these six elliptical galaxies appear to have significantly non-isothermal mass profiles. Fitting the mass profiles within 10 kpc, we find $0.88 < \zeta < 1.60$ and a mean $\langle\zeta\rangle = 1.10$. For NGC 1399, ζ does not change, for NGC 4486, ζ becomes much larger, possibly due to the shockfront at this radius, but for the remaining galaxies ζ decreases to values between 0.88 and 1.08. Calculating ζ from the mass profiles outside 10 kpc, we find higher values with a range $1.26 < \zeta < 2.16$ and a mean $\langle\zeta\rangle = 1.56$. This implies that the central 10 kpc of these galaxies may be isothermal, but outside this radius the circular velocity curves are rising. The rising circular velocity curves could be showing that we have probed the mass distribution sufficiently far out to observe the effects of the massive group/cluster-sized haloes in which these galaxies reside.

Fukazawa et al. (2006) obtained mass profiles by applying hydrostatic equilibrium to parametrised Chandra and XMM-Newton temperature and density profiles for a sample of 53 elliptical galaxies. They fit power-law mass models outside 10 kpc, finding on average $\zeta = 1.33 \pm 0.33$, which overlaps with our determination of 1.56.

Churazov et al. (2010) found a mean $\langle\zeta\rangle = 1.11$ for NGC 1399, NGC 4472, NGC 4486, NGC 4649 and NGC 5846, fitting their potentials between 0.1′ and 5′. Over the same radial range for the same galaxies, we obtain $\langle\zeta\rangle = 1.17$, which is only $\sim 5\%$ higher.

Humphrey & Buote (2010) derived mass profiles from a parametric Bayesian analysis of Chandra observations for a sample of 10 galaxies, groups and clusters. They obtained $0.95 < \zeta < 1.8$ fitting to the mass profiles between 0.2–10R_e but for the four galaxies in their sample, they obtained $0.95 < \zeta < 1.09$, i.e., close to isothermal. We believe that the differences between their results and ours is due to: i) Calculation of ζ over different radial ranges from ours and ii) environmental effects, i.e. our galaxies are located specifically at the centre of sub-groups, groups or clusters while their galaxies, though belonging to similar environments, are generally not at the centre. The radial range is important in the case of NGC 4649, the only galaxy common to both samples. They used data extending to about $\sim$ 17 kpc, converted to our assumed distance. If we look at Figure 7 we can see that there is an extra deprojected temperature and density point that we have from the XMM-Newton analysis, which increases the gradient of the mass profile. There is also reason to believe this increase because of how similar our derived circular velocity curve is to that from Shen & Gebhardt (2010) discussed in Section 2.6.2. For

NGC 1332 Humphrey & Buote (2010) used data only extending to $\sim$ 20 kpc, which also may not be sufficiently extended (our profiles all extend to at least $\sim$ 25 kpc and in the case of NGC 4486, they extend to almost 110 kpc.) NGC 720, NGC 4261 (for which they have data extending to $\sim$ 31 and $\sim$ 34 kpc) and NGC 1332 are not located at the centre of their respective environments. Therefore even if the profiles were as radially extended as ours, we would not expect the circular velocity curves to rise as much as for our sample galaxies, which are all located at the centre of their environments. For the groups and clusters in the sample of Humphrey & Buote (2010), they found mass profiles that increase more steeply than isothermal mass profiles, therefore supporting the hypothesis that we are partially probing the region where the group/cluster potentials start dominating. The comparison between calculating ζ within 10 kpc with calculating it over the whole radial range of the deprojected temperature and density profiles also supports this hypothesis.

Gerhard et al. (2001) analysed the dynamical models of Kronawitter et al. (2000) and found that their circular velocity curves are flat to within 10% for $R \gtrsim 0.2R_e$. These models use photometric and kinematic data extending to less than $1R_e$ for 9/21 of the galaxies, between 1–$2R_e$ for 6/21 of the galaxies and 2–$3R_e$ for 6/21 of the galaxies. Koopmans et al. (2009) solved constant-anisotropy spherical Jeans equations for 58 strong-lens early type galaxies using stellar velocity dispersion constraints and lensing-based total masses within the central effective radius. They found an average logarithmic mass-density slope of -2.085 (for an isothermal mass profile, one would expect -2.0) and that the dependence of this result on the value of the anisotropy parameter β is small. Both studies used elliptical galaxies that cover a range of luminosities and are not constrained to reside at the centre of sub-group/group/cluster environments. This means that for many of their galaxies, we have no reason to expect a rising circular velocity curve and for those that we do, the mass profiles may not be probing far out enough and/or the lack of extended photometric and kinematic constraints could be biasing the inner mass profile as discussed in Section 2.6.2.2.

2.6.4 *Correlations between the total circular velocity curves, the stellar component and the environment*

The Tully-Fisher relation links the luminous component to the total mass of the galaxies and for spiral galaxies is usually shown between the total luminosity and the flat part of the circular velocity curve. We plot an analogous relation for our sample between the total B-band luminosity at R_e against the total circular velocity from the X-rays at R_e, shown with black filled circles in Figure 17. We have also plotted with black open circles, the approximate total circular velocities at these radii if we take into account the average effects of the unresolved population of low-

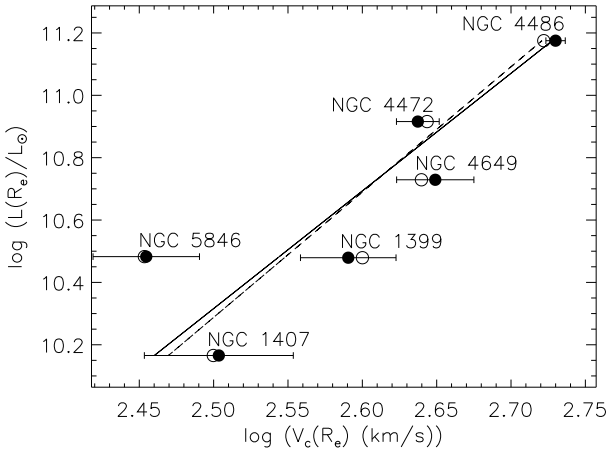

(a)

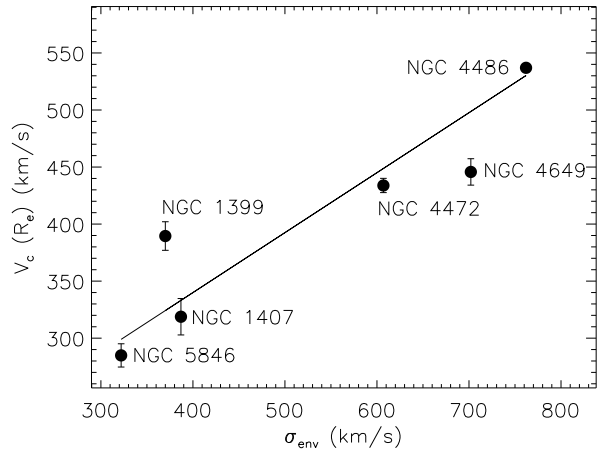

(b)

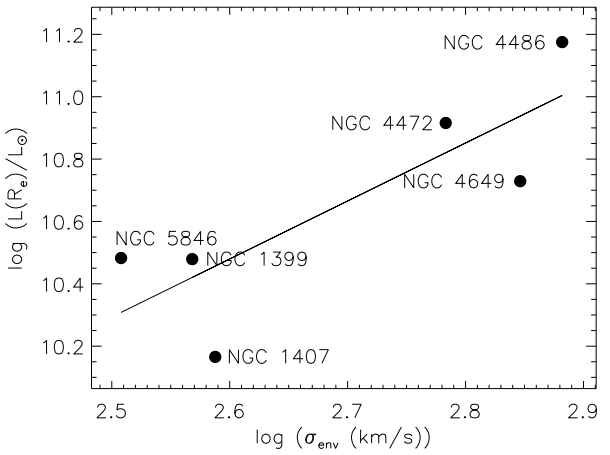

(c)

Figure 17: Correlations between the stellar component, the total circular velocity, and the environment: (a) Tully-Fisher relation between the luminosity of the stellar component at $1R_e$ and the total circular velocity from the X-rays at $1R_e$ (black filled circles) and associated 95% confidence range (horizontal bars). Also shown are the results of considering the average effect of the unresolved population of low-mass X-ray binaries and an abundance gradient (black open circles). (b) Total circular velocity from X-rays at $1R_e$ and the velocity dispersion of the environment (black filled circles). (c) Luminosity of the stellar component at $1R_e$ against the velocity dispersion of the environment (black filled circles). Solid black and dashed black lines show straight-line fits to the black filled circles and open circles respectively.

mass X-ray binaries and varying abundance profiles, as estimated by Churazov et al. (2010). The solid black and dashed black lines show straight lines fit to the black filled circles and black open circles respectively, considering the errors in the circular velocity. The lines have slopes of 3.77 ± 0.03 and 4.01 ± 0.03, very similar to the value of 4 in the Tully-Fisher relation for spiral galaxies and to the value of ~ 4 (private communication with J. Thomas) obtained for the sample of Coma cluster elliptical galaxies analysed in Thomas et al. (2009). PMCC values for the fits are 0.86 and 0.85, therefore supporting a linear correlation at a $\sim 95\%$ level of significance for a sample size of six. This implies that systems with more luminous stellar components tend to have higher circular velocities.

Figure 17(b) shows the relation between the circular velocity at R_e and the velocity dispersion of the surrounding environment from column (6) in Table 1. The solid line shows the best-fit straight line with a slope of 0.53 ± 0.02 and a PMCC value of 0.92, supporting a linear correlation at a 98% level of significance. This strongly implies that central galaxies residing in hotter environments (as measured by the velocity dispersions) have higher circular velocities. Figure 17(c) shows the logarithm of the luminosity at R_e against the logarithm of the velocity dispersion of the surrounding environment. The best-fit straight line has a PMCC value of 0.83, supporting a linear correlation at a level of $\sim 95\%$ significance. This implies that the luminosity of the galaxy residing at the centre of a sub-clump, group or cluster environment, is related to the velocity dispersion of the environment.

In environments where the local velocity dispersions are higher, the densities ($\sim \sigma^2/r^2$) are also greater, as the radii (0.7–1 Mpc) over which these velocity dispersions were calculated are comparable. Therefore one would expect that a larger number of systems would fall onto the central galaxy, resulting in a more luminous stellar component and a more massive dark matter halo. Brough et al. (2007) found that more X-ray luminous systems are intrinsically brighter in the K-band compared to less luminous X-ray luminous systems for their sample of three brightest group galaxies and three brightest cluster galaxies. In denser environments, one would expect the gas to be hotter and denser, and therefore more X-ray luminous, thereby corroborating the results of Brough et al. (2007).

2.7 CONCLUSIONS

In this Chapter, we describe a new non-parametric Bayesian approach to obtain mass distributions and associated confidence ranges from temperature and density profiles of hot gas in hydrostatic equilibrium. The method is able to successfully reconstruct the mass distribution of a test galaxy just within a 68% confidence range of the recovered models. We assume a smoothing prior to

ensure unique and physical mass distributions and calibrate this on the test galaxy.

We apply the procedure to the sample of six X-ray bright elliptical galaxies from Churazov et al. (2010), who used high-quality X-ray observations of Chandra and XMM-Newton to obtain temperature and density profiles of the hot gas. We find total mass distributions with an average mass of $\sim 1.5 \times 10^{12} M_{\odot}$ and average circular velocity of ~ 515 km/s at a radius of 25 kpc.

The total circular velocity curves of our sample are all rising in the outer parts as a result of both an increasing temperature profile and a logarithmic pressure gradient that generally increases in magnitude outwards. Therefore the mass distributions of our sample are not isothermal, suggesting that we are probing the mass distribution sufficiently far out to observe the effects of the massive group/cluster haloes in which these galaxies reside. Increasing circular velocity curves appear to contradict work done in the past but are most likely a consequence of: i) Samples in the literature not restricted to only massive elliptical galaxies and/or ii) mass profiles not being probed sufficiently far out.

The stellar components of our sample show a remarkable coherence in their surface-brightness profiles when scaled by the radius where $d\mu/d\log R = 2$. We find however that the effective radius is a better proxy for the luminosity of the stellar component. The dark matter mass fraction is 35–80% at $2R_e$ and increases to about 80–90% at the outermost radii.

Except in the case of NGC 1407, our determination of circular velocity curves from X-rays agrees well with previous X-ray determinations. When comparing our circular velocity curves with those found by dynamical models in the literature, we find that the X-ray circular velocity curves are often lower, particularly in the central 10 kpc. This is probably due to contributions from: i) Non-thermal pressures, ii) multiple-temperature components, iii) incomplete spatial coverage in the kinematic data used for the dynamical models, and iv) insufficiently general mass profiles explored in the dynamical modelling.

Looking at relations between the luminosity of the stellar component at R_e, the total circular velocity at R_e and the velocity dispersion of the environment, we find evidence for a dependence of the properties of central galaxies on their environment.

The next steps in this project are to extend the analysis to a larger sample of X-ray bright elliptical galaxies to examine the isothermality of their circular velocity curves, and to obtain more stringent constraints on how they compare with alternative methods of mass determinations, in particular through the construction of more radially extended dynamical models. This will enable us to build up a clearer picture of the connection between properties of central X-ray bright elliptical galaxies and the environment in which they reside.

Part II

DYNAMICAL MODELS

3

ORBITAL STRUCTURE FROM INVERSION OF THE JEANS EQUATIONS

This work is based on Das et al. (2008), published in Astronomische Nachrichten. This work is different from that submitted in my diploma thesis, which also looked at the halo of NGC 5846, because the anisotropy is explored using a more general technique.

We implement solutions to the spherical Jeans equations in the case of any known potential and test our implementation with isotropic and anisotropic Hernquist spheres.

We apply this implementation to the massive elliptical galaxy, NGC 5846, occurring at the centre of a group of galaxies. We use density and temperature profiles obtained from XMM-Newton observations to derive a potential out to $11R_e$, finding a circular velocity curve that is significantly higher than the extrapolation of dynamical models. This implies a halo more massive than previously thought.

Using an I-band surface-brightness profile and a projected velocity dispersion profile consisting of long-slit kinematic measurements and planetary nebula (PN) velocity dispersions, the solutions to the Jeans equations in the potential from X-rays find a highly radially anisotropic galaxy outside $0.7R_e$ with $\beta \sim 0.75$.

3.1 INTRODUCTION

Knowledge of the three-dimensional orbital structure of a galaxy is invaluable as it serves as a relic of its formation path. To obtain such an insight from observations of two-dimensional projected properties, one has to create dynamical models. These are usually constructed in an assumed potential by superposing a library of orbits (Schwarzschild, 1979; Thomas et al., 2005; van den Bosch et al., 2008) or distribution functions (e.g., Gerhard et al., 1998), or by constructing a system of particles (NMAGIC, de Lorenzi et al., 2007) that reproduces the observed surface brightness and kinematics. The degeneracy existing between the mass distribution, orbital structure and shape, is mitigated by fitting to higher-order moments of the LOSVD (Gerhard, 1993).

Kronawitter et al. (2000) constructed spherical dynamical models of round elliptical galaxies using data within $\sim 1R_e$, and found an isotropic to slightly radially anisotropic orbital structure. More recently de Lorenzi et al. (2008, 2009) created NMAGIC models of the intermediate-luminosity elliptical galaxies, NGC 4697 and NGC 3379, incorporating integral-field data and PNe velocity dispersions extending out to 5 and $7R_e$ respectively. These measurements probe the outer halo of these galaxies, where

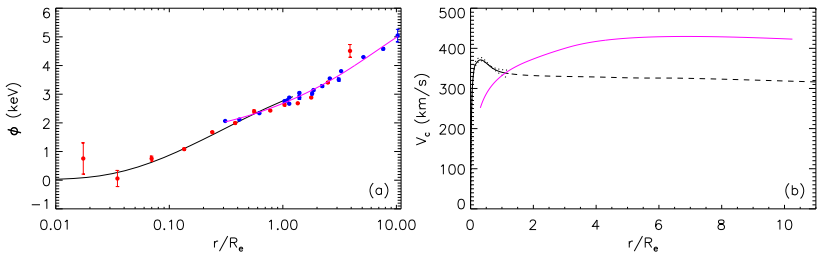

Figure 18: (a) Potential of NGC 5846: The blue dots refer to the potential derived from XMM-Newton observations and the solid pink line shows the best-fit cubic spline. For comparison, the potential derived from Chandra observations (red dots) and the potential corresponding to the best dynamical model of Kronawitter et al. (2000) (solid black line) are also shown. (b) Circular velocity curve of NGC 5846: The solid black line corresponds to the circular velocity curve of Kronawitter et al. (2000) over the range of their data and the dashed black line shows its extrapolation. The black dotted lines show the 95% confidence range. The solid pink line shows the differential of the best-fit cubic-spline to the potential derived from the XMM-Newton observations.

dynamical timescales are longer and the formation mechanism better preserved. They found a range of spherical and axisymmetric models consistent with the data, ranging from almost isotropic systems with diffuse dark matter haloes to highly radially anisotropic systems, accommodating moderately massive dark matter haloes.

To obtain more stringent constraints on the orbital structure in elliptical galaxies it would be conducive to derive the potential of the galaxy independently, to eliminate the degeneracy between mass and orbital structure. Massive ellipticals harbour a hot ($T \sim$ 1 keV) interstellar medium (ISM) in the form of a low density ($n < 0.1$ cm^{-1}) plasma trapped in the galaxy's gravitational potential. In massive ellipticals, the observed X-ray spectrum is dominated by emission from the ISM primarily via thermal bremsstrahlung and X-ray lines of heavy elements.

In quiescent galaxies, where the gas is not significantly distorted by interactions with companion galaxies, one can assume hydrostatic equilibrium and use the temperature and density profiles derived from X-ray spectra to obtain a mass profile (e.g., Fukazawa et al., 2006).

In a non-rotating spherical system, if the potential is known a priori then Binney & Mamon (1982) showed that the second-order Jeans equation for the intrinsic second-order velocity moments can be inverted using photometric observations and measurements of the projected second-order velocity moments. Simpler solutions were found by Tonry (1983) and Dejonghe & Merritt (1992), who also generalise their solution for all intrinsic velocity moments.

We apply the algorithm of Dejonghe & Merritt (1992) to NGC 5846. This is a massive, nearby elliptical galaxy located at the centre of a group of galaxies. It is an ideal galaxy to test the feasibility of using the potential derived from X-ray observations in which to invert the Jeans equations, as ample amounts of

data already exist in the literature across the X-ray and optical wavelengths. In addition, its optical and X-ray images are near-circular justifying a spherical model, and the rotation measured by the Planetary Nebula Spectrograph (PN.S) is negligible (Coccato et al., 2009). We adopt a distance of 24.2 Mpc and an effective radius $R_e = 81'' = 9.5$kpc (Cappellari et al., 2006, and references therein).

We shall discuss the derivation of the potential of NGC 5846 from X-ray observations in Section 3.2. We present the solution to the second-order Jeans equation for a non-rotating spherical system and its application to NGC 5846 to derive its orbital structure in Section 3.3.

3.2 DERIVATION OF POTENTIAL

The X-ray observations consist of temperature and density profiles derived by Finoguenov et al. (2006) from archival XMM-Newton observations, extending to almost $11R_e$, therefore enabling us to probe the potential deep into the halo of the galaxy.

We assume that the ISM surrounding NGC 5846 is composed of an ideal gas in hydrostatic equilibrium and spherically distributed. Following the robust algorithm presented in Churazov et al. (2008), we proceed by calculating the change in potential $\Delta\Phi$ between consecutive shells positioned at the radii of the derived temperature and pressure values. We estimate the errors using Monte Carlo simulations. Then we calculate the absolute potential profile by normalising to the potential calculated from the circular velocity curve of Kronawitter et al. (2000) for NGC 5846. Figure 18 (a) shows the potential we derive from XMM-Newton data. For comparison we also overplot the potential derived from Chandra observations (E. Churazov and W. Forman, private communication) using an analogous method, and the potential we calculated from the dynamical models of Kronawitter et al. (2000). In general the potentials seem to agree with each other. In the central $0.04R_e$ the Chandra potential is more erratic than that derived from the dynamical models, perhaps due to central AGN activity. Between 0.3-1.1R_e, the slope of the XMM-Newton potential is slightly flatter than that from Chandra and the dynamical models.

We fit a smooth cubic spline through the XMM-Newton potential and differentiate to obtain $V_c(r)^2 = rd\Phi/dr$, the circular velocity required for the Jeans equations. This is shown in Figure 18 (b) along with the circular velocity curve of Kronawitter et al. (2000). Taking the derivative accentuates any differences and this is especially apparent in this plot. It appears that in the central $1R_e$ the spatial information in the XMM-Newton observations is unable to reproduce the circular velocity curve to the same detail as the dynamical models. Outside this region, the XMM-Newton circular velocity curve rises steadily to a constant value of about 400-420 km/s between $\sim$ 2-11R_e, which is considerably higher

than the extrapolation of the dynamical models of Kronawitter et al. (2000).

Due to the possible uncertainties associated with the XMM-Newton circular velocity curve in the central R_e, we consider two different circular velocity curves for our Jeans models:

1. Total circular velocity as determined from the XMM-Newton observations.
2. Total circular velocity curve as determined from the dynamical models of Kronawitter et al. (2000) until $1.2R_e$ followed by that from the XMM-Newton observations.

3.3 DERIVATION OF ORBITAL STRUCTURE

3.3.1 *Inversion of the Jeans equations*

The dynamics of a non-rotating spherical system of stars with density, $j(r)$, moving in a potential with a circular velocity curve, $V_c(r)$, is governed by the second-order Jeans equation:

$$\frac{d}{dr}(j\sigma_r^2) + \frac{2\beta}{r} j\sigma_r^2 + \frac{jV_c^2}{r} = 0 \tag{3.1}$$

where $\sigma_r(r)$ is the intrinsic velocity dispersion and $\beta(r) = 1 - \sigma_\theta^2(r)/\sigma_r^2(r))$ quantifies the orbital structure.

In reality, we only have access to projected quantities from observations. The observed surface brightness profile, $I(R)$, can be deprojected to give the intrinsic luminosity density, $j(r)$, and the observed projected velocity dispersion, $\sigma_P(R)$, is related to the intrinsic radial velocity dispersion, $\sigma_r(r)$, through:

$$\sigma_P^2 = \frac{2}{I}\int_R^\infty j\sigma_r^2 \left(1 - \beta\frac{R^2}{r^2}\right) \frac{r}{(r^2 - R^2)^{1/2}} dr \tag{3.2}$$

Once $j(r)$ has been derived, Equations (3.1) and (3.2) can be solved to give $\sigma_r^2(r)$ and $\beta(r)$, done most simply by Dejonghe & Merritt (1992):

$$\begin{aligned}\sigma_r^2 = &- \frac{2}{\pi r^3 j}\int_r^\infty \left[\cos^{-1}\left(\frac{r}{R}\right) + \frac{r}{(R^2 - r^2)^{1/2}}\right] I\sigma_p^2 R dR \\ &+ \frac{2}{3r^3 j}\int_r^\infty \left(r'^3 + \frac{r^3}{2}\right) \frac{j(r')V_c(r')^2}{r'} dr'\end{aligned} \tag{3.3}$$

Then $\beta(r)$ is obtained by rearranging Equation (3.1):

$$\beta(r) = -\frac{V_c^2}{2\sigma_r^2} - \frac{1}{2}\frac{d\ln(j\sigma_r^2)}{d\ln r} \tag{3.4}$$

which expresses the derivative in log-log space, where it is almost linear.

3.3.2 *Tests*

We tested the implementation of this solution using self-consistent galaxy models described by a γ-model potential-density pair Dehnen (1993) and both a constant and the radially varying Osipkov-Merritt anisotropy profile (Osipkov, 1979; Merritt, 1985).

The intrinsic luminosity density of a γ-model is

$$j(r) = \frac{(3-\gamma)aL}{4\pi r^{\gamma}(r+a)^{4-\gamma}} \tag{3.5}$$

where a is a scale radius, L is the total luminosity and γ is a constant. The gravitational potential generated by this density results in a circular velocity curve given by:

$$V_c(r) = \left[\frac{GMr^{2-\gamma}}{(r+a)^{3-\gamma}}\right]^{1/2} \tag{3.6}$$

where $M = \Gamma L$ is the total luminous mass in $M_{\odot}$ and Γ is the mass-to-light ratio in $M_{\odot}/L_{\odot}$.

The Osipkov-Merritt anisotropy profile is given by:

$$\beta(r) = \frac{r^2}{r^2 + r_a^2} \tag{3.7}$$

where r_a is a scale radius, often called the anisotropy radius. For small r, this profile is isotropic. The model becomes increasingly radially anisotropic approaching 1 as $r \to \infty$. The transition is quite rapid and occurs at around the anisotropy radius. We carried out tests for:

1. $\gamma = 1.0$, $\beta = 0$
2. $\gamma = 1.0$, $\beta = 0.5$
3. $\gamma = 1.0$, $r_a = 2.41a$
4. $\gamma = 1.5$, $r_a = 2.41a$

For the first two cases the intrinsic and projected velocity dispersion profiles can be expressed analytically and in the latter two, they can be evaluated numerically from the known distribution function. In all four cases, the algorithm was able to reproduce the known intrinsic and projected velocity dispersion profiles to within 1%.

3.3.3 *Application to NGC 5846*

Cappellari et al. (2006) obtain an I-band surface-brightness profile for NGC 5846 and find that a de Vaucouleur's profile is able to reproduce it well, outside a radius of 10″. They obtain an effective radius of $R_e = 9.5$kpc and an I-band surface-brightness at the effective radius of $I_{e,I} = 23.3 L_{\odot}$ kpc^{-2}. For the intrinsic luminosity density, $j(r)$, we adopt the analytical approximation of

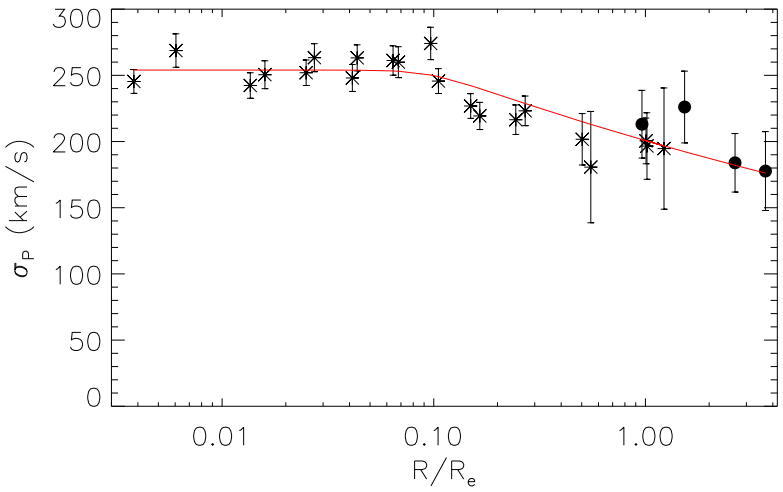

Figure 19: Black stars show the velocity dispersions of the stars, derived from the stellar kinematic data of Kronawitter et al. (2000). *Black dots* show the PNe velocity dispersions. The red line illustrates the best-fit profile from the adopted parameterisation.

Prugniel & Simien (1997) to the deprojection of de Vaucouleur's law.

We use the long-slit kinematics of Kronawitter et al. (2000), extending to about $1.2R_e$, and PNe velocity dispersions as measured by the PN.S Coccato et al. (2009), extending to almost $4R_e$. The long-slit kinematics were extracted along a major axis and a slit parallel to the minor axis, on both sides of the galaxy. As we are constructing a non-rotating spherical model of NGC 5846, we take the odd moments of the LOSVD (V and h_3) to be zero, and fold the σ and h_4 profiles symmetrically about the centre for the major axis, and about the major axis for measurements parallel to the minor axis. We also assign each of the kinematic data points with a radius equal to the distance from the centre of the galaxy. As these moments are derived from fitting a Gaussian to the LOSVD, σ differs from the true second-order projected moment by approximately $\sigma_P = \sigma(1 + \sqrt{6})h_4$. Errors are assigned to σ_P by applying the error propagation formula to the measured errors in σ and h_4.

The PNe velocity dispersions were calculated by binning their individual velocities into four circular annuli, with 35 PNe in the first three rings and 41 in the outermost ring, amounting to 146 PNe in total.

The total projected velocity dispersion profile, $\sigma_P(R)$, is shown in Figure 19 along with the adopted parameterisation. Within the central $0.1R_e$, the projected velocity dispersion is approximately constant at just above 250 km/s and then decreases almost linearly in the logarithmic radius scale to a value of almost 180 km/s at about $4R_e$.

Figure 20 show the output intrinsic radial velocity dispersion, anisotropy and reprojected velocity dispersion profiles we obtain

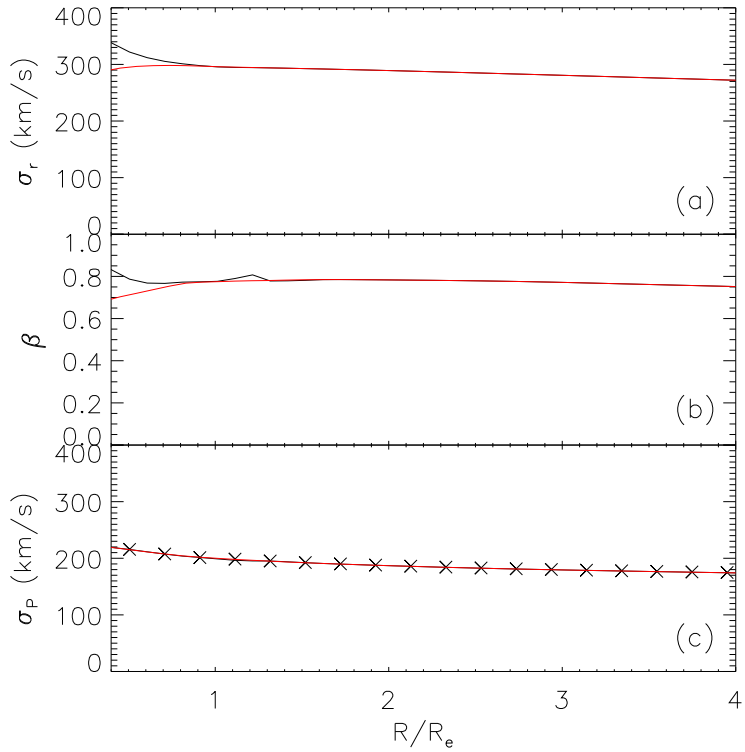

Figure 20: Plots showing the (a) intrinsic radial velocity dispersion; (b) anisotropy and; (c) reprojected velocity dispersion, profiles for the two adopted circular velocity curves, 1. (red), and 2. (black), described in Section 3.2. The black crosses in the third plot are extracted from the input parameterisation for the projected velocity dispersion profile.

from applying the algorithm to NGC 5846 in the two circular velocity curves described in Section 3.2. They are shown only outside $0.4R_e$ due to uncertainties in the XMM-Newton circular velocity curve in that region and also due to diverging solutions to the Jeans equation when the input profiles are not exactly in virial equilibrium with each other (Dejonghe & Merritt, 1992). Beyond $0.7R_e$ the three profiles agree almost exactly and show an anisotropy of $\beta \sim 0.75$ in the massive halo, suggesting the dominance of highly radial orbits in this region. We also constructed constant β models in the XMM-Newton potential and found $\beta = 0.8$ beyond $0.8R_e$. These results are reminiscent of the numerical simulations of Abadi et al. (2006), who find that the orbital structure of the stellar component of galaxies becomes increasingly radially anisotropic up to $\beta \sim 0.8$ at the virial radius.

The results in this Chapter must be confirmed by future models with more accurate determinations of the stellar density and X-ray mass profiles. There are also uncertainties associated with assuming X-ray mass determinations to determine the orbital structure, which will be discussed in later Chapters.

4

THE EDGE OF THE M87 HALO AND THE KINEMATICS OF THE DIFFUSE LIGHT IN THE VIRGO CLUSTER CORE

This work was published as Doherty et al. (2009) in A&A. My main contributions in this project have been in the calculations and writing of Sections 4.4.3 and 4.4.4.

To study the kinematics and dynamics of the extreme outer halo of M87, the central galaxy in the Virgo cluster, and its transition to the intracluster light (ICL). We present high resolution FLAMES/VLT spectroscopy of intracluster planetary nebula (PN) candidates, targeting three new fields in the Virgo cluster core with surface brightness down to $\mu_B = 28.5$. Based on the projected phase space information (sky positions and line-of-sight velocities) we separate galaxy and cluster components in the confirmed PN sample. We then use the spherical Jeans equation and the total gravitational potential as traced by the X-ray emission to derive the orbital distribution in the outer stellar halo of M87. We determine the luminosity-specific PN number for the M87 halo and the ICL from the photometric PN catalogues and sampled luminosities, and discuss the origin of the ICL in Virgo based on its measured PN velocities. We confirm a further 12 PNe in Virgo, five of which are bound to the halo of M87, and the remainder are true intracluster planetary nebulae (ICPNe). The M87 PNe are confined to the extended stellar envelope of M87, within a projected radius of ~ 160 kpc, while the ICL PNe are scattered across the whole surveyed region between M87 and M86, supporting a truncation of M87's luminous outer halo at a 2σ level. The line-of-sight velocity distribution of the M87 PNe at projected radii of 60 kpc and 144 kpc shows (i) no evidence for rotation of the halo along the photometric major axis, and (ii) that the velocity dispersion decreases in the outer halo, down to $\sigma_{last} = 78 \pm 25$ km s^{-1} at 144 kpc. The Jeans model for the M87 halo stars fits the observed line-of-sight velocity dispersion profile only if the stellar orbits are strongly radially anisotropic ($\beta \simeq 0.4$ at $r \simeq 10$ kpc increasing to 0.8 at the outer edge), and if additionally the stellar halo is truncated at $\simeq 150$ kpc average elliptical radius. The α-parameters for the M87 halo and the ICL are in the range of values observed for old (> 10 Gyr) stellar populations. Both the spatial segregation of the PNe at the systemic velocity of M87 and the dynamical model support that the stellar halo of M87 ends at ~ 150 kpc. We discuss several possible explanations for the origin of this truncation but are unable to discriminate between them: tidal truncation following an earlier encounter of M87 with another mass concentration in the Virgo core, possibly around M84, early AGN feedback effects, and adi-

abatic contraction due to the cluster dark matter collapsing onto M87. From the spatial and velocity distribution of the ICPNe we infer that M87 and M86 are falling towards each other and that we may be observing them just before the first close pass. The new PN data support the view that the core of the Virgo cluster is not yet virialised but is in an ongoing state of assembly, and that massive elliptical galaxies are important contributors to the ICL in the Virgo cluster.

4.1 INTRODUCTION

Over the past few years the diffuse intracluster light (ICL) has been the focus of many studies, both in nearby (Feldmeier et al., 2004; Mihos et al., 2005) and in intermediate redshift clusters (Zibetti et al., 2005; Krick & Bernstein, 2007). It has been found that the ICL is centrally concentrated and in many cases, including the diffuse outer halos of galaxies, comprises $\sim$10% of the total starlight in the cluster (Zibetti et al., 2005), and up to as much as $\sim$ 35% (Gonzalez et al., 2007).

Theoretical studies of the diffuse cluster light through simulations predict that the ICL is unmixed and therefore should exhibit a fair amount of sub-structure (Napolitano et al., 2003; Murante et al., 2004; Rudick et al., 2006). An important contribution to the diffuse light in clusters may come from the extended halos of giant galaxies: numerical simulations predict the presence of such halos around isolated galaxies out to several hundred kpc, consisting of stars shed by merging sub-units (Abadi et al., 2006). When these galaxies enter the cluster core, their halos would be stripped first by the tidal fields and later by the tidal shocking in the interaction with the cluster's central core and cD galaxy (Rudick et al., 2006; Murante et al., 2007).

Indeed the deep image of the Virgo cluster core by Mihos et al. (2005), reaching $\mu_V = 28$ mag arcsec^{-2}, shows a variety of features such as streamers, arcs and smaller features associated with individual galaxies. It also shows faint, very extended diffuse halos surrounding the large galaxies. In particular, around the giant elliptical galaxy M87, the Mihos et al. (2005) photometry reveals an extended stellar envelope at very low surface brightness levels, $\mu_V > 26.5$ mag arcsec^{-2}, with flattened isophotes (noted previously by Arp & Bertola, 1971; Weil et al., 1997), and out to $\sim 37'$ ($\simeq$ 161 kpc) along the semi-major axis.

The Virgo cluster has long been known to be dynamically unmixed, with complex sub-structures. This was first realised from the spatial and velocity distribution of Virgo galaxies (e.g. Binggeli et al., 1987, 1993). In particular Binggeli et al. (1993) found tentative evidence from the asymmetry in the velocity distribution of dwarf spheroidal galaxies that even the core of Virgo is not virialised, and suggested that the cluster is dynamically young, with two sub-clumps M87 and M86 falling in towards each other in the centre.

From photometry in $z \sim 0.1$ clusters (Gonzalez et al., 2005; Krick & Bernstein, 2007) and from kinematic studies of the ICL in nearby clusters (Arnaboldi et al., 2004; Gerhard et al., 2005, 2007) we have learned that the genuine ICL component, defined as the light radiated by stars floating freely in the cluster potential, and the extended halos of bright (elliptical) galaxies often overlap spatially, and cannot easily be distinguished from broad-band photometry alone. Kinematic information can complement the photometry. For surface brightness $\mu_B \lesssim 25\mathrm{mag/arcsec}^2$, integrated light spectroscopy can be used to measure the mean velocity and velocity dispersion in the outer halos of the brightest cluster galaxies (Sembach & Tonry, 1996; Kelson et al., 2002); however, reaching the faint surface brightness level of the true ICL component with this technique is very difficult. Since planetary nebulae (PNe) follow light (e.g. Coccato et al., 2009), the spectroscopic study of these tracers, both in the extended halos and the ICL, offers a way to identify and measure the kinematics of these diffuse stellar components down to very faint surface brightness ($\mu_B < 28.5$ in Virgo), but it is currently limited to clusters with distances < 100 Mpc (Gerhard et al., 2005).

For the Virgo cluster, there has been considerable success with a two-step approach of identifying PN candidates with narrow-band imaging followed by multi-object spectroscopy. Arnaboldi et al. (1996) observed the outer regions of the giant elliptical M86, measuring velocities for 19 objects. Three of these turned out to be true ICPNe, with velocities similar to that of the mean velocity of the Virgo cluster. Subsequently, 23 PNe were detected in a spectroscopic survey with 2dF on the 4m Anglo-Australian Telescope (Freeman et al., 2000; Arnaboldi et al., 2002). These results were all based on single line identifications, although the second oxygen line was seen with the right ratio in the composite spectrum of 23 PNe observed by Freeman et al. (2000). The first confirmation based on detecting the [OIII] doublet in a single PN spectrum was made in Arnaboldi et al. (2003). Expanding on this early work, we began a campaign to systematically survey PN candidates in the Virgo cluster using multi-object spectroscopy with the FLAMES/GIRAFFE spectrograph on the VLT (Arnaboldi et al., 2004, hereafter A04). A04 presented the first measurements of the velocity distribution of PNe from three survey fields in the Virgo cluster core and concluded that in two of these fields the light is dominated by the extended halos of the nearby giant elliptical galaxies, while the ICL component dominates the diffuse light in only one field, where a 'broad' line-of-sight velocity distribution is measured, and all PNe are true 'ICPNe'.

We here present PN velocity measurements from a further three pointings in the heart of the cluster core. We emphasise that these pointings are targeting faint surface brightness regions well outside of individual galaxies, in order to trace the ICPNe expected to be moving freely in the cluster potential, and thus to investigate the dynamical state of the ICL and of the core of

the Virgo cluster. The photometric/geometric classification of PNe as ICPNe is in fact revised later in this Chapter according to the dynamical information obtained from the line-of-sight (LOS) velocities of the confirmed PNe.

We give a summary of our observations and data reduction in Section 4.2 where we also discuss the sample completeness and show the final emission spectra. The distribution of measured line-of-sight velocities (LOSVD) and the projected phase-space diagram for these PNe are presented in Section 4.3. From these data we distinguish between ICPNe and PNe bound to the halo of M87. In Section 4.4 we discuss the rotation, velocity dispersion and physical extent of the stellar halo of M87, using the velocities of the PNe bound to M87 in the combined data sets of this Chapter and A04. We then construct a dynamical model based on the gravitational potential obtained from X-ray observations and the combined absorption-line and PN velocity dispersion data for the galaxy. Possible mechanisms for the truncation of M87's stellar halo are discussed in Section 4.4. In Section 4.5 we compute the luminosity-specific PN number $\alpha_{2.5}$ for both the M87 halo and the ICL in Virgo, and in Section 4.6 we discuss the implications of the ICPN LOSVD for our understanding of the dynamical status of the cluster core and the origin of the ICL in Virgo. Summary and conclusions of this Chapter are given in Section 4.7.

In what follows, we adopt a distance of 15 Mpc for M87, equivalent to a distance modulus of 30.88; therefore $1'' = 73$ pc.

4.2 OBSERVATIONS

The observations were taken in service mode (22 hrs, 076.B-0086 PI: M. Arnaboldi) over the nights 25-28th March 2006 using the FLAMES spectrograph on UT2/VLT in MEDUSA mode which allows spectra to be taken through up to 132 fibres simultaneously [1]. The data were taken in clear conditions with seeing $< 0.9''$. We used the high resolution grism HR504.8 centred at 504.8nm and with wavelength coverage 250Å and spectral resolution 20,000. With this setup, the instrumental broadening of the arc lines is FWHM = 0.29 Å or 17 kms^{-1}, and the error on the wavelength measurements is 0.0025 Å or 150 ms^{-1} (Royer et al., 2002).

Figure 21 shows the location of the selected fields targeted with FLAMES, including the three previous fields FCJ, CORE and SUB presented in A04, and the three new fields F4, F7_1, F7_2. The photometry used for the selection of PN candidates is from Feldmeier et al. (2003); his fields F4 and F7 contain the FLAMES fields F4 and (F7_1, F7_2), respectively.

1 See http://www.eso.org/sci/facilities/paranal/instruments/flames/overview.html

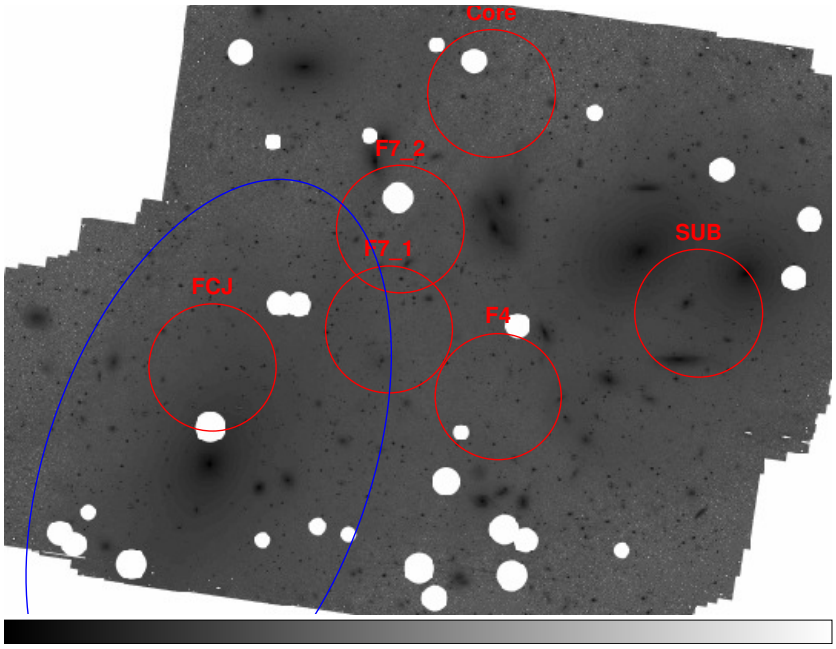

Figure 21: Deep image of the Virgo cluster core showing the diffuse light distribution (Mihos et al., 2005), with our target fields superposed. Target fields of the previous spectroscopy (A04) are shown as red circles and our new target fields as well. The blue ellipse shows the boundary used in the dynamical modeling in Section 4.4.4.

4.2.1 *Data reduction and sample completeness*

The data were reduced using the GIRAFFE pipeline[2] including bias subtraction, determining fibre location on the CCD, wavelength calibration, geometric distortion corrections and extraction of the one-dimensional spectra. The co-addition was carried out separately as a final step on the one-dimensional spectra as the fibres are allocated in a slightly different order for MEDUSA plates 1 and 2 and the pipeline does not account for this.

Table 4 shows the number of spectroscopically confirmed emission-line objects and planetary nebulae, with respect to the number of candidates targeted (N_{tot}), and the number of candidates targeted above the photometric completeness limit for each field (N_{cmp}).

A histogram showing the number of candidates versus number of confirmed emission-line objects by magnitude is shown in Figure 22. The photometric completeness limits ($\sim$ 90%) in the two photometric fields F4 (m_{5007}=26.6) and F7 (m_{5007}=26.8) are shown as blue dotted lines. These photometric completeness magnitude limits are defined as to where the signal-to-noise over the entire photometric measurement is nine per pixel or greater, corresponding to a photometric error of approximately 0.12 magnitudes (Feldmeier et al., 2003). The confirmation rate for emission-line objects above the completeness limit is then 40-70% depending on the field. This is comparable with the results from

2 The GIRAFFE pipeline is available at http://girbldrs.sourceforge.net.

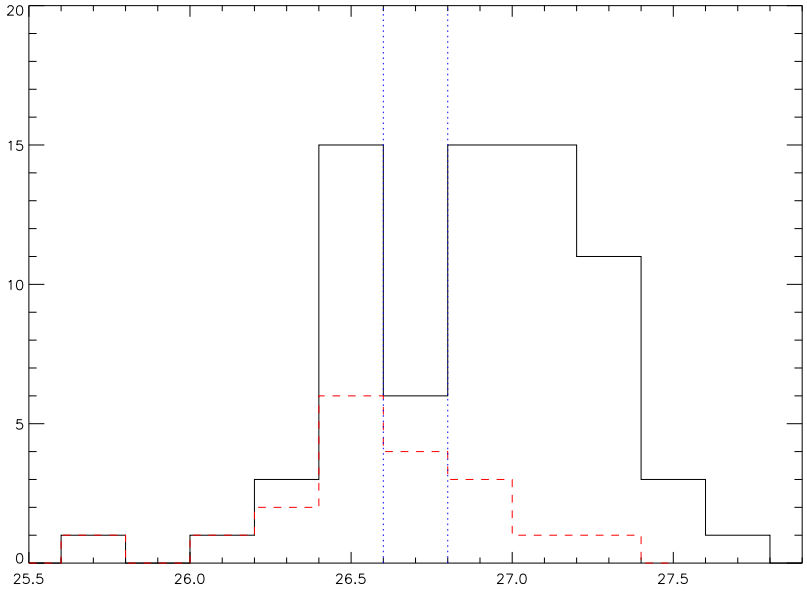

Figure 22: Histogram showing the m_{5007} magnitudes of all our observed targets (solid black line) over-plotted with those where emission lines were detected (red dashed line). The blue dotted lines show the photometric completeness limits for target fields F4 (26.6) and F7 (26.8).

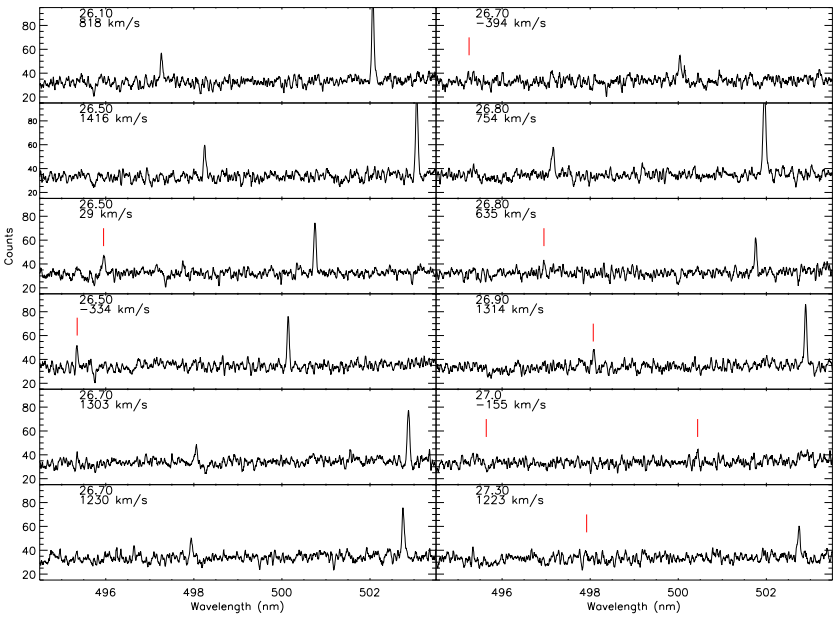

Figure 23: Spectra for the confirmed PNe, ranked by magnitude m_{5007} and smoothed by a factor 7 to 0.035nm per pixel. m_{5007} and the LOS velocities are labelled in the top left corner of each spectrum. The expected location of [O III]λ4959 is shown by a red dash, in the cases where not immediately obvious. The [O III]5007 line for the PNe with m_{5007}=27 and $v_{los} = -155$km s^{-1} has a signal-to-noise ratio of 3 and this is our weakest believable detection. A typical error in the velocities is 3 km/s; see Section 4.2.2.

Table 4: Observed fields and spectroscopic confirmations.

Field	F7_1	F7_2	F4
α(J2000.0)	12 28 53.70	12 28 46.40	12 27 43.35
δ(J2000.0)	+12 44 32.5	+13 00 20.5	+12 33 57.5
N^a_{tot}	22	28	25
N^b_{cmp}	13	12	8
N^c_{em}	9	5	5
N^d_{PN}	6	4[e]	3

[a] Total number of targets with allocated fibres.

[b] Number of targets with allocated fibres and m_{5007} brighter or equal to the completeness magnitude limit of the photometric survey.

[c] Number of spectra with detected emission line.

[d] Number of spectra with both [O III]λ 4959, 5007 Å detected.

[e] One of these is in common with F7_1, i.e., we have only 12 confirmed PNe in total, one of which was observed twice.

A04 (30-80% varying by field), and is a reasonable recovery rate given the following effects.

Firstly, if the astrometry is not very precise or if some rotation error is introduced in positioning the plate, then part or all of the flux from some objects may miss the fibres. This is more serious for faint objects as they will then not be detected above the noise. Indeed, in Figure 23 the total flux in the [O III]5007 Å line is not clearly correlated with the magnitude m_{5007} of the source, indicating that fibre positioning might be problematic. We measure the relative fluxes for the same [O III]5007 Å detection in different frames and find that it can in fact vary by up to a factor of two.

The likelihood of having false candidates above the completeness limit is very low. Each candidate ICPN was hand-inspected, and the code that finds the objects has been extensively tested on closer galaxies. In some cases (e.g., M51, Durrell et al. (2003)), there has been close to 100% recovery, using the same techniques as used to select the candidate ICPNe here.

However, below the photometric completeness limit the uncertainties are clearly much higher. Although many of the fainter objects are still likely to be ICPNe and were hence targeted spectroscopically, the probability for 'spillover' (Aguerri et al., 2005) increases substantially. Due to the photometric errors in the [OIII] fluxes some objects will be measured with a brighter flux than their real flux. If in addition their broad-band fluxes fall below the limiting magnitude of the off-band image they will be selected as ICPNe when they are in fact very faint continuum stars, due to the fact that they will have erroneously large negative colours.

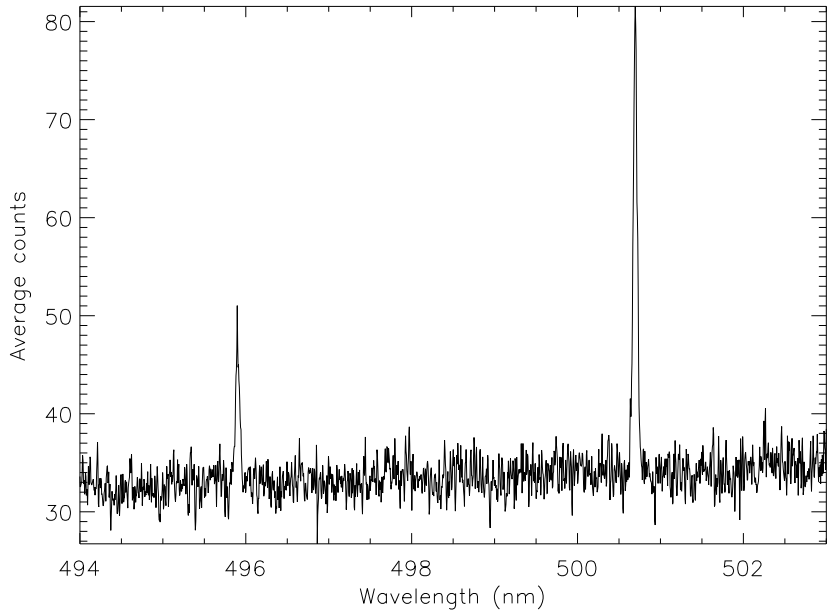

Figure 24: Combined spectrum of all 12 identified PNe, Doppler corrected to the rest-frame.

4.2.2 *Spectra of PNe and background emission line galaxies*

Figure 23 shows all of the spectra for the confirmed PNe, ranked by their photometric magnitude m_{5007}. For most of the PNe brighter than m_{5007}=27 we also detect the second line [O III]λ4959. The expected location of [O III]λ4959 is shown by a red dash, where not immediately obvious by eye. The target fields F7_1 and F7_2 overlap and have one source in common. The independently measured velocities for this source agree to within 3km s^{-1}.

Our weakest believable detection has a total signal-to-noise ratio S/N=3. As an additional check we create the average combined spectrum for the 12 identified PNe (Figure 24) and measured the equivalent width ratio of the two [OIII] lines. The ratio is 3 as expected if all identifications are real.

In Figure 25, examples of the other emission-line objects present in the sample are shown: an [O II] doublet, an asymmetric Ly$-\alpha$ line, and an unidentified broad emission line which might be an AGN (for example CIV1550 or CIII]1909). Alternatively, there is a possibility that the line is HeII at 1640Å in a LBG at higher redshift. Shapley et al. (2003) discuss that this is sometimes seen as nebular emission and also as much broader emission ($\sim$ 1500km s^{-1}) possibly from stellar winds. The FWHM of the lines we see is about $\sim$ 200km s^{-1} (observed frame). The contamination rate of these other emission-line objects is 7/19, or 37%.

The PN emission lines are all resolved, and thus we have been able to measure the expansion velocities of these PNe and to derive information on the masses of the progenitor stars. This work is presented in a companion paper (Arnaboldi et al., 2008).

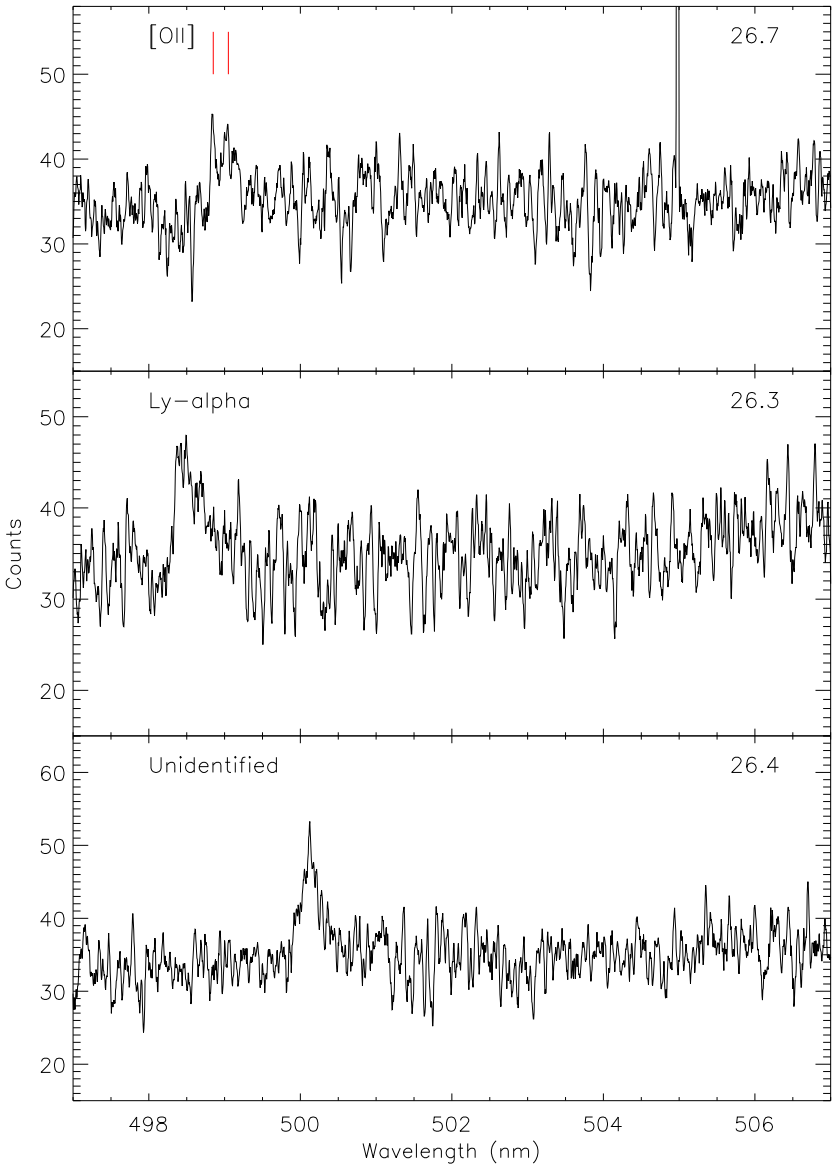

Figure 25: Examples of the other emission-line objects present in the sample, [OII], Ly$-\alpha$, and an unidentified broad emission line which we speculate might be HeII at 1640Å in a high-z LBG, or alternatively CIV 1550 or [CIII] 1909 from an AGN. The spectra have been smoothed to 0.035 nm per pixel. For comparison to Figure 23 the m_{5007} magnitudes are shown in the top right corner.

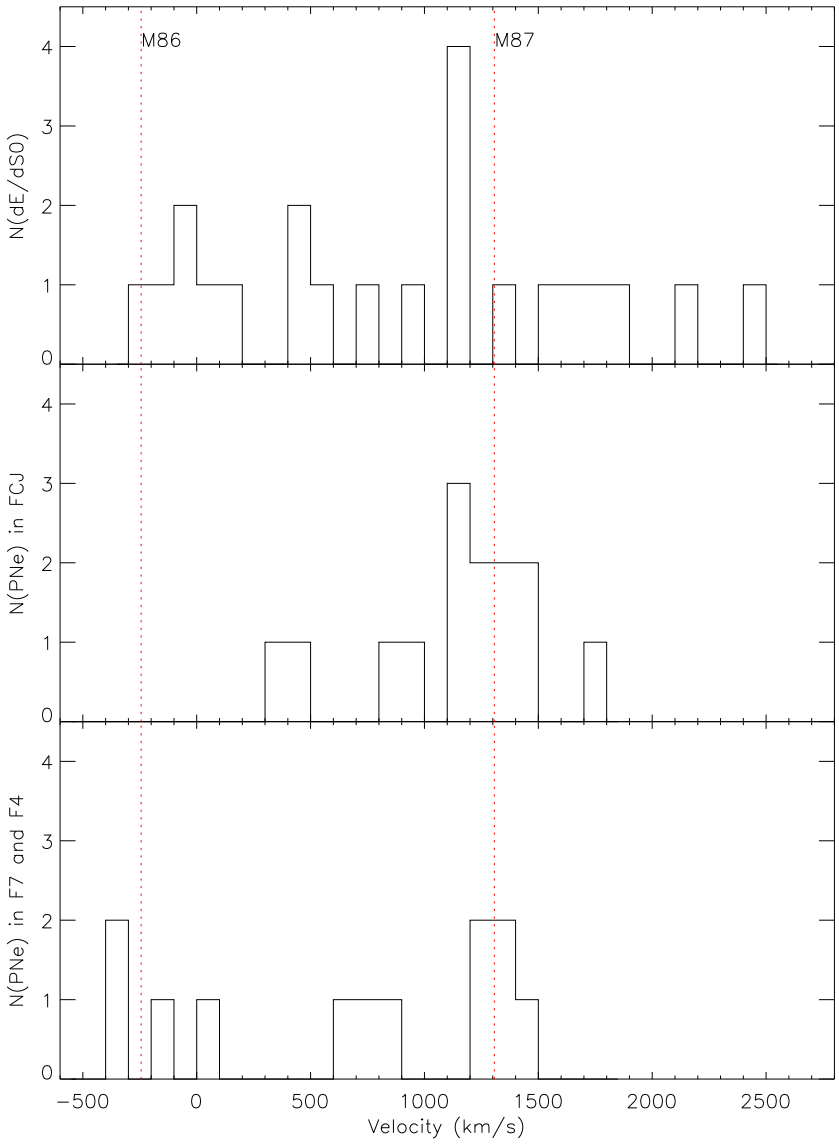

Figure 26: Radial velocity histograms. The bottom panel shows the velocity distribution of all identified PNe in the 3 new fields. The peak at $\sim$ 1300km s^{-1} corresponds to PNe bound to the halo of M87. They have a mean velocity of 1297 ± 35km s^{-1} and rms dispersion of 78 ± 25km s^{-1}. The middle panel shows the distribution of PN velocities in the previously surveyed FCJ field (A04), and the top panel shows the distribution of dwarf spheroidal LOS velocities in the same region of the Virgo cluster core, for comparison. The systemic velocities of M87 and M86 are shown with the dotted lines.

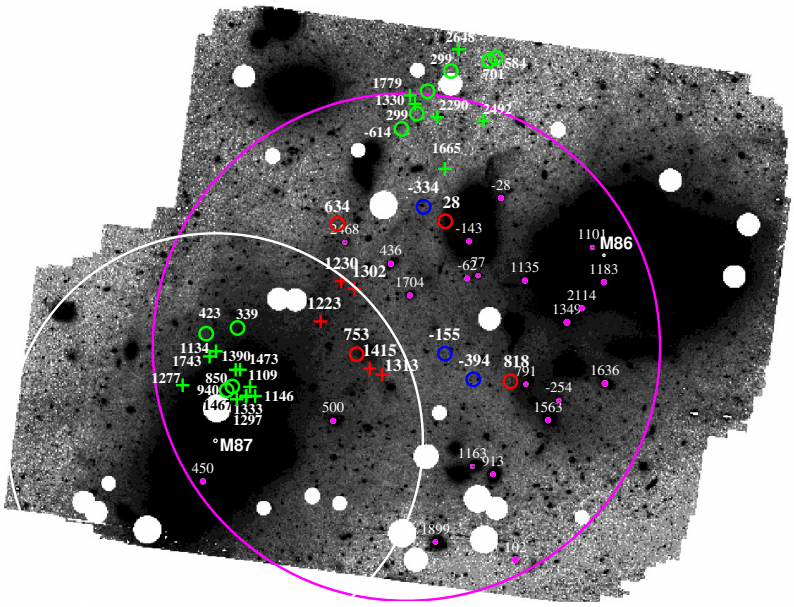

Figure 27: Deep image of the Virgo cluster core showing the distribution of the intracluster light (Mihos et al. (2005)). The spatial distribution of our spectroscopically confirmed PNe are overlaid. The A04 targets are shown in green. Our new targets are shown in red if redshifted with respect to Earth and blue if blueshifted. Objects with velocities higher than the mean velocity of Virgo (1100 km s^{-1}) are shown as crosses and those with lower velocities shown as circles. Dwarf spheroidals are marked as magenta dots. The velocities (in km s^{-1}) are labelled for all objects shown. The nominal 'edge' of the M87 halo at $\sim$ 160 kpc is indicated with a white circle. The pink circle has a 1.5 degree diameter and is centred on the projected midpoint of M87 and M86. North is up and East is to the left.

Here we concentrate on the kinematics, yielding information on the halo of M87 and the assembly history of the Virgo cluster.

4.3 LOSVD AND PROJECTED PHASE SPACE

Figure 26 shows the distribution of velocities of the newly identified PNe in the Virgo cluster core. The velocities have not been adjusted for a heliocentric correction, as the observations were almost all taken close to the equinox and the correction is within only $\pm$3km s^{-1}.

For the subsequent analysis, we combine these velocities with the A04 sample in the FCJ and Core fields. Figure 27 shows the location of these PNe on the deep image of the cluster core from Mihos et al. (2005), and Figure 28 shows their distribution in the projected phase-space plane defined by projected distance from M87 centre and line-of-sight velocity.

In the phase-space diagram Figure 28, we can identify two regions with very different characteristics: For projected distances $R < 2400''$ most of the PNe are strongly clustered around the systemic velocity of M87, $v_{sys} = 1307$ km s^{-1}. By contrast, for $R > 2400''$, the PN velocities spread widely over a velocity range more typical for the Virgo cluster. From the latter, intracluster

region we see a string of low PN velocities (800-400 km s^{-1}), extending inwards to the upper FCJ field (see Figure 27).

In the FCJ field at projected distance $R < 1300''$ there are two of these intracluster outliers at ~ 400 km s^{-1}. The remaining PNe are distributed symmetrically around v_{sys} and have mean velocity 1276 ± 71km s^{-1} and velocity dispersion $\sigma = 247$ km s^{-1}(A04); their velocity distribution is shown in the middle panel of Figure 26.

In the combined new F7/F4 fields at $R \sim 2000''$ we find five PNe tightly clustered around $v_{sys} = 1307$ km s^{-1}; these have mean velocity 1297 ± 35km s^{-1} and an rms dispersion of 78 ± 25km s^{-1}. At comparable radii there are two additional PNe with velocities of 753 and 634 km s^{-1}; compared to the previous five, these are 7σ and 8σ outliers. It is unlikely that one or two of these outliers are part of the same (very asymmetric) distribution as the five PNe clustered around v_{sys}. By contrast, they fit naturally into the stream leading from the FCJ outliers all the way into the ICL. We therefore identify as PNe bound to the M87 halo only those PNe which are clustered around the systemic velocity of M87. These are confined to radii $R < 2400''$.

The M87-bound PNe in the FCJ and combined F7/F4 fields are located at mean projected radii of 60 and 144 kpc, respectively. They correspond to the narrow peaks in the line-of-sight velocity distributions (LOSVD) in the lower and middle histograms in Figure 26.

Outside $R = 2400''$ in Figure 28 we find PNe at larger relative velocities to M87, with an approximately uniform distribution in the range -300 to 2600 km s^{-1}. Those in the radial range $2400'' < R < 3600''$ (the F7/F4 field) are confined to negative velocities with respect to M87. These are probably encroaching stars from M86 and other Virgo components[3]. By contrast, the PNe further than 3600″ from M87 (in the Core field) show a broad distribution of velocities, more characteristic of the cluster as a whole (see A04).

In the middle and bottom panels of Figure 26, the ICL PNe show up as approximately flat velocity distributions in their velocity range, besides the peak of velocities from PNe bound to M87. A flat distribution of velocities in addition to the peak near M87's systemic velocity is also seen in the LOSVD of the dwarf spheroidal galaxies in the same region of the Virgo cluster core (Binggeli et al., 1993) which is shown in the top panel of Figure 26. However, for the dwarf galaxies the flat velocity distribution extends to significantly more redshifted velocities, indicating that the dwarfs and ICL PNe kinematics can only partially be related.

3 They cannot be in the Local Group: the faintest PNe in the SMC have m_{5007}=23 (Jacoby & De Marco, 2002) so are still much brighter than the brightest Virgo PNe at m_{5007}=26.3.

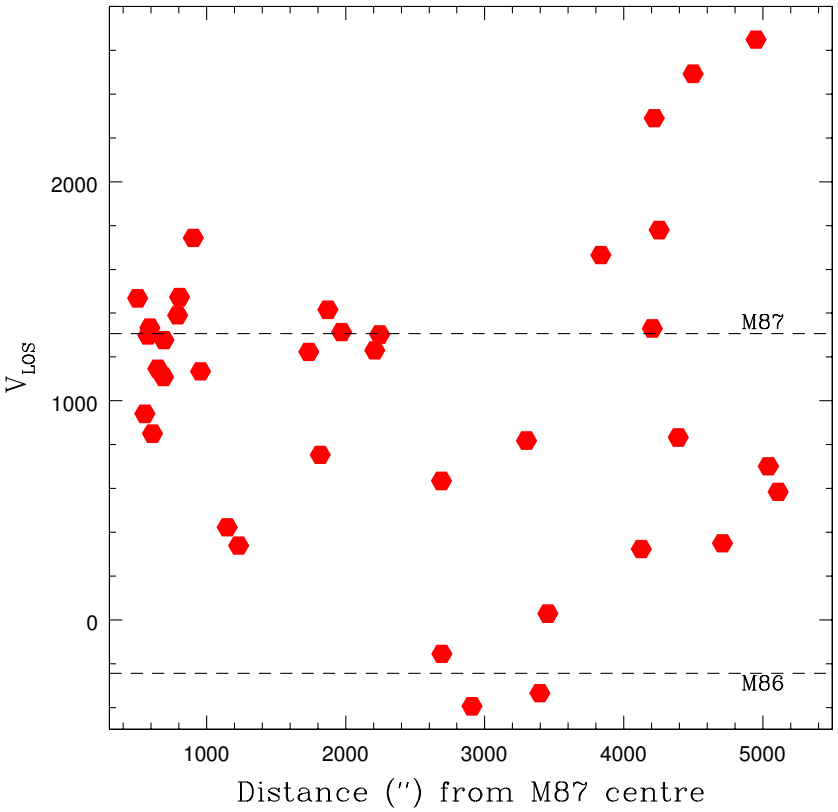

Figure 28: Distribution of line-of-sight velocity versus projected distance from the centre of M87 for all spectroscopically confirmed PNe in the new fields as well as the FCJ and Core fields of A04.

4.4 THE M87 HALO

We have seen from the phase-space diagram in Figure 28 that the PNe in the FCJ and F7/F4 fields divide into two components, one associated with the halo of M87, and the other with the unbound Virgo ICL. All PNe found around the M87 systemic velocity are within $R = 161$ kpc projected radius from the galaxy's centre. In the following subsections we combine our velocity measurements with the kinematic data in the literature, and discuss the rotation, velocity dispersion profile, dynamics and truncation of the outer M87 halo. Finally we consider possible origins of the truncation.

4.4.1 *Rotation of outer halo?*

First we ask whether there is any evidence in our data for rotation in the outer halo of M87. For the globular cluster (GC) system of M87, Cohen & Ryzhov (1997) inferred a rotation of about 100 km s^{-1} for $R \lesssim 35$ kpc, approximately about the minor axis of the galaxy intensity isophotes, using spectra of low resolution with errors for the GC velocities of order 100 km s^{-1}. Cohen (2000) added new data for GCs in the halo at $24 < R < 43$ kpc with smaller errors (typically $\sim$ 50km s^{-1}), and inferred a rotation of 300km s^{-1}. Côté et al. (2001) carried out an independent analysis using a new spectroscopic and photometric database (Hanes et al.,

2001) partly based on that of Cohen & Ryzhov (1997) and Cohen (2000), and similarly find ~ 160km s^{-1}. Côté et al. (2001) found that the metal rich GCs rotate everywhere about the photometric minor axis of the galaxy, while the metal poor GCs have a more complex behaviour: they rotate about the photometric minor axis of the galaxy between $15 < R < 40$ kpc, and about the major axis at $R < 15$ kpc.

If the PN population in the outer halo of M87 also rotated about the galaxy's photometric minor axis, similarly to the M87 GC system at $15 < R < 40$ kpc, we should see a signature along the major axis of the galaxy, that is, the mean velocities of the PN LOSVD peaks associated with M87 in our two pointings FCJ (A04; this is F3 in Feldmeier et al., 2003) and F7/F4 (Figure 21) should be offset from the systemic velocity of the galaxy (1307 km s^{-1}). From the extrapolated fit of Côté et al. (2001) to the GC radial velocities we would expect a negative constant offset of about 160 km s^{-1}at both field positions, i.e., a mean velocity of ~ 1150 km s^{-1}.

For the M87 sample of PNe identified in the phase-space diagram in Figure 28, we find a mean velocity of $\bar{v}_{\rm rad} = 1297 \pm 35$km s^{-1} in the new field (F7/F4) at mean projected radius $R = 144$ kpc. In the previously studied field (FCJ; A04) the mean velocity is 1276 ± 71km s^{-1} at mean $R = 60$ kpc. Thus we see no evidence for rotation of the outer stellar halo around the galaxy's minor axis in either the PN sample at $R = 60$ kpc or at $R = 144$ kpc. The rotation seen in the GCs may thus suggest that they do not trace the main stellar population of M87, or that they are contaminated with IC GCs with a LOSVD similar to the encroaching stars of M86 as seen in Figure 28 (see also Figure 1 of Côté et al., 2001). We have not surveyed fields along the minor axis, so we cannot check with PNe whether there is rotation about the major axis.

4.4.2 *Velocity dispersion profile*

With the new data, we can also now plot the velocity dispersion profile of M87 all the way out to $R = 144$ kpc from the centre of the galaxy. Figure 29 shows this as a function of projected radius from M87 centre. In the inner regions ($R < 25''$) we use the G-band absorption line measurements from the integrated stellar light of van der Marel (1994). In the region $25'' < R < 80''$ we use stellar velocity dispersions from Sembach & Tonry (1996). As these authors discuss, their data is systematically offset from most other datasets by $7 - 10\%$, due to using a larger slitwidth. Romanowsky & Kochanek (2001) calculate that this amounts to an additional instrumental dispersion of 183km s^{-1} and so we adjust the velocity dispersion by this amount (subtracting in quadrature) to bring it in line with the van der Marel dataset. We take the average of the velocity dispersions at each positive and negative R, assuming symmetry with respect to the galaxy's centre. We

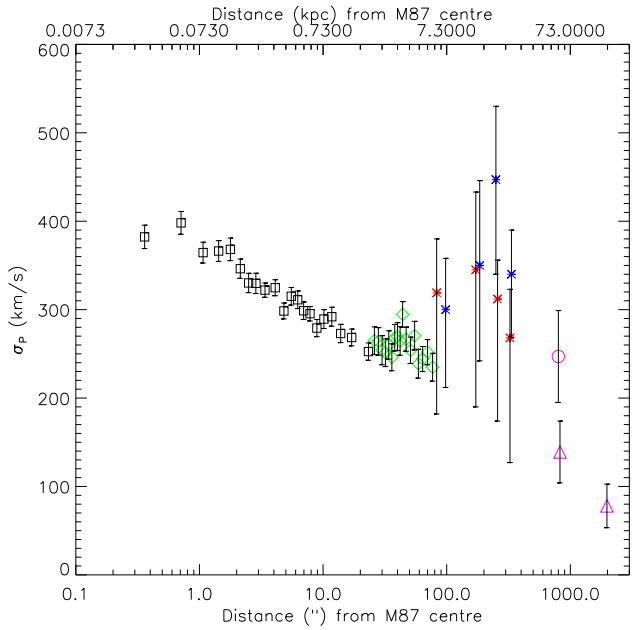

Figure 29: Velocity dispersion profile of M87, including stellar velocity dispersions from absorption-line spectra and discrete LOS velocity measurements from globular cluster and PN data. The squares are data points from van der Marel (1994), the green diamonds are based on Sembach & Tonry (1996), and the red and blue stars are velocity dispersions for the metal-rich and metal-poor GC samples of Côté et al. (2001), respectively. The magenta circle is the PN velocity dispersion determined in A04 and the magenta triangles are the PN dispersion values from the present work. These last two points are approximately along the major axis of the outer isophotes, which have ellipticity $\epsilon \simeq 0.43$.

exclude the Sembach & Tonry data in radial bins beyond 80″ as there is a discrepancy between the velocity dispersions at the corresponding opposite positions in radius along the axis and furthermore the values in those bins have large error bars. This may be due to low S/N in the outer part of the galaxy where the surface brightness is low and/or real anisotropies in the velocity dispersions. Either way we judge it better to exclude these data points as they are less trustworthy.

We also show in Figure 29 the data of Côté et al. (2001) for the metal-rich GCs out to 380″. We exclude the outer bins (380″ – 635″) where the error bars are close to 100% and therefore do not constrain the shape of the velocity dispersion profile in any way. The metal-poor GC system is more spatially extended than its metal-rich counterpart (see Figure 30 below and Côté et al., 2001) and may be composed of accreted and/or infalling remains of 'failed' or disrupted dwarfs: their velocity dispersion data are also shown in Figure 29, but do not trace the velocity dispersions of the M87 stars. We also note from Figure 1 of Côté et al. (2001) that the GC sample is likely to contain intracluster GCs just as our PN sample contains ICPNe, requiring a careful analysis of the GC LOSVDs.

Finally, the two outermost velocity dispersion points are from planetary nebulae presented in A04 and this Chapter. We note that when we bin the A04 data to be consistent with the binning

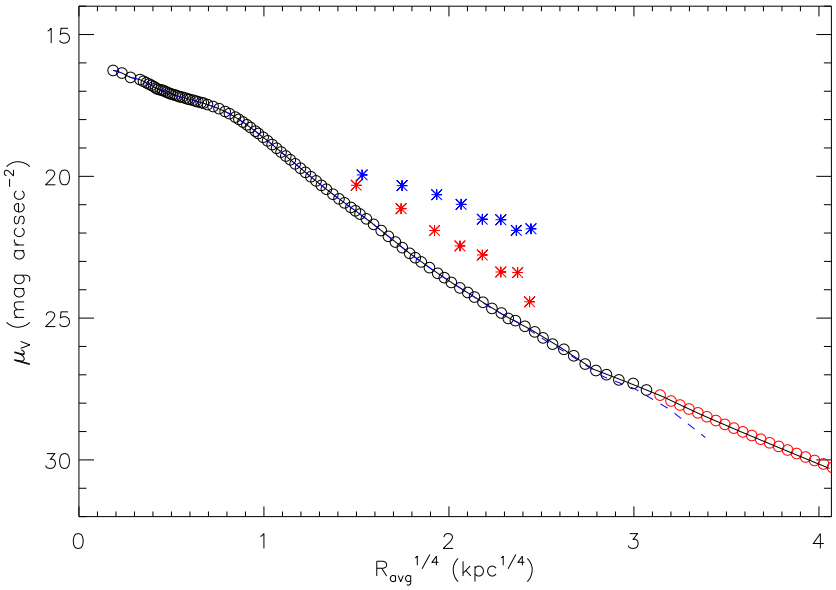

Figure 30: V-band surface brightness profile for M87 from Kormendy et al. (2009) shown with black circles along average ellipse radii R_{avg} of the isophotes. Red circles show the extrapolated Sérsic fit. The full line shows the reprojected three-dimensional luminosity model obtained from the extrapolated data, and the dashed line shows the reprojection of the luminosity model when truncated at average ellipse radius $R_{trunc} = 149$ kpc. For comparison, the number density profiles of the red and blue globular cluster populations from Côté et al. (2001) are also shown with arbitrary scaling as red and blue stars, respectively.

of the velocity distribution in this work (100km s^{-1} bins) the peak around M87 is resolved into a somewhat narrower peak of 9 objects, with two lower velocity and one higher velocity outliers (Figure 29). The mean and rms velocity of this peak of $\bar{v} = 1264$ km s^{-1} and $\sigma = 247$ km s^{-1}from A04 then change to 1292 ± 46km s^{-1} and 139 ± 23km s^{-1} respectively. It is possible that the larger value of σ_{PN} obtained by A04 could be due to the inclusion of some ICPNe from the component with uniform LOSVD seen in Figure 26. We carried out χ^2 tests[4] but could not distinguish between both interpretations. The dynamical model discussed below favours the high value of σ_{PN} at $R = 60$ kpc.

In any case, the PN velocity measurements show that the halo of M87 becomes colder at larger radii: the velocity dispersion decreases to 78km s^{-1} at $R \sim 140$ kpc.

4.4.3 *Truncation of the M87 stellar halo*

In the FCJ field, there are M87 halo PNe detected throughout, but in the F7/F4 fields, the PNe around the systemic velocity of M87 (=1307 km s^{-1}) appear to be found only within a projected radius

4 We carried out a χ^2 test for the (FCJ;A04) sample and i) a broad Gaussian ($\bar{v} = 1264$ km s^{-1} and $\sigma = 247$ km s^{-1}), ii) a uniform distribution plus a narrow Gaussian ($\bar{v} = 1264$ km s^{-1} and $\sigma = 139$ km s^{-1}). Because of the limited statistics of the PN sample in this field, the results depend on the velocity range chosen for the test. In a $700 - 1650$ km s^{-1} range, the two distributions fit the data equally well with 80% probability, while the broad Gaussian is ruled out in a $350 - 1650$ km s^{-1} range.

of $R = 161$ kpc (see the spatial distribution of the spectroscopically confirmed PNe in Figure 27). At projected radii $R > 161$ kpc from the centre of M87, we find only the encroaching stars of M86 and other Virgo components. We now investigate whether this spatial and velocity segregation is significant and indicates that the M87 stellar halo is truncated.

Kormendy et al. (2009) present a composite V-band surface-brightness profile for M87 out to 135 kpc along the semi-major-axis. This is shown with black circles in Figure 30, with the semi-major axis of each isophote replaced by the average ellipse radius, $R_{avg} = (ab)^{1/2}$ of the isophote. We will use the latter in the construction of the spherical Jeans models in Section 4.4.4. Kormendy et al. (2009) fit a Sérsic profile to the semi-major axis profile excluding the central core and the last two data points (which may have a significant ICL contamination), and obtain the following best-fit parameters: $\mu_e = 25.71$, $R_e = 704'' = 51.2$ kpc, $n = 11.885$. We use this Sérsic fit to the surface brightness profile (see Figure 30) to compute the luminosity of the M87 halo at radii outside the available photometry. We note that the description of M87 as a classical E0 or E1 galaxy is based on short exposure optical images, while in deep images its isophotes show marked eccentricity. For the extrapolation we assume an ellipticity $\epsilon = 0.43$ and position angle (PA$= -25^\circ$), based on the outer parts of the ellipticity and position angle profiles in Kormendy et al. (2009). We then evaluate the M87 halo luminosities in the regions of overlap between the photometric and spectroscopic fields, in which, respectively, the photometric identification and spectroscopic follow-up of the PNe was carried out. These are shown by the coloured regions in Figures 31. For ellipticity $\epsilon = 0.43$, the PNe belonging to M87 appear to be found within an average ellipse radius $R_{avg} = 149$ kpc. We use the isophote corresponding to this radius to demarcate the region containing PNe belonging to M87 (in red in Figure 31) from the region containing no PNe belonging to M87 (in green in Figure 31). Table 5 gives the areas and the V-band luminosities of the various regions obtained. On the basis of the Sérsic fit, the ratio of the M87 luminosity in the F7-green and in the F7-red area is 0.92.

From the number of spectroscopically confirmed M87 PNe in the F7-red area (i.e., 5), and the ratio of the M87 halo luminosities from the Sérsic fit (i.e., 0.92), we can then predict the expected number of PNe at the M87 systemic velocity in the F7-green area, to be $5 \times 0.92 = 4.6$ PNe. The observational result of zero M87 PNe detected in the F7-green area thus implies a truncation of the M87 stellar halo at $R_{avg} > 149$ kpc, at a $\simeq 2\sigma$ level. This radius tells us the location of the outermost PN in terms of the average ellipse radii and we now refer to it as the truncation radius R_{trunc}.

This is a surprising result: the numerical simulations of Abadi et al. (2006) find that the luminous halos around isolated galaxies

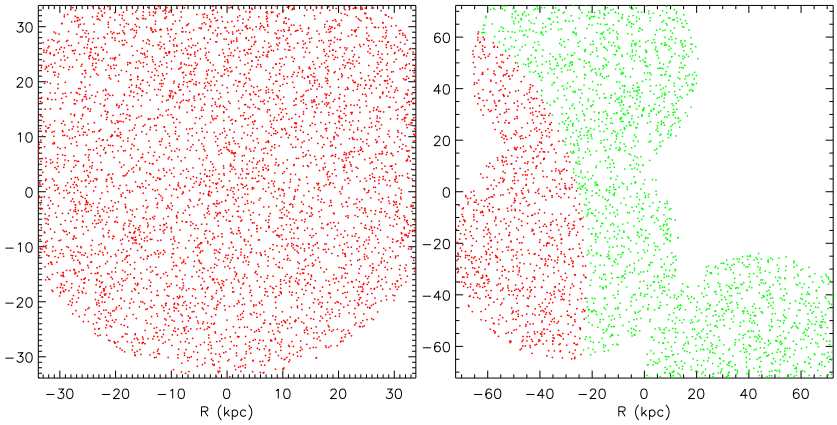

Figure 31: Left: The red region is the intersection between the photometric field FCJ and the FLAMES (FCJ) pointing. Right: The red region is the part of the intersection between the photometric field F7 from Feldmeier et al. (2003) and the regions jointly covered by the F7_1, F7_2 and F4 FLAMES circular pointings, which is within the isophote with an average ellipse radius, $R_{trunc} = 149$ kpc. This covers the region containing PNe with velocities bound to M87. The green region is the part of the intersection between the F7 region and the FLAMES pointings as before, but outside R_{trunc}, where no PNe associated with the M87 velocity peak are found.

Table 5: M87 halo PNe and sampled luminosities.

Field	N_{spectr}	Area kpc^2	L $L_{V,\odot}$
FCJ red	12	4157	8.7×10^9
F7 red	5	4349	1.3×10^9
F7 green	0	8909	1.2×10^9

should extend to the virial radius, i.e., to several hundred kpc and well beyond their traditional luminous radius. It is therefore not obvious why there should be a truncation of the M87 stellar halo, see Section 4.4.5. One question is whether the truncation we see occurs only at the targeted $P.A.$ within an opening angle $\delta P.A.$, say, rather than at all azimuths, and whether when azimuthally averaged, the halo light distribution would extend to larger radii. This could be the case if we had reached the radii where the stellar halo of M87 has a significant amount of substructure, similar to the outer Milky Way halo (Bell et al., 2008). For example, we might explain the spatial segregation of the M87 halo PNe in terms of a cold stellar shell at our field position, followed by a steeper surface brightness profile at those $P.A.$ whereas at other $P.A.$ the profile would be shallower. This would also explain the small σ_{PN} that we measure in our fields at $R = 144$ kpc, as the stars populating shells are near to the apocentres of their elongated orbits.

To assess this we must reconsider the photometric structure of M87. Within a semi-major axis of ~ 160 kpc and $\mu_V \lesssim 27.5$, the surface brightness distribution around M87 is well approximated

by an extended envelope with $c/a \simeq 0.57$ (Mihos et al., 2005; Kormendy et al., 2009). This ellipsoidal component includes the diffuse fan of stellar material, which extends along the projected southeast semi-major axis out to $\sim$ 100 kpc (Arp & Bertola, 1971; Weil et al., 1997), but is otherwise fairly smooth. At larger radii and fainter surface brightnesses, the light distribution is a superposition of the outer halo of M87 and the ICL and is brightest in the range of *P.A.* towards M86 where our target fields are. At these radii it does show irregular features and some radial streamers, and our fields are large enough to include several of these. In fact, some of our outermost M87 PNe may be close to an arc-like feature in the Mihos et al. (2005) image beyond which little light is seen. However, both the earlier results of Weil et al. (1997) who reported the apparent lack of sharp-edged fine structures around M87, and our independent inspection of the Mihos et al. (2005) image near M87, provide no evidence for a large number of "shell-like" features at various azimuths and radii around M87. This is true both inside and outside our truncation isophote, and in particular around $R \sim 60$ kpc, where the PN data already indicate a falling velocity dispersion profile (see Figure 29).

Further investigation of the extended luminosity distribution around M87 would require quantitative photometry of the deep image of Mihos et al. (2005), and a large-area and wide-angle PN velocity survey to separate the outer halo of the galaxy from the ICL with better statistics.

In what follows, we follow an independent approach and test the hypothesis of a truncated stellar halo in M87 dynamically. We will verify whether we can make a dynamical model for M87 in which the stellar velocity dispersion reaches low values everywhere around M87, and the total gravitational potential is traced by the X-ray emission of the hot gas.

4.4.4 *The mass distribution and anisotropy in the M87 outer halo*

The smooth photometric and X-ray emission profiles indicate that the outer halo of M87 is in approximate dynamical equilibrium. With the extended velocity dispersion profile we are now able to create dynamical models of M87 to infer the orbital structure in the outermost halo. In a spherical system, the intrinsic velocity dispersions of a population of stars with density j moving in a potential Φ are related by the second-order Jeans equation

$$\frac{d}{dr}\left(j(r)\sigma_r^2(r)\right) + \frac{2\beta}{r} j\sigma_r^2(r) + j(r)\frac{d\Phi}{dr} = 0 \qquad (4.1)$$

where the anisotropy parameter $\beta(r) = 1 - (\sigma_\theta(r)/\sigma_r(r))^2$ quantifies the orbital structure of the system. Its value spans a range between $-\infty$ signifying purely tangential orbits and 1 signifying purely radial orbits. These intrinsic quantities are now in terms of the three-dimensional radius, r.

Therefore if we know the potential Φ, density of stars j and assume a radial dependence for the anisotropy, we can solve for the intrinsic radial (σ_r) and tangential (σ_θ) velocity dispersion profiles. These can then be projected and compared with the observed projected velocity dispersion profile to fix the parameters of the assumed anisotropy profile. Under the spherical assumption, the radii of the observables will be the average ellipse radii R_{avg} introduced in Section 4.4.3.

One method of deriving the potential of a galaxy is to use electron density and temperature profiles obtained from X-ray measurements of the thermal bremsstrahlung emission from the hot interstellar medium surrounding massive elliptical galaxies. If the gas is relatively undisturbed then we can assume that the gas is in hydrostatic equilibrium and thus derive the potential.

Nulsen & Böhringer (1995) use *ROSAT* data and a maximum likelihood method to deduce the most likely mass profile in the Virgo cluster core, extending from the centre of M87 out to 300 kpc. They parametrise this profile with a model composed of two (approximate) isothermal mass distributions, one attributed to the mass of M87 with a mass per unit length $\mu = 3.6 \times 10^{10} M_\odot$ kpc^{-1} and the other to the dark matter of the cluster with a mass per unit length $M_0/a = 12.4 \times 10^{10} M_\odot$ kpc^{-1} and a core radius $a = 42$ kpc. This parametrisation is given as

$$M(r) = \mu r + M_0[(r/a) - \arctan(r/a)]. \tag{4.2}$$

This mass profile is related to the potential through $rd\Phi(r)/dr = \mathrm{v}_c(r)^2/r = GM(r)/r^2$, where $\mathrm{v}_c(r)$ is the circular velocity at r. It is more easily calculated than the potential but also independent of distance. The circular velocity profile is shown in Figure 32 and increases from a minimum circular velocity of 393 kms^{-1} to eventually a maximum velocity of 830 kms^{-1}. For comparison the same profile is shown with M_0 adjusted so that the maximum velocity reached is 700 kms^{-1}, the value suggested by the extrapolation of newer observations taken with XMM-Newton (Matsushita et al., 2002).

The density of the stars was obtained through the deprojection of the surface-brightness profile of M87. To obtain the intrinsic luminosity density, we adopt the Kormendy et al. (2009) profile (also missing the last two data points), and using their Sérsic fit, extrapolate to very large radii, see Section 4.4.3; then we employ the standard deprojection formula. In Figure 30, the Sérsic extrapolation is shown by the red circles and the reprojection of the intrinsic luminosity density is shown by the solid black line which follows the circles very well.

Finally, the radial dependence we adopt for the anisotropy profile is given by

$$\beta(r) = \beta_m \frac{r + r_1}{r + r_2} \tag{4.3}$$

where $r_1 < r_2$, β_m is the maximum anisotropy reached at large r, $\beta_m r_1/r_2$ is the minimum anisotropy and r_2 represents the scale

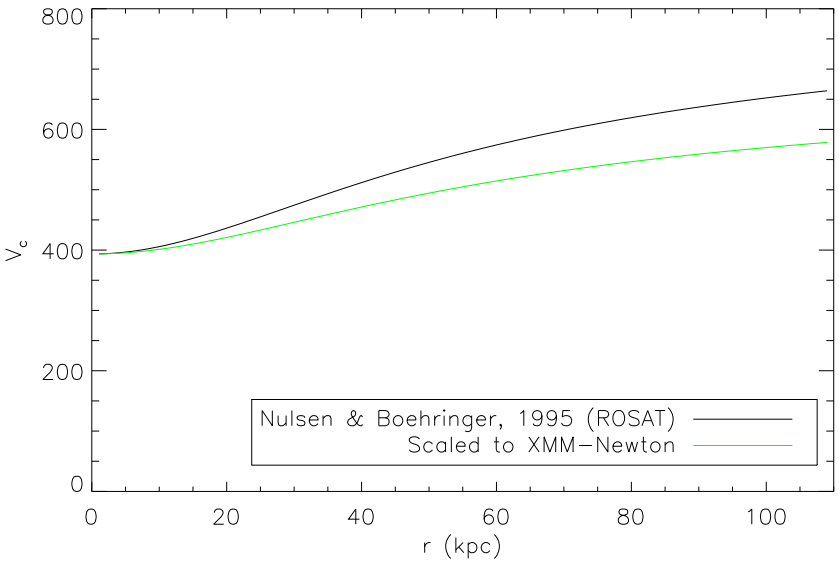

Figure 32: Circular velocity profiles for M87 from X-ray data.

of the transition from the minimum anisotropy to the maximum anisotropy. This solves the Jeans equation (4.1) as a first-order differential equation with the integrating factor

$$\text{I.F.} = j(r) r^{2\beta_m x} (r + r_2)^{2\beta_m (1-x)} \tag{4.4}$$

where $x = r_1/r_2$ so that

$$\sigma_r^2(r) = \frac{1}{\text{I.F.}} \int_r^\infty \text{I.F.} \frac{v_c^2}{r'} dr'. \tag{4.5}$$

Then the projected velocity dispersion, σ_P, is obtained by projecting the intrinsic velocity dispersions along the line of sight. These integrals were determined numerically.

To obtain a dynamical model for the Sérsic light distribution in the potential implied by Figure 32, we fixed the minimum and maximum anisotropy using constant anisotropy models and then employed a χ^2 minimisation approach to deduce the best-fit r_2 for the solution in Equation (4.5). This minimisation takes into account the long-slit data, the σ_{PN} point at 60 kpc from A04, and the new σ_{PN} point at 144 kpc, but not the globular cluster data. The best-fit model is shown by the solid black line in Figure 33. It fits the data very well within 6 kpc but it is unable to reproduce the low PN velocity dispersions in the outer parts, at $R_{avg} = 52$ kpc and $R_{avg} = 131$ kpc, where it would predict LOSVDs with dispersions of 350-400 km s^{-1}.

On the basis of the results in Section 4.4.3, we assume now that the galaxy's intrinsic luminosity density is truncated at $r = R_{trunc} = 149$ kpc (i.e., in a spherical system the intrinsic truncation radius is the same as the projected truncation radius). The reprojection of this truncated intrinsic luminosity density is also shown in Figure 30 by the blue dashed line. We construct a Jeans model for the truncated luminosity distribution in the same way as above. Finally, to check the influence of the assumed potential on the results, we have evaluated one further model, also

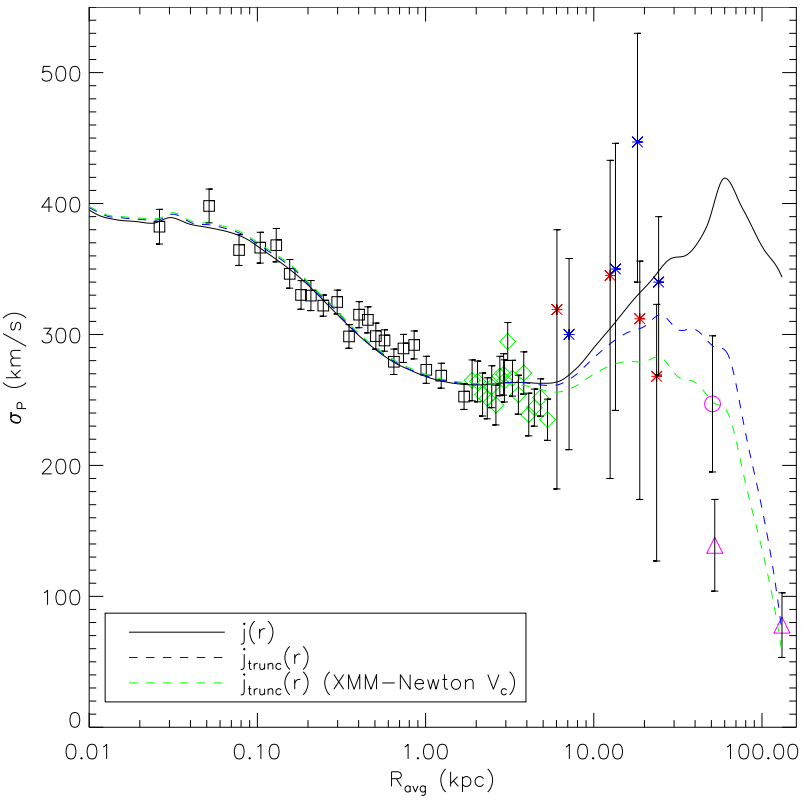

Figure 33: Velocity dispersion profiles derived for Jeans models with spherical symmetry and surface brightness profiles as in Figure 30; see text. The velocity dispersion data points are shown at their average ellipse radii R_{avg}, computed with the ellipticity profile. For the globular cluster velocity dispersions this is not possible; these are not used in constructing the Jeans models. Symbols are as in Figure 29.

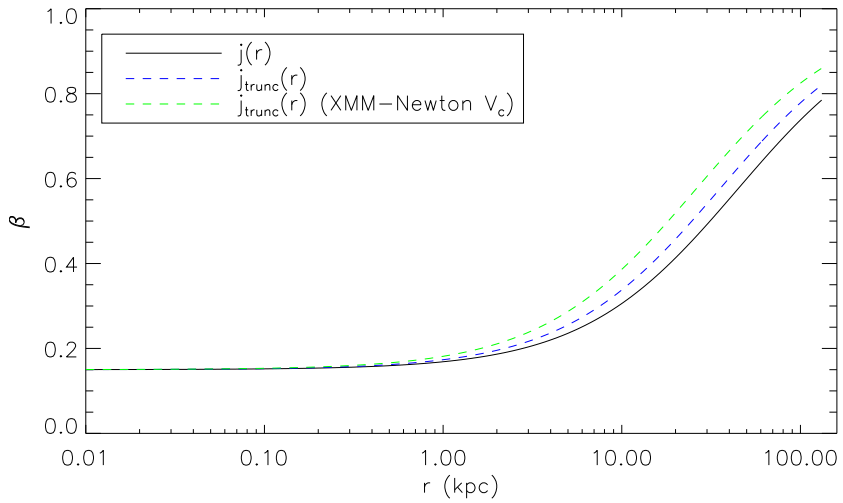

Figure 34: Anisotropy profiles for the best-fit models: they imply a mildly radially anisotropic orbital distribution ($\beta \approx 0.15$) in the centre that becomes highly radially anisotropic in the outer halo ($\beta \approx 0.8$).

assuming a truncation in the luminosity density but using the circular velocity that was adjusted to the analysis of XMM-Newton observations in Matsushita et al. (2002). The corresponding Jeans models are shown in Figure 33 with the blue and green dashed lines respectively, with the second model dipping slightly lower in the outer parts, reflecting the lower potential in this region.

Both truncated models behave as the untruncated Sérsic model in the centre, but fall much more steeply at radii $R_{avg} > 30$ kpc, thus being able to reproduce the outermost σ_{PN} data points at $R_{avg} = 52$ and $R_{avg} = 131$ kpc (corresponding to projected radii $R = 60$ and $R = 144$ kpc). At $R_{avg} = 52$ kpc, the truncated models predict a velocity dispersion which favours the higher value of σ_{PN}, i.e., 247 km s^{-1}. Figure 34 shows that the best-fit models imply a mildly radially anisotropic orbital distribution ($\beta \approx 0.15$) in the centre that becomes highly radially anisotropic in the outer halo ($\beta \approx 0.8$).

We conclude that, under the assumption of spherical symmetry, the Jeans models can only reproduce the low PN velocity dispersion measurements in the outer halo of M87 at $R_{avg} > 30$ kpc only with a truncation of the intrinsic luminous density.

In principle, this dynamical argument could be circumvented if at the position of our outer fields the stellar halo of M87 was strongly flattened along the line-of-sight. In this case σ_{PN} could be low at these radii independent of a truncation. However, at ~ 150 kpc radius such a flattening is likely to be local and would have arisen from the geometry of accretion, rather than signifying an angular momentum supported global structure collapsed from even $\lambda^{-1} \simeq 20$ times further out. Thus the well-mixed, three-dimensional stellar halo of M87 would then have ended at even smaller radii. Also note that in this case we could still not explain the lack of PNe at the M87 systemic velocities for radii greater than R_{trunc} (see Figure 28 and the discussion in Section 4.4.3.)

4.4.5 *On the possible origin of a truncated stellar halo in M87*

Summarising the last two sections, there are two independent and mutually consistent pieces of evidence that the stellar halo of M87 ends at $R_{trunc} \simeq 150$ kpc: the lack of PNe around the systemic velocity of M87 beyond this radius, and the very low velocity dispersion in the outer halo.

In well-mixed, dense galaxy clusters it is expected that galaxies are tidally truncated by the cluster's tidal field (Merritt, 1984; Ghigna et al., 1998). The tidal effects are strongest near the cluster core radius and the approximation $r_{\rm tidal} \simeq r_{\rm peri}\sigma_{\rm halo}/\sigma_{\rm clus}$ for the tidal radius is found to work well. Here $r_{\rm peri}$ is the pericentre of the galaxy's orbit in the cluster, and $\sigma_{\rm halo}$ and $\sigma_{\rm clus}$ are the velocity dispersions of the galaxy halo and the cluster, respectively. The tidal truncation of the dark matter halos of galaxies has been detected with combined strong and weak lensing observations in several dense clusters (Natarajan et al., 1998, 2002; Limousin et al., 2007; Halkola et al., 2007). Tidal radii of between 15 and 60 kpc have been found, in agreement with predictions.

The case of M87 is not so simple though. M87 is at the centre of at least a subcluster potential well, traced by the X-ray emission and the dark matter mass profile derived from it (Nulsen & Böhringer, 1995; Schindler et al., 1999, see Figure 32). A galaxy at the centre of its cluster experiences a symmetric gravitational field from the cluster dark matter, and is consequently not gravitationally truncated (Merritt, 1984). On the other hand, M87 has a relative motion of ~ 300 km/s with respect to the galaxies in the cluster core (Binggeli et al., 1993), and the galaxy distribution in the core is complicated and not centred on M87, containing a strong concentration around M84/M86 (Binggeli et al., 1987). It is possible that the M84/M86 concentration including the associated dark matter exerts a significant tidal field on M87. There is no obvious feature in the density of the X-ray emitting gas at $R_{trunc} \sim 150$ kpc around M87, but because the total mass within the truncation radius appears to be already dominated by cluster dark matter, a tidal truncation of the M87 mass distribution may be difficult to see in X-ray observations. However, if M87 was currently tidally truncated by a tidal field with assumed mass centre towards M84/M86, we would expect to see some of the tidally dissolved stars as PNe in our outer F7 fields at slightly redshifted velocities with respect to the systemic velocity. Within the limited statistics, we do not see any PNe with such velocities outside a projected radius of 161 kpc, see Section 4.4.3. This suggests that if there has been a tidal truncation, it would have occurred some time ago during the interaction with another mass concentration. The most likely candidate in the Virgo core may be that around M84; at a relative velocity with respect to M87 of about 300 km s^{-1}, M84 could have travelled their current projected separation in ~ 1 Gyr.

On the other hand, due to the dynamical youth of the Virgo cluster, it is also possible that M87 has not been tidally affected yet, and is more similar to an isolated massive elliptical galaxy. As already mentioned in Section 4.4.3, the luminous halos around isolated galaxies are expected from numerical simulations (Abadi et al., 2006) to extend to the virial radius, i.e., to several hundred kpc, and well beyond their traditional luminous radius. Hence we now consider the possible origins of the truncation of the M87 stellar halo in the context of isolated galaxies.

One possible explanation might lie in the fact that M87 is an old galaxy with a massive nuclear black hole, which points to much stronger AGN activity in the past than is apparent now. The feedback from its AGN through the surrounding hot gas might at some redshift z_f have stopped the star formation in nearby satellite galaxies through, e.g., ram pressure stripping. When these satellites later accreted onto the galaxy, they would have predominantly added dark matter to the outer halo, so that the virial radius R_V of M87 kept growing, but the luminous radius stalled at $R_V(z_f)$. On this assumption, we can estimate z_f from the redshift dependence of the virial radius.

The X-ray observations show that the hot gas extends out to 300 kpc (Nulsen & Böhringer, 1995; Matsushita et al., 2002). The derived integrated mass profile of the total gravitating matter shows a change in slope at about 30 kpc (Matsushita et al., 2002), and then increases linearly at large radii (see Figure 32 above). The mass distribution inferred from the X-ray measurements thus provides evidence for two components: a galaxy dark matter component and a cluster dark matter component. From the modeling of Nulsen & Böhringer (1995) and the rotation curve in Figure 32 we can estimate the maximum circular velocity generated by the M87 galaxy halo now to be $v_{max,M87} \simeq 400 \mathrm{km\ s^{-1}}$. Using the results of Bullock et al. (2001), this corresponds to a present-day virial mass $M_V(z=0) \simeq 2.0 \times 10^{13} M_\odot$ and virial radius $R_V(z=0) \simeq 470$ kpc, several times larger than the truncation radius inferred from both the PN number counts and the outer halo dynamics, $R_{trunc} \simeq 149$ kpc. For the same $v_{max,M87}$, the virial radius of M87 would have been 149 kpc at redshift $z_f \simeq 2.9$, arguing that feedback would need to have been effective quite early-on to explain the observed truncation radius.

A second possible explanation would assume that the accretion of dark matter and satellites onto M87 ceased with the collapse of the Virgo cluster core. In the new potential after the collapse, the satellites would both have been deflected from their nearly radial orbits with respect to M87, and have significantly larger impact velocities than previously, making accretion and merging with M87 suddenly less likely. The total mass of M87 would thus not increase any further, stalling at the virial mass at that redshift. Moreover, the rotation curve in Figure 32 shows that with the on-going collapse of the Virgo cluster a substantial cluster dark matter cusp has since built up within the halo of M87. The likely

effect of this is an adiabatic contraction of the galaxy's luminous and dark halo.

The two-component mass model of Nulsen & Böhringer (1995) (see equation 4.2) for the present-day mass distribution predicts within $R_{trunc} \simeq 149$ kpc, a galaxy mass of $M(R_{\rm trunc})_{\rm M87} \simeq 5.4 \times 10^{12} M_{\odot}$ and a cluster dark matter mass of $M(R_{trunc})_{\rm Virgo} = 1.2 \times 10^{13} M_{\odot}$, assuming a flat rotation curve for the galactic contribution to the mass. The luminous mass of M87, (4-5)$\times 10^{11} M_{\odot}$ (Cappellari et al., 2006), is consistent with the estimated total galaxy mass. As an example, consider truncation of the accretion onto M87 by the collapse of the Virgo core at redshift $z = 0.5$. Using a lower $v_{c,mx,M87} \simeq 300$km s^{-1} for the M87 halo before adiabatic contraction and again the results of Bullock et al. (2001), the virial mass and radius at that redshift become $M_V(z = 0.5) \simeq 6.2 \times 10^{12} M_{\odot}$ and virial radius $R_V(z = 0.5) \simeq 300$ kpc. An (over)estimate of the adiabatic contraction can be obtained from angular momentum conservation at the outer radius, i.e., $GM_V(z = 0.5)R_V(z = 0.5) = G[M(R_{trunc})_{\rm M87} + M(R_{trunc})_{\rm Virgo}]R_{trunc}$, giving $R_{trunc}/R_V(z = 0.5) = 0.3$. This suggests that the observed truncation radius could well be the relic of the virial radius from the time when the cluster core collapsed.

It is clear that more data are needed to pursue this question further. In particular, a larger number of PNe all around M87 would be very useful to set stronger constraints on the tidal hypothesis.

4.5 THE LUMINOSITY-SPECIFIC PN NUMBER FOR THE M87 HALO AND THE ICL IN VIRGO

The physical quantity which ties a PN population to the luminosity of its parent stars, is the luminosity-specific PN number $\alpha = N_{PN}/L_{gal}$, where N_{PN} is the number of all PNe in the population[5] and L_{gal} is the bolometric luminosity of the parent stellar population. Observations show that this quantity varies with the $(B - V)$ colour of the stellar continuum light (Hui et al., 1993), and simple stellar population models predict that it is a function of the age and metallicity of the parent stellar population (Buzzoni et al., 2006). Furthermore, within the framework of single stellar populations models, the α parameter quantifies the average PN lifetime τ_{PN} (Villaver et al., 2002; Ciardullo et al., 2005) via the relation $\alpha = \mathcal{B}\tau_{PN}$, where $\mathcal{B}$ is the 'specific evolutionary flux' and is nearly constant (see Buzzoni et al., 2006, for a detailed discussion). The PN samples in elliptical galaxies and the ICL are all confined to the brightest 1 to 2.5 magnitudes of the PNLF. Therefore we use the $\alpha_{2.5}$ parameter, defined in terms of $N_{2.5}$, the number of PNe down to 2.5 magnitudes below the PNLF cut-off: $\alpha_{2.5}$ equals about one tenth of α according to the double exponential formula of Ciardullo et al. (1989) for the PNLF.

5 This is given by the integral over the whole eight magnitude range of the Planetary Nebula Luminosity Function (PNLF).

We can use the number of photometrically detected PNe in the FCJ, F7/F4 fields, and the luminosities of both the M87 halo and the ICL populations sampled in the surveyed areas, to compute the $\alpha_{2.5}$ values for these two components. Since the M87 halo and the ICL coexist at the two field positions, we determine the fraction of the PNe in the photometric sample bound to the M87 halo or in the ICL according to the fraction of spectroscopically confirmed PNe associated with each component in the LOSVD, i.e., with the narrow M87 peak or the nearly uniform velocity distribution for the ICL.

Luminosity of the ICL - We estimate the luminosities of the ICL stellar population in our fields from the deep photometry of Mihos et al. (2005). Such surface brightness measurements for the diffuse light generally contain the cumulative contributions from extended galaxy halos, the true ICL, and from excess unresolved background galaxies above that adopted from the sky subtraction. Depending on the method of sky subtraction, the homogeneous part of the last component may be included in the sky measurement. The photometry of Mihos et al. (2005) shows a 'plateau' of the surface brightness at a value of $\mu_V = 27.7$ half way between M87 and M86, where the F7/F4 fields are situated. As we have seen in Sections 4.4.3, 4.4.4, there is no contribution from the halo of M87 to the plateau. Williams et al. (2007) estimate the surface brightness of background galaxies from their deep imaging survey with the Hubble Space Telescope's Advanced Camera for Surveys (ACS), in a small (intracluster) field within our field F4. These galaxies, which are resolved in the ACS data, would contribute a diffuse surface brightness of $\mu_V \simeq 28.6$ in ground-based data. The sky subtraction procedure adopted by Mihos et al. (2005) would have already subtracted this component if its surface brightness is similar in the edges of the mosaic where the sky was measured. In the following, we therefore use $\mu_V = 27.7$ for the ICL surface brightness in this region, with a possible uncertainty of a few tenths of a magnitude due to a possible inhomogeneity of the background sources.

The $\alpha_{2.5}$ values and their implications - In what follows we make the assumption that the ICL surface brightness is constant in the FCJ, F7/F4 fields at this value of $\mu_V \sim 27.7$ mag arcsec^{-2}. In Table 6 we give the corresponding ICL luminosities and the number of spectroscopically confirmed PNe from the ICL in these fields, N_{spectr}. In Table 7 we give the number of PNe in the complete photometric samples in the overlap area covered by the spectroscopic follow-up, N_{phot}, and the fraction of PNe in the M87 halo and the ICL according to their measured LOSVDs. Because of the small number statistics, we compute $\alpha_{2.5}$ for the M87 halo in FCJ, and for the ICL in F7, where their respective contributions are largest.

The N_{phot} of each field is scaled by a factor

$$\Delta = \frac{\int_{M^*}^{M^*+2.5} PNLF(m)dm}{\int_{m^*}^{m_{lim}} PNLF(m)dm} \tag{4.6}$$

Table 6: ICL PNe and sampled luminosities in the coloured regions of Figure 31.

Field	N_{spectr}	Area	L
		kpc^2	$L_{V,\odot}$
FCJ red	2	4157	1.2×10^9
F7 red + green	7	13258	3.8×10^9

Table 7: Number of PNe in the photometric samples, for the M87 halo and the ICL.

Field	N_{phot}	N_{phot}	N_{phot}
		M87	ICL
FCJ	16[a]	14	2
F7	24[b]	10	14

[a] Number of PNe above the photometric completeness limit from Aguerri et al. (2005).

[b] Number of PNe above the photometric completeness from Table 4 in F7_1 and F7_2.

where PNLF(m) is the analytic expression for the PNLF (Ciardullo et al., 1989), M^* and m^* denote the absolute and apparent magnitude of its bright cutoff, respectively, and m_{lim} is the photometric m_{5007} limiting magnitude in each field. This scaling ensures that we account for all PNe within 2.5 mag of M^*.

The V-band luminosities in each field are converted to bolometric luminosities according to

$$L_{bol} = L_{V,\odot} 10^{-0.4(BC_V + 0.07)}. \tag{4.7}$$

According to Buzzoni et al. (2006), a value of $BC_V = -0.85$ mag can be taken as a representative correction for all galaxy types within 10% uncertainty.

Finally, we obtain the bolometric luminosity-specific PN number $\alpha_{2.5}$: For the M87 halo light at the FCJ position it is $\alpha_{2.5,M87} = 3.1 \times 10^{-9}$ PN $L_\odot^{-1}$, and for the ICL at the F7 position it is $\alpha_{2.5,ICL} = 7.2 \times 10^{-9}$ PN $L_\odot^{-1}$. The values of $\alpha_{2.5}$ for different stellar populations are well documented (Ciardullo et al., 2005; Buzzoni et al., 2006; Coccato et al., 2009): $\alpha_{2.5}$ in the range $3 - 10 \times 10^{-9}$ PN $L_\odot^{-1}$ are observed for bright ellipticals and Sos. Both the $\alpha_{2.5}$ values obtained for the ICL and for the M87 halo stars are consistent with those of old (> 10 Gyr) stellar populations.

Uncertainties in the $\alpha_{2.5}$ values - The luminosity of the M87 halo is computed using Monte Carlo integration of the Sérsic fit to the surface brightness from Kormendy et al. (2009) in the FCJ field, and the errors here are of the order of few percent.

The luminosity of the ICL is computed using $\mu_V = 27.7$ from Mihos et al. (2005). We independently estimated the ICL surface brightness by comparing the reprojected surface brightness

profile of the M87 halo with the Sérsic fit of Kormendy et al. (2009) in the F7 field. This results in an azimuthally averaged ICL $\mu_V = 28.5$. While 50% fainter than the measurement of Mihos et al. (2005), the two values may be quite consistent when taking into account that the ICL is observed mostly on the side of M87 towards M86/M84.

Considering the uncertainties in the surface brightness for the M87 halo and ICL, and the statistical errors in the number of detected PNe, the $\alpha_{2.5}$ values for M87 and ICL differ at the $\sim 2\sigma$ level. We speculate that $\alpha_{2.5,ICL}$ is a factor 2 larger than $\alpha_{2.5,M87}$ because of different metallicity distributions in the ICL and the M87 halo, with a larger fraction of metal-poor stars in the intracluster component, as shown by Williams et al. (2007).

4.6 ICL AND THE DYNAMICS OF THE VIRGO CLUSTER CORE

4.6.1 *ICPNe and dwarf spheroidals*

The LOSVDs in Figure 26 show the dynamical components in the Virgo cluster core: the halo of M87, and the ICL component traced by a broad PN velocity distribution. This component covers the velocity range from 1300 km s^{-1}down to the systemic velocity of M86 at -244 km s^{-1}. Overlaying the spatial coordinates of the PNe on the deep image of the Virgo cluster core (Figure 27; Mihos et al. (2005)) we can easily see the association of the PN components identified in the velocity - position space, with the morphological components of the surface brightness distribution in the Virgo core. The M87 PNe are confined to still relatively bright regions covered by the M87 halo, while the ICL PNe are scattered across the whole region.

For comparison, we examine the phase space distribution of dwarf elliptical galaxies in a region covering our target fields for the PNe spectra, i.e., in a 1.5 degree diameter circle centred on the midpoint of M87 and M86 (Figure 27). The aim is to search for possible associations between our ICPNe and the positions and velocities of the dwarf galaxies. The top panel of Figure 26 shows a histogram of the LOS velocities for all dwarfs in the region marked in Figure 27. The velocities form a flat, uniform distribution extending to larger positive velocities than the ICPNe. We ask whether any of the PNe could be physically associated with the dwarf galaxies. There are only two potential associations: one is between a PN with velocity 818km $s^{-1}$and a close-by dE at 791km s^{-1}. This dE has total blue apparent magnitude 15.4, i.e., M_B=-15.48 (using the assumed distance) or L_B=1.4 $\times$ $10^8 L_\odot$. According to Ciardullo et al. (2005), galaxies fainter than $M_B \sim -19$ and bluer than $V - I < 1.1$ produce about one [O III]-bright PN in every $4 \times 10^8 L_\odot$. It is therefore unlikely that the dwarf galaxy in question produced the PN detected here (as the expected number is 0.35) although it cannot be ruled out completely. On the other hand, the second association may well

be genuine: this is of a PN with velocity +28km s^{-1} and a close-by Sb spiral galaxy to its west, which has velocity 30km s^{-1} and B_{tot}=10.91 (and therefore is capable of producing between 85 and 2000 PNe depending on its age, see Buzzoni et al. (2006)).

Although the majority of the ICPNe do not appear to be physically associated with the dwarf galaxies (i.e., the PNe are unlikely to originate in the dwarfs), their distribution in velocity space is at least partially similar, indicating that they follow similar dynamics.

4.6.2 *Dynamical status of the Virgo core*

The velocity distribution of dwarf spheroidals (dE+dS0) in a 2° radius circular region centred on M87 is very flat and broad, with the peak of the distribution at 1300 km s^{-1} and a long tail of negative velocities (Binggeli et al., 1993). The LOSVD of the ICPNe now confirms that this asymmetry is also present in the very centre of the Virgo core, in a region of 1° diameter. Figure 28 shows that velocities near the systemic velocity of M86 are seen to about half-way from M86 to M87.

The asymmetry and skewness of the LOSVD may arise from the merging of subclusters along the LOS as described by Schindler & Böhringer (1993). In their simulations of two merging clusters of unequal mass, the LOSVD is found to be highly asymmetric with a long tail on one side and a cut-off on the other side, shortly ($\sim 10^9$ yrs) before the subclusters merge.

The observed LOSVDs of the PNe, GCs (Côté et al., 2001), and (dE+dS0) in the Virgo core may therefore be interpreted as additional evidence that the two massive subclusters in the Virgo core associated with the giant ellipticals M87 and M86 are currently falling towards each other - more or less along the LOS, with M87 falling backwards from the front and M86 forwards from the back - and will eventually merge, i.e. the entire core of the Virgo cluster must then be out of virial equilibrium and dynamically evolving.

The distribution of the brightest galaxies in Virgo also favours a recent and on-going assembly: West & Blakeslee (2000) found that Virgo's brightest elliptical galaxies tend to be aligned along the principal axis of the cluster (which is inclined by only about 10-15 degrees to the line of sight) and which on larger scales connects Virgo to the rich cluster Abell 1367. This work suggests that the formation of the cluster is driven by infall along this filament.

Do the halos of M87 and M86 already touch each other, or are they just before their close pass? PNLF distances (Jacoby et al., 1990) and ground-based surface brightness fluctuation distances (Tonry et al., 2001) indicate that M86 is behind M87 by just under ∼0.15 magnitudes. The globular cluster LF turnover also suggests that M86 is likely 0.1 to 0.2 magnitudes more distant than the main body of Virgo (Kundu & Whitmore, 2001). However, the

most recent surface brightness fluctuation measurements by Mei et al. (2007) find that M87 and M86 are only at very slightly different distances. Within the errors, the distance moduli (M87: 31.18 ± 0.07, M86: 31.13 ± 0.07) are consistent with being either at the same distance or separated by 1-2 Mpc. Unfortunately the evidence from the relative distances of M87/M86 is not conclusive at this stage.

4.6.3 *Implications for the formation of the ICL*

The observational facts concerning the ICL in the Virgo cluster core are:

1. The LOSVD of the ICPNe is not symmetrically distributed around the systemic velocity of M87. Those between M87 and M86 are mostly at 'bluer' velocities, i.e., < 800 km s^{-1}. "Red" velocities are only seen in the field $0.^{\circ}8$ north of the line connecting M87 with M86; see Figure 27.

2. While the dwarf spheroidals' (dE+dS0) LOSVD in the region marked in Figure 27 extend into 'red' velocities, up to 2500 km s^{-1}, ICPNe with velocities greater than 1800 km s^{-1}are seen only at its northern perimeter, while those in the region between M87 and M86 are confined to < 800 km s^{-1}(see Figures 26, 27, 28). This is not a consequence of the filter used in the photometric selection of these objects, which still has a transmission of 50% to [OIII]λ5007 at $\sim$2275km s^{-1} (Feldmeier et al., 2003). [6]

3. The morphology of the ICL between M87 and M86 is 'diffuse'; it is mostly not in tidal tails or streams (Mihos et al., 2005).

4. The measured $\alpha_{2.5}$ parameter for the ICL is in the observed range for old stellar populations.

5. The metallicity distribution of the RGB stars associated with the ICL in the Williams et al. (2007) field is broad, with a peak at about 0.1 solar, and the best model of Williams et al. (2007) indicates an old stellar population (> 10Gyr).

Point 1) indicates that the ICL did not have the time to phase mix yet, supporting the idea that much of this diffuse component is falling towards M87 together with the M86 group. Points 2) and 3) argue against the origin of this ICL from current harassment of dwarf irregulars by the cluster potential (Moore et al., 1996), firstly because none of the ICPNe between M87 and M86 are found at velocities redder than 800 km s^{-1}, while we see nearby dwarf galaxies in the $1800 < v_{LOS} < 2500$ km s^{-1} range, and secondly because the diffuse morphology of the ICL suggests

6 There may be a different, small selection effect due to the finite limiting magnitude of the photometric PN survey, as the ICPN that we detect are slightly biased towards objects on the near side of the cluster core.

that it has not recently been dissolved from the dwarfs, but had time to phase mix at earlier times in the sub-component of the Virgo cluster which is now falling towards M87. Points 4) and 5) indicate that the parent stellar population of the ICPNe is an old population, and point 5) makes dwarf spheroidals unlikely progenitors (recall that the dSph analysed by Durrell et al. (2007) had a narrow metallicity distribution at [Fe/H]$\simeq -2$). Dwarf elliptical galaxies have a wider metallicity distribution, and they could be disrupted during passages through the high-density regions around M87. Some of the observed ICPNe could trace stars on a stream from such a disruption event (particularly, those at $v_{LOS} \sim 800$ km s^{-1}), but those at low velocities in Figure 28 are falling in with M86, so have not crossed the dense regions yet. Point 3) then implies that these must have been part of the diffuse halo of the M86 group.

We conclude that we have found observational evidence in the Virgo core for the mechanism described by Rudick et al. (2006): we observe the diffuse component 'pre-processed' in the M86 sub-group, which is or has been gravitationally unbound from M86 as this substructure is being accreted by M87. The idea that the diffuse light is being stripped from the M86 sub-group is consistent with the observed highly skewed LOSVD and with the predictions from the simulations of Schindler & Böhringer (1993). Note that the light in the M86 subgroup is tidally stripped by the more massive M87 component, while these two sub-structures merge along the LOS; we do not see a diffuse ICL with a broad velocity component redwards of the systemic velocity of M87, because it has not yet been formed.

This scenario is also consistent with the simulations of Murante et al. (2007). Their statistical analysis of the diffuse star particles in a hydrodynamical cosmological simulation indicates that most of the ICL is associated with the merging tree of the brightest cluster galaxy, and about 80% of the ICL is liberated shortly before, during and shortly after major mergers of massive galaxies. The results from Murante et al. (2007) imply that the main contribution to the ICL comes from merging in earlier sub-units whose merger remnants later merge with the final cD galaxy. Similarly, Rudick et al. (2006) predict that violent merging events quickly add ICL, and without or between these events, the ICL fraction rises only slowly. Once the M86 subgroup has finally merged with M87, this will have created the most massive galaxy in the then Virgo cluster, and the ICL in the future Virgo core will indeed have originated mainly from the progenitors associated with its merging tree.

4.7 SUMMARY AND CONCLUSIONS

Using high resolution multi-object spectroscopy with FLAMES/MEDUSA on the VLT we confirm a further 12 PNe in the Virgo cluster, located between 130 and 250 kpc from the centre of M87,

and obtain their radial velocities. For most of these objects we also detect the second line [O III]λ 4959Å. These PNe trace the kinematics of diffuse light in Virgo, at typical surface brightness of $\mu_V = 27.5$.

The phase-space distribution for the new sample of PN velocities combined with earlier measurements at 60 and 150 kpc from M87 illustrates the hierarchical nature of structure formation. One group of PNe has an unrelaxed distribution of velocities with a range characteristic for the still assembling Virgo cluster core, while the second group has a narrow velocity distribution which traces the bound, cold outer halo of M87. We summarise our results for these two groups in turn.

4.7.1 *Dynamical status of the Virgo cluster and origin of the ICL*

Seven of the newly confirmed PNe are genuine intracluster PNe in the Virgo core, not bound to M87. Their spatial and velocity distribution indicates that we are witnessing the gravitational stripping of the diffuse light component around the M86 group, as this sub-structure is being accreted by the more massive M87. We do not see a diffuse ICL with a broad velocity distribution including red-shifted velocities around M87, because it presumably has not been formed yet.

On the basis of the LOSVDs of ICPNe and galaxies in the Virgo core, we surmise that M87 and M86 are falling towards each other nearly along the line of sight, and that we may be observing them in the phase just before the first close pass. We thus conclude that the heart of the Virgo cluster is still far from equilibrium.

Finally, the $\alpha_{2.5}$ values determined for the ICL indicate an old stellar population. This is consistent with the analysis by Williams et al. (2007) of the colour-magnitude diagram (CMD) for ICL red giant stars, which showed an old stellar population ($\gtrsim 10$ Gyr) with a large spread of metallicities. Differently, the CMD for a nearby dwarf spheroidal galaxy indicates a similarly old, but metal-poor stellar population (Durrell et al., 2007). Together with the observed v_{LOS} distribution of the ICPNe, these results suggest that at least some of the ICL in Virgo originates from stars unbound from the brightest and most massive galaxies.

4.7.2 *The M87 halo*

The other five of the newly confirmed PNe are associated with the bound halo of M87, at a mean projected radius $R = 144$ kpc from the centre of the galaxy. These PNe have velocities close to the systemic velocity of M87, with a small dispersion, and are furthermore segregated spatially from the rest of the (intracluster) PNe, as shown in Figures 27 and 28.

The LOSVDs of the M87 PNe both in the new fields and in the FCJ field of A04 are consistent with no rotation of the outer halo around the photometric minor axis, outside $R = 15$ kpc.

We cannot test whether the halo is rotating around the major axis. The rms velocity dispersion for the 5 M87 PNe at 144 kpc is 78 ± 25 km s^{-1}, much smaller than the central velocity dispersion. Together with the results of A04, this indicates that the M87 halo becomes 'dynamically' cold beyond 50 kpc radius.

The PNe around the systemic velocity of M87 are confined to radii $R \leq 161$ kpc. The absence of M87 PNe at larger radii with respect to the extrapolated Sérsic fit to the surface brightness profile from Kormendy et al. (2009), despite being based on small numbers, is significant at the $\sim 2\sigma$ level. This suggests that the edge of M87 has been detected, and it occurs at quite a large average ellipse radius - $R_{trunc} = 149$ kpc.

We have tested the hypothesis of a truncated stellar halo dynamically, using the observed stellar kinematics of the M87 halo. Combining all the velocity dispersion data available in the literature with our new M87 σ_{PN} data, we have solved the spherical Jeans equation assuming a total gravitational potential as traced by the X-ray emission. Within this framework, the Jeans model is able to reproduce the 'cold' PN velocity dispersion in the outer halo of M87 only if (i) the orbital structure in the outer halo becomes highly radially anisotropic, with $\beta > 0.4$ at $r > 10$ kpc, *and* (ii) the intrinsic luminous density is truncated. This dynamical argument can be circumvented only if the stellar distribution were strongly flattened along the line-of-sight in the surveyed fields. At these radii this flattening would be local and imply that the spheroidal stellar halo would end at even smaller radii.

The evidence for the truncation of the luminous halo of M87 thus comes from both the spatial distribution of the PNe with velocities near the systemic velocity of M87 (Figure 28), and from the small velocity dispersions in both the A04 field and in the new fields near the outer edge.

The reason for the truncation is not obvious; we discuss possible mechanisms in Section 4.4.5. Differently from some dense clusters where lensing analysis indicates that galaxies outside the cluster centre are tidally truncated by the dark matter cusp of the cluster, M87 in Virgo is located at the centre of the deepest potential well traced by the X-ray isophotes. We also do not see unbound PNe with velocities near 1300 km/s further out from M87. This suggests that if there has been a tidal truncation, it would have occurred some time ago during the interaction with another mass concentration, such as around the other massive galaxy in the Virgo core, M84. Alternatively, due to the dynamical youth of the Virgo cluster, it is also possible that M87 has not been tidally disturbed yet, and is more similar to an isolated massive elliptical galaxy and should thus still be accreting matter (Abadi et al., 2006). In this case possible explanations for the truncation could be early AGN feedback effects that indirectly truncate star formation in accreting satellites, or adiabatic contraction of the M87 halo due to cluster dark matter collapsing onto the galaxy.

The existing data cannot discriminate between these scenarios. The next step in this project is therefore to obtain a sample of at least a few hundred measured PN velocities covering the whole M87 halo. This is required to verify that the velocity dispersion decreases everywhere around the galaxy, and to obtain statistically better constraints on phase-space structures in the surrounding ICL, including possible stars tidally dissolved from M87. With a homogeneous imaging and spectroscopic PN survey covering the whole halo of M87 out to 40 arcmin we will be able to accurately measure the rotation, radial anisotropy of the orbits, and truncation of the outer halo of M87.

5

USING NMAGIC TO PROBE THE DARK MATTER HALO AND ORBITAL STRUCTURE OF THE X-RAY BRIGHT, MASSIVE ELLIPTICAL GALAXY, NGC 4649

This work has been submitted as Das et al. (2011) to MNRAS.

We create axisymmetric models of the massive elliptical galaxy NGC 4649, using the N-body made-to-measure code, NMAGIC, and kinematic constraints from long-slit and planetary nebula (PN) data. We explore a range of potentials based on previous determinations from X-ray observations and a dynamical model fitting globular cluster (GC) velocities and a stellar density profile. The X-ray mass distributions are similar in the central region but have varying outer slopes, while the GC mass profile is higher in the central region and on the upper end of the range further out. Our models cannot differentiate between the potentials in the central region, and therefore if non-thermal pressures or multi-phase components are present in the hot gas, they must be smaller than previously inferred. In the halo, we find that the PN velocities are sensitive tracers of the mass, preferring a less massive halo than that derived from the GC mass profile, but similar to one of the mass distributions derived from X-rays. Our results show that the GCs may form a dynamically distinct system, and that the properties of the hot gas derived from X-rays in the outer halo have considerable uncertainties that need to be better understood. Estimating the mass in stars using photometric information and stellar population mass-to-light ratios, we infer a dark matter mass fraction in NGC 4649 of ~ 0.35 at 1 R_e and ~ 0.77 at 4 R_e. We find that the stellar orbits are isotropic to mildly radial in the central ~ 12 kpc depending on the potential assumed. Further out, the orbital structure becomes slightly more radial along R and more isotropic along z, regardless of the potential assumed. In the equatorial plane, azimuthal velocity dispersions dominate over meridional velocity dispersions, implying that meridional velocity anisotropy is the mechanism for flattening the stellar system.

5.1 INTRODUCTION

Massive elliptical galaxies are huge conglomerates of stars, dark matter and hot gas, often residing at the centres of dense environments. They are believed to evolve through a complex formation process, manifested in the intricate structure of their orbits. Understanding the distribution of mass in massive ellipticals is vital

for obtaining constraints on the dark matter content and on the orbital structure of the stars.

The hot, low-density gas surrounding massive elliptical galaxies produces X-ray spectra consisting of emission lines and continuous emission from thermal bremsstrahlung radiation. The spectra can be modelled to obtain the density and temperature profiles of the gas. If the gas is relatively undisturbed then we can assume hydrostatic equilibrium and derive the total mass distribution from the density and temperature profiles (e.g. Nulsen & Böhringer, 1995; Fukazawa et al., 2006; Humphrey et al., 2006; Churazov et al., 2008; Nagino & Matsushita, 2009, and Chapter 2 in this thesis).

Another common method for obtaining mass profiles of massive elliptical galaxies is through the creation of dynamical models. They can be constructed by superposing a library of orbits (e.g. Rix et al., 1997; Gebhardt et al., 2003; Thomas et al., 2004; Cappellari et al., 2006; van den Bosch et al., 2008) or distribution functions (e.g. Dejonghe et al., 1996; Gerhard et al., 1998; Kronawitter et al., 2000), or by constructing a system of particles (NMAGIC, de Lorenzi et al., 2008, 2009) such that the projection of the system best reproduces observed surface-brightness and kinematic profiles. These give the mass distribution and orbital structure of the galaxies simultaneously.

Obtaining the mass distribution from X-rays is obviously a simpler way and this can then be used as input in the dynamical models of galaxies, therefore mitigating the usual mass-anisotropy degeneracy. This would provide more stringent constraints on the orbital structure derived from dynamical models. Before doing this however, one has to understand why there are discrepancies between mass profiles determined from X-rays and from dynamical models, and how significant these discrepancies are. In Chapter 2 we compared their X-ray mass determinations for a sample of six nearby massive elliptical galaxies to the most recent dynamical mass determinations with inconclusive results. The most common discrepancy between the two is in the central $\sim$ 10 kpc. The X-ray circular velocity curve, $V_c^2 = GM/r$ is on average generally about 20% lower than the dynamical result in this region. Based on work by Churazov et al. (2010), in Chapter 2 we speculated that the most likely sources of this discrepancy are: 1) Non-thermal contributions to the pressure that are not considered in the application of hydrostatic equilibrium, 2) multiphase components in the gas, 3) a lack of spatially extended observational constraints in the dynamical models, and 4) mass profiles in the dynamical models that are not sufficiently general.

In this Chapter, we would like to look in more detail at NGC 4649 (M60), residing at the centre of a sub-clump in the Virgo cluster. It is the fourth brightest early-type galaxy in the cluster. Long-slit kinematics from De Bruyne et al. (2001) and Pinkney et al. (2003) show a high velocity dispersion of $\sim$ 400 km/s in the centre, and a mean velocity of $\sim$ 100 km/s along the major

axis. There is also the recent catalogue of GC line-of-sight (LOS) velocities from Hwang et al. (2008), building on the catalogue from Bridges et al. (2006). They found significant rotation in the GC system, of order 141 km/s, and an average velocity dispersion of 234 km/s.

There are several mass distributions determined for NGC 4649 from X-ray data using ROSAT data (Trinchieri et al., 1997), Chandra data (Brighenti & Mathews, 1997; Humphrey et al., 2006, 2008) and a combination of Chandra and XMM-Newton data (Nagino & Matsushita, 2009; Churazov et al., 2010, and Chapter 2 in this thesis). The mass profiles are similar in the central ~ 12 kpc except that of Humphrey et al. (2006), which is a little higher. Further out they all point towards the existence of a massive dark matter halo, but the precise value of the circular velocity varies between $\sim$ 380–500 km/s at 20 kpc according to Hwang et al. (2008) and Chapter 2.

There are also several dynamical models in the literature combining the photometric and kinematic data described above. Bridges et al. (2006) used axisymmetric Schwarzschild models and Hwang et al. (2008) used Jeans models to fit GC LOS velocities and long-slit kinematics in the X-ray potential from Humphrey et al. (2006). They found an isotropic to a modestly tangential orbital structure. Shen & Gebhardt (2010) used axisymmetric Schwarzschild models to fit additionally kinematics from the Hubble Space Telescope (HST) and carried out an independent mass analysis. They confirmed the presence of a supermassive black hole in the centre and a dark matter halo. Their best-fit mass profile is higher than the mass profiles derived from X-ray observations in the central ~ 12 kpc and in the outer parts agrees best with the mass distribution in Chapter 2.

In this work we use the made-to-measure particle-based code NMAGIC (de Lorenzi et al., 2007) to create dynamical models of NGC 4649. We use photometric profiles from Kormendy et al. (2009), long-slit kinematic data from Pinkney et al. (2003) and LOS velocities measured for a new catalogue of 298 PNe described in a companion paper (Teodorescu et al., 2010, to be submitted to ApJ). The PNe trace the kinematics out to about 416″, similar to the GCs, but with more than double the number of tracers. There is also strong evidence that PNe are good tracers of the stellar density and kinematics in early-type galaxies (Coccato et al., 2009). We explore mass distributions based on the determinations in Chapter 2 and Shen & Gebhardt (2010), which only differ in the central ~ 12 kpc.

With our models we wish to address the following questions:

1. How massive is the dark matter halo in NGC 4649?
2. What is the orbital structure of the stars in NGC 4649?
3. Is the potential derived from X-ray observations accurate enough to determine dark matter mass fractions and the orbital structure in the halo of massive elliptical galaxies?

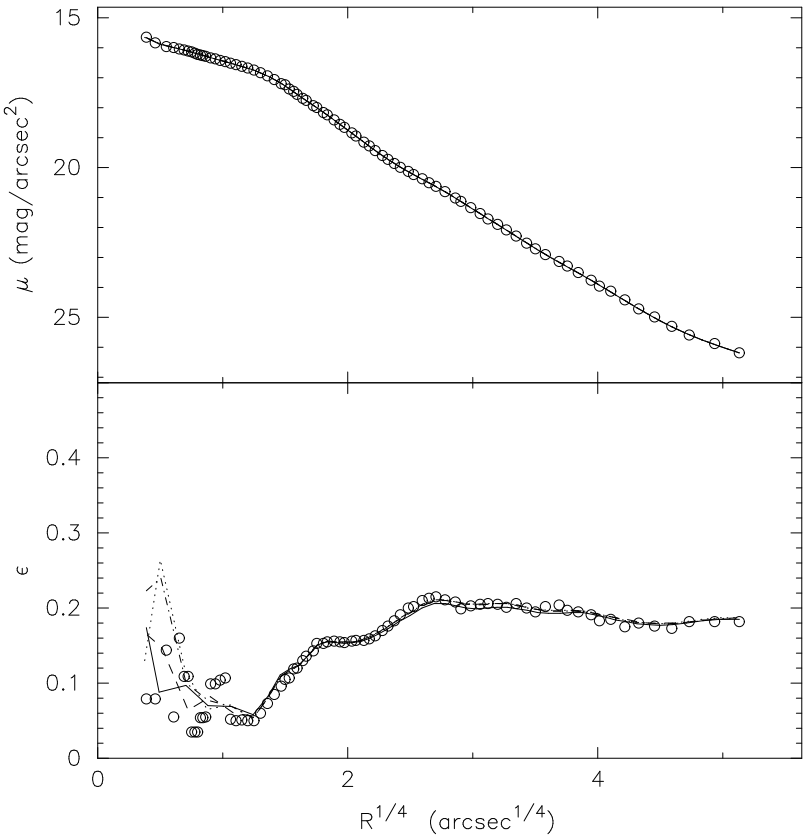

Figure 35: Projected light distribution in NGC 4649: The black circles in the top panel show the measured V-band surface-brightness profile and the lines show the reprojected surface-brightness profiles from the axisymmetric deprojections. The black circles in the bottom panel shows the measured ellipticity profile and the lines show the ellipticity profiles of the reprojected light distributions from the axisymmetric deprojections. We carry out deprojections assuming inclinations of 45° (solid), 60° (dashed) 75° (dotted) and 90° (dash-dotted).

4. Are the dark matter mass and orbital structure in the halo derived from PNe consistent with that derived from GCs?

We assume that NGC 4649 is at a distance of 16.83 Mpc (Tonry et al., 2001) and therefore $1'' = 82$ pc. We also assume an effective radius of 10.5 kpc (Kormendy et al., 2009).

In Sections 5.2 and 5.3, we describe the photometric and kinematics constraints we use for the projected distribution function of the stars. In Section 5.4, we describe the dynamical models we create with NMAGIC and discuss the implications of our results in Section 5.5. We end with our conclusions in Section 5.6.

5.2 CONSTRAINTS ON THE DISTRIBUTION OF STARS

5.2.1 *Photometric data*

We use the V-band photometry of Kormendy et al. (2009) that combines new measurements with published profiles, and extends out to 693″ along the major axis. Figure 35 shows the measured surface-brightness and ellipticity profiles. The surface-brightness profile has a central core with a shallow decay ex-

tending to about 4″ and then falls off more steeply outwards. Kormendy et al. (2009) fit a Sérsic profile between 5–488″, finding a Sérsic index, $n = 5.36$. The ellipticity of the isophotes is around 0.1 in the central 2.5″ but then increases to about 0.2 in the outer parts. The average position angle (measured from North towards East in the sky) of the major axis from the profile in Kormendy et al. (2009) is $102^\circ \pm 6^\circ$, consistent with the value of 105° adopted by Pinkney et al. (2003) for the kinematic data (see Section 5.3.1). Therefore we also adopt a value of 105° for the major axis.

5.2.2 *3-D density distribution of the stars*

To obtain the intrinsic distribution of the stars we assume that they form an oblate, axisymmetric system. We use the code of Magorrian (1999) that finds a smooth axisymmetric density distribution consistent with the surface-brightness distribution, for some assumed inclination angle. It chooses the solution that maximises a penalised likelihood, ensuring a smooth 3-D luminosity density.

We carry out axisymmetric deprojections for inclinations of $i = 45^\circ$, $i = 60^\circ$, $i = 75^\circ$ and $i = 90^\circ$. The maximum inclination angle of $i = 45^\circ$ is calculated using the relation between apparent flattening, q, intrinsic flattening, ξ, and inclination, i[1]:

$$q^2 = \cos^2 i + \xi^2 \sin^2 i \tag{5.1}$$

The maximum apparent flattening from the isophotal analysis is 0.79 and if we assume a maximum intrinsic flattening of 0.5 then the most face-on inclination allowed is 45°.

Figure 35 shows the reprojection of the output deprojected profiles compared with the original input surface-brightness and ellipticity profiles. They fit the measured profiles very well except in the central arcsec. Here the ellipticity profile is not so well defined, because the isophotes are close to circular as a result of seeing.

5.3 CONSTRAINTS ON THE DISTRIBUTION OF STELLAR VELOCITIES

As kinematic constraints, we combine long-slit kinematics probing the central region and planetary nebula (PN) LOS velocities that probe the outer regions of NGC 4649. Figure 36 illustrates the spatial coverage of the kinematic data. We assume that the x-axis increases along East and that the y-axis increases along North, and then we rotate the coordinate system to align the x-axis with the major axis and the y-axis with the minor axis.

1 $i = 0^\circ$ corresponds to a face-on system, and $i = 90^\circ$ corresponds to an edge-on system.

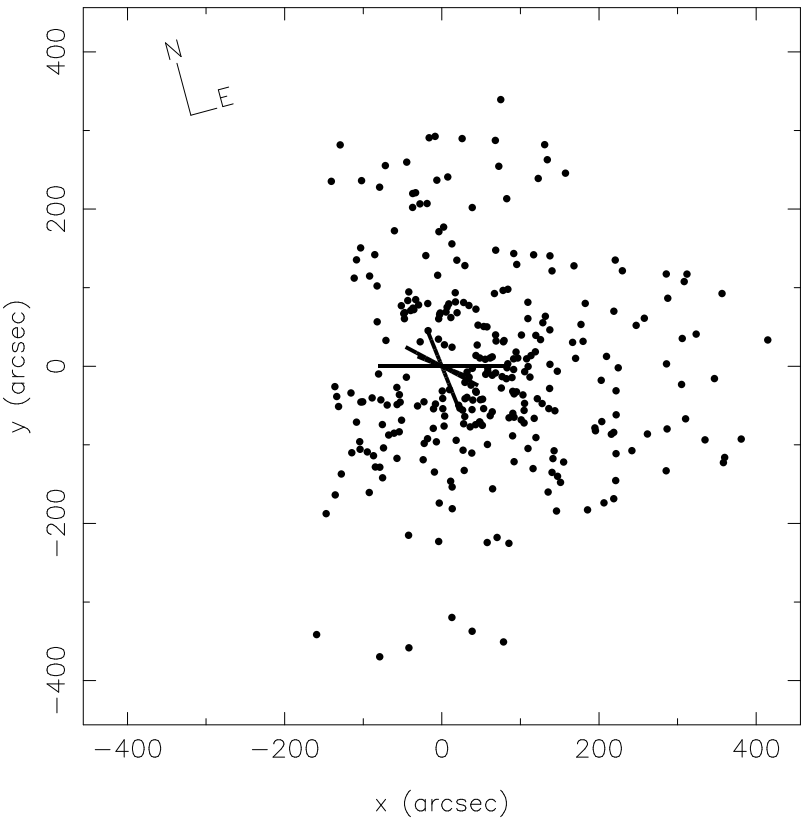

Figure 36: Kinematic constraints for NGC 4649: The filled, black circles show the positions of the PNe and the black lines show the positions of the slits. The x-axis is along the major axis of the galaxy and the y-axis is along the minor axis. Directions of North and East are shown in the top-left corner.

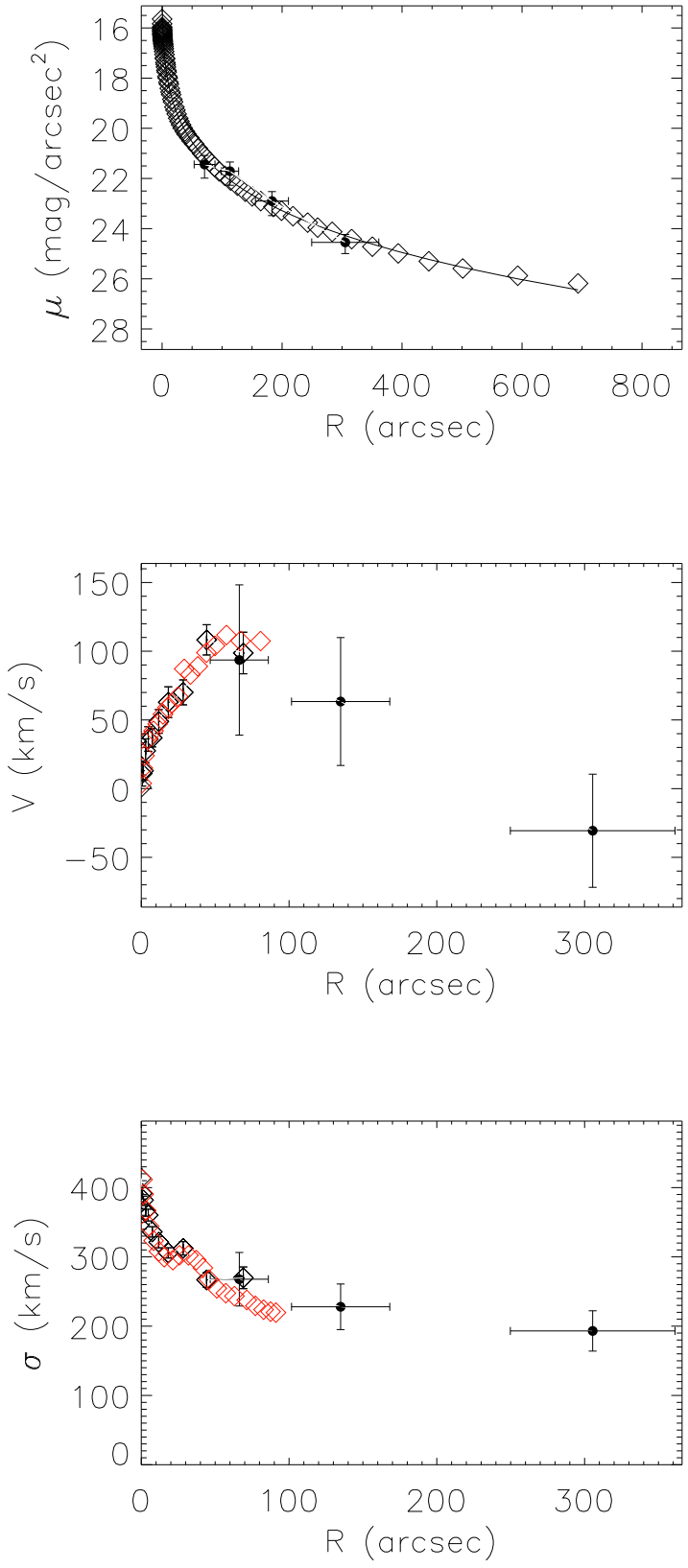

Figure 37: Comparison of PN data against stellar surface-brightness and long-slit data, along the major axis: (a) Black diamonds show the surface-brightness profile measured from the photometry and the black circles show the scaled number density from PNe along with Poissonian errors. The black diamonds in (b) and (c) show the mean velocity and velocity dispersion profiles respectively, measured from the long slits, and the black circles show the mean velocity and velocity dispersion profiles measured from the PNe. Red diamonds show long-slit kinematic data adapted from De Bruyne et al. (2001).

5.3.1 *Long-slit kinematics*

We use the long-slit absorption-line kinematics of Pinkney et al. (2003), obtained from STIS/HST measurements and ground-based spectroscopic measurements on the 2.4m MDM telescope. They were measured along position angles of 105° (the major axis), 127°, 133° and 173° measured from North towards East in the sky, and extending to 69″ (5.6 kpc), 28″ (2.3 kpc), 44″ (3.6 kpc) and 44″ (3.6 kpc) respectively. The location and orientation of these slits are shown in Figure 36. Pinkney et al. (2003) derive line-of-sight (LOS) mean velocity, velocity dispersion and the higher-order Gauss-Hermite moments h_3 and h_4. Figures 37(b) and (c) show the mean velocity and velocity dispersion profiles measured by the long-slit data along the major axis. The mean velocity increases from zero at the centre to about 110 km/s at $\sim 45''$ and then decreases to about 95 km/s at $\sim 70''$. The velocity dispersion decreases from about 410 km/s at the centre to about 270 km/s at $\sim 70''$. For comparison we have overplotted long-slit kinematic data along the major axis, averaged over both sides of the galaxy from De Bruyne et al. (2001). The agreement is very good.

5.3.2 *Planetary nebulae*

To enable us to probe the mass and orbital structure in the halo of NGC 4649 we use the LOS velocities derived from observations of PNe, using FORS2 on the VLT and FOCAS on Subaru. The observations and calculation of the velocities are described in a companion paper (Teodorescu et al. 2010, to be submitted to ApJ). Outliers were removed using a σ-clipping algorithm and contaminants from the neighbouring spiral, NGC 4647, were removed using the technique developed by McNeil et al. (2010). The decontaminated catalogue consists of 298 PNe extending from 27″ (2.2 kpc) to 416″ (33.9 kpc), therefore overlapping with the long-slit kinematic data. The filled, black circles in Figure 36 show the location of the PNe and Figure 37(a) compares the measured major-axis V-band surface brightness with the number density profile of the PNe. The PN number density profile is calculated in a cone of angular width 30° centred on the major axis, and then scaled to match the photometry. We do not consider incompleteness corrections, which are especially important in the central region where the bright stellar component masks PNe (e.g. Coccato et al., 2009). However, the PNe number density and surface-brightness profiles agree well, even at the innermost point, implying that PNe are tracers of the stellar kinematics. Figure 37(b) shows the mean velocity profile of the PNe calculated in a 30°-cone centred on the major axis. In the region of overlap with the long-slit kinematics, the mean velocity profiles agree and further out the PNe mean velocity profile decreases outwards to about -20 km/s at $\sim 310''$. The large errors bars associated

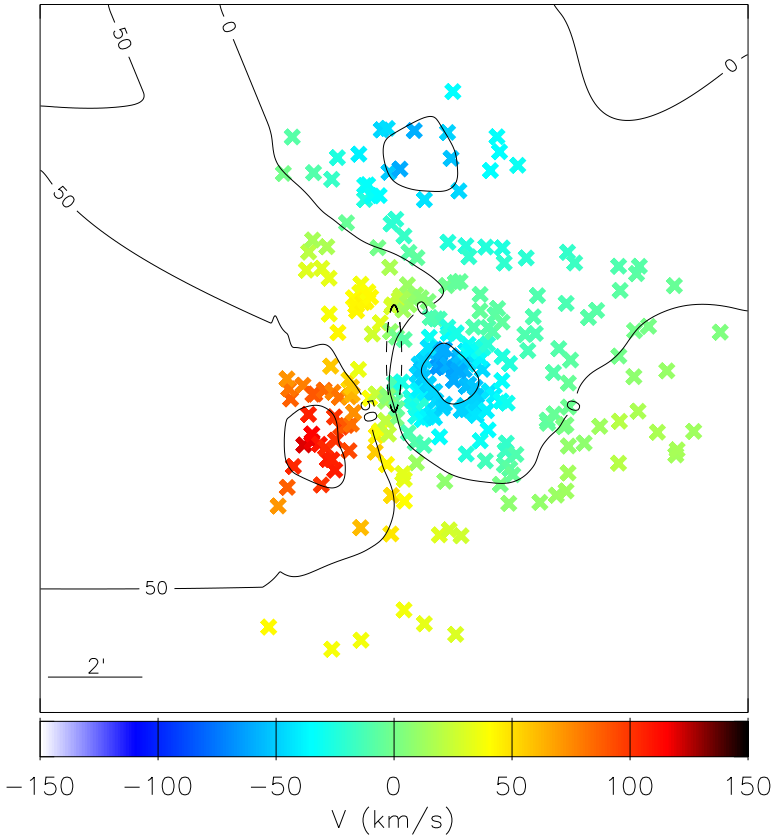

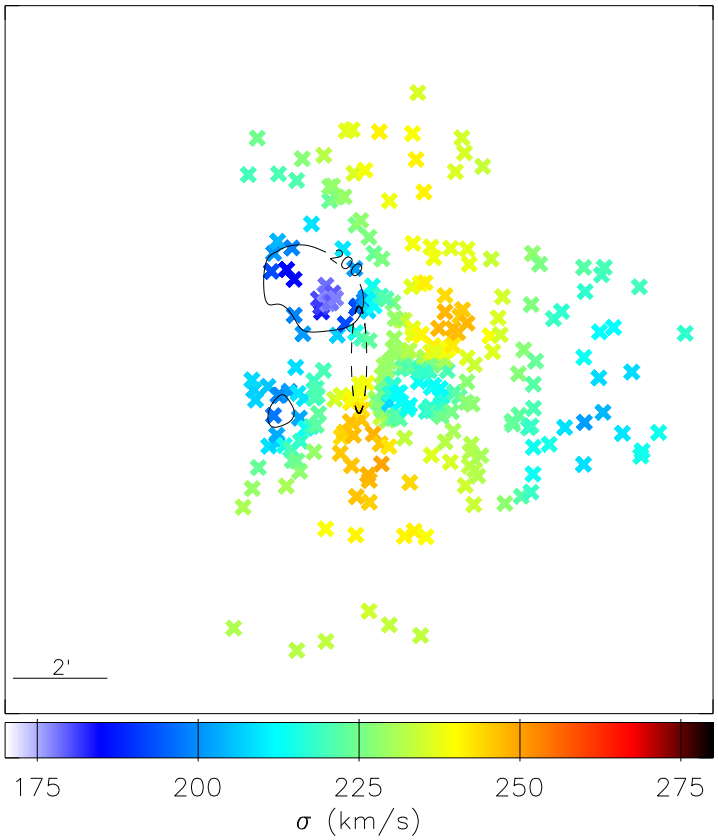

Figure 38: Smoothed PN kinematic maps: (a) Mean velocity, (b) velocity dispersion.

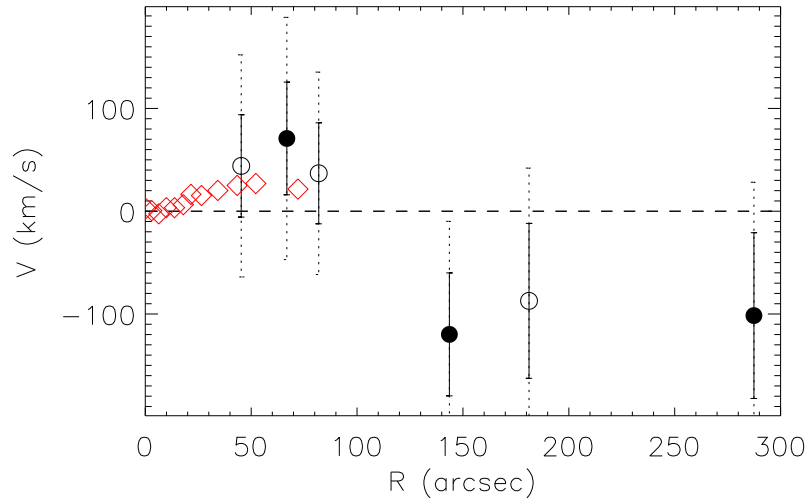

Figure 39: Minor-axis mean velocity profile: The filled, black circles show the mean velocity profile derived along a 30°-cone centred on the minor axis. The open, black circles show the mean velocity profile derived along a pseudo slit of width 60″ centred on the minor axis. The solid black bars denote the 1-σ errors and the dotted black bars denote the 2-σ errors. Red diamonds show long-slit kinematic data adapted from De Bruyne et al. (2001).

with the mean velocity profile derived from PNe also allow for a much shallower decrease in the outer parts and a mean velocity at 310″ consistent with zero. The consistent long-slit and PN major-axis profile show that the rotation of the stars increases to about 100 km/s at 50″ and then starts decreasing outwards. Figure 37(c) shows the velocity dispersion profile of the PNe in a 30°-cone centred on the major axis. The profile agrees with that of the long-slit kinematics from both Pinkney et al. (2003) and De Bruyne et al. (2001) in the region of overlap and then continues to fall less steeply to a value of about 200 km/s at $\sim$ 310″.

Figures 38(a) and (b) show smoothed mean velocity and velocity dispersion maps for the region of NGC 4649 covered by the PNe, created by the PNpack suite of IDL routines from Coccato et al. (2009). Rotation approximately about the minor axis is seen clearly in (a). There is also a group of PNe in the top of the field that imply that there may also be some rotation about the major axis, a signature of triaxiality. To investigate the strength of this signature, we generate 100 pseudo sets of PN LOS velocities at the same positions as the original data, assuming that the LOSVD at each point in space is defined by the mean velocity and velocity dispersion of the smoothed fields generated from the original data. For each of the pseudo data sets, we create new smoothed mean velocity and velocity dispersion maps and then extract mean velocity profiles along a pseudo slit of width 60″ and a cone of angular width 30°, centred on the minor axis. Figure 39 shows the resulting minor-axis mean velocity profiles in both cases. The profile along the pseudo slit, is almost consistent with zero within 1-σ errors and both profiles are consistent with

zero within 2-σ errors. The long-slit kinematics of De Bruyne et al. (2001) also show some rotation along the minor axis at about 20 km/s between 50–80″. We do not plot their last point of $\sim$ 90 km/s at the last radius of $\sim$ 95″, as it appears unphysically higher than the rest of the profile. It would however still be in agreement with the PN minor-axis mean velocity profile and is much less than the measured velocity dispersion. Therefore there is some evidence for triaxiality but it is weak, making it difficult to constrain the viewing angles of the system. Therefore we will proceed with models assuming an oblate, axisymmetric stellar distribution.

5.4 DYNAMICAL MODELS

Here we describe how we set up the initial model and how we prepare the photometric and kinematic target observables for creating dynamical models with the N-body code NMAGIC. We then describe how we obtain models first fitting to the light and long-slit constraints, and then models fitting light, long-slit and planetary nebula (PN) constraints.

5.4.1 *NMAGIC*

NMAGIC is an N-body made-to-measure code described in de Lorenzi et al. (2007) that has been successfully applied to the intermediate-luminosity elliptical galaxies NGC 4697 (de Lorenzi et al., 2008) and NGC 3379 (de Lorenzi et al., 2009). It finds the best intrinsic distribution of stars and their velocities that projects to fit the photometric and kinematic data. The code builds on the particle-based made-to-measure method of Syer & Tremaine (1996) by accounting for observational errors, therefore allowing for an assessment of how well the model fits the target data. There have also been recent implementations of this method by Dehnen (2009) and Long & Mao (2010).

NMAGIC starts with some initial particle model, where each particle has 3-D spatial coordinates, 3-D velocity coordinates and a weight. The particles are advanced according to the gravitational force to sample their orbits and the weights of the particles are adjusted simultaneously according to the force-of-change (FOC) equation, given in Equation (10) of de Lorenzi et al. (2007) and Equation (22) of de Lorenzi et al. (2008). This equation maximises the merit function, F, which is a sum over the weight entropy of the particle system, χ^2 terms measuring the goodness-of-fit to the density and long-slit target observables, and a likelihood term, measuring the goodness-of-fit to the PN target observables. The entropy term ensures that the intrinsic distributions are smooth.

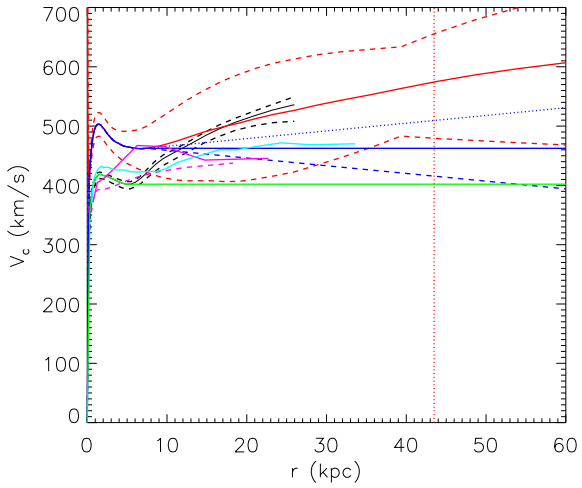

Figure 40: Circular velocity curves of NGC 4649: The solid ($VC1$) and dashed black lines show the best-fit circular velocity curve and associated 95% confidence range from Chapter 2. The solid ($VC2$) and dashed red lines show the best-fit circular velocity curve and associated 68% confidence range from Shen & Gebhardt (2010). The vertical red dotted line shows the maximum projected radius of the kinematic constraints. The blue lines show the circular velocity curves based on that from Shen & Gebhardt (2010) but with the outer slope reduced to 0.106 ($VC3$, dotted), 0.000 ($VC4$, solid) and -0.106 ($VC5$, dashed). The green line shows the circular velocity curve based on that from Chapter 2 but with the outer slope reduced to 0.000 ($VC6$). For comparison, the circular velocity curves obtained by Humphrey et al. (2006) (solid, pink), Humphrey et al. (2008) (dashed, pink), and Nagino & Matsushita (2009) (cyan) are overplotted.

5.4.1.1 *The gravitational force*

The stellar contribution to the gravitational force acting on the stars can be calculated directly from the particles via the Poisson equation. A dark matter halo can then be added as an additional component in the force, as was done for NGC 4697 and NGC 3379. In this work we treat the whole gravitational force as an external force acting on the system, and therefore it can take any form. In the first instance we consider the circular velocity curves derived for NGC 4649 in Chapter 2 ($VC1$) using X-ray observations and Shen & Gebhardt (2010) ($VC2$) using optical observations and dynamical models. These two mass distributions only differ in the central $\sim$ 12 kpc and are shown in Figure 40. The X-ray observations give information on the temperature and density profiles of the hot gas in massive elliptical galaxies. If the hot gas is approximately spherical and in hydrostatic equilibrium, then the temperature and density profiles are related to the circular velocity curve by:

$$V_c^2 = -\frac{k_b T}{\mu m_p} \frac{\mathrm{d} \ln P}{\mathrm{d} \ln r} \tag{5.2}$$

where T is the temperature of the gas and r is the 3-D radius from the centre of the galaxy. $\mu = 0.61$ is the average gas particle mass in terms of the proton mass, m_p. This value of μ corresponds to a helium number density of 7.92×10^{-2} and 0.5 solar abundance of heavier elements. We assume that the gas is ideal and therefore the gas pressure $P = nk_B T$, where n is the particle number density of the gas. In Chapter 2 we apply hydrostatic equilibrium using a new non-parametric Bayesian approach to density and temperature profiles of the hot gas derived from Chandra and XMM-Newton observations (Churazov et al., 2010).

The best-fit mass profile of Shen & Gebhardt (2010) was obtained from axisymmetric Schwarzschild models assuming a stellar density profile from Kormendy et al. (2009) and fitting to long-slit kinematic constraints from Pinkney et al. (2003) and GC LOS velocities from Hwang et al. (2008).

In both cases we assume that the gravitational force is spherically symmetric. Therefore as the stars are assumed to be oblate axisymmetric, the dark matter halo must be prolate in the centre where the stars dominate, and almost spherical in the outer parts where the dark matter dominates.

5.4.1.2 *The initial particle model*

We set up an initial model of 750000 particles extending to $\sim 2500''$. We assume a density distribution of the particles given by a spherical deprojection of the circularly-averaged surface-brightness profile. We define the intrinsic stellar velocity distribution using the circularity functions of Gerhard (1991), resulting in an anisotropy profile ($\beta = 1 - \sigma_\theta^2/\sigma_r^2$) that is isotropic in the centre but moderately radial ($\beta \sim 0.5$) in the outer parts. This choice reflects the results of numerical simulations by Abadi et al.

Table 8: Best-fit NMAGIC models for NGC 4649 assuming different inclinations in the X-ray ($VC1$, left in columns (2)–(5)) and dynamical ($VC2$, right in columns (2)–(5)) potentials : (1) Inclination assumed for model, (2) χ^2 per A_{lm} target observable, (3) χ^2 per long-slit target observable, (4) χ^2 per target observable, and (5) the merit function.

i (°)	χ^2_{alms}	$\chi^2_{\text{long-slit}}$	χ^2	$-F$
(1)	(2)	(3)	(4)	(5)
45	0.468, 0.260	0.632, 0.521	0.534, 0.366	1374.3,1108.0
60	0.179, 0.210	0.537, 0.469	0.324, 0.315	746.4,713.0,
75	0.141, 0.187	0.542, 0.477	0.304, 0.304	644.6,641.6
90	0.220, 0.196	0.655, 0.518	0.396, 0.326	761.5,661.5

(2006) and Oñorbe et al. (2007). We then solve for the energy part of the distribution function assuming a potential given by $VC1$. The particles' coordinates and velocities are chosen according to the complete distribution function after Debattista & Sellwood (2000) and they are assigned equal weights of $w_i = 1/750000$ to produce the initial particle model. As the gravitational field is fixed with time in our models, the orbits of the particles will not change with time. Therefore our initial particle model is conceptually very similar to the orbit libraries used as initial conditions in Schwarzschild models.

5.4.1.3 *Preparation of stellar density target observables*

We represent the 3-D luminosity density profiles obtained for each inclination from Magorrian's deprojection code in terms of A_{lm} coefficients (de Lorenzi et al., 2007) between 4″ and 2450″. 4″ is the innermost radius of the X-ray circular velocity curve ($VC1$) and 2450″ is the radius at which the density of the initial particle model starts falling off from the deprojected density profile. As the stellar distribution is assumed to be axisymmetric we set higher moments that describe non-axisymmetry to zero. We calculate the A_{lm}s over a grid of 60 radii. Poissonian errors are assumed on the radial mass profile and errors are determined for the higher-order mass moments using Monte-Carlo simulations in which particle realisations of the density field of the target model are generated.

5.4.1.4 *Preparation of kinematic target observables*

As we are assuming that the stellar distribution in NGC 4649 is an oblate, axisymmetric system rotating about its minor axis, for every mass element at (x, y, v), we can assume that there is also a mass element at $(-x, -y, -v)$ and a mass element at $(-x, y, -v)$. Therefore we can add three more long slits at position angles of $105° - 68° = 37°$, $105° - 28° = 77°$ and $105° - 22° = 83°$, which are spatial reflections around the x-axis of the long slits positioned at 173°, 133° and 127°. The PNe are increased 4-fold

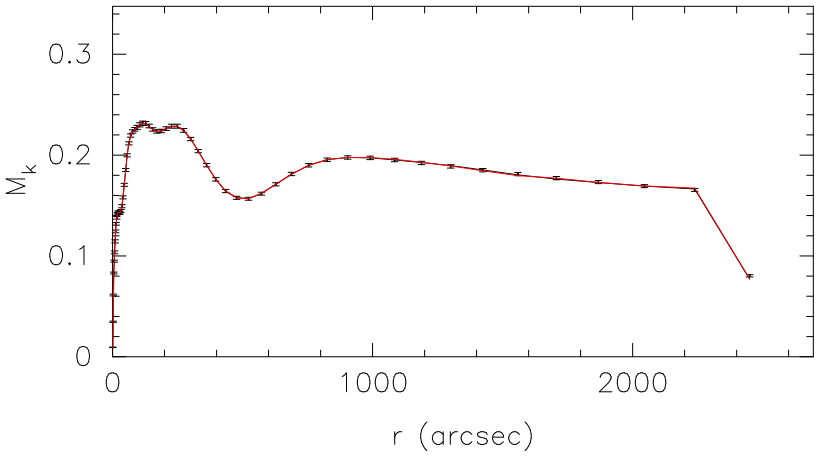

Figure 41: Fit to the first moment of the A_{lm}s or differential stellar mass distribution for an inclination of 75° in the circular velocity curves $VC1$ (black) and $VC2$ (red).

by imposing the above reflections, resulting in a sample of 1192 PNe. As NMAGIC is a particle-based code, the weight of each particle will be changed more evenly over each orbit with the 4-fold sample compared to the unfolded sample.

For NMAGIC the light in each of the slit cells needs to be calculated, as the light-weighted kinematics are fit rather than the kinematics directly. The light in the cells is calculated by integrating the surface-brightness distribution over the dimensions of each of the slit cells (assumed to have a width of 5″) using a Monte-Carlo integration scheme.

To fit the PN LOS velocities, we use the likelihood method used in de Lorenzi et al. (2008, 2009). In this method the particles are binned in radial and angular segments to calculate the LOSVD in each segment. Then the likelihood of each PN belonging to the LOSVD of its segment is maximised for all the PNe. For the binning, we choose 3 radial bins (corrected for an average projected ellipticity of 0.857) and 6 equally-spaced angular bins with the first centred on the major axis.

5.4.1.5 *Logistics of a 'run'*

For each run we fit to the desired data starting with the initial particle model generated above. There is an initial relaxation phase of 2000 steps where the particles are advanced according to the force and their weights are not changed. We then have another 2000 steps during which we temporally smooth the observables and the weights of the particles are still not changed. Then the core phase of the run starts, where the particles are advanced according to the gravitational force and the weights of the particles are changed according to the FOC. Once the fractional change in the total χ^2 falls to less than 1.5×10^{-3} we define the model to have converged. Finally this is followed by a free evolution, where the particles are advanced for a further 20000

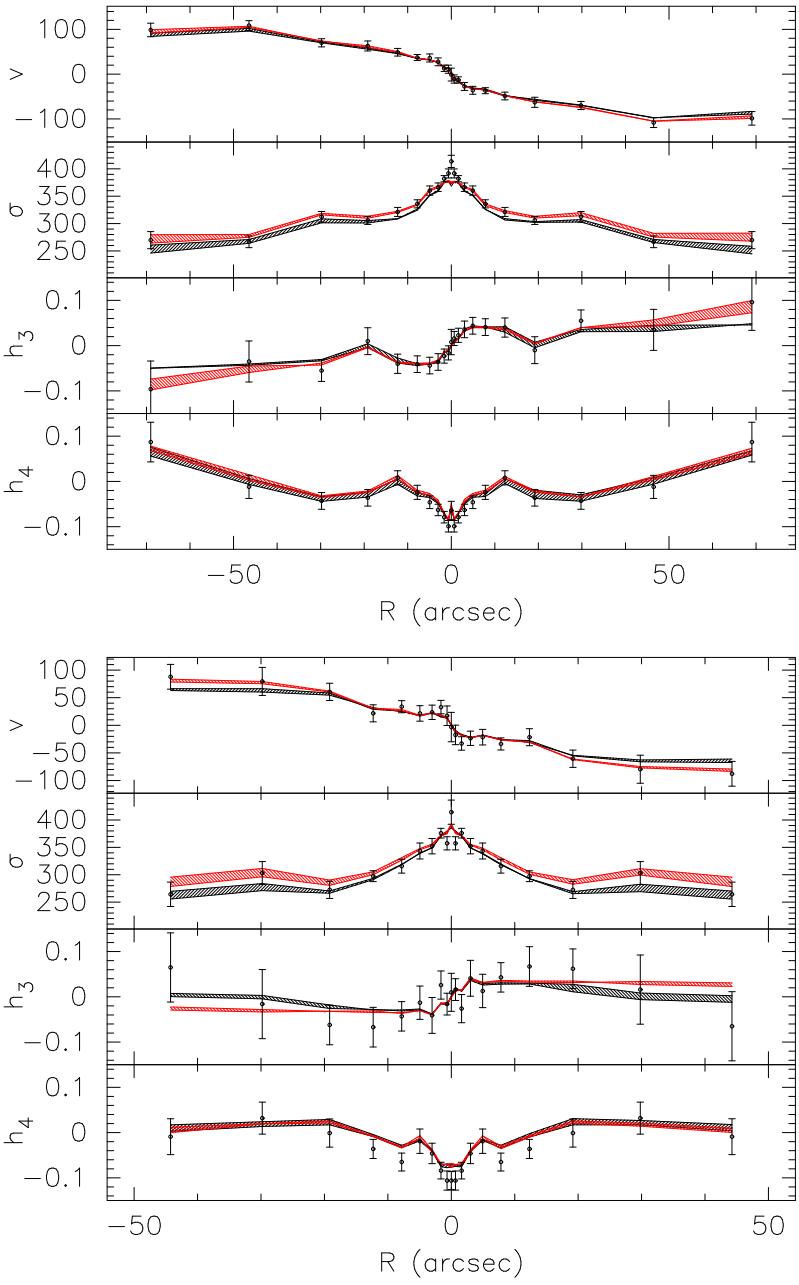

Figure 42: Fits to the long-slit data along the major axis (left panel) and along a slit placed at a position angle of 133° (right panel): From the top down are shown mean velocity, velocity dispersion and the Gauss-Hermite moments h_3 and h_4 for all the inclinations we probe for the slit placed along the major axis. Filled black circles show the data, the black region shows the models for the various inclinations probed in $VC1$, and the red region shows the models probed for the various inclinations in $VC2$.

steps and the weights are no longer changed, to check that the converged model has been sufficiently phase-mixed. The particles are advanced using an adaptive leapfrog scheme.

In the FOC, the respective contributions of the A_{lm}s, long-slit kinematic and PNe kinematic terms can be very different. If the errors are very small as for the A_{lm}s, then they have a large contribution to the FOC. The errors on the PNe are much larger however, and therefore the contributions of the PN data to the FOC are smaller. Therefore changes made to the weights of the particles by the PN data can be erased by changes made according to the other data. For this reason, we amplify the contributions of the long-slit data by 2 and the PN data by a factor 20, so that the orbital structure we derive for the stars is really a true reflection of all the information we have.

5.4.2 *Models fitting density and long-slit kinematic constraints only*

First we would like to understand whether the observational constraints are able to differentiate between the dynamical mass model of Shen & Gebhardt (2010) ($VC2$) and the X-ray mass profiles in the literature, which are lower in the central ~ 12 kpc. For the X-ray mass profile, we choose that derived in Chapter 2 ($VC1$), which is very similar to that of Shen & Gebhardt (2010) in the outer parts. As the potentials only differ in the central 12 kpc, and the PNe kinematic constraints are much weaker than the density and long-slit kinematic constraints, we will not include the PNe for these models. This saves considerable computational time because the PNe are further out and therefore the particles need to be integrated for longer there. Additionally the likelihood method is itself computationally expensive.

We carry out NMAGIC models assuming inclinations of 45°, 60°, 75° and 90° for the stellar distribution, for which we also carried out the deprojections of the photometry. Table 8 shows the χ^2 per data point for the density observables, the long-slit kinematics, all the observables, and the merit function F of the final models in each inclination and potential. NMAGIC fits to the light-weighted kinematic observables as well as the light in each cell, and therefore the long-slit χ^2 is calculated as a sum over these variables.

We find that both potentials prefer an inclination of 75° of the stellar system, and in this inclination, neither potential is preferred by the combination of the photometric and long-slit constraints.

5.4.2.1 *Fits to the observables*

Figure 41 shows the fits in both potentials to the first moment of the A_{lm}s or differential stellar mass distribution for the most favoured inclination of 75°, in potentials $VC1$ and $VC2$. The fits are almost indistinguishable from each other, and fit the density constraints very well. Figure 42 shows the fits to the v, σ, h_3

Table 9: Systematic differences between model and data for v, σ, h_3 and h_4, averaged over each of the first four slits for radii outside 4′, and then average over all the slits.

Potential	Slit PA (°)	v	σ	h_3	h_4
Xray	105	0.131	-0.196	-0.013	0.032
($VC1$)	127	-0.005	-0.048	-0.036	-0.179
	133	0.110	-0.015	-0.014	0.165
	173	0.041	-0.170	0.033	-0.003
	All	0.073	-0.111	-0.007	0.009
Dynamical	105	0.041	0.113	-0.012	0.149
($VC2$)	127	-0.043	0.086	-0.013	-0.141
	133	-0.032	0.228	0.018	0.188
	173	0.038	0.128	0.031	0.067
	All	0.019	0.139	0.006	0.073

and h_4 moments along the major-axis slit and the slit placed along 133°, for both potentials and all inclinations. In general the fits are very similar but there are some systematic differences. The models in $VC1$ produce mean velocity profiles with a lower magnitude ($\sim$ 5–20 km/s), a lower velocity dispersion ($\sim$ 10–30 km/s), an h_3 moment with a lower magnitude (0.01–0.02) and an h_4 moment that is very marginally lower on average. These differences are generally a small fraction of the error bars.

All the models find a χ^2 per data point less than 1. Then if the number of degrees of freedom is approximately equal to the number of data points, then we can be satisfied that we are fitting the data well, and even over-fitting. In reality however, the number of degrees of freedom is difficult to estimate because it is equal to the number of constraints subtracted by the number of parameters. The number of parameters is equal to the number of model parameters (e.g. halo, M/L, inclination) plus the number weights that we are fitting, which is the number of particles. The number of constraints is equal to the number of data points plus the number of constraints introduced by the entropy function, which is difficult to quantify.

We now attempt a $\Delta\chi^2$ analysis as done for example in Shen & Gebhardt (2010). If we say each of our models could be characterised by four parameters (inclination, mass-to-light ratio and two parameters for the dark matter halo), then $\Delta\chi^2$ for 1-σ is 4.7, or 0.003 per data point for 1615 observables (960 A_{lm} and 655 long-slit target observables). Therefore in the absence of systematic errors, any models more than 0.003 per data point greater than the minimum χ^2 per data point can be ruled out because we know they must definitely be outside the 1-σ confidence range around the true best model. Table 8 shows that the density observables most prefer an inclination of 75° but the long-slit observables most prefer an inclination of 60°, in both potentials. Considering the data altogether, both potentials prefer an inclina-

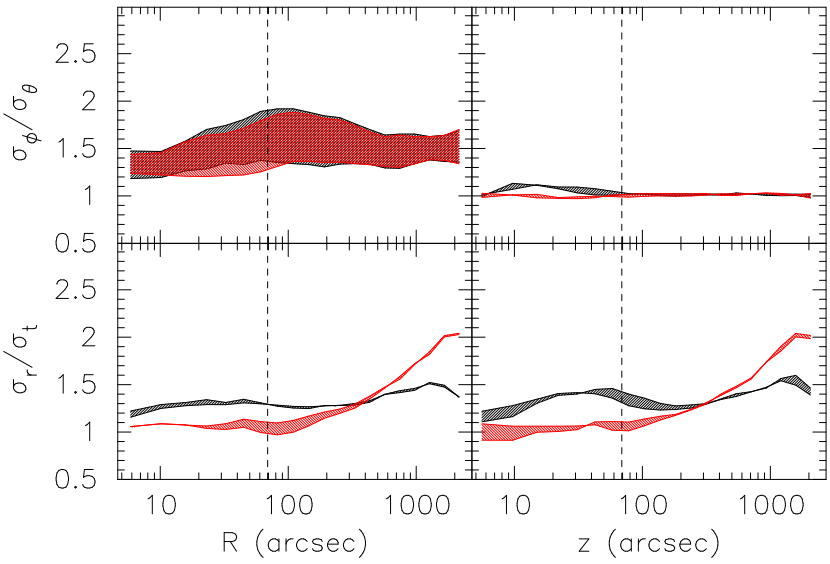

Figure 43: Intrinsic kinematics: The left set of panels show the ratio of the radial velocity dispersion to the tangential velocity dispersion (bottom), and the ratio of the azimuthal velocity dispersion to the meridional velocity dispersion (top), along R. The right set of panels show the same along z. The black region corresponds to the models carried out for various inclinations in $VC1$ and the red region corresponds to the models carried out for various inclinations in $VC2$, fitting photometric and long-slit constraints only. The dashed black line shows the radial extent of the kinematic constraints.

tion of 75°. Generally the dynamical potential is preferred over the X-ray potential except for in the most favoured inclination, where $VC1$ and $VC2$ are equally preferred. As the remaining models achieve a χ^2 of more than 0.003 per data point away from the minimum χ^2 of 0.304 per data point, we would rule them out with 1-σ confidence using the $\Delta\chi^2$ approach.

We also quantify the systematic difference, ΔS, between the model and data in both potentials:

$$\Delta S = \frac{1}{n}\sum_{j=1}^{j=n}\frac{K_{M,j} - K_{O,j}}{\epsilon_{K,j}} \tag{5.3}$$

where K represents the observable v, σ, h_3 or h_4, M is the model value, O is the observed value and n is the number of observables. ΔS is calculated for each moment averaged over each of the first four slits (the remaining three slits are only reflections of the first three) for radii outside 4", and then averaged over all the slits. Only the results in the most favoured inclination of 75° are shown in Table 9. In $VC1$, the magnitude of the model mean velocity is a little higher, while the velocity dispersion is systematically a little lower than the observations. The systematic differences in the h_3 and h_4 moments are smaller. In $VC2$, the systematic differences are biggest also in the velocity dispersion, which is higher than the observations on average, and in the h_4, which are also systematically higher. Systematic differences between the model and the data seem comparable in both potentials and are higher than $\sqrt{\Delta\chi^2 = 0.003} = 0.055$ per data point, even though we have

Table 10: Best-fit NMAGIC models for NGC 4649 for an inclination of 75° in a range of circular velocity curves: (1) Circular velocity curve, (2) χ^2 per A_{lm} target observable, (3) χ^2 per long-slit target observable, (4) χ^2 per target observable, (5) log-likelihood of PNe belonging to particle LOSVDs, and (6) the merit function.

V_c	χ^2_{alms}	$\chi^2_{\text{long-slit}}$	χ^2	$-LH$	$-F$
(1)	(2)	(3)	(4)	(5)	(6)
$VC2$	0.268	0.510	0.366	3107.0	4232.3
$VC3$	0.201	0.496	0.321	3097.1	4087.1
$VC4$	0.196	0.489	0.315	3087.0	3988.7
$VC5$	0.236	0.480	0.335	3079.7	4006.0
$VC6$	0.213	0.818	0.458	3067.2	4091.3

averaged over positive and negative systematic deviations. This implies that perhaps neither mass model is exactly correct and that the true mass distribution lies somewhere in between, or that systematic effects (e.g. triaxiality) play a role. This also means that the $\Delta\chi^2$ approach should be used with caution as it assumes that the model hypotheses are correct.

5.4.2.2 *The orbital structure*

As we have assumed an oblate, axisymmetric system, we can average the intrinsic kinematics over the azimuthal angle, ϕ. This reduces the spatial coordinates to R in the equatorial plane, which is the major axis of the system, and z in the meridional plane, the minor axis of the system. Figure 43 shows the ratio of radial to tangential velocity dispersions (σ_r/σ_t), and the ratio of azimuthal to meridional velocity dispersions ($\sigma_\phi/\sigma_\theta$) along R and z. The tangential velocity dispersion is defined as $\sigma_t = \sqrt{(\sigma_\theta^2 + \sigma_\phi^2)/2}$. Within the radial extent of the kinematic constraints, there is a bias towards radial orbits in $VC1$ along R and z with $(\sigma_r/\sigma_t)_{max} \sim 1.5$ In the same region the orbital structure in $VC2$ is almost isotropic along R and z. On average the ratio of the radial to tangential velocity dispersions is 1.2–1.3 higher in $VC1$ than in $VC2$ throughout. The two components of tangential velocity dispersions have similar contributions in both potentials along z, and in the equatorial plane the azimuthal dispersions dominate. In both potentials, variation with inclination is greatest in the ratio between the azimuthal and meridional dispersions along R.

5.4.3 *Models fitting density, long-slit kinematic constraints and planetary nebula line-of-sight velocities*

Now we will carry out models including also the PN kinematics, so that we can check whether the PN kinematics are consistent with the halo in the mass determinations of Chapter 2 and Shen

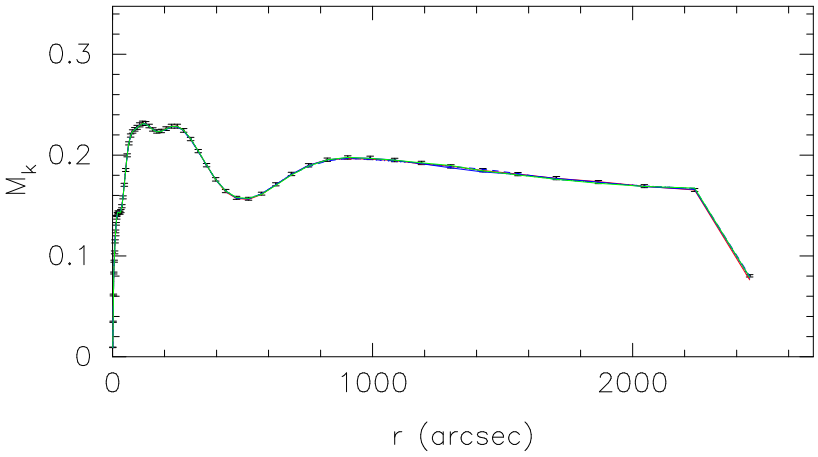

Figure 44: Fit to the first moment of the A_{lm}s or differential stellar mass distribution for an inclination of 75° in potentials $VC2$ (solid, red), $VC3$ (dotted, blue), $VC4$ (solid, blue), $VC5$ (dashed, blue) and $VC6$ (green).

& Gebhardt (2010). As both potentials have almost the same halo we first carry out a model in the potential of Shen & Gebhardt (2010) ($VC2$). We find that the model velocity dispersions are systematically too high and therefore repeat models in a range of potentials with less massive haloes (see Figure 40 and Table 10. Incorporating the PNe, the models prefer a halo with a significantly lower circular velocity of $\sim$ 463 km/s compared to that of Shen & Gebhardt (2010).

5.4.3.1 *Fits to the observables*

Figures 44, 45 and 46 show the fits to the first moment of the A_{lm}s, the fits to the Gauss-Hermite moments along the major axis and the fits to the PN LOS velocities, in $VC2$, for an inclination of 75°. Table 10 shows the statistics of the fits obtained for the new model incorporating the PN data. Even though visually the fits look very much the same in the A_{lm}s and long-slit, the χ^2 values for the fit to the A_{lm}s and long-slit are slightly higher than before, though still much less than 1. This shows that in this potential, by trying to fit the PNe, the fits to the A_{lm}s and long-slit are slightly compromised. Looking at the PN kinematics, it appears that the mean velocity profiles are fit well but the velocity dispersions of the model are systematically higher than that measured by the PNe. This implies that the PNe are not consistent with the outer part of $VC2$, and therefore also $VC1$ (both potentials agree very well outside $\sim$ 12 kpc).

5.4.3.2 *Fits in less massive haloes*

As the PNe dispersions are systematically lower than predicted by the models, we also investigate additional circular velocity curves with less massive haloes (Figure 40). We fit a straight line to $VC2$ outside 91" and obtain a slope of 0.212. We create three additional curves where the outer slopes are 0.106 ($VC3$), 0.0

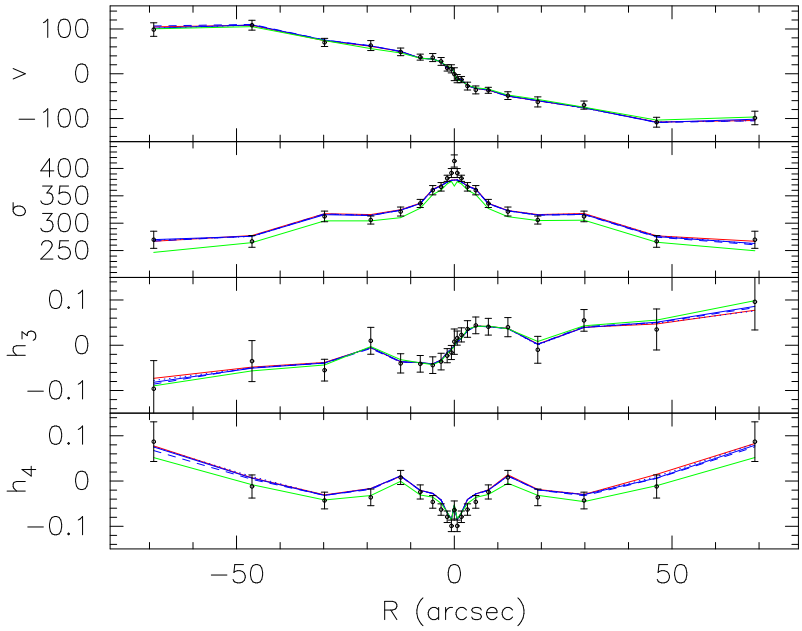

Figure 45: Fits to the long-slit data: From the top down are shown mean velocity, velocity dispersion and the Gauss-Hermite moments h_3 and h_4 for an inclination of 75° and for the slit placed along the major axis. Filled, black circles show the data and the lines show fits in potentials $VC2$ (solid, red), $VC3$ (dotted, blue), $VC4$ (solid, blue), $VC5$ (dashed, blue), and $VC6$ (green).

($VC4$) and -0.106 ($VC5$). Finally we consider a curve that follows $VC1$ until 59″ and then also has an outer slope of 0.0 ($VC6$). The model fits in these potentials are overplotted on Figures 44, 45, 46 and the statistics of the fits are given in Table 10. The χ^2 values show that the A_{lm}s and long-slit data most prefer $VC4$, and the likelihood values show that the PNe most prefer $VC6$. The merit function F is a combination of the χ^2 values, likelihood and entropy, and this is a maximum in the potential $VC4$. Therefore we consider this the best of the potentials tried. The differences between the models in the A_{lm}s and fits to the long-slit kinematics are small except in σ and h_4, which are systematically lower in $VC6$ compared to potentials $VC2$–$VC5$. Figure 46 shows that the PNe velocity dispersions are however very sensitive to the mass in the halo.

5.4.3.3 *The orbital structure*

Figure 47 shows that within $\sim 70''$ the intrinsic velocity dispersions are isotropic to mildly radial along R and z in potentials $VC2$–$VC5$ and moderately radial in $VC6$, consistent with the findings in Section 5.4.2.2. Further out until the radial extent of the PN kinematic constraints, the orbital structure in all potentials becomes moderately radial along R and more isotropic along z. The two components of tangential velocity dispersions have similar contributions in both potentials, and in the equatorial plane the azimuthal dispersions dominate over meridional velocity dispersions.

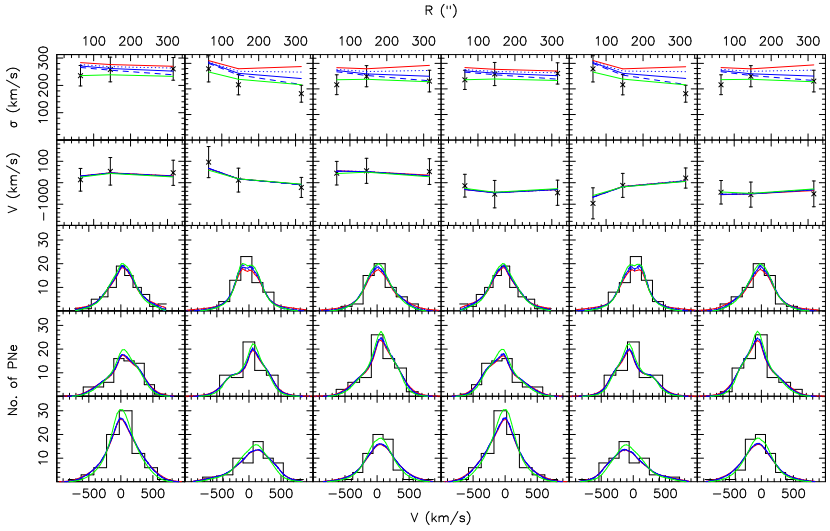

Figure 46: Fits to the PN data for an inclination of 75°. Each of the plots in the bottom three rows shows the LOSVD in segments. Going up are segments at radii of 64″, 145″ and 316″ and going right are angular segments centred on 0° (major axis), 60°, 120°, 180°, 240°, 300°. The kinematics along the latter three segments are reflections of the kinematics along the first three segments because of the oblate, axisymmetry imposed on the observational constraints. The top two sets of panels show the mean velocity and velocity dispersion profiles along the angular segments. The fits are in potentials $VC2$ (solid, red), $VC3$ (dotted, blue), $VC4$ (solid, blue), $VC5$ (dashed, blue), and $VC6$ (green).

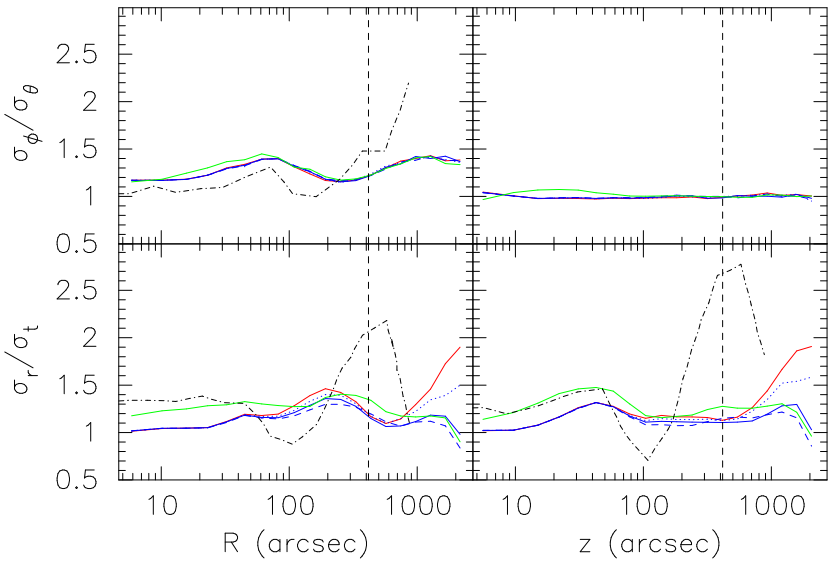

Figure 47: Intrinsic kinematics: The left set of panels show the ratio of the radial velocity dispersion to the tangential velocity dispersion (bottom), and the ratio of the azimuthal velocity dispersion to the meridional velocity dispersion (top), along R. The right set of panels show the same along z. The dash-dotted black line shows the results of Shen & Gebhardt (2010) who fit GC kinematics instead of PN kinematics. The fits are done in potentials $VC2$ (solid, red), $VC3$ (dotted, blue), $VC4$ (solid, blue), $VC5$ (dashed, blue), and $VC6$ (green). The dashed black line shows the radial extent of the kinematic constraints.

5.5 DISCUSSION

Here we discuss what we have learned about the dark matter halo, orbital structure and inclination of the stellar system in NGC 4649. We also discuss whether the PNe and GC systems are dynamically consistent with each other, and whether the X-ray mass distributions can be used to determine dark matter mass fractions and orbital structures in massive elliptical galaxies.

5.5.1 *The dark matter halo of NGC 4649*

Figure 40 shows the circular velocity curves that we have probed in this work, compared to other recent determinations from Chandra observations (Humphrey et al., 2006, 2008) and a combination of Chandra and XMM-Newton observations (Nagino & Matsushita, 2009). Our models fitting only density and long-slit kinematic constraints cannot distinguish between the circular velocity curves in Chapter 2 and Shen & Gebhardt (2010), which differ only in the central $\sim$ 12 kpc. A look at the systematic differences between the models and observations in these potentials suggests that the true circular velocity curve in the central $\sim$ 12 kpc is probably in the range between 425–500 km/s.

Models created incorporating additionally PN kinematics prefer a circular velocity curve that is flat outside $\sim$ 12 kpc at a value of $\sim$ 463 km/s. This is most consistent with the X-ray determination of Nagino & Matsushita (2009), slightly higher than the determinations of Humphrey et al. (2006, 2008), and lower than the determinations in Chapter 2 and Shen & Gebhardt (2010). The sensitivity of the PN velocity dispersions to the circular velocity curve in the halo may be a result of a light density profile that falls off approximately as -3 and an almost flat circular velocity curve. Gerhard (1993) showed that for such systems, the projected velocity dispersions are constant and independent of anisotropy. The constant circular velocity V_c is then related to the constant projected velocity dispersion σ_P by $V_c = \sqrt{3} \times \sigma_P$. The average velocity dispersion of the PNe outside $\sim$ 70″ is $\sim$ 240 km/s, therefore predicting a circular velocity in the halo of 416 km/s. This lies in between the value of 383 km/s of $VC6$, the halo most preferred by just the PNe, and the value of 463 km/s of $VC4$, the halo most preferred considering all the data together.

To estimate the dark matter mass fraction, we first calculate the luminosity enclosed within radius r by integrating over the luminosity density profile obtained from the spherical deprojection of the surface-brightness profile. Then to obtain the mass in stars we multiply this with a stellar population mass-to-light ratio of 7.8 in the V-band (Trager et al., 2000), assuming no variation with radius. Assuming that the mass in gas is negligible, we subtract the mass in stars from the total mass. Figure 48 shows the dark matter mass fractions corresponding to the potentials we have explored and the potentials from the literature shown in

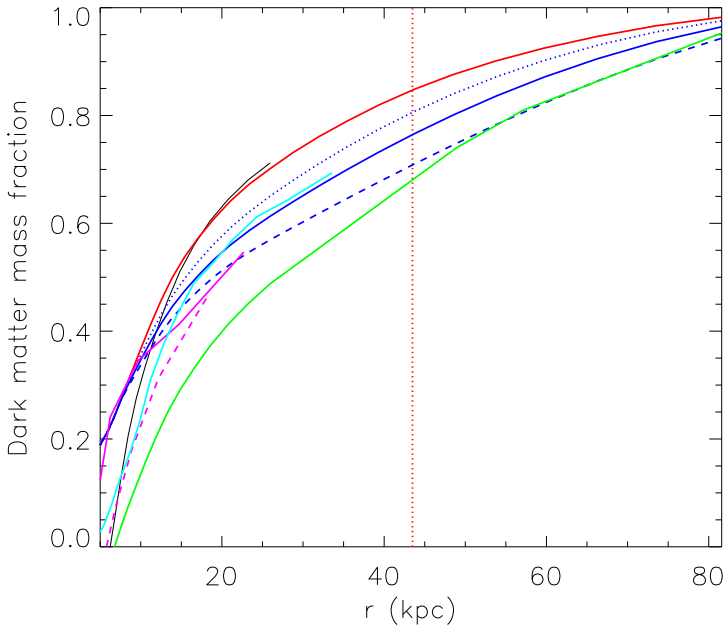

Figure 48: Dark matter mass fraction of NGC 4649 according to potentials $VC1$ (black), $VC2$ (red), $VC3$ (solid, blue), $VC4$ (dotted, blue), $VC5$ (dashed, blue), and $VC6$ (green). For comparison, the dark matter mass fractions calculated from circular velocity curves obtained by Humphrey et al. (2006) (solid, pink), Humphrey et al. (2008) (dashed, pink), and Nagino & Matsushita (2009) (cyan) are also overplotted.

Figure 40. The dark matter mass fraction corresponding to our best potential $VC4$ is $\sim$ 0.35 at about 10 kpc or 1 R_e, 0.5 at about 17 kpc (1.6 R_e) and $\sim$ 0.77 at the radius of the last PN ($\sim$45 kpc $\approx$ 4 R_e). Figure 48 shows that our determination is most similar to that of Nagino & Matsushita (2009) as for the circular velocity curve.

There are also several determinations of dark matter fractions for other elliptical galaxies in the literature. Nagino & Matsushita (2009) analysed Chandra and XMM-Newton observations for a sample of 22 elliptical galaxies and found equality between dark matter and luminous matter at around 3 R_e and a dark matter mass fraction of around 0.66 at $\sim$ 6 R_e. Gerhard et al. (2001) and Thomas et al. (2007) found dark matter mass fractions within 1 R_e of 10–40% and 10–50% respectively, for samples of nearby and Coma cluster elliptical galaxies. Gerhard et al. (2001) found equality between the mass contributions of the dark matter and luminous components at 2–4 R_e, and for the Coma galaxies with sufficiently spatially extended data (generally the less luminous ellipticals), Thomas et al. (2007) found dark matter mass fractions between 65–75% at 4 R_e.

Treu & Koopmans (2004) used a combined lensing and stellar dynamical approach to obtain the dark matter mass fractions of elliptical and lenticular galaxies up to a redshift of 1, and found projected values of 0.15–0.65 within a cylinder of radius 1 R_e. For massive early-type galaxies taken from the SLACS survey,

Auger et al. (2009) and Auger et al. (2010) found that the dark matter fraction within $R_e/2$ ranged between $\sim$ 0.3–0.7 assuming a Chabrier stellar IMF (the Salpeter stellar IMF gives lower dark matter mass fractions that are sometimes negative), with more massive galaxies having higher dark matter mass fractions. Grillo (2010) used simple mass models to estimate a dark matter mass fraction of $0.64^{0.08}_{0.11}$ projected inside a cylinder of radius 1 R_e for a sample of approximately 170000 massive, elliptical galaxies observed in SDSS, from which the SLACS sample is obtained. We estimate the effect of projection on the dark matter mass fraction by assuming an NFW density profile for the dark matter profile, with a virial radius of 300 kpc and a concentration of 10 (typical for elliptical galaxies). The ratio of the dark matter mass within a cylinder of length two virial radii along the LOS and radius R_e, to that within a sphere of radius 1 R_e is about 2. Assuming that the ratio of the stellar mass between the two regions is almost 1, then the dark matter mass fraction calculated within a sphere of radius 1 R_e would be lower, for example 0.47 instead of 0.64.

Oñorbe et al. (2007) analysed the mass and velocity distributions of elliptical-like objects at zero redshift in a set of self-consistent hydrodynamical simulations set in the current cosmological paradigm. They found that the objects are embedded in massive, dark matter haloes with dark matter mass fractions ranging between about 0.3–0.6 at 1 R_e.

To summarise, there is a range in the dark matter mass fractions at 0.5–1 R_e in the literature, and the value we obtain for NGC 4649 is near the middle of this range. Further out, the dark matter mass fractions obtained by Gerhard et al. (2001), Thomas et al. (2007) and Nagino & Matsushita (2009) suggest on average a more diffuse dark matter halo than the one we find for NGC 4649. This may be because their samples include elliptical galaxies at a range of luminosities, while massive elliptical galaxies like NGC 4649 may have more massive dark matter haloes (e.g. Cappellari et al., 2006; Auger et al., 2010).

5.5.2 *Orbital structure in NGC 4649*

The central $\sim$ 70″ of NGC 4649 has an isotropic ($\beta = 1 - \sigma_t^2/\sigma_r^2 \sim 0$) to mildly radial ($\beta \sim 0.4$) orbital structure according to the dynamical potential of Shen & Gebhardt (2010) and the X-ray potential of Chapter 2, $VC1$, between which we are unable to distinguish. If we assume that the true mass distribution in the central $\sim$ 12 kpc lies somewhere between these two, as suggested by the systematic differences between the models and the observations in the two potentials, then we can infer an orbital structure in this region of $\beta \sim 0.2 \pm 0.2$. Using additionally the PN constraints and exploring several potentials, we find that the orbital structure outside $\sim$ 70″ becomes slightly more radial ($\beta \sim 0.5$) along R, but more isotropic along z, with little dependence on the exact halo assumed. Along R, the azimuthal velocity

dispersions are slightly higher than the meridional velocity dispersions throughout, indicating that the stellar system may be flattened by a meridional anisotropy in the velocity dispersion tensor (Dehnen & Gerhard, 1993a,b; Thomas et al., 2009). Thomas et al. (2009) also use axisymmetric toy models to show that flattening by meridional anisotropy maximises the entropy for a given density distribution. Along z, the azimuthal and meridional velocity dispersions are equal, as one would expect for an oblate, axisymmetric system.

There is no general consensus on the orbital structure in the outer parts of elliptical galaxies. Dynamical models fitting outer kinematics of intermediate-luminosity elliptical galaxies have found a moderately radial orbital structure in the halo of NGC 4697 (de Lorenzi et al., 2008). In NGC 3379, de Lorenzi et al. (2009) found that systems with both isotropic and moderately radial orbital structures were consistent with the data, and Napolitano et al. (2009) found moderately radial anisotropy in the halo of NGC 4494. Dynamical models fitting outer kinematics in more massive elliptical galaxies such as NGC 1399 (Schuberth et al., 2010, the GCs used are believed to trace the stellar kinematics in this galaxy) and NGC 4374 (Napolitano et al., 2010) have found mildly radial and isotropic orbital structures in the halo respectively. For the elliptical galaxies in the Coma cluster, which have a range of luminosities, Thomas et al. (2007) found mild radial anisotropy along the major axis and sometimes tangential anisotropy along the minor axis.

From simulations, Abadi et al. (2006) found that the outer haloes of massive ellipticals are strongly radial due to smaller galaxies that have been accreted on to the central object. The analysis of Oñorbe et al. (2007) of elliptical-like objects at zero redshift also found a radial orbital structure for the stars at an almost constant value of $\beta \sim 0.5$ throughout. Thomas et al. (2009) analysed the orbital structure of collisionless disc merger remnants from Naab & Burkert (2003) and found them to be strongly radially anisotropic.

To summarise, dynamical models show that the orbital structure in the halo of massive elliptical galaxies is isotropic to quite radial, but less so than expected from simulations. (Thomas et al., 2009) arrived at a similar conclusion and suggested that this could be due to gas dissipational effects.

5.5.3 *The inclination of NGC 4649*

The surface-brightness and long-slit kinematic constraints in both potentials $VC1$ and $VC2$ prefer an inclination of 75° out of the four inclinations we have probed. As we only explore a coarse grid of inclinations at intervals of 15°, we can attach an error of 7.5° to our best inclination. Thus it appears that even if the X-ray potential may not be completely correct throughout, it may be used to find an approximate value for the inclination of the

system. This appears to be contrary to the work done for example by Krajnović et al. (2005), who found a degeneracy in the determination of the inclination in their construction of axisymmetric models for the elliptical galaxy NGC 2974. However, we have assumed the same spherical total potential in all the inclinations for our first set of models, and only the stellar distribution was axisymmetric and varied according to the inclination. To understand this issue in more depth, a range of mass profiles need to be explored in each inclination to see whether equally good but different mass profiles can be found for each of the inclinations.

5.5.4 *Are the PNe and GCs dynamically consistent with each other?*

The NMAGIC models show that the PN kinematics prefer a less massive halo and a less radial orbital structure than that derived from models using the stellar density profile and GC kinematics in Shen & Gebhardt (2010). However if both the PN and GC systems are in equilibrium, the same halo should be preferred although the orbital structure may be different. To obtain a deeper insight into this discrepancy, we examine the photometric and kinematic constraints assumed for the PNe and GCs in more detail. Figure 49(a) compares the velocity dispersion profile calculated in circular rings from the PNe to those for red, blue, and all GCs calculated by Hwang et al. (2008). The errors bars on the GC kinematics are not shown because they mask all the other points but are approximately twice as big as the errors shown on the PN velocity dispersions. One can see that between 100″ and 200″, the PN velocity dispersions appear to be in agreement with the dispersions measured by the blue GCs (and therefore the total sample because the blue GCs dominate in numbers). The velocity dispersion of the red GCs decreases to almost 150 km/s at ∼210″ and then increases dramatically to about 320 km/s at ∼390″. The last PN velocity dispersion point at ∼350″ calculated in a ring extending from 260–440″ has a value of 203 ± 19 km/s. Averaging all the GCs velocity dispersions in this region gives $\sim 240 \pm 22$ km/s for 61 GCs, which would correspond to the values fit by Shen & Gebhardt (2010). This is only just consistent and therefore it is possible that the PNe and GCs trace different kinematics.

Figure 49(b) compares the surface-brightness distribution of the stars with the scaled surface number densities calculated from the PNe and from Hwang et al. (2008) for all the GCs, the red GCs and the blue GCs. Between 200–450″, the surface densities of the whole GC population follows the stellar surface-brightness distribution well. Further in, the GC density profile is shallower than that of the stars and outside this region the density profile falls off more steeply than the stars, though the associated errors are larger. Therefore the density profile of the GCs appears to be different from that of the stars.

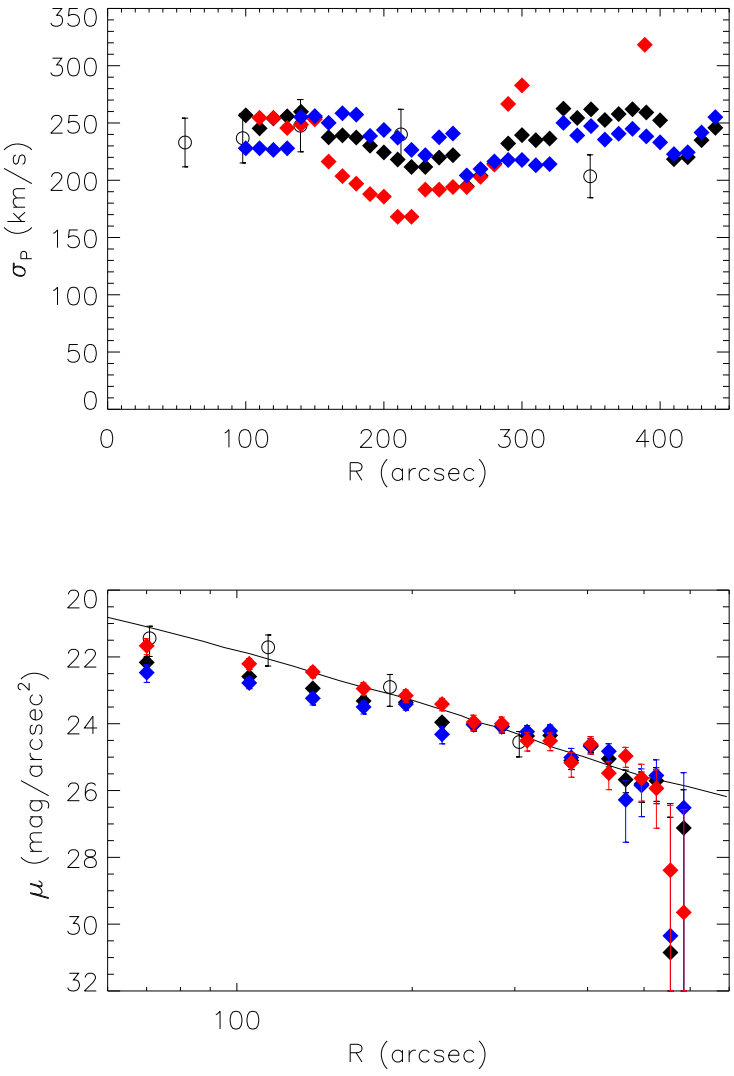

Figure 49: Properties of the GC populations: (a) Velocity dispersion profiles of all GCs (filled, black diamonds), red GCs (filled, red diamonds) and blue GCs (filled, blue diamonds) compared to that measured by the PNe (open, black circles). The errors on the GC velocity dispersions are approximately twice as big as the errors shown on the PN velocity dispersions. (b) Surface number density profiles of all GCs (filled, black diamonds), red GCs (filled, red diamonds) and blue GCs (filled, blue diamonds) compared to the stellar surface-brightness distribution (solid, black line) and the surface number density of PNe (open, black circles).

The GCs could still be in equilibrium however but just form a separate dynamical system in the same potential. This can be quantified using the spherical second-order Jeans equation, relating the second-order moments of the intrinsic velocity distribution to the density profile of the stars, and the potential in which they move (Binney & Tremaine, 1987):

$$\frac{\mathrm{d}}{\mathrm{d}r}(\nu(r)\sigma_r^2(r)) + \frac{2\beta(r)}{r}\nu(r)\sigma_r^2(r) + \nu(r)\frac{V_c^2}{r} = 0 \qquad (5.4)$$

where V_c is the circular velocity curve, σ_r is the intrinsic velocity dispersion of the tracer in the radial direction, ν is the number density of the tracer, and the anisotropy $\beta = 1 - \sigma_t^2/\sigma_r^2$.

This equation shows that as the PNe and GCs are residing in the same halo but have different density profiles and probably different kinematics, for the GCs to be in equilibrium, they must also have a different orbital structure. We can estimate the orbital structure most easily for the case of a power-law density profile, constant anisotropy and constant circular velocity curve. Therefore we fit a power law to the surface-brightness measured by the stars outside 200" and find a best-fit index of $n_{\mathrm{stars}} = -2.2$. For the globular clusters we find $n_{\mathrm{gcs}} = -3.0$ (ignoring the second last point, which seems unphysically low). The power-law indicies of the intrinsic density profiles are then -3.2 and -4.0 respectively. The projected velocity dispersion is ~ 240 km/s outside 200", and we assume a circular velocity of 463 km/s in the halo from our best potential $VC4$. Solving the Jeans equation and the equation relating projected velocity dispersions to intrinsic velocity dispersions, we find $\beta \sim -1$ for the GCs. This is different from the average value of $\beta \sim 0.4$ outside 200" obtained by Shen & Gebhardt (2010), who assume the stellar density profile for the GCs. Our value agrees better with the modestly tangentially biased velocity ellipsoid inferred by Hwang et al. (2008) from spherical Jeans equations using the true GC density profile and the mass distribution from X-rays in Humphrey et al. (2006), which is more consistent with the mass distribution we find from the PNe.

To summarise, we show that the GCs may be in equilibrium in the potential of NGC 4649, but this equilibrium is dynamically distinct from the stars and PNe. Therefore to infer the mass of the dark matter halo, the correct density profile and kinematics need to be used.

5.5.5 *Are the mass distributions from X-rays accurate enough to determine dark matter mass fractions and orbital structures?*

Using the photometric and long-slit kinematic constraints in the dynamical potential from Shen & Gebhardt (2010) and the X-ray potential from Chapter 2, we find that the same inclination of 75° is preferred for the stellar system. In this inclination we are unable to distinguish between them. As the X-ray potentials from Humphrey et al. (2006, 2008) and Nagino & Matsushita (2009)

are similarly low in the central $\sim$ 12 kpc, we would expect a similar result if one of these were used instead. Looking at the systematic differences between the models and observations in the two potentials suggests that the true mass distribution in the central $\sim$ 12 kpc lies somewhere in between. By assuming the X-ray mass distribution, a maximum systematic error of 0.4 in β is made, i.e. one finds a more radial orbital structure.

From our results, we do not see compelling evidence for non-thermal pressure contributions in the gas or multi-phase components in the gas in the central $\sim$ 12 kpc. If they exist, their effects are smaller than would be inferred from the potential of Shen & Gebhardt (2010). This is consistent with the work of Brighenti et al. (2009). They model the hot gas in NGC 4649 using 2-D gas-dynamical computations and find that a turbulent pressure is required in NGC 4649, but it has a much smaller contribution than the thermal pressure.

In the halo, the mass distribution most preferred by incorporating the PN data is less massive than that found in the X-ray analysis of Chapter 2, slightly more massive compared to the halo found in Humphrey et al. (2006, 2008), and similar to that found by Nagino & Matsushita (2009). The dark matter mass fractions derived in the halo depend highly on the mass distribution assumed. The orbital structure in the halo however does not change much between the potentials explored. Still the important question arises: why do the X-ray mass distributions differ in the outer regions? Looking at the temperature and pressure profiles used in Chapter 2, we find that at $\sim$ 25 kpc, the temperature profiles are consistent but the pressure profiles are not. The pressure calculated from the Chandra data is higher than that calculated from the XMM-Newton data, resulting in a flatter pressure profile in the outer parts. Looking at Equation (5.2) shows that this will result in a lower circular velocity curve. In Chapter 2, we use both sets of observations but omit the final points due to uncertainties associated with the deprojection, and therefore do not use the Chandra point at 25 kpc. Humphrey et al. (2006) do use this point however. Therefore it seems that the outer slope of the mass distribution from X-rays can be quite uncertain and possible effects that need to be explored in more detail are deprojection issues, metallicity gradients in the hot gas, and outflows.

To summarise, we believe that using the X-ray mass distribution may lead to a systematically more radial orbital structure in the central region. Models with the X-ray mass profile however are able to derive the inclination of the stellar system and the orbital structure in the halo. Therefore until the uncertainties in the derivation of X-ray mass distributions are better understood, it is best to use them in conjunction with a dynamical mass analysis.

5.6 CONCLUSIONS

We have created dynamical models of the Virgo elliptical galaxy NGC 4649, using the highly flexible made-to-measure N-body code, NMAGIC, and observational constraints given by surface-brightness data, long-slit kinematics, and planetary nebula (PN) velocities. We explore a range of potentials based on X-ray mass distributions in the literature, which are similar in the central regions, but have different outer slopes, and a dynamical potential derived from globular cluster (GC) velocities and a stellar density profile. The GC dynamical model prefers more mass in the central region compared to the X-ray potentials, and is on the top end of the range of X-ray mass profiles further out.

Our models are not able to differentiate between the X-ray and GC mass profiles in the central $\sim$ 12 kpc, and the systematic differences suggest that the true circular velocity curve in the central $\sim$ 12 kpc may lie somewhere between 425–500 km/s. Therefore if non-thermal pressures or multi-temperature components exist in the central region, their contribution is less than previously inferred.

Outside $\sim$ 12 kpc, the observational constraints prefer a circular velocity curve that is flat with a value of $\sim$ 463 km/s, most consistent with the X-ray determination of Nagino & Matsushita (2009). The PN velocity dispersions are very sensitive to the circular velocity curve in the halo, possibly a result of a stellar density profile that falls off approximately as -3 and an almost flat circular velocity curve (Gerhard, 1993). The discrepancy between the halo mass preferred by the PN kinematics and that corresponding to the GC dynamical model shows that if the GCs are in equilibrium, they are dynamically distinct from the stars and PNe. Therefore the correct density profile and kinematics need to be used to infer the mass of the dark matter halo.

We find a dark matter mass fraction of 0.35 at 1 R_e for NGC 4649, which is generally in agreement with the values in the literature. At 4 R_e we obtain a dark matter mass fraction of 0.77, suggesting a more massive halo than typical for the samples analysed by Gerhard et al. (2001), Thomas et al. (2007) and Nagino & Matsushita (2009). This may be because their samples include elliptical galaxies at a range of luminosities, while massive elliptical galaxies like NGC 4649 may have more massive dark matter haloes (e.g. Cappellari et al., 2006; Auger et al., 2010).

We find an orbital structure that is isotropic to mildly radial in the central $\sim$ 12 kpc, depending on the potential assumed. Further out, we find that the orbital structure becomes slightly more radial along R, but more isotropic along z, with little dependence on the exact halo assumed. Along R, the azimuthal velocity dispersions are slightly higher than the meridional velocity dispersions throughout, indicating that the stellar system may be flattened by a meridional anisotropy (Dehnen & Gerhard, 1993a; Thomas et al., 2009). The orbital structure in the halo of

NGC 4649 is less radial than expected from simulations, possibly due to gas dissipational effects (Thomas et al., 2009).

Assuming a mass distribution from X-rays leads to a systematically more radial orbital structure in the central region, but recovers the orbital structure in the halo. The inclination of the stellar system is also recovered. Until the uncertainties in the derivation of X-ray mass distributions are better understood, it is best to use them in conjunction with a dynamical mass analysis.

6

THE DARK MATTER HALO OF THE CENTRAL FORNAX GALAXY, NGC 1399

Preliminary models are created of NGC 1399, the central galaxy in the Fornax cluster, using the dynamical modelling code NMAGIC. We use photometric constraints based on optical surface-brightness images, and kinematic constraints based on long-slit kinematic data and a combined sample of both planetary nebula (PN) and globular cluster (GC) velocities. As the total potential we consider a stellar contribution with a constant mass-to-light ratio and a logarithmic dark matter potential. Our most preferred circular velocity curve agrees very well with the previous less radially extended dynamical analysis in the central $\sim 60''$. Further out however, the discrete tracer velocity dispersions are very sensitive to the halo mass and prefer a more diffuse dark matter halo than previously found, which is also significantly lower than that determined in Chapter 2 from X-ray observations. The dark matter mass fraction in our preferred model is ~ 0.05 at 1 R_e and ~ 0.55 at 5 R_e, lower than that found by the previous dynamical model.

6.1 INTRODUCTION

The outer haloes of elliptical galaxies extend many times beyond the luminous bulge observed in optical images. They are fascinating regions to explore because they are thought to be dark-matter dominated and therefore are invaluable laboratories for testing the current cosmological paradigm.

The current cosmological paradigm (ΛCDM) predicts that all stellar conglomerates are surrounded by dark matter haloes following a universal density profile (Navarro et al., 1996). The inner slope can however change when considering the interplay between dark matter particles and baryons (e.g. Blumenthal et al., 1986; El-Zant et al., 2001; Gnedin et al., 2004; Romano-Díaz et al., 2008) due to effects of dynamical friction, transfer of angular momentum, and baryonic adiabatic contraction.

There are several methods available to us for estimating the dark matter content in elliptical galaxies. Dynamical models of elliptical galaxies provide constraints on the dark matter content and the orbital structure of the stars. They can be constructed by superposing a library of orbits (e.g. Rix et al., 1997; Gebhardt et al., 2003; Thomas et al., 2004; Cappellari et al., 2006; van den Bosch et al., 2008) or distribution functions (e.g. Dejonghe et al., 1996; Gerhard et al., 1998; Kronawitter et al., 2000), or by constructing a system of particles (NMAGIC, de Lorenzi et al., 2008, 2009) such that the projection of the system best reproduces observed surface-brightness and kinematic profiles. Some of the galaxies in the

sample of Mehlert et al. (2000) and the novel use of spectrographs by (e.g. Weijmans et al., 2009; Gebhardt & Thomas, 2009; Proctor et al., 2009) have enabled kinematics to be probed to 3–4 R_e, but it is the use of discrete tracers such as planetary nebulae (PNe) and globular clusters (GCs) in the last twenty years that have really enabled kinematics to be probed out to 6–7 R_e. These data have been used to probe the mass distribution and orbital structure in several massive elliptical galaxies (e.g. Hui et al., 1995; Côté et al., 2003; Peng et al., 2004; Bridges et al., 2006; Gebhardt & Thomas, 2009; Romanowsky et al., 2009; Shen & Gebhardt, 2010; Napolitano et al., 2010, and in Chapters 3, 4, and 5).

The mass distributions of giant elliptical galaxies can be probed using two additional methods. Strong gravitational lensing has enabled the dark matter mass fraction to be constrained within an Einstein radius, typically 0.5 R_e, (Bolton et al., 2006; Koopmans et al., 2006; Bolton et al., 2008; Auger et al., 2009; Ruff et al., 2010). The most massive elliptical galaxies also harbour copious amounts of hot, low-density gas producing X-ray spectra dominated by emission lines and continuous emission from thermal bremsstrahlung radiation. The spectra can be modelled to obtain the density and temperature profiles of the gas. If the gas is relatively undisturbed then we can assume hydrostatic equilibrium and derive the total mass distribution from the density and temperature profiles (e.g. Nulsen & Böhringer, 1995; Fukazawa et al., 2006; Humphrey et al., 2006; Churazov et al., 2008; Nagino & Matsushita, 2009, and in Chapter 2). With the advent of the Chandra and XMM-Newton telescopes this has enabled the mass distribution to be probed in detail out to 10 R_e.

In Chapter 2, we compared the mass profiles from X-rays to those from dynamical models and found that the X-ray mass profiles were often lower in the central $\sim$ 10 kpc, possibly due to non-thermal pressure contributions, multiple temperature components in the gas, insufficiently general mass profiles probed in the dynamical modelling or insufficiently extended kinematic data in the dynamical modelling. The outer regions seemed to agree better in general but there are only a handful of radially extended dynamical models. Additionally, in the axisymmetric, dynamical models of the massive elliptical galaxy NGC 4649 in Chapter 5, we found that PNe in the halo preferred a less massive halo than the X-rays from Chapter 2, though it is more similar to the X-ray mass distribution in Nagino & Matsushita (2009). It is evident that there are some issues with the derivation of mass profiles from X-ray information that need to be better understood, and therefore we believe it is important to carry out independent mass analyses with dynamical models to constrain the total mass distribution.

NGC 1399 is a massive, nearby elliptical galaxy located at the centre of the Fornax cluster of galaxies. It has been the subject of many studies in the last ten years. Drinkwater et al. (2001) analysed the dynamics in the Fornax cluster of galaxies using

dwarf galaxies and found that the velocity dispersion of the subcluster surrounding NGC 1399 is 370 km/s.

NGC 1399 has been studied a few times in the X-rays. Paolillo et al. (2002) used ROSAT observations to obtain a mass profile within 42 kpc. They found that the halo is quite disturbed in the outer parts. Churazov et al. (2008) obtained a mass profile for NGC 1399 from Chandra and XMM-Newton observations, and in Chapter 2 we applied a new non-parametric Bayesian approach to the same data. We found a dark matter mass fraction of ~ 0.2 at 1 R_e and almost 0.75 at 3 R_e.

Saglia et al. (2000) and Kronawitter et al. (2000) constructed dynamical models from superposing spherical distribution functions and fitting surface-brightness and long-slit kinematic constraints. They found that the dark matter mass contributes at most about 33% of the total mass at 8 kpc (0.8 R_e) and 0.50–0.75 at 35 kpc (3.3 R_e). Schuberth et al. (2010) carried out Jeans models with GC LOS velocities between 6 and 100 kpc. They concluded that the kinematics of the red GCs are consistent with the long-slit kinematics of Saglia et al. (2000). McNeil et al. (2010) measured the velocity dispersion profile out to about 40 kpc using a new catalogue of PN LOS velocities. They found that the profile is consistent with the projected kinematics of a model from Kronawitter et al. (2000), created assuming a mass distribution in the lower end of the 95% confidence range about their best-fit mass profile. This suggests that the PNe may prefer a more diffuse halo than the long-slit kinematic constraints.

In this Chapter we would like to carry out dynamical models of NGC 1399 using the made-to-measure N-body code NMAGIC. We use surface-brightness profiles constraining the distribution of stars, and long-slit kinematics, PN LOS velocities and GC LOS velocities constraining the distribution of stellar velocities. The questions we would like to answer are:

1. How massive is the dark matter halo of NGC 1399?
2. Is the dynamical mass modelling consistent with the X-rays for NGC 1399?

We adopt a distance of 19.95 Mpc (i.e. $1'' = 97$ pc) from measurements using surface-brightness fluctuations (Tonry et al., 2001) and an effective radius of 4.7 kpc (John Kormendy, private communication).

In Section 6.2, we describe the photometric and kinematic constraints. In Section 6.3, we describe the models we create with the dynamical modelling tool NMAGIC. We discuss the implications of our results in Section 6.4.

6.2 OBSERVATIONAL CONSTRAINTS

Here we discuss the observational constraints we use for NMAGIC. We describe the photometric constraints based on surface-brightness images and the kinematic constraints based on a combination of

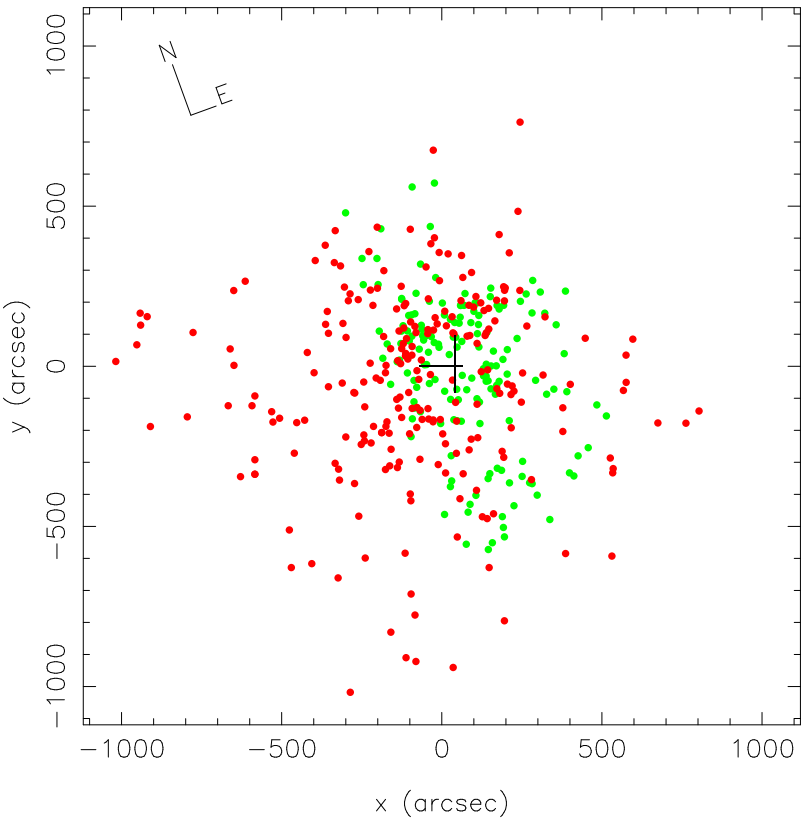

Figure 50: Kinematic constraints for NGC 1399: The green filled circles show the positions of the PNe, the red filled circles show the positions of the GCs and the black lines show the positions of the slits. The x-axis is along the major axis of the galaxy and the y-axis is along the minor axis.

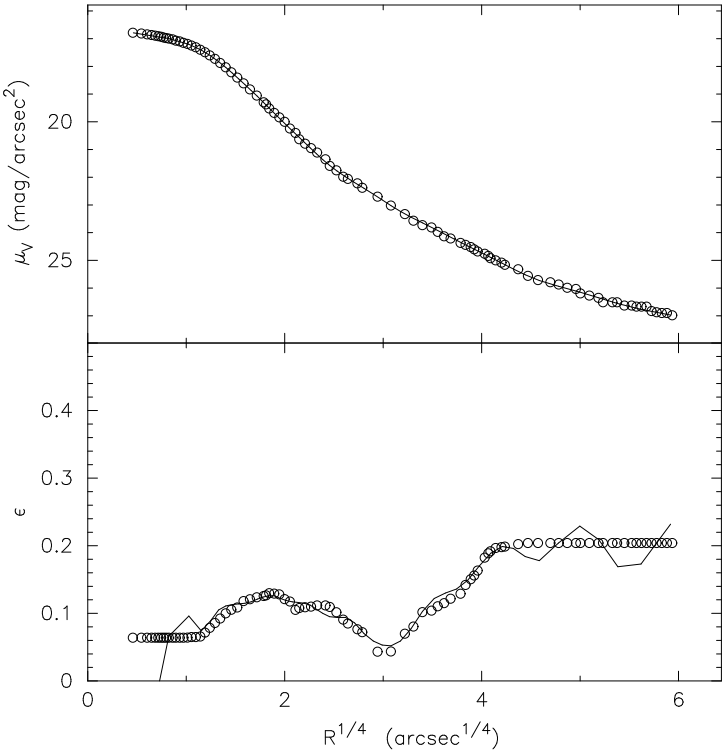

Figure 51: Projected light distribution in NGC 1399: The black circles in the top panel show the measured V-band surface-brightness profile and the lines show the reprojected surface-brightness profiles from the axisymmetric deprojection, assuming an inclination of 90°. The black circles in the bottom panel show the measured ellipticity profile and the lines show the ellipticity profiles of the reprojected light distributions from the axisymmetric deprojections.

long-slit spectroscopy for the inner parts, and planetary nebula (PN) and globular cluster (GC) velocities extending to the outer halo. Figure 50 illustrates the radial coverage of the kinematic data. We have orientated the coordinate system to align the x-axis with the major axis and the y-axis with the minor axis.

6.2.1 *Photometric data*

We use the B-band surface-brightness profile of Saglia et al. (2000) extending to ∼3000″. It combines V-band Hubble Space Telescope data from Lauer et al. (1995) covering the central region, ground-based B-band CCD data from Bicknell et al. (1989) covering the intermediate region, and photographic V-band data from Schombert (1986) covering the outermost region. We use the data only till 1241″, due to uncertainties in the sky subtraction further out. For the ellipticity profile we use Caon et al. (1994), which extends out to 375″. We assume a constant ellipticity profile further out, with an ellipticity equal to that at 375″.

6.2.2 *Long-slit kinematics*

The stellar kinematics are taken from Saglia et al. (2000). They fit the line-of-sight (LOS) velocity, velocity dispersion and Gauss-

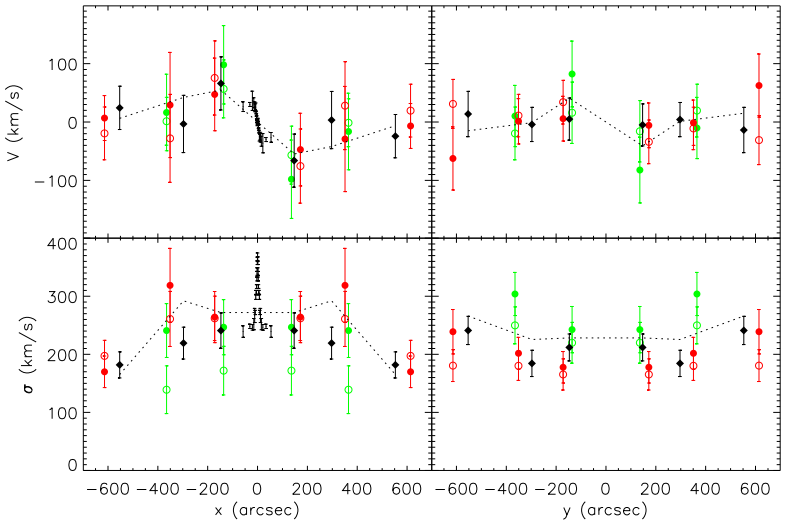

Figure 52: Comparison of long-slit PN and GC kinematics for NGC 1399: Major-axis (left panels) and minor-axis (right panels) velocity (top panels) and velocity dispersion (bottom panels) profiles. The black dots show the long-slit kinematics, the filled (open) green circles show the PN kinematics (robust kinematics), the filled (open) red circles show the GC kinematics (robust kinematics) and the black, dotted line (filled, black diamonds) shows the kinematics (robust kinematics) of the combined PN and GC sample.

Hermite moments, h_3 and h_4, to absorption-line spectra obtained using EMMI/NTT in La Silla. Their data were taken from slits placed along the major axis and parallel to the minor axis, 42″ in the direction of the positive major axis. The slits extend to $\sim$ 60″ and $\sim$ 90″ respectively. Figure 50 shows the location and orientation of these slits. Figure 52 shows the long-slit kinematics along the major-axis slit. The rotation is small and of the order of 50 km/s. The velocity dispersion is almost 400 km/s in the centre and then decreases rapidly to $\sim$ 240 km/s at 60″.

6.2.3 *Discrete tracers*

In order to examine regions of interest outside the reach of integrated-light spectroscopy, we use LOS velocities of PNe from FORS1/VLT (McNeil et al., 2010) and GCs from FORS2/VLT and GMOS (Schuberth et al., 2010). PNe in general (Coccato et al., 2009) and the red GCs in NGC 1399 (Bassino et al., 2006; Schuberth et al., 2010; McNeil et al., 2010) have been shown to be good tracers of the stellar density and kinematics in the regions of overlap.

The catalogue of McNeil et al. (2010) consists of 187 PNe measured with a counter-dispersed spectroscopy technique. Using a friendless outlier algorithm they found 12 low-velocity PNe. They then employed a probabilistic approach based on PN number densities and velocities to assign membership of the PNe to NGC 1399 and the neighbouring NGC 1404, and found 146 belonging to NGC 1399, 23 to NGC 1404 and 6 unassigned PNe.

Due to the possibility of contamination from the low-velocity subcomponent and the sensitivity of the velocity dispersion profile to velocities in the wings, we derive kinematic profiles using both the traditional method and the robust-fitting technique described in McNeil et al. (2010). We use the sample of 146 PNe and the 12 suspected to be part of the low-velocity subcomponent, tracing the kinematics from 48–679″. Velocity and velocity dispersion profiles are obtained along 90°-cones centred on the major and minor axes and then an instrumental dispersion of 37 km/s is subtracted in quadrature. The robust-fitting technique avoids using the tails of the distribution by using only objects within two standard deviations of the mean. The median of these objects is taken to be the velocity, and the velocity dispersion is corrected based on the shape of Gaussian distributions. The 12 PNe deemed to be low-velocity outliers by the friendless outlier algorithm in McNeil et al. (2010) all lie outside the 2-σ limit imposed by the robust-fitting technique, and therefore their inclusion has no effect in deriving the robust kinematic profiles.

For the GCs we use the RIII catalogue described in Table 3 of Schuberth et al. (2010) consisting of 243 objects and with extreme velocities removed. These are the red GCs, shown by McNeil et al. (2010) to be in good agreement with the PNe in terms of spherical kinematics. We remove NGC 1404 contaminants using the same method employed for the PN catalogue in McNeil et al. (2010), leaving a catalogue of 236 GCs tracing the kinematics from $\sim$ 47–1213″. We again calculate the velocity and velocity dispersion profiles using the traditional method and the robust-fitting technique, along cones with an angular width of 90° centred on the major and minor axes. We then subtract the instrumental dispersion of 70 km/s in quadrature.

We also calculate the kinematics and robust kinematics for the combined PN and GC sample. We subtract an instrumental dispersion of 56[1] km/s in quadrature. 11 out of the 12 PNe deemed to be low-velocity outliers in McNeil et al. (2010) lie outside the 2-σ limits imposed by the robust-fitting technique.

Figure 52 shows the profiles derived using both methods for the different samples. The velocity profiles are generally consistent with each other and with the long-slit kinematics, though the robust velocity profiles are less bumpy. The robust velocity dispersion profiles are also less bumpy. They are generally consistent with each other and with the long-slit kinematics, but appear to be systematically lower than the profiles calculated using the traditional method. In the case of the PNe, this is possibly a result of the low-velocity outliers being included in the calculation of the traditional velocity dispersion profiles, and there may be a similar scenario for the GCs. The robust velocity dispersion in the outside bin along the major axis is especially low for the PNe. This may be a result of a small number of PNe in this bin due to the field locations, resulting in a more ragged velocity distri-

1 $56 = \sqrt{(37^2 \times 158 + 70^2 \times 236)/394}$

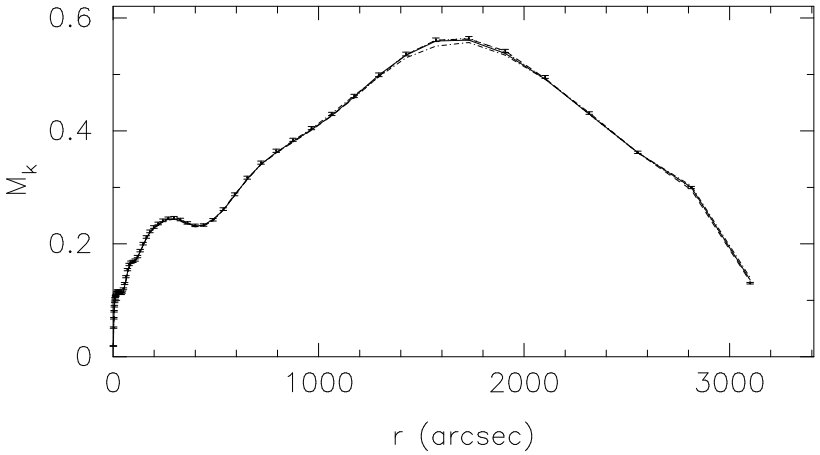

Figure 53: The differential mass distribution of the stars: The black points show the A_{00} coefficient or differential stellar mass distribution calculated from the surface-brightness data. The lines show A_{00} for Models A (solid), B (dashed), C (dotted), and D (dot-dashed).

bution. The robust-fitting algorithm may have then erroneously thrown out the ends of this velocity distribution.

We use the robust kinematics of the combined sample, which do not appear to be affected by the low-velocity outliers or too few objects. For the combined sample, the rotation is almost consistent with zero along the major axis, and is consistent with zero along the minor axis. The velocity dispersion decreases from $\sim$ 240 km/s at 147″ to $\sim$ 180 km/s at 553″ along the major axis and is $\sim$ 220 km/s along the minor axis. Both profiles are consistent with being constant outside $\sim$ 50″.

6.3 AXISYMMETRIC MODELS WITH NMAGIC

Here we describe how we create axisymmetric models with NMAGIC. We briefly describe how NMAGIC works, how we set up the initial particle model, and how we specify the gravitational force acting on the stars. Then we discuss models we create to probe the mass-to-light ratio of the stars and the mass of the dark matter halo.

6.3.1 *NMAGIC*

NMAGIC (de Lorenzi et al., 2007) is a particle-based code, used to find the intrinsic phase-space distribution of the stars that best projects to match the available information from photometric and kinematic data. This dynamical modelling tool has already been used to examine the outer haloes of the intermediate-luminosity elliptical galaxies NGC 4697 (de Lorenzi et al., 2008) and NGC 3379 (de Lorenzi et al., 2009), and the massive elliptical galaxy NGC 4649 (Chapter 5).

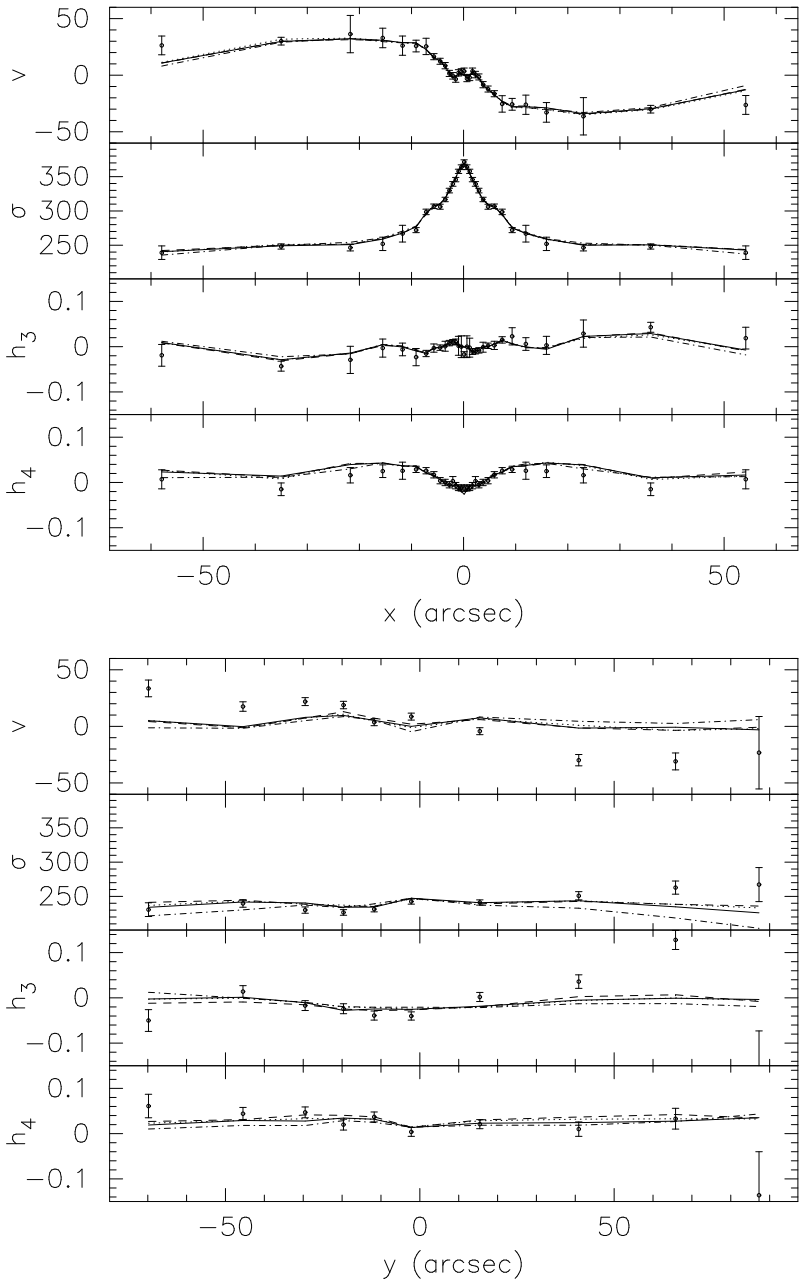

Figure 54: Long-slit kinematic profiles: The v, σ, h_3, and h_4 profiles along the major axis (left panel) and parallel to the minor axis (right panel), given by the data (black points). The lines are for Models A (solid), B (dashed), C (dotted, and D (dot-dashed).

The galaxy is represented by a particle model, where each particle has a 6-D phase-space coordinate and a variable weight. The particle orbits are integrated according to some gravitational force, and the particle weights are adjusted simultaneously to maximise the merit function, F. The merit function is a sum over the pseudo-weight entropy of the particle system, χ^2 terms measuring the goodness-of-fit to the density and kinematic target observables, and if desired, a likelihood term, measuring the goodness-of-fit to LOS velocities of discrete tracers. The prescription for changing the weights is the force-of-change (FOC) equation, given in Equation (1) of de Lorenzi et al. (2007).

6.3.2 *Preparing target observables*

6.3.2.1 *Luminosity density target observables*

Instead of fitting the surface-brightness constraints directly, we first deproject the photometric profiles using the code of Magorrian (1999), assuming an axisymmetric stellar system. The deprojection code maximises a penalised likelihood to find a smooth axisymmetric density distribution consistent with the surface-brightness distribution for some assumed inclination of the stellar system. We assume an inclination of $i = 90°$[2].

The output deprojected profiles are reprojected to compare with the original input surface-brightness and ellipticity profiles and are shown in Figure 51. The reprojected profiles fit the measured profiles very well except in the central arcsec and beyond $\sim 260''$. The ellipticity profile is not so well defined in the centre because the isophotes are close to circular as a result of seeing. The artificial setting of a constant ellipticity in both regions may have also contributed to the bumpy model profiles.

The deprojected luminosity density profile is represented in terms of A_{lm} coefficients (de Lorenzi et al., 2007) over a grid of 60 radii between $1.5''$ out to $3100''$. Within a radius of $1.5''$, the deprojected density profile decreases inwards as a result of numerical inaccuracies. $3100''$ corresponds to the radius at which the density of the initial particle model starts falling off from the deprojected density profile. Higher moments that describe non-axisymmetry are set to zero. Poissonian errors are assumed on the radial mass profile and errors are determined for the higher-order mass moments using Monte-Carlo simulations in which particle realisations of the density field of the target model are generated. The A_{00} coefficient describing the differential stellar mass distribution is shown in Figure 53.

6.3.2.2 *The kinematic target observables*

As we assume an axisymmetric stellar distribution in NGC 1399, we can point-symmetrise the kinematic data. We fold the major-

2 $i = 0°$ corresponds to a face-on system, and $i = 90°$ corresponds to an edge-on system.

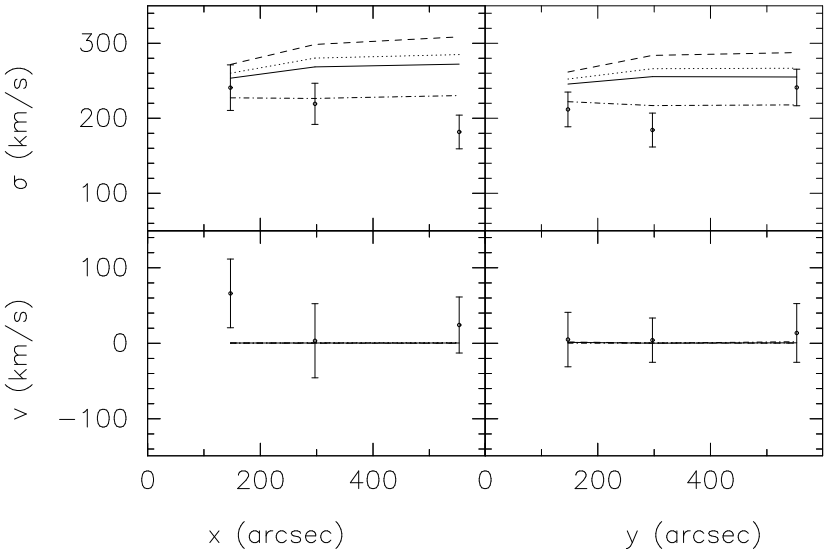

Figure 55: Discrete tracer kinematic profiles: v and σ profiles along the major (left panel) and minor (right panel) axes given by the data (black points). The lines are for models A (solid), B (dashed), C (dotted), and D (dot-dashed).

axis kinematics about the centre of the galaxy and for the discrete kinematics the sample is doubled by adding a discrete point at $(-x, -y, -v)$, for every (x, y, v).

As light-weighted kinematics are fit rather than the kinematics directly, the light in each of the slit cells needs to be calculated. This is calculated by integrating the surface-brightness distribution over the dimensions of each of the slit cells (assumed to have a width of 5″) using a Monte-Carlo integration scheme. The point-symmetrised long-slit kinematics along the major and minor axes are shown in Figure 54.

In the halo of NGC 1399, the power-law index of the density profile is close to -3, the circular velocity curve is almost constant (Saglia et al., 2000; Kronawitter et al., 2000), and therefore the projected velocity dispersion is approximately independent of anisotropy and directly depends on the mass (Gerhard, 1993). Therefore to probe the dark matter halo, we only need to fit the robust median velocities and velocity dispersions of the combined sample of discrete tracers, which is much less computationally expensive compared to fitting the individual LOS velocities. The velocities and velocity dispersions can be fit like the long-slit kinematics, and therefore the light is calculated in each of the bins. The point-symmetrised median velocities and velocity dispersions along the major and minor axes are shown in Figures 50 and 55.

6.3.3 *Initial conditions*

We first set up an initial model consisting of 750000 particles extending from $\sim$ 1.5″ to $\sim$ 3100″. We assume a total mass profile from the lower end of the 95% confidence range of mass

Table 11: NMAGIC models for NGC 1399: The columns give (1) the model, (2) the scale radius r_0 of the halo, (3) maximum circular velocity v_0 of the halo, (4) stellar B-band mass-to-light ratio corresponding to the halo, and χ^2 measures of the goodness of the fit to the (5) A_{lm}s, (6) long-slit data, (7) major-axis long-slit data, (8) discrete tracer data, and (9) all the data.

Model	r_0	v_0	M/L_B	$\chi^2_{\rm alms}$	$\chi^2_{\rm ls}$	$\chi^2_{\rm majls}$	$\chi^2_{\rm dt}$	χ^2
	(″)	(km/s)	$(M_\odot/L_{B,\odot})$					
(1)	(2)	(3)	(4)	(5)	(6)	(7)	(8)	(9)
A	275	375	10.0	0.35	1.51	0.62	2.40	0.59
B	300	450	9.78	0.30	1.44	0.66	5.83	0.61
C	275	400	9.93	0.33	1.53	0.59	3.42	0.60
D	350	300	10.07	0.58	2.14	0.91	0.79	0.84

profiles found from spherical dynamical models of NGC 1399 in Kronawitter et al. (2000). McNeil et al. (2010) had found that the projected velocity dispersion profile of this mass model matched the spherical velocity dispersion profile calculated from the PN LOS velocities very well. We assume a density distribution of the particles given by a spherical deprojection of the circularly-averaged photometric profiles. For the intrinsic distribution of stellar velocities we use the circularity functions of Gerhard (1991), resulting in an anisotropy profile ($\beta = 1 - \sigma_\theta^2/\sigma_r^2$) that is isotropic throughout. The particles' coordinates and velocities are chosen using the procedure from Debattista & Sellwood (2000) and they are initially assigned equal weights of $w_i = 1/750000$.

6.3.4 *Exploring mass models*

We explore a range of potentials where the total potential is assumed to be due to stars and dark matter. We assume a stellar mass contribution (Φ_*) that follows the stellar luminosity profile. This is calculated from the stars during the NMAGIC run using a potential solver to solve Poisson's equation. The mass-to-light ratio is calculated using the efficient scheme implemented in NMAGIC and described in Section 3.6 of de Lorenzi et al. (2008). It is assigned an initial value of 10 in the B band, based on the models of Saglia et al. (2000) andKronawitter et al. (2000). For the dark matter mass contribution ($\Phi_{\rm DM}$) we assume a logarithmic profile (Binney & Tremaine, 1987):

$$\Phi_{\rm DM} = \frac{1}{2} v_0^2 \ln(r^2 + r_0^2) \tag{6.1}$$

where v_0 is the maximum circular velocity, and r_0 is the scale radius. Our models will therefore show how the addition of discrete tracer constraints affect the halo parameters derived. The dark matter halo is added in NMAGIC as an external force acting on the system.

We first relax the initial model in the potential for 2000 steps where the particles are advanced according to the potential and

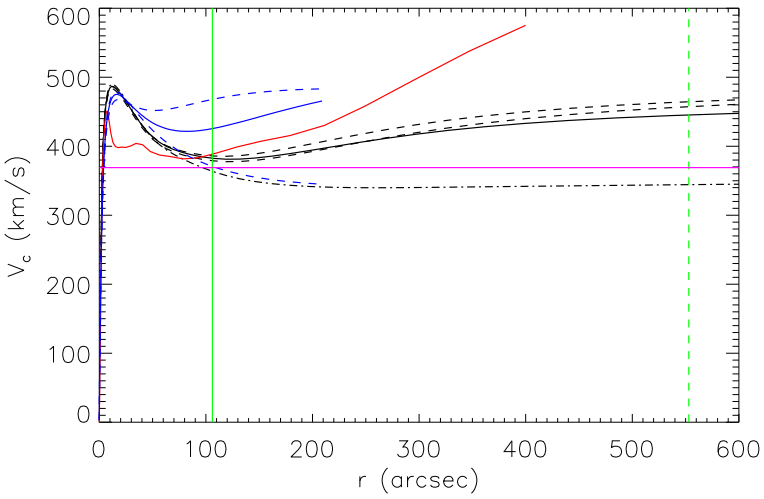

Figure 56: Circular velocity curves of NGC 1399: The black lines show the circular velocity curves corresponding to models A (solid), B (dashed), C (dotted), and D (dot-dashed). The red line shows the circular velocity curve obtained from X-ray observations in Chapter 2. The solid, blue line shows the circular velocity curve obtained from spherical dynamical models (Kronawitter et al., 2000) and the dashed, blue lines show the associated 95% confidence range. The pink line shows the value of the circular velocity predicted directly from the velocity dispersions of the discrete kinematic tracers. The vertical green lines show the radial extent to which the models from Kronawitter et al. (2000) are reliable (solid) and the radial extent of the kinematic data used in this work (dashed).

their weights are not changed. We then temporally smooth the model observables for a further 2000 steps during which the particles are advanced but their weights still not changed. Then the main phase of the run starts, where the particles are advanced according to the gravitational force and the weights of the particles are changed according to the FOC. Once the fractional change in the total χ^2 falls to less than 1.5×10^{-3} we define the model to have converged. Finally, this is followed by a free evolution, where the particles are advanced for a further 30000 steps and the weights are no longer changed, to check that the converged model has been sufficiently phase-mixed. The particles are advanced using an adaptive leapfrog scheme.

We first examine a coarse grid of haloes with scale radii r_0 ranging between 50–350″ based on values explored in Saglia et al. (2000) and maximum circular velocities V_0 ranging between 300–600 km/s, based on the results of Saglia et al. (2000) and the velocity dispersion of 370 km/s measured for the surrounding sub-cluster (Drinkwater et al., 2001), which suggests a circular velocity of 523 km/s for an isothermal halo. We then use the bisection method to approach the best mass profile and stop once we resolve r_0 to within 25″ and v_0 to within 25 km/s, because at this resolution it becomes difficult to differentiate between the various potentials.

Table 11 shows the halo parameters, stellar mass-to-light ratios in the B-band, and χ^2 values for the models with the lowest χ^2

considering all the data together (Model A), only the long-slit data (Model B), only the major-axis long-slit data (Model C), and only the discrete tracer data (Model D). The corresponding circular velocity curves are shown in Figure 56 and the fits to the observational constraints are shown in Figures 53, 54, and 55.

The circular velocity curves corresponding to Models A, B, and C are very similar to each other. They rise to a maximum of ∼490 km/s at ∼ 10″ , then fall steeply to just below 400 km/s at ∼ 100″, before rising again gently to 450–470 kms/ at 600″. Model D is very similar within 100″ but then falls a little more to ∼ 340 km/s, and stays reasonably constant at this value. Therefore the total mass profile most preferred when considering the fits to only the discrete tracer kinematics implies a considerably less massive halo than when considering all the data together. These results also show that the long-slit kinematics dominate over the discrete tracers in their contributions to the total χ^2.

The fits to the A_{lm} constraints are generally excellent. The χ^2 is a little worse for Model D compared to the others due to a systematically lower differential mass distribution of the model between ∼ 1300–1900″.

The fits to the major-axis long-slit data are generally very good. Only Model D is visually distinguishable. The model velocities at the outermost point at ∼55″ are a little lower than the data and the model h_4 is systematically a little higher outside ∼10″. The fits to the long-slit kinematics parallel to the minor axis are a lot worse. We have imposed axisymmetry on the stellar distribution, and therefore the model kinematics are representative of an axisymmetric system, i.e. they are symmetric about the major axis. The data however show rotation of the order of ∼ 30 km/s about the major axis and gradients in the other profiles as well. Therefore the χ^2 for the fits to these data are much higher, as shown by comparing columns (6) and (7) in Table 11.

The fits to the velocity profiles of the discrete tracers are very good and hardly distinguishable from each other. The velocity dispersion of the discrete tracers are however very sensitive to the model, and only consistent with Model D. The velocity dispersion profiles of the other models are systematically too high.

To summarise, the circular velocity curves of Models A–D are very similar within ∼ 100″, but further out that of Model D is considerably lower. As the discrete tracers are the only kinematic data in the halo and because they are very sensitive to the halo mass, while the density and long-slit constraints are less so, our preferred model is Model D.

6.4 DISCUSSION

Here we will discuss what we have learned about the total mass distribution, the mass-to-light ratio of the stars, the dark matter content, and the orbital structure in NGC 1399.

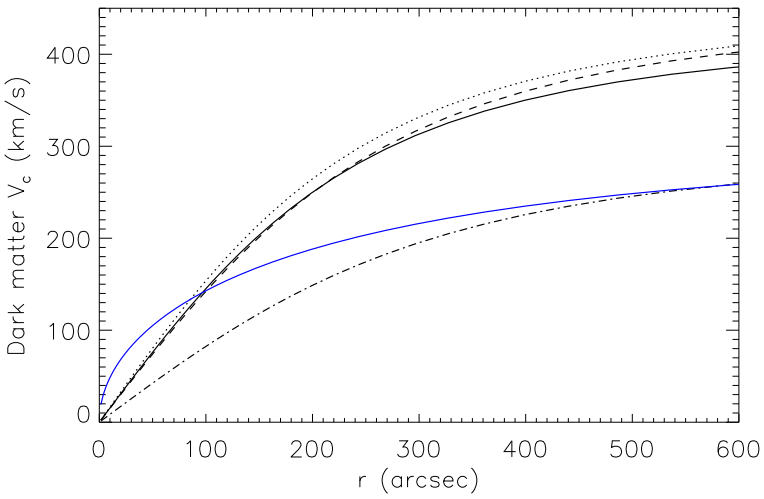

Figure 57: Dark matter circular velocity curves of NGC 1399: The black lines show the dark matter circular velocity curves corresponding to models A (solid), B (dashed), C (dotted), and D (dot-dashed). The blue line shows an NFW dark matter circular velocity curve for a halo with a scale radius of 80 kpc.

6.4.1 *The total circular velocity curve in NGC 1399*

The total circular velocity curve is well defined in the centre with a maximum circular velocity of about 490 km/s at $\sim$ 10″ $\sim$ 1 kpc. The circular velocity falls to 400 km/s between 70–80″ or 7–8 kpc. Further out the preferred Model D has a circular velocity of $\sim$ 340 km/s at 553″, the radius of the last kinematic data point.

A circular velocity of 369 km/s is predicted from the average total velocity dispersion of the discrete kinematic tracers of $\sim$ 213 km/s, assuming the relation from Gerhard (1993) for a system with constant circular velocity and a density profile with a power-law index close to -3 (shown in Figure 56). This value is reasonably close to the circular velocity of Model D in the halo, supporting the method used to obtain the best mass profiles.

The apparent inconsistencies between the long-slit and PN data sets could be a result of incorrect assumptions that we have made about the shape of the dark matter density profile. For example, it could be more centrally concentrated than a logarithmic potential (which maximises the stellar contribution to the total potential), as is the case for the NFW profile (Navarro et al., 1996) and dark matter distributions that consider the effects of the adiabatic contraction of baryons (Blumenthal et al., 1986). This would place more mass in the centre where the long-slit kinematic data is, but keep the halo less massive as preferred by the discrete tracers. Figure 57 shows the dark matter circular velocity curves corresponding to Models A–D. The ideal dark matter halo would be one as least as massive as that for Models A–C out to about 100″, the radial extent of the long-slit kinematics, which then does not rise too much further out. An NFW profile with a scale radius of 80 kpc is overplotted as an example. To investigate this

issue in more detail, models should also be created exploring NFW parameters.

The geometrical shape of the stellar distribution may also be different than assumed. The gradients in the kinematic profiles parallel to the minor axis could be a signature of a triaxial stellar distribution. In a triaxial potential, there is more freedom in the orbital structure, and therefore it may be possible to find a halo that fits both sets of kinematics. The gradient could alternatively be a result of the contamination of the low-velocity subcomponent found in the PN sample, as discussed in McNeil et al. (2010).

Our curve is very similar to the best model found by Kronawitter et al. (2000) in the central $\sim 10''$ and then lies between the middle and the lower end of the 95% confidence range further out.

The circular velocity curve of NGC 1399 derived in Chapter 2 from X-ray gas temperature and density profiles is lower than the dynamical curves in the central $\sim 100''$. Possible explanations for this discrepancy are discussed in Churazov et al. (2010) and Chapter 2. The X-ray curve is within the 95% confidence range of the dynamical curve of Kronawitter et al. (2000) between $\sim$ 100–200″, and is only just above our preferred model. Further out, the X-ray circular velocity curve rises steeply to a value of $\sim$ 570 km/s at $\sim 400''$, much higher than the values corresponding to our best models. This discrepancy in the outer parts between the dynamical and X-ray circular velocity curves is similar to that found for NGC 4649 in Chapter 5. Possible explanations are uncertainties associated with deprojection, metallicity gradients in the hot gas and outflows of gas.

6.4.2 *Mass-to-light ratio of the stars in NGC 1399*

The mass-to-light ratio of the stars corresponding to our most preferred model is $\sim$10.1 and lowest value is $\sim$9.8 for Model B. This range is an upper limit on the stellar mass-to-light ratio because a logarithmic dark matter halo maximises the stellar mass contribution in the centre. NFW profiles for example have higher dark matter densities in the centre, and therefore for the same total mass, a smaller stellar mass and therefore a lower stellar mass-to-light ratio would be derived.

As expected, our value is very similar to the value of 10 derived by Saglia et al. (2000) and Kronawitter et al. (2000), who also assume logarithmic dark matter haloes and fit the same photometry and long-slit kinematic data. Napolitano et al. (2005) obtained a B-band stellar mass-to-light ratio of $10.4^{+3.3}_{-2.7}$ from single-burst stellar population models, in agreement with our value.

6.4.3 *The dark matter content of NGC 1399*

The variation of the fraction of dark matter mass to total mass with radius is calculated for Models A–D and shown in Figure

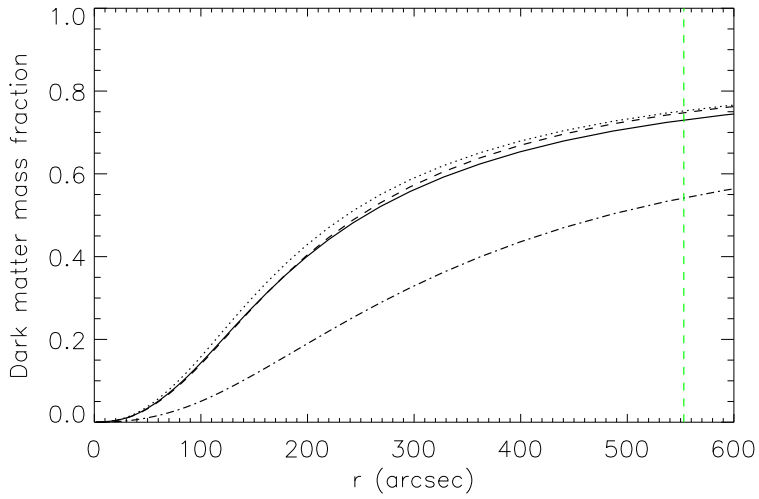

Figure 58: Dark matter mass fraction of NGC 1399: The lines show the dark matter mass fractions corresponding to models A (solid), B (dashed), C (dotted), and D (dot-dashed). The dashed green line show the radial extent of the kinematics used in this work.

58. Our most preferred model, Model D, has a dark matter mass fraction of ∼0.05 at 1 $R_e = 109''$, and ∼0.55 at 5 $R_e = 553''$, the radius of the outermost velocity dispersion point of the discrete tracers. Upper limits are approximately given by the dark matter mass fractions for Models A–C, which are ~ 0.15 at 1 R_e and ~ 0.75 at 5 R_e.

The Sloan Lens ACS (SLACS) survey found a minimum dark matter mass fraction of 0.38 ± 0.07 at 1 R_e in massive elliptical galaxies within $z \sim 0.36$ (Bolton et al., 2008). Ruff et al. (2010) found a dark matter mass fraction of 0.42 ± 0.08 within 0.5 R_e for strong lenses at $z \sim 0.5$ from the Legacy Survey (SL2S).

Analysis of Chandra observations found a reasonably flat total mass-to-light ratio in the central R_e that increases by about an order of magnitude at $\sim 10\,R_e$, implying that dark matter accounts for about 90% of the total mass at this radius (Humphrey et al., 2006). Joint analyses of Chandra and XMM-Newton observations have found dark matter mass fractions of 0.14–0.50 at 1 R_e (Fukazawa et al., 2006), ∼0.5 at $\sim 3\,R_e$ and ∼0.67 at $\sim 6\,R_e$ (Nagino & Matsushita, 2009), and ∼ 35–80% at 2 R_e, rising to a maximum of ∼ 80–90% at the outermost radii (Chapter 2).

Spherical and axisymmetric dynamical models of elliptical galaxies have found dark matter mass fractions of 10-50% within 1 R_e (Gerhard et al., 2001; Cappellari et al., 2006; Thomas et al., 2007).

The preferred dark matter mass profile we find for NGC 1399 appears to be more diffuse than what has been found in the literature, which suggests that perhaps the halo has been stripped in the past, for example in encounters with other galaxies in the cluster, and then had sufficient time to find a new dynamical equilibrium.

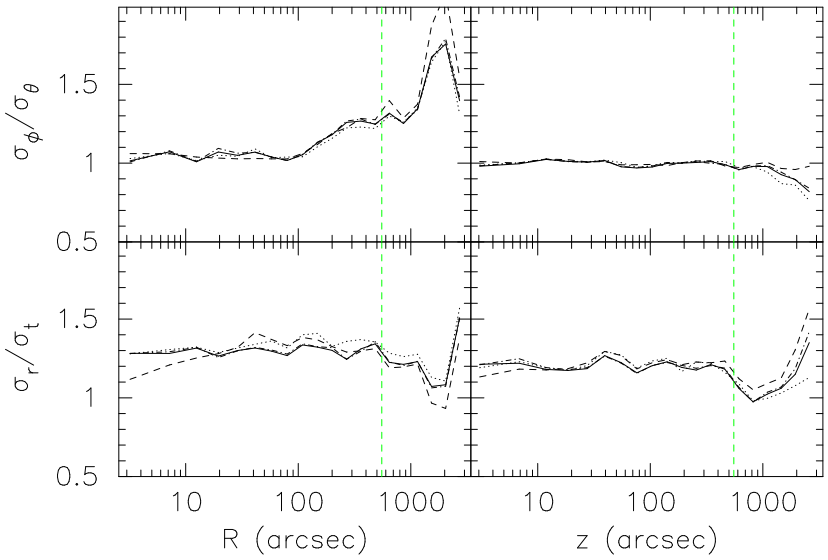

Figure 59: Internal kinematics of NGC 1399: The left panels show the ratio of the radial velocity dispersion to the tangential velocity dispersion (bottom), and the ratio of the azimuthal velocity dispersion to the meridional velocity dispersion (top), along *R*, the major axis. The right panels show the same along *z*, the minor axis. The lines correspond to models A (solid), B (dashed), C (dotted), and D (dot-dashed). The dashed green line shows the radial extent of the kinematics used in this work.

6.4.4 *The orbital structure of NGC 1399*

The orbital structure is very similar between the four models. The ratio of the radial velocity dispersions to tangential velocity dispersions within the maximum projected radius of the kinematic data is ~ 1.25 along the major axis and ~ 1.2 along the minor axis. The ratio of azimuthal to meridional velocity dispersions is about 1.1 until about 100" and then rises to 1.4. The lack of change in the orbital structure between the different models shows that there has not been much change from the orbital structure of the initial particle model. This supports the theory that the velocity dispersions in the halo are independent of anisotropy, as they are unable to drive a change in the anisotropy during the NMAGIC runs. Therefore to constrain the orbital structure in this region we need to fit the individual LOS velocities of the kinematic tracers using a robust-fitting technique that is integrated into NMAGIC.

7

CONCLUDING SUMMARY

Massive elliptical galaxies are bright ellipsoidal stellar conglomerates harbouring huge amounts of hot gas and residing in massive dark matter haloes. Much work has been devoted to obtaining mass distributions of these galaxies from X-ray observations of the hot gas, and obtaining both mass distributions and the orbital structure from dynamical models that fit optical observations. X-ray data can provide constraints out to $\sim 10\ R_e$, but there are uncertainties involved in their analysis that need to be better understood. Optical data provide strong constraints but generally only within 1–2 R_e. Therefore there has not been much comparison between the mass distributions obtained using the two methods in the halo. The halo is also especially interesting as the dark matter dominates there and the dynamical timescales of the stars are longer, therefore better preserving past formation events in the orbital structure of the stars. Probing the halo is therefore important for placing constraints on the formation of massive elliptical galaxies in the current cosmological paradigm.

In the present work, the outer haloes of a sample of six nearby massive elliptical galaxies have been examined in detail. NGC 1399 is located at the centre of the Fornax cluster, NGC 1407 and NGC 5846 at the centre of groups, and NGC 4472 (M49), NGC 4486 (M87) and NGC 4649 (M60) at the centre of sub-clumps in the Virgo cluster. NGC 4486 is at the centre of the most massive sub-component in the Virgo cluster.

A novel non-parametric method based on Bayesian statistics has been developed for obtaining mass profiles from density and temperature profiles of the surrounding hot gas. The method has been applied to profiles obtained from deep Chandra and XMM-Newton observations for the sample. Dynamical models using the made-to-measure N-body code, NMAGIC, were carried out for NGC 1399 and NGC 4649 to find the mass distribution in the halo, fitting kinematic constraints from planetary nebula (PN) and globular cluster (GC) velocities. The dark matter content has also been inferred by estimating the stellar mass content from surface-brightness images and single stellar population models.

The NMAGIC models of NGC 1399 and NGC 4649, along with dynamical models created of NGC 4486 and NGC 5846 assuming potentials from X-rays and using Jeans equations, have placed constraints on the orbital structure of the stars far out into the halo.

7.1 THE POTENTIAL OF MASSIVE ELLIPTICAL GALAXIES

7.1.1 *The total mass distribution*

The analysis of the surrounding hot gas has found velocity curves that rise outwards due to both an increasing temperature profile and an increasing logarithmic pressure gradient profile. Fitting a power-law model $M \propto r^{\zeta}$ to the total mass profiles found that the central $\sim$ 10 kpc of these galaxies may be isothermal, but further out their mass distribution rises more steeply than isothermal. The rising circular velocity curves could indicate the presence of the massive group/cluster-sized haloes in which these galaxies reside. The dynamical mass analyses of NGC 1399 and NGC 4649 found however that more isothermal mass distributions are consistent with the kinematics as traced by PNe and GCs in the halo.

Previous work examining the isothermality of total mass distributions has not found a coherent picture. X-ray analyses have found mass distributions that are isothermal (Humphrey et al., 2006), mildly steeper than isothermal (Churazov et al., 2010) and considerably steeper than isothermal (Fukazawa et al., 2006). Dynamical models and combined dynamical modelling and strong lensing results have generally found isothermal mass distributions (Gerhard et al., 2001; Thomas et al., 2007; Koopmans et al., 2009). The present work has shown that the discrepancies may be attributed to different radial ranges over which ζ is calculated, different ranges of luminosities of the galaxies in the sample, and environmental effects, i.e. the galaxies examined in this work are located specifically at the centre of sub-groups, groups or clusters.

Moving from a global comparison to individual comparisons between various determinations of mass distributions for a single galaxy, it was found that X-ray circular velocity curves are often lower in the central $\sim$10 kpc compared to those from dynamical models. Further out, except in NGC 1407 and NGC 4486 (in this galaxy AGN outflows are thought to considerably disrupt the hot gas), mass determinations from different X-ray analyses and dynamical modelling (where available) are comparable.

In the central $\sim$ 12 kpc, the dynamical models of NGC 4649 could not distinguish between a previous dynamical mass model fitting GC kinematics and assumed to trace stellar kinematics, and the X-ray mass distribution determined in this work. A look at the systematic differences in this region suggested that the true mass distribution possibly lies somewhere in between. Further out in both the dynamical models of NGC 1399 and NGC 4649, the discrete tracer velocity dispersions are very sensitive to the mass in the halo and were found to prefer more isothermal mass distributions, rather than the rising circular velocity curves of the previous GC dynamical model and the X-ray analyses in this work.

7.1.2 *Why are the mass distributions not quite in agreement?*

In terms of the average isothermality of the total mass distribution it was shown that the value derived could depend on the radial range over which the index is calculated, the size of the galaxy, and the local environment of the galaxy. For example, the centres of galaxies could be isothermal but further out as the mass distribution starts reflecting that of the group or cluster, the circular velocity curves would start rising. The dynamical models of NGC 4649 and NGC 1399 show isothermal mass distributions throughout however, even though they are both at the centres of dense local environments.

Further in, the dynamical mass profiles tend to be higher than the X-ray mass profiles. The X-ray work combined with the dynamical models of NGC 4649 suggesting that the central discrepancy is due to a combination of mass profiles that are insufficiently general in the dynamical modelling, non-thermal contributions of up to $\sim$35% in the pressure (possibly with stronger effects in NGC 4486), and multiple-temperature components in the hot gas.

In the halo, the discrepancies are most likely to be due to the X-ray analyses as the derived mass profile depends on the radial range of data used and possibly the deprojection carried out. There are also uncertainties associated with the metal abundances in the hot gas that can affect the circular velocity curve. In the spectral analysis used to determine the density and temperature profiles of the hot gas for the sample of galaxies in this work (Churazov et al., 2010) the metal abundance was assumed to be constant. The maximum effect of this assumption compared to allowing for an abundance gradient was $\sim$ 4% in the circular velocity, with a tendency to increase the circular velocity curve. Although this does not explain why the X-ray circular velocity curves are higher in the outer parts, it is something to consider in the future with deeper observations or better instruments. Outflows of gas from AGN activity for example could heat up the gas leading to higher temperatures but as these emanate from the centre, one would expect the gas to be hotter further in. The hot gas could also perhaps be stripped in the outer parts by encounters with nearby galaxies in the dense surrounding environments. This could cause the density gradient to be inflated and therefore higher circular velocity curves.

7.1.3 *Total mass and the local environment*

Despite the uncertainties associated with determining mass profiles from X-ray analyses, the six massive elliptical galaxies in our sample were found to follow the Tully-Fisher relation with slope $\sim$4, the same dependence as found for Coma cluster elliptical galaxies analysed in Thomas et al. (2009) (*private communication* with J. Thomas) and for spiral galaxies. The Tully-Fisher relation

implies that systems with more luminous stellar components also have larger total masses and therefore more massive dark matter haloes.

The luminosities of the galaxies and their total masses were also found to correlate with the number density of systems in the local environment. This is consistent with the merger theory for the formation of elliptical galaxies as a larger number of systems are expected to fall onto the central galaxy in denser environments, resulting in a more luminous stellar component and a more massive dark matter halo.

7.1.4 *The dark matter content*

Assuming that the baryonic mass component in the galaxy is solely composed of stars and that the stellar mass-to-light ratio is constant with radius, the dark matter fractions inferred from the X-ray mass distributions were found to range between 50–80% at $2R_e \sim$ 6.5–59 kpc in all galaxies except NGC 1407 where it is $\sim$ 35%. Further out, the profiles converge to a value between 80–90%, pointing uniformly to a massive dark matter halo. The larger range in the dark matter mass fractions further in may indicate dark matter mass profiles that have different shapes or different contributions from non-thermal pressures and multiple-temperature components. Our NMAGIC models of NGC 1399 and NGC 4649 found dark matter haloes on the diffuse side, with dark matter mass fractions of 55% and 20% at 2 R_e and 80% and 5% at 5 R_e respectively.

In the literature the central dark matter mass fraction within 1 R_e has been constrained using several methods and for many galaxies. Dynamical models and X-ray analyses for elliptical galaxies spanning a range of luminosities have found dark matter mass fractions of 10-50% within 1 R_e (Gerhard et al., 2001; Cappellari et al., 2006; Fukazawa et al., 2006; Thomas et al., 2007). Simple mass models of a very large sample of massive elliptical galaxies in the Sloan Digital Sky survey however found a higher dark matter mass fraction of $\sim$ 0.64 at 1 R_e, as this value is projected along the line of sight (LOS). This value agrees better with those from strong lensing results, which also quote projected dark matter mass fractions finding values between $\sim$ 0.3–0.7 (Auger et al., 2009, 2010; Ruff et al., 2010) at $R_e/2$ and a minimum value of $\sim$ 0.38 at 1 R_e for massive elliptical galaxies. The self-consistent hydrodynamical simulations of Oñorbe et al. (2007) set in the current cosmological paradigm found dark matter mass fractions ranging between 0.3–0.6 at 1 R_e in the haloes surrounding elliptical-like objects. Some of these works suggest that more massive elliptical galaxies may have higher dark matter mass fractions (Cappellari et al., 2006; Auger et al., 2009, 2010).

Further out there are a handful of constraints from dynamical models for samples of galaxies. The spherical dynamical models of Gerhard et al. (2001) predict equality between stellar and dark

matter mass distributions at 2–4 R_e and for the Coma galaxies with sufficiently spatially extended data (generally the less luminous ellipticals), Thomas et al. (2007) found dark matter mass fractions between 65–75% at 4 R_e. X-ray analyses have been able to probe the dark matter mass fractions further out and have found ∼0.5 at $\sim 3\,R_e$ and ∼0.67 at $\sim 6\,R_e$ (Nagino & Matsushita, 2009) and $\sim$ 0.9 at 10 R_e (Humphrey et al., 2006).

The results of the present work are in broad agreement with literature, except for the dark matter halo of NGC 1399, which was found to be especially diffuse. The halo could have been stripped by encounters with other galaxies in the cluster in the past.

7.2 THE DISTRIBUTION OF ORBITS IN MASSIVE ELLIPTICAL GALAXIES

The orbital structure has been analysed in the four massive elliptical galaxies, NGC 1399, NGC 4486, NGC 4649, and NGC 5846. Spherical Jeans equations and an X-ray mass distribution were used for NGC 4486 and NGC 5846 to fit long-slit and PN kinematic constraints extending to 160 kpc ($\sim 3R_e$) and 38 kpc ($\sim 4R_e$). The orbital structure of the stars was found to be mildly radial in the central region and highly radial in the halo ($\beta \sim 0.8$) in NGC 4486, and highly radial ($\beta \sim 0.8$) throughout in NGC 5846. The findings later in this work confirming some problems with the X-ray analyses support new independent mass analyses, which may affect these results.

Exploring a range of mass profiles using axisymmetric NMAGIC models, the orbital structure was found to be mildly radial in the centre in NGC 1399 and NGC 4649. Further out, the orbital structure is almost isotropic along R and z in NGC 1399 (though stronger constraints need to be obtained by using individual velocities of the discrete tracers rather than the velocity dispersions), and in NGC 4649 is slightly more radial further out along R, but more isotropic along z. In both galaxies the azimuthal velocity dispersions are slightly higher than the meridional velocity dispersions throughout along R, indicating that the stellar system may be flattened by a meridional anisotropy in the velocity dispersion tensor (Dehnen & Gerhard, 1993a,b; Cappellari et al., 2007; Thomas et al., 2009).

These models have also shown that the velocity dispersions in the halo for these massive elliptical galaxies are almost independent of anisotropy in the halo. Therefore an efficient approach to adopt in independent mass analyses is to first use the velocity dispersions to estimate the best mass profile, as was done for NGC 1399. Then models should be carried out in a range of mass profiles close to this mass profile, fitting instead the LOS velocities, which entail higher-order information and therefore provide constraints on the anisotropy.

In the literature, the orbital structure in the central R_e has generally been found to be isotropic to mildly radial (Gerhard et al., 2001; Koopmans et al., 2006). Further out, simulations have unanimously found moderately to highly radially anisotropic haloes (Jesseit et al., 2005; Abadi et al., 2006; Oñorbe et al., 2007; Thomas et al., 2009) due to smaller galaxies that have been accreted on to the central object (Abadi et al., 2006; Naab et al., 2009). Dynamical models on the other hand have found a range of anisotropies further out (de Lorenzi et al., 2008, 2009; Napolitano et al., 2009, 2010; Schuberth et al., 2010) with more massive elliptical galaxies having possibly even less radial orbital structures (Schuberth et al., 2010; Napolitano et al., 2010) as was also found for NGC 1399 and NGC 4649. For NGC 4486 and NGC 5846, highly radially anisotropic haloes were found, but this needs to be verified using independent mass analyses.

7.2.1 *Constraints on formation channels for massive elliptical galaxies*

Much recent work with simulations of the formation of massive elliptical galaxies (e.g. van Dokkum et al., 2008; Naab et al., 2009) has supported a scenario where the outer haloes of massive elliptical galaxies expand spatially and become less dense from redshift ~ 2 until the present day through the accretion of smaller neighbouring systems. The simulations however predict that this should result in moderately to highly radial orbital structures in the halo, which have not been found from the dynamical models of NGC 1399 and NGC 4649 in this work, and NGC 4374 in Napolitano et al. (2010). This means that either the density evolution in the outer parts is due to a mechanism other than minor mergers, or that some mechanism is not considered in the simulations that could allow the orbital structure in the halo to be less radial. Gas dissipation during a merger can have a significant effect on the properties of the final remnant (Barnes & Hernquist, 1996; Cox et al., 2006; Naab et al., 2006; Robertson et al., 2006; Jesseit et al., 2007; Thomas et al., 2009). Naab et al. (2006) showed that only 10% gas is required to suppress central box orbits (which make the central orbital structure more radial), and there may be a similar effect further out.

7.3 FUTURE AGENDA

Dynamical models using NMAGIC still need to be carried out for a broader range of mass profiles for NGC 1399 to find examine whether a common halo can be found for the long-slit and discrete tracer data. The models need to be carried out fitting the discrete velocities for NGC 1399 in the best potential, to obtain stronger constraints on the orbital structure. Given the uncertainties regarding the X-ray mass distributions, it would be insightful

to also carry out independent mass analyses using NMAGIC for NGC 1407, NGC 4472, NGC 4486, and NGC 5846.

To obtain a more detailed understanding on how the orbital structure constrains formation mechanisms of massive elliptical galaxies, a more thorough comparison of the dynamical structure of the sample of massive elliptical galaxies to that expected from the numerical simulations of A. Burkert and T. Naab (e.g. Naab et al., 2009) can be carried out. They simulate the formation of elliptical galaxies from galaxy mergers for varying progenitor mass ratios and gas fractions in a cosmological context, and are currently creating a new library of high-resolution simulations of massive elliptical galaxies. The orbital structures, projected kinematics and dark matter profiles of their simulated merger remnants can be compared with those derived for our galaxies, serving both as a test of the simulations and as a method to differentiate between various channels for forming massive elliptical galaxies.

An interesting extension to this work on massive elliptical galaxies could be the creation of more detailed models with NMAGIC of the central regions, which carry imprints of the formation processes that are thought to have occurred earlier than in the halo. A currently contentious issue is the inner slope of the dark matter density profile, which is dependent upon the interplay between baryons and dark matter particles through processes such as adiabatic contraction and AGN feedback (e.g. Del Popolo, 2010). Determining the inner slope would help put constraints on the importance of the various processes, but requires high-resolution data. Combining this data with the constraints on the global dark matter content and orbital structure from the models using PNe would be a powerful method for determining the inner slope of the dark matter density profile.

The modelling work described above would determine the dynamical structure of all massive elliptical galaxies in the Virgo Cluster, several in the Fornax Cluster and several in other groups of galaxies. Thomas et al. (2009) carried out a complete survey of the dynamical structure of elliptical galaxies in the Coma cluster, which is located further away at 100 Mpc. A fascinating avenue to explore would be to compare the properties of the orbital structure and dark matter content of massive elliptical galaxies between the various environments, therefore enabling us to better understand the effect of environment on the evolution of massive elliptical galaxies.

Part III

APPENDIX

BIBLIOGRAPHY

Abadi M. G., Navarro J. F., Steinmetz M., 2006, MNRAS, 365, 747

Aguerri J. A. L., Gerhard O. E., Arnaboldi M., Napolitano N. R., Castro-Rodriguez N., Freeman K. C., 2005, AJ, 129, 2585

Antonuccio-Delogu V., 1991, A&A, 247, 45

Arnaboldi M., Aguerri J. A. L., Napolitano N. R., Gerhard O., Freeman K. C., Feldmeier J., Capaccioli M., Kudritzki R. P., Méndez R. H., 2002, AJ, 123, 760

Arnaboldi M., Doherty M., Gerhard O., Ciardullo R., Aguerri J. A. L., Feldmeier J. J., Freeman K. C., Jacoby G. H., 2008, ApJ, 674, L17

Arnaboldi M., Freeman K. C., Mendez R. H., Capaccioli M., Ciardullo R., Ford H., Gerhard O., Hui X., Jacoby G. H., Kudritzki R. P., Quinn P. J., 1996, ApJ, 472, 145

Arnaboldi M., Freeman K. C., Okamura S., Yasuda N., Gerhard O., Napolitano N. R., Pannella M., Ando H. e. a., 2003, AJ, 125, 514

Arnaboldi M., Gerhard O., Aguerri J. A. L., Freeman K. C., Napolitano N. R., Okamura S., Yasuda N., 2004, ApJ, 614, L33

Arnold R., 1995, MNRAS, 276, 293

Arnouts S., Schiminovich D., Ilbert O., Tresse L., Milliard B., Treyer M., Bardelli S., Budavari T., Wyder T. K., Zucca E., Le Fèvre O., Martin D. C., Vettolani G., Adami C., and 51 coauthors 2005, ApJ, 619, L43

Arp H., Bertola F., 1971, ApJ, 163, 195

Auger M. W., Treu T., Bolton A. S., Gavazzi R., Koopmans L. V. E., Marshall P. J., Bundy K., Moustakas L. A., 2009, ApJ, 705, 1099

Auger M. W., Treu T., Bolton A. S., Gavazzi R., Koopmans L. V. E., Marshall P. J., Moustakas L. A., Burles S., 2010, ApJ, 724, 511

Bacon R., Copin Y., Monnet G., Miller B. W., Allington-Smith J. R., Bureau M., Carollo C. M., Davies R. L., Emsellem E., Kuntschner H., Peletier R. F., Verolme E. K., de Zeeuw P. T., 2001, MNRAS, 326, 23

Bahcall J. N., Sarazin C. L., 1977, ApJ, 213, L99

Barnes J. E., 1988, ApJ, 331, 699

Barnes J. E., 1992, ApJ, 393, 484

Barnes J. E., Hernquist L., 1996, ApJ, 471, 115

Bassino L. P., Faifer F. R., Forte J. C., Dirsch B., Richtler T., Geisler D., Schuberth Y., 2006, A&A, 451, 789

Baum W. A., 1959, PASP, 71, 106

Bekki K., Shioya Y., 1997, ApJ, 478, L17+

Bell E., Zucker D. B., Belokurov V., Sharma S., et al. 2008, ApJ, 680, 295

Bender R., Burstein D., Faber S. M., 1993, ApJ, 411, 153

Bender R., Doebereiner S., Moellenhoff C., 1988, A&AS, 74, 385

Bender R., Saglia R. P., Gerhard O. E., 1994, MNRAS, 269, 785

Bender R., Surma P., Doebereiner S., Moellenhoff C., Madejsky R., 1989, A&A, 217, 35

Bernardi M., 2009, MNRAS, 395, 1491

Bertin G., Bertola F., Buson L. M., Danzinger I. J., Dejonghe H., Sadler E. M., Saglia R. P., de Zeeuw P. T., Zeilinger W. W., 1994, A&A, 292, 381

Bertin G., Ciotti L., Del Principe M., 2002, A&A, 386, 149

Bertola F., Galletta G., Capaccioli M., Rampazzo R., 1988, A&A, 192, 24

Beuing J., Dobereiner S., Bohringer H., Bender R., 1999, MNRAS, 302, 209

Bezanson R., van Dokkum P. G., Tal T., Marchesini D., Kriek M., Franx M., Coppi P., 2009, ApJ, 697, 1290

Bicknell G. V., Bruce T. E. G., Carter D., Killeen N. E. B., 1989, ApJ, 336, 639

Binggeli B., Popescu C. C., Tammann G. A., 1993, A&AS, 98, 275

Binggeli B., Tammann G. A., Sandage A., 1987, AJ, 94, 251

Binney J., 1978, MNRAS, 183, 501

Binney J., Mamon G. A., 1982, MNRAS, 200, 361

Binney J., Tremaine S., 1987, Galactic dynamics

Blakeslee J. P., Lucey J. R., Tonry J. L., Hudson M. J., Narayanan V. K., Barris B. J., 2002, MNRAS, 330, 443

Blumenthal G. R., Faber S. M., Flores R., Primack J. R., 1986, ApJ, 301, 27

Blumenthal G. R., Faber S. M., Primack J. R., Rees M. J., 1984, Nature, 311, 517

Bolton A. S., Burles S., Koopmans L. V. E., Treu T., Moustakas L. A., 2006, ApJ, 638, 703

Bolton A. S., Burles S., Treu T., Koopmans L. V. E., Moustakas L. A., 2007, ApJ, 665, L105

Bolton A. S., Treu T., Koopmans L. V. E., Gavazzi R., Moustakas L. A., Burles S., Schlegel D. J., Wayth R., 2008, ApJ, 684, 248

Bosma A., van der Kruit P. C., 1979, A&A, 79, 281

Bournaud F., Jog C. J., Combes F., 2005, A&A, 437, 69

Bower R. G., Lucey J. R., Ellis R. S., 1992, MNRAS, 254, 601

Bridges T., Gebhardt K., Sharples R., Faifer F. R., Forte J. C., Beasley M. A., Zepf S. E., Forbes D. A., Hanes D. A., Pierce M., 2006, MNRAS, 373, 157

Brighenti F., Mathews W. G., 1997, ApJ, 486, L83+

Brighenti F., Mathews W. G., Humphrey P. J., Buote D. A., 2009, ApJ, 705, 1672

Bringhurst R., 2002, The Elements of Typographic Style. Version 2.5, Hartley & Marks, Publishers, Point Roberts, WA, USA

Brough S., Proctor R., Forbes D. A., Couch W. J., Collins C. A., Burke D. J., Mann R. G., 2007, MNRAS, 378, 1507

Brown B. A., Bregman J. N., 1998, ApJ, 495, L75+

Brown B. A., Bregman J. N., 2001, ApJ, 547, 154

Bullock J. S., Kolatt T. S., Sigad Y., Somerville R. S., Kravtsov A. V., Klypin A. A., Primack J. R., Dekel A., 2001, MNRAS, 321, 559

Buote D. A., Jeltema T. E., Canizares C. R., Garmire G. P., 2002, ApJ, 577, 183

Busarello G., Capaccioli M., Capozziello S., Longo G., Puddu E., 1997, A&A, 320, 415

Busarello G., Longo G., Feoli A., 1992, A&A, 262, 52

Buzzoni A., Arnaboldi M., Corradi R. L. M., 2006, MNRAS, 368, 877

Canizares C. R., Fabbiano G., Trinchieri G., 1987, ApJ, 312, 503

Caon N., Capaccioli M., D'Onofrio M., 1993, MNRAS, 265, 1013

Caon N., Capaccioli M., D'Onofrio M., 1994, A&AS, 106, 199

Cappellari M., 2008, MNRAS, 390, 71

Cappellari M., Bacon R., Bureau M., Damen M. C., Davies R. L., de Zeeuw P. T., Emsellem E., Falcón-Barroso J., Krajnović D., Kuntschner H., McDermid R. M., Peletier R. F., Sarzi M., van den Bosch R. C. E., van de Ven G., 2006, MNRAS, 366, 1126

Cappellari M., Emsellem E., Bacon R., Bureau M., Davies R. L., de Zeeuw P. T., Falcón-Barroso J., Krajnović D., Kuntschner H., McDermid R. M., Peletier R. F., Sarzi M., van den Bosch R. C. E., van de Ven G., 2007, MNRAS, 379, 418

Carollo C. M., Danziger I. J., 1994, MNRAS, 270, 523

Churazov E., Forman W., Jones C., Böhringer H., 2003, ApJ, 590, 225

Churazov E., Forman W., Vikhlinin A., Tremaine S., Gerhard O., Jones C., 2008, MNRAS, 388, 1062

Churazov E., Tremaine S., Forman W., Gerhard O., Das P., Vikhlinin A., Jones C., Böhringer H., Gebhardt K., 2010, MNRAS, 404, 1165

Ciardullo R., Jacoby G. H., Dejonghe H. B., 1993, ApJ, 414, 454

Ciardullo R., Jacoby G. H., Ford H. C., Neill J. D., 1989, ApJ, 339, 53

Ciardullo R., Sigurdsson S., Feldmeier J. J., Jacoby G. H., 2005, ApJ, 629, 499

Ciotti L., Lanzoni B., Renzini A., 1996, MNRAS, 282, 1

Coccato L., Arnaboldi M., Gerhard O., Freeman K. C., Ventimiglia G., Yasuda N., 2010, A&A, 519, A95+

Coccato L., Gerhard O., Arnaboldi M., Das P., Douglas N. G., Kuijken K., Merrifield M. R., Napolitano N. R., Noordermeer E., Romanowsky A. J., Capaccioli M., Cortesi A., de Lorenzi F., Freeman K. C., 2009, MNRAS, 394, 1249

Cohen J. G., 2000, AJ, 119, 162

Cohen J. G., Ryzhov A., 1997, ApJ, 486, 230

Corsini E. M., Wegner G., Saglia R. P., Thomas J., Bender R., Thomas D., 2008, ApJS, 175, 462

Côté P., McLaughlin D. E., Cohen J. G., Blakeslee J. P., 2003, ApJ, 591, 850

Côté P., McLaughlin D. E., Hanes D. A., Bridges T. J., Geisler D., Merritt D., Hesser J. E., Harris G. L. H., Lee M. G., 2001, ApJ, 559, 828

Cowie L. L., Henriksen M., Mushotzky R., 1987, ApJ, 317, 593

Cowie L. L., Songaila A., Hu E. M., Cohen J. G., 1996, AJ, 112, 839

Cox T. J., Dutta S. N., Di Matteo T., Hernquist L., Hopkins P. F., Robertson B., Springel V., 2006, ApJ, 650, 791

Cretton N., Rix H., de Zeeuw P. T., 2000, ApJ, 536, 319

Das P., Gerhard O., Churazov E., Zhuravleva I., 2010, MNRAS, pp 1419–+

Das P., Gerhard O., Coccato L., Churazov E., Forman W., Finoguenov A., Böhringer H., Arnaboldi M., Capaccioli M., Cortesi A., de Lorenzi F., Douglas N. G., Freeman K. C., Kuijken K., and 4 coauthors 2008, Astronomische Nachrichten, 329, 940

Das P., Gerhard O., Mendez R., Teodorescu A., 2011, Using NMAGIC to probe the dark matter halo and orbital structure of the massive elliptical galaxy, NGC 4649 (M60), submitted to MNRAS

Davies R. L., 1981, MNRAS, 194, 879

Davies R. L., Efstathiou G., Fall S. M., Illingworth G., Schechter P. L., 1983, ApJ, 266, 41

Davies R. L., Illingworth G., 1983, ApJ, 266, 516

Davis L. E., Cawson M., Davies R. L., Illingworth G., 1985, AJ, 90, 169

De Bruyne V., Dejonghe H., Pizzella A., Bernardi M., Zeilinger W. W., 2001, ApJ, 546, 903

de Lorenzi F., Debattista V. P., Gerhard O., Sambhus N., 2007, MNRAS, 376, 71

de Lorenzi F., Gerhard O., Coccato L., Arnaboldi M., Capaccioli M., Douglas N. G., Freeman K. C., Kuijken K., Merrifield M. R., Napolitano N. R., Noordermeer E., Romanowsky A. J., Debattista V. P., 2009, MNRAS, 395, 76

de Lorenzi F., Gerhard O., Saglia R. P., Sambhus N., Debattista V. P., Pannella M., Méndez R. H., 2008, MNRAS, 385, 1729

de Rijcke S., Michielsen D., Dejonghe H., Zeilinger W. W., Hau G. K. T., 2005, A&A, 438, 491

de Vaucouleurs G., 1948, Annales d'Astrophysique, 11, 247

Debattista V. P., Moore B., Quinn T., Kazantzidis S., Maas R., Mayer L., Read J., Stadel J., 2008, ApJ, 681, 1076

Debattista V. P., Sellwood J. A., 2000, ApJ, 543, 704

Dehnen W., 1993, MNRAS, 265, 250

Dehnen W., 2009, MNRAS, 395, 1079

Dehnen W., Gerhard O. E., 1993a, in I. J. Danziger, W. W. Zeilinger, & K. Kjär ed., European Southern Observatory Conference and Workshop Proceedings Vol. 45 of European Southern Observatory Conference and Workshop Proceedings, Dynamical Structure of Oblate Elliptical Galaxies. pp 327–+

Dehnen W., Gerhard O. E., 1993b, MNRAS, 261, 311

Dejonghe H., de Bruyne V., Vauterin P., Zeilinger W. W., 1996, A&A, 306, 363

Dejonghe H., Merritt D., 1992, ApJ, 391, 531

Dekel A., Birnboim Y., Engel G., Freundlich J., Goerdt T., Mumcuoglu M., Neistein E., Pichon C., Teyssier R., Zinger E., 2009, Nature, 457, 451

Del Popolo A., 2010, MNRAS, 408, 1808

Diehl S., Statler T. S., 2008, ApJ, 687, 986

Dirsch B., Richtler T., Geisler D., Forte J. C., Bassino L. P., Gieren W. P., 2003, AJ, 125, 1908

Djorgovski S., Davis M., 1987, ApJ, 313, 59

Doherty M., Arnaboldi M., Das P., Gerhard O., Aguerri J. A. L., Ciardullo R., Feldmeier J. J., Freeman K. C., Jacoby G. H., Murante G., 2009, A&A, 502, 771

D'Onofrio M., Capaccioli M., Zaggia S. R., Caon N., 1997, MNRAS, 289, 847

Dopita M. A., Jacoby G. H., Vassiliadis E., 1992, ApJ, 389, 27

Dressler A., Lynden-Bell D., Burstein D., Davies R. L., Faber S. M., Terlevich R., Wegner G., 1987, ApJ, 313, 42

Drinkwater M. J., Gregg M. D., Colless M., 2001, ApJ, 548, L139

Duffy A. R., Schaye J., Kay S. T., Dalla Vecchia C., Battye R. A., Booth C. M., 2010, MNRAS, 405, 2161

Durrell P. R., Mihos J. C., Feldmeier J. J., Jacoby G. H., Ciardullo R., 2003, ApJ, 582, 170

Durrell P. R., Williams B. F., Ciardullo R., Feldmeier J. J., von Hippel T., Sigurdsson S., Jacoby G. H., Ferguson H. C., Tanvir N. R., Arnaboldi M., Gerhard O., Aguerri J. A. L., Freeman K., Vinciguerra M., 2007, ApJ, 656, 746

Eggen O. J., Lynden-Bell D., Sandage A. R., 1962, ApJ, 136, 748

Einasto Y. I., 1969, Astrophysics, 5, 67

El-Zant A., Shlosman I., Hoffman Y., 2001, ApJ, 560, 636

Emsellem E., Cappellari M., Krajnović D., van de Ven G., Bacon R., Bureau M., Davies R. L., de Zeeuw P. T., Falcón-Barroso J., Kuntschner H., McDermid R., Peletier R. F., Sarzi M., 2007, MNRAS, 379, 401

Emsellem E., Cappellari M., Peletier R. F., McDermid R. M., Bacon R., Bureau M., Copin Y., Davies R. L., Krajnović D., Kuntschner H., Miller B. W., de Zeeuw P. T., 2004, MNRAS, 352, 721

Faber S. M., Dressler A., Davies R. L., Burstein D., Lynden-Bell D., 1987, in S. M. Faber ed., Nearly Normal Galaxies. From the Planck Time to the Present Global scaling relations for elliptical galaxies and implications for formation. pp 175–183

Faber S. M., Jackson R. E., 1976, ApJ, 204, 668

Faber S. M., Wegner G., Burstein D., Davies R. L., Dressler A., Lynden-Bell D., Terlevich R. J., 1989, ApJS, 69, 763

Feldmeier J. J., Ciardullo R., Jacoby G. H., Durrell P. R., 2003, ApJS, 145, 65

Feldmeier J. J., Mihos J. C., Morrison H. L., Harding P., Kaib N., Dubinski J., 2004, ApJ, 609, 617

Finoguenov A., Davis D. S., Zimer M., Mulchaey J. S., 2006, ApJ, 646, 143

Fontana A., Pozzetti L., Donnarumma I., Renzini A., Cimatti A., Zamorani G., Menci N., Daddi E., Giallongo E., Mignoli M., Perna C., Salimbeni S., Saracco P., Broadhurst T., Cristiani S., D'Odorico S., Gilmozzi R., 2004, A&A, 424, 23

Forbes D. A., Brodie J. P., Huchra J., 1997, AJ, 113, 887

Forbes D. A., Franx M., Illingworth G. D., Carollo C. M., 1996, ApJ, 467, 126

Forman W., Jones C., Churazov E., Markevitch M., Nulsen P., Vikhlinin A., Begelman M., Böhringer H., Eilek J., Heinz S., Kraft R., Owen F., Pahre M., 2007, ApJ, 665, 1057

Forman W., Jones C., Tucker W., 1985, ApJ, 293, 102

Forman W., Schwarz J., Jones C., Liller W., Fabian A. C., 1979, ApJ, 234, L27

Franx M., Illingworth G., de Zeeuw T., 1991, ApJ, 383, 112

Franx M., Illingworth G., Heckman T., 1989, ApJ, 344, 613

Freeman K. C., 1970, ApJ, 160, 811

Freeman K. C., Arnaboldi M., Capaccioli M., Ciardullo R., Feldmeier J., Ford H., Gerhard O., Kudritzki R., Jacoby G., Méndez R. H., Sharples R., 2000, in Combes F., Mamon G. A., Charmandaris V., eds, Dynamics of Galaxies: from the Early Universe to the Present Vol. 197 of Astronomical Society of the Pacific Conference Series, Intracluster Planetary Nebulae in the Virgo Cluster. p. 389

Fried J. W., Illingworth G. D., 1994, AJ, 107, 992

Fukazawa Y., Botoya-Nonesa J. G., Pu J., Ohto A., Kawano N., 2006, ApJ, 636, 698

Gavazzi G., Boselli A., Scodeggio M., Pierini D., Belsole E., 1999, MNRAS, 304, 595

Gavazzi R., Treu T., Rhodes J. D., Koopmans L. V. E., Bolton A. S., Burles S., Massey R. J., Moustakas L. A., 2007, ApJ, 667, 176

Gebhardt K., Richstone D., Tremaine S., Lauer T. R., Bender R., Bower G., Dressler A., Faber S. M., Filippenko A. V., Green R., Grillmair C., Ho L. C., Kormendy J., Magorrian J., Pinkney J., 2003, ApJ, 583, 92

Gebhardt K., Thomas J., 2009, ApJ, 700, 1690

Gerhard O., Arnaboldi M., Freeman K. C., Kashikawa N., Okamura S., Yasuda N., 2005, ApJ, 621, L93

Gerhard O., Arnaboldi M., Freeman K. C., Okamura S., Kashikawa N., Yasuda N., 2007, A&A, 468, 815

Gerhard O., Jeske G., Saglia R. P., Bender R., 1998, MNRAS, 295, 197

Gerhard O., Kronawitter A., Saglia R. P., Bender R., 2001, AJ, 121, 1936

Gerhard O. E., 1981, MNRAS, 197, 179

Gerhard O. E., 1991, MNRAS, 250, 812

Gerhard O. E., 1993, MNRAS, 265, 213

Gerhard O. E., 1994, in G. Contopoulos, N. K. Spyrou, & L. Vlahos ed., Galactic Dynamics and N-Body Simulations Vol. 433 of Lecture Notes in Physics, Berlin Springer Verlag, Elliptical galaxies. pp 191–274

Ghigna S., Moore B., Governato F., Lake G., Quinn T., Stadel J., 1998, MNRAS, 300, 146

Glazebrook K., Abraham R. G., McCarthy P. J., Savaglio S., Chen H., Crampton D., Murowinski R., Jørgensen I., Roth K., Hook I., Marzke R. O., Carlberg R. G., 2004, Nature, 430, 181

Gnedin O. Y., Kravtsov A. V., Klypin A. A., Nagai D., 2004, ApJ, 616, 16

Gonzalez A. H., Zabludoff A. I., Zaritsky D., 2005, ApJ, 618, 195

Gonzalez A. H., Zaritsky D., Zabludoff A. I., 2007, ApJ, 666, 147

Grillo C., 2010, ApJ, 722, 779

Halkola A., Seitz S., Pannella M., 2007, ApJ, 656, 739

Hanes D. A., Côté P., Bridges T. J., McLaughlin D. E., Geisler D., Harris G. L. H., Hesser J. E., Lee M. G., 2001, ApJ, 559, 812

Harris W. E., Whitmore B. C., Karakla D., Okoń W., Baum W. A., Hanes D. A., Kavelaars J. J., 2006, ApJ, 636, 90

Hernquist L., 1992, ApJ, 400, 460

Hernquist L., 1993, ApJ, 409, 548

Heyl J. S., Hernquist L., Spergel D. N., 1995, ApJ, 448, 64

Hjorth J., Madsen J., 1995, ApJ, 445, 55

Hoffman L., Cox T. J., Dutta S., Hernquist L., 2010, ApJ, 723, 818

Hopkins P. F., Cox T. J., Dutta S. N., Hernquist L., Kormendy J., Lauer T. R., 2009, ApJS, 181, 135

Hubble E. P., 1936, Realm of the Nebulae

Hui X., Ford H. C., Ciardullo R., Jacoby G. H., 1993, ApJ, 414, 463

Hui X., Ford H. C., Freeman K. C., Dopita M. A., 1995, ApJ, 449, 592

Humphrey P. J., Buote D. A., 2010, MNRAS, pp 135–+

Humphrey P. J., Buote D. A., Brighenti F., Gebhardt K., Mathews W. G., 2008, ApJ, 683, 161

Humphrey P. J., Buote D. A., Brighenti F., Gebhardt K., Mathews W. G., 2009, ApJ, 703, 1257

Humphrey P. J., Buote D. A., Gastaldello F., Zappacosta L., Bullock J. S., Brighenti F., Mathews W. G., 2006, ApJ, 646, 899

Huterer D., Turner M. S., 1999, PhRvD, 60, 081301

Hwang H. S., Lee M. G., Park H. S., Kim S. C., Park J., Sohn Y., Lee S., Rey S., Lee Y., Kim H., 2008, ApJ, 674, 869

Illingworth G., 1977, ApJ, 218, L43

Irwin J. A., Sarazin C. L., 1998, ApJ, 494, L33+

Jacoby G. H., Ciardullo R., Ford H. C., 1990, ApJ, 356, 332

Jacoby G. H., De Marco O., 2002, AJ, 123, 269

Jaffe W., 1983, MNRAS, 202, 995

Jedrzejewski R. I., 1987, MNRAS, 226, 747

Jesseit R., Naab T., Burkert A., 2005, MNRAS, 360, 1185

Jesseit R., Naab T., Peletier R. F., Burkert A., 2007, MNRAS, 376, 997

Kelson D. D., Zabludoff A. I., Williams K. A., Trager S. C., Mulchaey J. S., Bolte M., 2002, ApJ, 576, 720

Kent S. M., 1984, ApJS, 56, 105

Kereš D., Katz N., Fardal M., Davé R., Weinberg D. H., 2009, MNRAS, 395, 160

King I. R., 1966, AJ, 71, 276

Komatsu E., Smith K. M., Dunkley J., Bennett C. L., Gold B., Hinshaw G., Jarosik N., Larson D., Nolta M. R., Page L., Spergel D. N., Halpern M., Hill R. S., Kogut A., and 7 coauthors 2010, ArXiv e-prints

Koopmans L. V. E., Bolton A., Treu T., Czoske O., Auger M. W., Barnabè M., Vegetti S., Gavazzi R., Moustakas L. A., Burles S., 2009, ApJ, 703, L51

Koopmans L. V. E., Treu T., Bolton A. S., Burles S., Moustakas L. A., 2006, ApJ, 649, 599

Koprolin W., Zeilinger W. W., 2000, A&AS, 145, 71

Kormendy J., 1977, ApJ, 218, 333

Kormendy J., 1990, Did elliptical galaxies form by mergers or by dissipative collapse?. pp 499–502

Kormendy J., Bender R., 1996, ApJ, 464, L119+

Kormendy J., Fisher D. B., Cornell M. E., Bender R., 2009, ApJS, 182, 216

Krajnović D., Cappellari M., Emsellem E., McDermid R. M., de Zeeuw P. T., 2005, MNRAS, 357, 1113

Krick J. E., Bernstein R. A., 2007, AJ, 134, 466

Kronawitter A., Saglia R. P., Gerhard O., Bender R., 2000, A&AS, 144, 53

Kundu A., Whitmore B. C., 2001, AJ, 121, 2950

La Barbera F., Busarello G., Merluzzi P., de la Rosa I. G., Coppola G., Haines C. P., 2008, ApJ, 689, 913

La Barbera F., de Carvalho R. R., de La Rosa I. G., Lopes P. A. A., 2010, MNRAS, 408, 1335

Lauer T. R., 1985, ApJS, 57, 473

Lauer T. R., Ajhar E. A., Byun Y., Dressler A., Faber S. M., Grillmair C., Kormendy J., Richstone D., Tremaine S., 1995, AJ, 110, 2622

Lauer T. R., Gebhardt K., Faber S. M., Richstone D., Tremaine S., Kormendy J., Aller M. C., Bender R., Dressler A., Filippenko A. V., Green R., Ho L. C., 2007, ApJ, 664, 226

Lee J., Suto Y., 2003, ApJ, 585, 151

Lee M. G., Park H. S., Hwang H. S., Arimoto N., Tamura N., Onodera M., 2010, ApJ, 709, 1083

Liddle A. R., 2009, ArXiv e-prints

Limousin M., Kneib J. P., Bardeau S., Natarajan P., Czoske O., Smail I., Ebeling H., Smith G. P., 2007, A&A, 461, 881

Łokas E. L., Mamon G. A., 2003, MNRAS, 343, 401

Long R. J., Mao S., 2010, MNRAS, 405, 301

Lynden-Bell D., 1967, MNRAS, 136, 101

Magorrian J., 1999, MNRAS, 302, 530

Mahdavi A., Trentham N., Tully R. B., 2005, AJ, 130, 1502

Mandelbaum R., Seljak U., Cool R. J., Blanton M., Hirata C. M., Brinkmann J., 2006, MNRAS, 372, 758

Mathews W. G., 1978, ApJ, 219, 413

Mathews W. G., Brighenti F., 2003, ApJ, 599, 992

Matković A., Guzmán R., 2005, MNRAS, 362, 289

Matsushita K., Belsole E., Finoguenov A., Böhringer H., 2002, A&A, 386, 77

McDermid R. M., Emsellem E., Shapiro K. L., Bacon R., Bureau M., Cappellari M., Davies R. L., de Zeeuw T., Falcón-Barroso J., Krajnović D., Kuntschner H., Peletier R. F., Sarzi M., 2006, MNRAS, 373, 906

McNeil E. K., Arnaboldi M., Freeman K. C., Gerhard O. E., Coccato L., Das P., 2010, A&A, 518, A44+

Mehlert D., Saglia R. P., Bender R., Wegner G., 2000, A&AS, 141, 449

Mei S., Blakeslee J. P., Côté P., Tonry J. L., West M. J., Ferrarese L., Jordán A., Peng E. W., Anthony A., Merritt D., 2007, ApJ, 655, 144

Méndez R. H., Riffeser A., Kudritzki R., Matthias M., Freeman K. C., Arnaboldi M., Capaccioli M., Gerhard O. E., 2001, ApJ, 563, 135

Merritt D., 1984, ApJ, 276, 26

Merritt D., 1985, MNRAS, 214, 25P

Merritt D., Navarro J. F., Ludlow A., Jenkins A., 2005, ApJ, 624, L85

Merritt D., Tremblay B., 1994, AJ, 108, 514

Meza A., Navarro J. F., Steinmetz M., Eke V. R., 2003, ApJ, 590, 619

Mihos J. C., Harding P., Feldmeier J., Morrison H., 2005, ApJ, 631, L41

Mihos J. C., Hernquist L., 1994, ApJ, 437, L47

Moore B., Katz N., Lake G., Dressler A., Oemler A., 1996, Nature, 379, 613

Murante G., Arnaboldi M., Gerhard O., Borgani S., Cheng L. M., Diaferio A., Dolag K., Moscardini L., Tormen G., Tornatore L., Tozzi P., 2004, ApJ, 607, L83

Murante G., Giovalli M., Gerhard O., Arnaboldi M., Borgani S., Dolag K., 2007, MNRAS, 377, 2

Naab T., Burkert A., 2003, ApJ, 597, 893

Naab T., Jesseit R., Burkert A., 2006, MNRAS, 372, 839

Naab T., Johansson P. H., Ostriker J. P., 2009, ApJ, 699, L178

Naab T., Johansson P. H., Ostriker J. P., Efstathiou G., 2007, ApJ, 658, 710

Naab T., Khochfar S., Burkert A., 2006, ApJ, 636, L81

Nagino R., Matsushita K., 2009, A&A, 501, 157

Napolitano N. R., Capaccioli M., Romanowsky A. J., Douglas N. G., Merrifield M. R., Kuijken K., Arnaboldi M., Gerhard O., Freeman K. C., 2005, MNRAS, 357, 691

Napolitano N. R., Pannella M., Arnaboldi M., Gerhard O., Aguerri J. A. L., Freeman K. C., Capaccioli M., Ghigna S., Governato F., Quinn T., Stadel J., 2003, ApJ, 594, 172

Napolitano N. R., Romanowsky A. J., Capaccioli M., Douglas N. G., Arnaboldi M., Coccato L., Gerhard O., Kuijken K., Merrifield M. R., Bamford S. P., Cortesi A., Das P., Freeman K. C., 2010, ArXiv e-prints

Napolitano N. R., Romanowsky A. J., Coccato L., Capaccioli M., Douglas N. G., Noordermeer E., Gerhard O., Arnaboldi M., de Lorenzi F., Kuijken K., Merrifield M. R., O'Sullivan E., Cortesi A., Das P., Freeman K. C., 2009, MNRAS, 393, 329

Natarajan P., Kneib J.-P., Smail I., 2002, ApJ, 580, L11

Natarajan P., Kneib J.-P., Smail I., Ellis R. S., 1998, ApJ, 499, 600

Navarro J. F., Frenk C. S., White S. D. M., 1996, ApJ, 462, 563

Navarro J. F., Hayashi E., Power C., Jenkins A. R., Frenk C. S., White S. D. M., Springel V., Stadel J., Quinn T. R., 2004, MNRAS, 349, 1039

Navarro J. F., Ludlow A., Springel V., Wang J., Vogelsberger M., White S. D. M., Jenkins A., Frenk C. S., Helmi A., 2010, MNRAS, 402, 21

Nipoti C., Londrillo P., Ciotti L., 2002, MNRAS, 332, 901

Noyola E., Gebhardt K., Bergmann M., 2008, ApJ, 676, 1008

Nulsen P. E. J., Böhringer H., 1995, MNRAS, 274, 1093

Oñorbe J., Domínguez-Tenreiro R., Sáiz A., Serna A., 2007, MNRAS, 376, 39

Osipkov L. P., 1979, Pis ma Astronomicheskii Zhurnal, 5, 77

O'Sullivan E., Forbes D. A., Ponman T. J., 2001, MNRAS, 328, 461

Paolillo M., Fabbiano G., Peres G., Kim D., 2002, ApJ, 565, 883

Peletier R. F., Davies R. L., Illingworth G. D., Davis L. E., Cawson M., 1990, AJ, 100, 1091

Peng E. W., Ford H. C., Freeman K. C., 2004, ApJ, 602, 705

Perlmutter S., Aldering G., Goldhaber G., Knop R. A., Nugent P., Castro P. G., Deustua S., Fabbro S., Goobar A., Groom D. E., Hook I. M., Kim A. G., Kim M. Y., Lee J. C., and 19 coauthors 1999, ApJ, 517, 565

Pinkney J., Gebhardt K., Bender R., Bower G., Dressler A., Faber S. M., Filippenko A. V., Green R., Ho L. C., Kormendy J., Lauer T. R., Magorrian J., Richstone D., Tremaine S., 2003, ApJ, 596, 903

Prada F., Klypin A. A., Simonneau E., Betancort-Rijo J., Patiri S., Gottlöber S., Sanchez-Conde M. A., 2006, ApJ, 645, 1001

Proctor R. N., Forbes D. A., Romanowsky A. J., Brodie J. P., Strader J., Spolaor M., Mendel J. T., Spitler L., 2009, MNRAS, 398, 91

Prugniel P., Simien F., 1996, A&A, 309, 749

Prugniel P., Simien F., 1997, A&A, 321, 111

Rees M. J., Ostriker J. P., 1977, MNRAS, 179, 541

Richstone D. O., 1980, ApJ, 238, 103

Richstone D. O., Tremaine S., 1984, ApJ, 286, 27

Riess A. G., Filippenko A. V., Challis P., Clocchiatti A., Diercks A., Garnavich P. M., Gilliland R. L., Hogan C. J., Jha S., Kirshner R. P., Leibundgut B., Phillips M. M., Reiss D., Schmidt B. P., and 6 coauthors 1998, AJ, 116, 1009

Rix H., de Zeeuw P. T., Cretton N., van der Marel R. P., Carollo C. M., 1997, ApJ, 488, 702

Robertson B., Cox T. J., Hernquist L., Franx M., Hopkins P. F., Martini P., Springel V., 2006, ApJ, 641, 21

Romano-Díaz E., Shlosman I., Hoffman Y., Heller C., 2008, ApJ, 685, L105

Romanowsky A. J., Douglas N. G., Arnaboldi M., Kuijken K., Merrifield M. R., Napolitano N. R., Capaccioli M., Freeman K. C., 2003, Science, 301, 1696

Romanowsky A. J., Kochanek C. S., 2001, ApJ, 553, 722

Romanowsky A. J., Strader J., Spitler L. R., Johnson R., Brodie J. P., Forbes D. A., Ponman T., 2009, AJ, 137, 4956

Royer F., Blecha A., North P., Simond G., Baratchart S., Cayatte V., Chemin L., Palsa R., 2002, in Starck J.-L., Murtagh F. D., eds, Astronomical Data Analysis II. Edited by Starck, Jean-Luc; Murtagh, Fionn D. Proceedings of the SPIE, Volume 4847, pp. 184-194 (2002). Vol. 4847 of Presented at the Society of Photo-Optical Instrumentation Engineers (SPIE) Conference, Toward accurate radial velocities with the fiber-fed GIRAFFE multi-object VLT spectrograph. pp 184–194

Rubin V. C., Thonnard N., Ford Jr. W. K., 1978, ApJ, 225, L107

Rudick C. S., Mihos J. C., McBride C., 2006, ApJ, 648, 936

Ruff A. J., Gavazzi R., Marshall P. J., Treu T., Auger M. W., Brault F., (UCSB Melbourne U. o., IAP SLAC 2010, ArXiv e-prints

Saglia R. P., Kronawitter A., Gerhard O., Bender R., 2000, AJ, 119, 153

Sáiz A., Domínguez-Tenreiro R., Serna A., 2004, ApJ, 601, L131

Sancisi R., Allen R. J., Sullivan III W. T., 1979, A&A, 78, 217

Saracco P., Longhetti M., Andreon S., 2009, MNRAS, 392, 718

Sarazin C. L., 1986, Reviews of Modern Physics, 58, 1

Sarazin C. L., 1990, in H. A. Thronson Jr. & J. M. Shull ed., The Interstellar Medium in Galaxies Vol. 161 of Astrophysics and Space Science Library, Cooling flows and X-ray emission in early-type galaxies. pp 201–238

Schindler S., Binggeli B., Böhringer H., 1999, A&A, 343, 420

Schindler S., Böhringer H., 1993, A&A, 269, 83

Schombert J. M., 1986, ApJS, 60, 603

Schuberth Y., Richtler T., Dirsch B., Hilker M., Larsen S. S., Kissler-Patig M., Mebold U., 2006, A&A, 459, 391

Schuberth Y., Richtler T., Hilker M., Dirsch B., Bassino L. P., Romanowsky A. J., Infante L., 2010, A&A, 513, A52+

Schwarzschild M., 1979, ApJ, 232, 236

Sembach K. R., Tonry J. L., 1996, AJ, 112, 797

Sérsic J. L., 1963, Boletin de la Asociacion Argentina de Astronomia La Plata Argentina, 6, 41

Shapley A. E., Steidel C. C., Pettini M., Adelberger K. L., 2003, ApJ, 588, 65

Shen J., Gebhardt K., 2010, ApJ, 711, 484

Silk J., 1977, ApJ, 211, 638

Simien F., Prugniel P., 1997, A&AS, 122, 521

Sizikov V. S., 1969, Astrophysics, 5, 150

Spolaor M., Forbes D. A., Hau G. K. T., Proctor R. N., Brough S., 2008, MNRAS, 385, 667

Spolaor M., Hau G. K. T., Forbes D. A., Couch W. J., 2010, MNRAS, 408, 254

Statler T. S., Dejonghe H., Smecker-Hane T., 1999, AJ, 117, 126

Syer D., Tremaine S., 1996, MNRAS, 282, 223

Teodorescu A. M., Méndez R. H., Saglia R. P., Riffeser A., Kudritzki R., Gerhard O. E., Kleyna J., 2005, ApJ, 635, 290

Thomas J., Jesseit R., Saglia R. P., Bender R., Burkert A., Corsini E. M., Gebhardt K., Magorrian J., Naab T., Thomas D., Wegner G., 2009, MNRAS, 393, 641

Thomas J., Saglia R. P., Bender R., Thomas D., Gebhardt K., Magorrian J., Corsini E. M., Wegner G., 2005, MNRAS, 360, 1355

Thomas J., Saglia R. P., Bender R., Thomas D., Gebhardt K., Magorrian J., Corsini E. M., Wegner G., 2007, MNRAS, 382, 657

Thomas J., Saglia R. P., Bender R., Thomas D., Gebhardt K., Magorrian J., Corsini E. M., Wegner G., 2009, ApJ, 691, 770

Thomas J., Saglia R. P., Bender R., Thomas D., Gebhardt K., Magorrian J., Richstone D., 2004, MNRAS, 353, 391

Tiret O., Salucci P., Bernardi M., Maraston C., Pforr J., 2010, MNRAS, pp 1737–+

Tonry J. L., 1983, ApJ, 266, 58

Tonry J. L., Dressler A., Blakeslee J. P., Ajhar E. A., Fletcher A. B., Luppino G. A., Metzger M. R., Moore C. B., 2001, ApJ, 546, 681

Toomre A., 1977, in B. M. Tinsley & R. B. Larson ed., Evolution of Galaxies and Stellar Populations Mergers and Some Consequences. pp 401–+

Tortora C., Napolitano N. R., Romanowsky A. J., Capaccioli M., Covone G., 2009, MNRAS, 396, 1132

Trager S. C., Faber S. M., Worthey G., González J. J., 2000, AJ, 120, 165

Tremblay B., Merritt D., 1996, AJ, 111, 2243

Trentham N., Tully R. B., Mahdavi A., 2006, MNRAS, 369, 1375

Treu T., Ellis R. S., Liao T. X., van Dokkum P. G., 2005, ApJ, 622, L5

Treu T., Koopmans L. V. E., 2004, ApJ, 611, 739

Trinchieri G., Fabbiano G., 1985, ApJ, 296, 447

Trinchieri G., Fabbiano G., Canizares C. R., 1986, ApJ, 310, 637

Trinchieri G., Fabbiano G., Kim D., 1997, A&A, 318, 361

Trinchieri G., Pellegrini S., Wolter A., Fabbiano G., Fiore F., 2000, A&A, 364, 53

Trujillo I., Burkert A., Bell E. F., 2004, ApJ, 600, L39

Trujillo I., Cenarro A. J., de Lorenzo-Cáceres A., Vazdekis A., de la Rosa I. G., Cava A., 2009, ApJ, 692, L118

Trujillo I., Feulner G., Goranova Y., Hopp U., Longhetti M., Saracco P., Bender R., Braito V., Della Ceca R., Drory N., Mannucci F., Severgnini P., 2006, MNRAS, 373, L36

van Albada T. S., Bahcall J. N., Begeman K., Sancisi R., 1985, ApJ, 295, 305

van de Ven G., Hunter C., Verolme E. K., de Zeeuw P. T., 2003, MNRAS, 342, 1056

van den Bosch R. C. E., de Zeeuw P. T., 2010, MNRAS, 401, 1770

van den Bosch R. C. E., van de Ven G., Verolme E. K., Cappellari M., de Zeeuw P. T., 2008, MNRAS, 385, 647

van der Marel R. P., 1994, MNRAS, 270, 271

van der Marel R. P., Franx M., 1993, ApJ, 407, 525

van Dokkum P. G., Franx M., Förster Schreiber N. M., Illingworth G. D., Daddi E., Knudsen K. K., Labbé I., Moorwood A., Rix H., Röttgering H., Rudnick G., Trujillo I., van der Werf P., and 3 coauthors 2004, ApJ, 611, 703

van Dokkum P. G., Franx M., Kriek M., Holden B., Illingworth G. D., Magee D., Bouwens R., Marchesini D., Quadri R., Rudnick G., Taylor E. N., Toft S., 2008, ApJ, 677, L5

Verolme E. K., de Zeeuw P. T., 2002, MNRAS, 331, 959

Villaver E., Manchado A., García-Segura G., 2002, ApJ, 581, 1204

Visvanathan N., Sandage A., 1977, ApJ, 216, 214

Weijmans A., Cappellari M., Bacon R., de Zeeuw P. T., Emsellem E., Falcón-Barroso J., Kuntschner H., McDermid R. M., van den Bosch R. C. E., van de Ven G., 2009, MNRAS, 398, 561

Weil M. L., Bland-Hawthorn J., Malin D. F., 1997, ApJ, 490, 664

Weil M. L., Hernquist L., 1996, ApJ, 460, 101

Werner N., Zhuravleva I., Churazov E., Simionescu A., Allen S. W., Forman W., Jones C., Kaastra J. S., 2009, MNRAS, 398, 23

West M. J., Blakeslee J. P., 2000, ApJ, 543, L27

White III R. E., Sarazin C. L., 1991, ApJ, 367, 476

Williams B. F., Ciardullo R., Durrell P. R., Vinciguerra M., Feldmeier J. J., Jacoby G. H., Sigurdsson S., von Hippel T., Ferguson H. C., Tanvir N. R., Arnaboldi M., Gerhard O., Aguerri J. A. L., Freeman K., 2007, ApJ, 656, 756

Woodley K. A., Harris W. E., Beasley M. A., Peng E. W., Bridges T. J., Forbes D. A., Harris G. L. H., 2007, AJ, 134, 494

Zhang Z., Xu H., Wang Y., An T., Xu Y., Wu X., 2007, ApJ, 656, 805

Zibetti S., White S. D. M., Schneider D. P., Brinkmann J., 2005, MNRAS, 358, 949

ACKNOWLEDGMENTS

I am grateful to my supervisor Ortwin Gerhard and the International Max Planck Research School for giving me the opportunity of doing a PhD in astrophysics. I am also very thankful to my tutors at university, Philipp Podsiadlowski and Christian Wolf, and my masters project supervisors, Roger Davies and Davor Krajnović, for encouraging me to pursue a PhD. I also thank Ortwin for always keeping me on the ball and for his thorough approach to science, which have resulted in much better papers.

I thank the Max Planck Institute for Extraterrestrial Physics, the Excellence Cluster, the Marie Curie fellowships, and Mount Stromlo Observatory for the research and travel funding that have financed my PhD and enabled me to attend conferences all over the world. This in addition to the numerous lectures and seminars at the Max Planck institutes and Excellence Cluser in Garching have very much augmented my educational experience.

I would like to thank all the scientists that I have had the opportunity to work with: Eugene Churazov, Hans Böhringer, Ken Freeman, and the Planetary Nebula Spectrograph team. It has been a pleasure to be a part of the dynamics group, and for this I thank Orwtin, Lodovico, Inma, Kanak, Lucia, Giulia, Xufen, Emily, and Arianna. I would also like to thank Ralf Bender and Roberto Saglia in the OPINAS group for many useful discussions.

The friends that I have made in Munich have made the experience here especially enjoyable. Margie, Paula, Tom, Hauke, and Julius have always been there. Knitting exchanges and the gym spring immediately to mind when I think of Margie and Paula, and international cooking when I think of Tom. The lovely Damian was the youngest person I had ever met, and I am very glad to have been part of the first few years of his life. Emily and Arianna were only here for a year but we had a lot of fun together. I am especially indebted to Emily for looking after me so well in Australia. It has been great to be with Caroline, Silvia, Shy, and Mona for the last few years and it is very sad to see our group dissipate. I thank Eva for being my gig buddy and both Eva and Niv for being the ideal postdocs: cool and with lots of papers. I thank Brigitta for asking me to do the Arangetram with her, and Aunty and Simone for supporting us the whole way.

I have missed my dad, mum, Tanya and Anupam very much. My mum has been fantastic in always cooking me copious amounts of food to take back with me. I thank my dad for picking me up at any airport in the south of England at any time. I thank Michael and Felicity for making me feel very much at home in Victoria while I have been writing up. Finally I would like to thank James to whom I have the greatest pleasure of being engaged and who has been incredibly supportive throughout the whole thesis.

COLOPHON

This thesis was typeset with LaTeX 2_ε using Hermann Zapf's *Palatino* and *Euler* type faces (Type 1 PostScript fonts *URW Palladio L* and *FPL* were used). The listings are typeset in *Bera Mono*, originally developed by Bitstream, Inc. as "Bitstream Vera". (Type 1 PostScript fonts were made available by Malte Rosenau and Ulrich Dirr.)

The typographic style was inspired by *The Elements of Typographic Style* (Bringhurst, 2002). It is available for LaTeX via CTAN at http://www.ctan.org/tex-archive/macros/latex/contrib/classicthesis/.